THIRD ORDER NONLINEARITY OF ORGANIC MOLECULES

by

HONGHUA HU
B.S. Zhejiang University, China 2003
M.S. Zhejiang University, China 2006

A dissertation submitted in partial fulfillment of the requirements
for the degree of Doctor of Philosophy
in CREOL, The College of Optics and Photonics
at the University of Central Florida
Orlando, Florida

Summer Term
2012

Major Professors: Eric W. Van Stryland and David J. Hagan

ABSTRACT

The main goal of this dissertation is to investigate the third-order nonlinearity of organic molecules. This topic contains two aspects: two-photon absorption (2PA) and nonlinear refraction (NLR), which are associated with the imaginary and real part of the third-order nonlinearity ($\chi^{(3)}$) of the material, respectively. With the optical properties tailored through meticulous molecular structure engineering, organic molecules are promising candidates to exhibit large third-order nonlinearities.

Both linear (absorption, fluorescence, fluorescence excitation anisotropy) and nonlinear (Z-scan, two-photon fluorescence, pump-probe) techniques are described and utilized to fully characterize the spectroscopic properties of organic molecules in solution or solid-state form. These properties are then analyzed by quantum chemical calculations or other specific quantum mechanical model to understand the origins of the nonlinearities as well as the correlations with their unique molecular structural features. These calculations are performed by collaborators.

The 2PA study of organic materials is focused on the structure-2PA property relationships of four groups of dyes with specific molecular design approaches as the following: (1) Acceptor-π-Acceptor dyes for large 2PA cross section, (2) Donor-π-Acceptor dyes for strong solvatochromic effects upon the 2PA spectra, (3) Near-infrared polymethine dyes for a symmetry breaking effect, (4) Sulfur-squaraines vs. oxygen-squaraines to study the role of sulfur atom replacement upon their 2PA spectra. Additionally, the 2PA spectrum of a solid-state single crystal made from a Donor-π-Acceptor dye is measured, and the anisotropic nonlinearity is studied with respect to different incident polarizations. These studies further advance our

understanding towards an ultimate goal to a predictive capability for the 2PA properties of organic molecules.

The NLR study on molecules is focused on the temporal and spectral dispersion of the nonlinear refraction index, n_2, of the molecules. Complicated physical mechanisms, originating from either electronic transitions or nuclei movement, are introduced in general. By adopting a prism compressor / stretcher to control the pulsewidth, an evolution of n_2 with respect to incident pulsewidth is measured on a simple inorganic molecule –carbon disulfide (CS_2) in neat liquid at 700 nm and 1064 nm to demonstrate the pulsewidth dependent nonlinear refraction. The n_2 spectra of CS_2 and certain organic molecules are measured by femtosecond pulses, which are then analyzed by a 3-level model, a simplified "Sum-over-states" quantum mechanical model. These studies can serve as a precursor for future NLR investigations.

This dissertation is dedicated to my family.

ACKNOWLEDGMENTS

It is a special privilege to have this opportunity working under the guidance of Drs. Eric Van Stryland and David Hagan. I am grateful for their advices and patience, which helped me pass through all the difficulties despite their busy schedule. To meet my professors' expectation is not an easy task, but it eventually taught me more than I could imagine.

I am so indebt to Dr. Olga Przhonska, who provides me not only the molecules but also guided me into and through the research in organics. I would also thank Drs. Scott Webster, Dmitry Fishman, and Lazaro Padilha, who taught me almost every experimental skill in the lab. The research conducted in NLO group is truly collaborative, so I would express my acknowledgement to our collaborators in the United States and all over the world. Without their support, the comprehensive work included in this dissertation would not have been possible.

My special thanks go to Dr. George Stegeman, who is not only a great professor showing me the magic of nonlinear optics but also an aspiring cheerleader whose encouragement sometimes was indispensable in my pursuit of this PhD degree, especially at difficult times. It is really a pleasant experience to work with my fellow NLO team members Trenton Ensley, Davorin Pecili, Himansu Pattanaik, Mattew Reichert, Manuel Ferdinandus, Brendan Turnbull, and former members Drs. Claudiu Cirloganu, Gero Nootz, Peter Olszak and Mihaela Balu. Team work is the spirit to survive in this group.

I would like to express my appreciation to my committee (and former) members Dr. Boris Zeldovich, Dr. Florencio Hernandez and Dr. Kevin Belfield for their valuable advices in my dissertation. Finally I would thank all my friends and acquaintances in CREOL, and my friends in Dr. Kevin Belfield's group of chemistry department.

TABLE OF CONTENTS

LIST OF FIGURES

LIST OF TABLES

LIST OF NOMENCLATURE

Acronym/Unit	Description
1PA	One-Photon Absorption
1PF	One-Photon Fluorescence
2PA	Two-Photon Absorption
2PF	Two-Photon Absorption Induced Fluorescence
ACN	Acetonitrile
AOS	All Optical Switching
ASF	Asymmetrical Form
BLA	Bond Length Alternation
cm	centimeter
CS_2	Carbon Disulfide
CW	Continuous Wave
D	Debye (unit of dipole moment, equal to 3.33×10^{-30} C·m)
D-2PA	Degenerate Two-Photon Absorption
DCM	Dichloromethane
DFG	Difference Frequency Generation
DOB	Diethylamino-coumarin-dioxaborine
ESA	Excited-State Absorption
eV	electron volt (1.6×10^{-19} V)
FOM	Figure of Merit
fs	femtosecond

FWHM	Full-Width-of-Half-Maximum
GM	Goppert-Mayer
GVD	Group Velocity Dispersion
GW	Gigawatt
HOMO	Highest Occupied Molecular Orbital
HW1/e^2M	Half-Width-1/e^2-of-Maxium
ISC	Inter-system Crossing
ISRE	Intermediate State Resonance Enhancement
kHz	Kilohertz
LUMO	Lowest Unoccupied Molecular Orbital
mJ	millijoule
μJ	microJoule
μm	micrometer
MO	Molecular Orbital
NIR	Near-Infrared
nJ	nanoJoule
nm	nanometer
NLO	Nonlinear Optics
NLR	Nonlinear Refraction
ns	nanosecond
OD	Optical Density
OKE	Optical Kerr Effect
OPG/OPA	optical parametric generator / amplifier

O-SD	Oxygen Squaraine
PD	Polymethine Dye
PMT	Photomultiplier tube
ps	picosecond
pTHF	poly-Tetrahydrofuran
RGM	Refractive Goppert-Mayer
SB	Symmetry Breaking
SF	Symmetrical Form
SFG	Sum Frequency Generation
SHG	Second Harmonic Generation
SOS	Sum-Over-States
S-SD	Sulfur Squaraine
SO-SD	Sulfur-Oxygen Squaraine
UV	Ultra Violet
WLC	White-Light Continuum

CHAPTER 1 INTRODUCTION

1.1 Background and Motivation

The third order nonlinearity, namely the third order susceptibility ($\chi^{(3)}$), of matter has been responsible for diverse physical phenomena including but not limited to third-harmonic generation, two-photon absorption (2PA), nonlinear refraction (NLR), four-wave mixing (FWM), Raman Spectroscopy, *etc* [1,2]. Since it is too wide a topic for this dissertation to deal with, we only focus on two important phenomena: two-photon absorption and nonlinear refraction.

The two-photon absorption (2PA) is a process of simultaneous absorption of two photons to promote an electron from its initial ground state into an excited state. It was first theoretically predicted by Göppert-Mayer in the 1930s [3]; however, not until the invention of the laser in the 1960s was the experimental demonstration of 2PA possible [4]. Comparing to one-photon absorption (1PA), there are two key features of 2PA: 1) the energy of each photon is usually below the bandgap (lowest transition energy) of the material, i.e., negligible 1PA, which allows the photon to penetrate deep into the material. Since the excitation wavelength is also less than the main transition energy, and usually in the near-infrared (NIR) wavelength range, 2PA excitation also reduces the scattering inside the medium and is less likely to cause photochemical decomposition of material. 2) The probability of 2PA is proportional to the square of the irradiance, as opposed to the linear dependence upon input irradiance in 1PA; therefore, 2PA excitation, as well as the following process triggered by 2PA (e.g. fluorescence, *etc*), is very localized inside the medium. The small depth of focus (proportional to z^{-4} in 2PA, as opposed to z^{-2} in 1PA, where z is the axial propagation distance) allows more freedom of manipulation of the beam in 3D space. Due to these significant advantages of 2PA, there are a great variety of

applications including but not limited to optical limiting [5,6], biological microscopic imaging [7], optical data storage [8], micro-fabrication [9], 2PA induced lasing [10], and photodynamic therapy [11] *etc*.

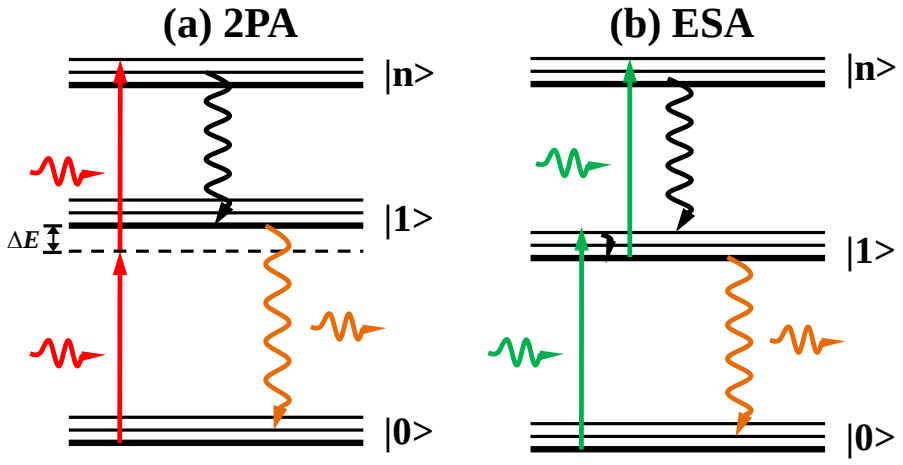

Figure 1.1: Schematic energy level diagram of 2PA (a) and ESA (b)

In the formalism of nonlinear optics, the 2PA is related with the imaginary part of $\chi^{(3)}$, as to be discussed in Chapter 2. It is conceptually different from another two-photon process, so called excited-state absorption (ESA). Similar to 2PA, ESA is also a two-photon-involved process; however, these two photons are absorbed *sequentially*, as opposed to *simultaneously* in 2PA. The schematic energy level diagram of 2PA and ESA are shown in Figure 1.1. For 2PA, since the photon energy is below the lowest transition energy of the molecular system, the energy mismatch (ΔE as shown in Figure 1.1a) between the photon energy and the lowest transition energy requires the second photon energy to arrive within ultrashort time period (~10^{-15} seconds for 2PA in the visible [12]) determined by the uncertainty principle [13] to complete the 2PA process. This is the fundamental reason 2PA process is an instantaneous process, which is only possible at relatively large irradiance of the excitation (to increase the probability of finding two photons at

ultrashort time scale). In ESA, the energy of the first photon is equal or larger than the lowest molecular transition energy, which directly promotes the ground state electron into the 1st excited state (see Figure 1.1b). This is a real transition so the electron can stay in the 1st excited state for the lifetime of the state, i.e. typically 10^{-8}~10^{-12} seconds for typical organic dyes. During this period, another photon can be absorbed, followed by exciting the 1st excited state electron into higher excited states. In this sense, ESA is a cascaded 1PA ($\chi^{(1)}:\chi^{(1)}$) process, of which the induced nonlinearity is cumulative (i.e. the magnitude of absorption depends upon the excitation pulsewidth) and is non-instantaneous. Note that ESA can also be induced by 2PA, of which the electron is promoted by 2PA, followed by a rapid relaxation to the 1st excited state, and then excited into higher excited states by absorbing a third photon [14]. This is actually a higher order ($\chi^{(3)}:\chi^{(1)}$) process. Without distinguishing these two processes, the magnitude of 2PA can be overestimated by orders of magnitudes [15].

The nonlinear refraction (NLR) is a phenomenon related with the change of material refractive index due to change of the input excitation irradiance. This is essentially an optical Kerr effect, of which the driving field is an optical field, as opposed to electro-optic Kerr effect driven by applied electric field of low frequency. In contrast to the 2PA process, NLR is connected with the real part of $\chi^{(3)}$, and only affects the phase of light propagating through the material without absorption necessarily taking place. NLR leads to self- or cross-phase modulation of the beams involved. The physical origin of NLR is much more complicated compared to 2PA, involving both electronic transitions and nuclear response, and thus depends upon the duration of excitation. Detailed introduction of various origins can be found in Chapter 5. The first experimental demonstration of nonlinear refraction is probably the self-focusing effect observed soon after the invention of the Ruby laser [16,17]. For a medium of which the

refractive index increases with input irradiance, when a strong laser beam travels through this medium, the transverse irradiance profile induces a refractive index gradient of the medium acting as a positive lens, which causes the laser beam itself to focus inside the medium. Nonlinear refraction is also one of the key mechanisms of soliton generation [18] and white-light continuum (WLC) generation [19], *etc*. One important application of the NLR is ultrafast all-optical switching (AOS), of which a material with large nonlinear refractive index (n_2) but minimum nonlinear absorption (e.g. 2PA, excited state absorption, Raman loss, *etc*) is desirable [20]. A figure of merit (FOM), equivalent or proportional to $\mathrm{Re}(\chi^{(3)})/\mathrm{Im}(\chi^{(3)})$, is then introduced [20,21] to evaluate how well a device can perform in AOS without significant detrimental effect of the 2PA loss.

Organic materials, with the capability of the optical properties being tailored by molecular structure modification, are good candidates to study their nonlinear optical properties [22]. A class of organic dyes of particular interest in this dissertation is called linear π-conjugated chromophores, which contains a molecular chain composed by alternate single and double covalent bonds, as shown in Figure 1.2. A single bond contains only one σ bond (axial overlap of *p* type atomic orbitals), while the double bond contains a σ-bond and a π-bond (featured by lateral overlap of *p* type atomic orbitals) [23]. The further overlap of these π-bonds on the molecular chain enables electrons (called π-electrons) of these π-bonds to move freely along the molecular chain; therefore such a molecular chain is usually called a π-conjugated chain. Two end groups are usually attached to the end of π-conjugated chain, represented by R_1 and R_2 in Figure 1.2. In some cases, a bridge group is inserted into the center of the conjugation chain to maintain chemical stability or further enhance the optical nonlinearity. Linear π-conjugated chromophores often manifest very large transition dipole moments [24,25] that can induce strong

optical nonlinearities at the molecular level. Substitution with different end groups, i.e., electron donors (D) or electron acceptors (A), yields different structural architectures: symmetrical quadrupolar D-π-D (or D-π-A-π-D), A-π-A (or A-π-D-π-A), or asymmetrical dipolar D-π-A (or push-pull) dyes demonstrating different optical properties.

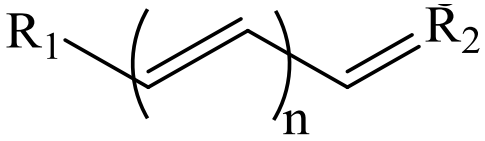

Figure 1.2: Schematic structure of a linear π-conjugated chromophore; n is the length of the conjugation chain; R_1 and R_2 are end groups

The 2PA properties of organic material have been under investigation for decades. The very large 2PA cross section of linear π-conjugated molecular system was first discovered by Albota *et al* in 1998 [26]. It triggered chemists to synthesize linear π-conjugated chromophores with different structural modifications to study their optical properties. Structure-property studies have been initiated by various research groups [24,27-35]. This structure-property relations contain of structural modifications in terms of symmetry, conjugation length, the donor or acceptor strength, solvism, *etc*, and determining how these changes affect properties, here the NLO properties. Quantum chemical calculations are also involved to understand molecular geometry, charge distribution and energy level structure of the chromophores [36-38]. In this dissertation, we will continue our 2PA study of linear π-conjugated chromophore into the NIR wavelengths range, and with more meticulous structure modification to its end group or bridges. More important is the phase of the organic material from liquid solution to solid-state, of which the molecular density is maximized. Therefore strong molecular interactions between adjacent

chromophore molecules are necessary to be taken into account. This will further enrich our knowledge base of structure-2PA property relations of organic materials.

On the basis of Kramers-Krönig relations [39] for the third order nonlinearity, each 2PA transition would induce a certain amount of variation of nonlinear refractive index, n_2, near the 2PA peak, given that the 2PA band is far below the absorption edge. As the photon energy approaches to the absorption edge of the material, a strong AC-stark effect, seen in semiconductors [40], leads to a strong negative n_2 of the material.. Although the study of 2PA of organic materials is diverse and rich in the nonlinear optics community, the research on nonlinear refraction of organic materials is relatively scarce. Part of the reason is that the measurement for organic molecules is usually conducted in the liquid solutions. Since the 2PA from solvent is essentially zero at the wavelength of interest, the 2PA measurement only probes the 2PA of the solute and thus is background-free from any solvent influence. On the other hand, the NLR from solvent is dominantly large due to the relatively small concentration of the solute ($<10^{-3}$ M); a separation of nonlinear refraction from solute and solvent is usually beyond the signal-noise limit of current experimental setups. There are a few reports showing large NLR of bisdioxaborine [41], extended-squaraine [24], and bis(diarylaminostyryl) chromophores [42] in solution or thin-film form at certain wavelengths despite the presence of large 2PA which reduces the FOM for AOS applications. More recently, a molecular design strategy to improve the FOM at certain wavelength is proposed, as shown in Figure 1.3. An ideal molecule should have two separate 2PA states (marked as $|m\rangle_{2PA}$ and $|n\rangle_{2PA}$ in Figure 1.3) below the twice of energy of the lowest 1PA state (marked as $|1\rangle_{1PA}$) [20]. In this case, the incident photon energy can be tuned close to $|1\rangle_{1PA}$ state, but with twice the photon energy between $|m\rangle_{2PA}$ and $|n\rangle_{2PA}$ states.

Therefore, a large negative n_2 (real part of $\chi^{(3)}$) is achieved without detrimental 2PA loss (imaginary part of $\chi^{(3)}$). This approach is realized for bis(selenopyrylium) heptamethine dye [20].

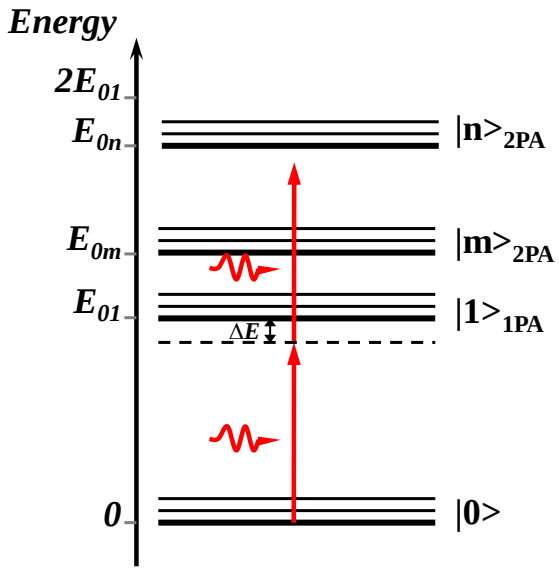

Figure 1.3: Strategy to improve FOM of a molecular system with enhanced negative n_2. [20]

In this dissertation, we will start with the study of NLR dispersion of a neat liquid composed of a simple molecule –carbon disulfide (CS_2), and its dependence upon input pulsewidth to demonstrate the mixed origins of the NLR; furthermore, with the NLR dispersion of some organic molecules obtained by an improvement of the single wavelength Z-scan technique, we will utilize the quantum mechanical approach to analyze both the 2PA spectrum and NLR dispersion of these molecules. These investigations will serve as a precursor for more advanced studies of the structure-NLR properties of organic molecules.

1.2 Dissertation Statement

The purpose of this dissertation is to study the third-order nonlinearity of organic molecules which can be divided into two parts. The first part is to further advance the investigation of the structure-2PA property of the organic molecules absorbing at NIR wavelengths. Four sets of dyes are introduced with different approaches to the structural modifications. Nonlinear spectroscopic characterization, joint with linear spectroscopic measurements, is performed for these dyes to investigate the spectral positions and magnitudes of 2PA. Quantum chemical analysis is performed to correlate the linear and nonlinear optical properties with the structure motif changes. Furthermore, the investigation of 2PA is extended to an organic single crystal, which provides information of molecular interactions in the solid-state phase. The second part is to study the NLR properties of molecules starting from a simple inorganic molecule $-CS_2$, and then extend this certain organic dyes. The complicated physical origin of NLR is demonstrated by the pulsewidth dependent magnitude of the NLR, while the NLR dispersion is consistent with a relatively simple quantum mechanical model.

1.3 Dissertation Outline

This dissertation is organized as the following: Chapter1 introduces the concept of the third-order nonlinearity and provides the motivation to study optical nonlinearities of a specific type of organic molecules: linear π-conjugated chromophore. Chapter 2 introduces the formalism of the third-order optical nonlinearity in nonlinear optics and introduces a quantum mechanical model ("Sum-over-states" model) to describe the dispersion behavior of the bound electronic third-order nonlinearity of materials. Chapter 3 discusses the linear and nonlinear

spectroscopic characterization techniques involved in this dissertation. Chapter 4 introduces the molecular design approach to extend the absorption of organic dyes into the NIR wavelength range without the cost of photochemical stability; four groups of dyes with unique structural modifications are included to study the 2PA properties of these dyes in correlation with their chemical structures. In addition to their solution-based study, we also investigate 2PA properties of a single crystal made from one of these dyes. Quantum chemical analysis is also presented to help understand the origin of these 2PA bands (This analysis is performed by our collaborators). Chapter 5 briefly introduces the multiple origins of nonlinear refraction of the material, and then studies the nonlinear refraction of CS_2 in terms of its input pulsewidth and wavelength dependence. It is further extended to certain linear π-conjugated chromophores to measure their NLR dispersion, which is then analyzed by a simple 3-level model. Chapter 6 gives concluding remarks and proposes work for further research.

CHAPTER 2 THE THEORY OF BOUND ELECTRONIC THIRD ORDER NONLINEARITIES FOR A MOLECULAR SYSTEM

As a branch of physics, optical science basically deals with the fundamental rules governing the interaction between light and matter. Such interaction contains two mutual aspects: the incident light field induces a property change of the matter; and perturbation in turn modifies the optical field of light. In the "linear" optics domain, the incident light is rather weak in the sense that the induced material response is *linearly* proportional to the optical field. The absorption and refractive index of the material is thus independent of the incident light field. It is the invention of an intense and coherent light source – the Laser, which dramatically changed the behavior of material "reacting" to the incident light. The nonlinear response of materials upon the application of a strong optical field brings in a whole new world of exciting physical phenomena which gives birth to "nonlinear optics".

While the subject of nonlinear optics is too broad to handle in the scope of this dissertation, we mainly focus our discussion on the third-order nonlinearity of material, more specifically, the irradiance dependent absorption and refraction of the molecular system. This chapter begins with a brief description of linear and nonlinear material polarization, which is the "reaction" of material upon the input radiation and the driving term for linear and nonlinear response. The concept of two-photon absorption (2PA) and nonlinear refraction (NLR) is then introduced as part of the third order nonlinearity of the material. A "sum-over-states" (SOS) model is introduced to describe the bound electronic nonlinearity of the material [43]. To simplify the "SOS" model, a so called "3-level" model, which considers only the 3 most important electronic states involved in the transitions, is thereby derived. The spectral dispersion of 2PA and bound-electronic NLR is discussed under this "3-level" model.

2.1 Polarization of the Material

To quantify the material response upon light radiation, a macroscopic polarization P of the material is introduced as the function of the *total* electric field E as:

$$P(t) = \sum_{n=1} P^{(n)}(t) = \varepsilon_0 \sum_{n=1} \int_{-\infty}^{\infty} .. \int_{-\infty}^{\infty} \int_{-\infty}^{\infty} \chi_{..}^{(n)}(t-t_1';t-t_2';t-t_3';...t-t_n') \times E_1(t_1')E_2(t_2')E_3(t_3')..E_n(t_n')dt_1'dt_2'dt_3'..dt_n' \quad (2.1)$$

Where $P^{(n)}$ corresponds to n-th order polarization of the material induced by an n-times interaction of the incident electric field. $\chi^{(n)}$ is the n-th order susceptibility of the material as a function of space (not shown here) and time t. The fact that the induced material polarization is a result of a temporal convolution between the material susceptibility and the input electric field generally implies that the response of a material can be *non-instantaneous*. Not shown in this equation is that the response of the material can also be non-local; however, we are not explicitly addressing this problem in this dissertation because most molecular system involved have a local response.

To make the problem simple, we assume E_1, E_2, E_3 …E_n are monochromatic continuous wave (CW) with frequency ω_1, ω_2, ω_3…ω_n, respectively. Equation 2.1 can also be transformed into Equation 2.2 by the principle of Fourier transform [1]:

$$P_i(\omega) = \sum_{n=1} P^{(n)}(\omega) = \varepsilon_0 \sum_{n=1} \left(\int_{-\infty}^{\infty} ... \int_{-\infty}^{\infty} \int_{-\infty}^{\infty} \chi^{(n)}(-\omega;\omega_1,\omega_2,\omega_3,...\omega_n) \times E_1(\omega_1)E_2(\omega_2)E_3(\omega_3)...E_n(\omega_n)\delta(\omega-\omega_1-\omega_2-\omega_3-...-\omega_n)d\omega_1 d\omega_2 d\omega_3 ...d\omega_n \right) \quad (2.2)$$

where $\chi^{(n)}(\omega)$ is proportional to Fourier transform of $\chi^{(n)}(t)$ written as

$$\chi_{\cdot\cdot}^{(n)}(-\omega;\omega_1,\omega_2,\omega_3,...\omega_n)=\int_{-\infty}^{\infty}...\int_{-\infty}^{\infty}\int_{-\infty}^{\infty}\chi_{\cdot\cdot}^{(n)}(t_1,t_2,...t_n)e^{-i(\omega_1 t_1+\omega_2 t_2+\omega_3 t_3+...+\omega_n t_n)}dt_1dt_2dt_3...dt_n. \qquad (2.3)$$

Here we explicitly write $\chi^{(n)}(-\omega;\ \omega_1,\ \omega_2,\ \omega_3)$ to illustrate the result of interaction with *n* electric fields.

Linear optics keeps only the 1st order polarization of the material, and thus the linear absorption coefficient and linear refractive index are determined by $\chi^{(1)}$.

The 2nd order susceptibility $\chi^{(2)}$ is related with 2nd order nonlinearity of the material which is responsible for physical phenomena such as second harmonic generation (SHG), sum- or difference- frequency generation (SFG or DFG), optical rectification and electro-optic effects [1].

The 3rd order nonlinearity of the material is related to the 3rd order susceptibility of the material $\chi^{(3)}$, which corresponds to physical phenomena being discussed in the next section.

The effect of material polarization upon optical wave propagation inside a dielectric non-magnetic material is described by the wave equation derived from Maxwell equations:

$$\nabla\times\nabla\times E+\frac{1}{c^2}\frac{\partial^2}{\partial t^2}E=-\mu_0\frac{\partial^2}{\partial t^2}(P^{(1)}+P^{(NL)}) \qquad (2.4)$$

Where $c=\sqrt{\mu_0\varepsilon_0}$ is the speed of light in vacuum; μ_0 is the vacuum permeability; $P^{(NL)}$ is the nonlinear polarization of the material. In this case, the fact that the polarization of the material is the driving term in Equation 2.4 indicates that it can modify not only the propagation behavior of the incident wave, but also generate optical waves with new frequencies distinguishable from the original wave.

2.2 The Irradiance Dependent Third-Order Nonlinearity of the Material

The third order polarization of material can be written as

$$P_i^{(3)}(\omega) = \int_{-\infty}^{\infty}\int_{-\infty}^{\infty}\int_{-\infty}^{\infty} \chi_{ijkl}^{(3)}(-\omega;\omega_1,\omega_2,\omega_3)\times E_j(\omega_1)E_k(\omega_2)E_l(\omega_3)\delta(\omega-\omega_1-\omega_2-\omega_3)d\omega_1 d\omega_2 d\omega_3 \quad (2.5)$$

The dummy indices *i*, *j*, *k* and *l*, corresponding to Cartesian axes *x*, *y*, and *z*, indicate that the complex $\chi_{ijkl}^{(3)}$ is a fourth rank tensor. Generally, depending on the different combination of frequencies, $P^{(3)}$ can drive different physical phenomena [1]:

1. $3\omega_1$ *etc.* corresponds to third harmonic generation (THG) related with $\chi_{ijkl}^{(3)}(-3\omega_1;\ \omega_1,\ \omega_1,\ \omega_1)$, *etc.*
2. $\chi_{ijkl}^{(3)}(-\omega_1;\ \omega_1,\ \omega_1,\ -\omega_1)$ *etc.* corresponds to degenerate two-photon absorption (D-2PA) and nonlinear refraction (D-NLR); while $\chi_{ijkl}^{(3)}(-\omega_1;\ \omega_1,\ \omega_2,\ -\omega_2)$ *etc.* is responsible for non-degenerate two-photon absorption (ND-2PA) and nonlinear refraction (ND-NLR). Both processes are irradiance dependent, which is automatically phase matched. These are the two primary processes discussed in this dissertation.
3. $\chi_{ijkl}^{(3)}(-2\omega_1+\omega_2;\ \omega_1,\ \omega_1,\ -\omega_2)$, *etc.* is related with stimulated Raman scattering (SRS) or coherent anti-Stokes Raman scattering (CARS).
4. It is worth noting that cascaded $\chi^{(2)}:\chi^{(2)}$ can also contribute to third order nonlinearity of the material [44].

Let's consider only one element $\chi_{xxxx}^{(3)}$ with electric field polarized in the *x* direction containing the single frequency, ω_1(single Eigenmode input). We can define the electric field of the incident light as

$$E(t) = \frac{1}{2}\mathrm{E}(\omega_1)\mathrm{e}^{-\mathrm{i}\omega_1 \mathrm{t}} + c.c \quad (2.6)$$

where E represents the complex amplitude of the electric field. The Fourier transform pair of Equation 2.6 can be written as:

$$E(\omega) = \int_{-\infty}^{\infty} E(t)e^{-i\omega t}dt$$
$$= \frac{1}{2}\mathrm{E}(\omega_1)\delta(\omega-\omega_1) + \frac{1}{2}\mathrm{E}^{*}(\omega_1)\delta(\omega+\omega_1) \qquad (2.7)$$

Similarly the polarization of the material with single frequency ω' can be written as

$$P^{(3)}(t) = \frac{1}{2}\mathrm{P}^{(3)}(\omega')\mathrm{e}^{-\mathrm{i}\omega' \mathrm{t}} + c.c$$
$$P^{(3)}(\omega) = \frac{1}{2}\mathrm{P}^{(3)}(\omega')\delta(\omega - \omega') + c.c \qquad (2.8)$$

The irradiance dependent process is related with

$$P_{\mathrm{x}}^{(3)}(\omega_1) = \frac{1}{4}\varepsilon_0 \hat{\chi}_{xxxx}^{(3)}(-\omega_1;\omega_1,\omega_1-\omega_1)E_x(\omega_1)E_x^{*}(\omega_1)E_x(\omega_1)$$
$$= \frac{1}{4}\varepsilon_0 \hat{\chi}_{xxxx}^{(3)}(-\omega_1;\omega_1,\omega_1-\omega_1)\left|E_x(\omega_1)\right|^2 E_x(\omega_1) \qquad (2.9)$$

where $\hat{\chi}_{xxxx}^{(3)}(-\omega_1;\omega_1,\omega_1-\omega_1)$ can be expressed as

$$\hat{\chi}_{xxxx}^{(3)}(-\omega_1;\omega_1,\omega_1-\omega_1)$$
$$= \chi_{xxxx}^{(3)}(-\omega_1;\omega_1,\omega_1,-\omega_1) + \chi_{xxxx}^{(3)}(-\omega_1;\omega_1,-\omega_1,\omega_1) + \chi_{xxxx}^{(3)}(-\omega_1;-\omega_1,\omega_1\omega_1) \qquad (2.10)$$

which implies that it is the summation of three possible $\chi^{(3)}$ processes. Only under Kleinman symmetry (i.e. ω_1 is far away from resonance frequency) does these three $\chi^{(3)}$ equal to each other (detailed formalism is discussed in APPENDIX A).

To describe how $P^{(3)}$ is coupled into the wave propagation, we assume plane wave input with propagation along the *z* direction. Equation 2.4 can then be written as

$$\frac{\partial^2 E}{\partial z^2} - \frac{n^2}{c^2}\frac{\partial^2}{\partial t^2}E = \mu_0 \frac{\partial^2}{\partial t^2}(P^{(3)}) \qquad (2.11)$$

Under CW plane wave input, the E and $P^{(3)}$ can be expressed as

$$E_x(z,t) = \frac{1}{2}\mathrm{E}_0(z)\mathrm{e}^{i(k_1 z-\omega_1 t)} + c.c$$
$$P_x^{(3)}(z,t) = \frac{1}{2}\mathrm{P}_0^{(3)}(z)\mathrm{e}^{i(k_p z-\omega_1 t)} + c.c \qquad (2.12)$$

where k_1 and k_p are the wave vector of the incident electric field and induced material polarization respectively. Applying Equation 2.12 into Equation 2.11, we can obtain

$$\left(\frac{\partial^2 \mathrm{E}_0}{\partial \mathrm{z}^2} + 2ik_1\frac{\partial \mathrm{E}_0}{\partial \mathrm{z}}\right) = -\omega^2\mu_0\mathrm{P}_0 e^{i\Delta kz} \qquad (2.13)$$

where $\Delta k = \vec{k}_p - \vec{k}_1$. If the electric field doesn't change dramatically within several wavelengths of propagation, the slowly varying envelope approximation may be applied to Equation 2.13 as $\left|\frac{\partial^2 \mathrm{E}_0}{\partial \mathrm{z}^2}\right| << \left|2k_1\frac{\partial \mathrm{E}_0}{\partial \mathrm{z}}\right|$. By applying Equation 2.9, Equation 2.13 can be transformed into

$$\frac{\partial \mathrm{E}_0}{\partial \mathrm{z}} = i\frac{\omega_1}{8nc}[\mathrm{Re}(\hat{\chi}^{(3)}_{xxxx}) + i\,\mathrm{Im}(\hat{\chi}^{(3)}_{xxxx})]\left|\mathrm{E}_0\right|^2\mathrm{E}_0 \qquad (2.14)$$

where the complex $\chi^{(3)}$ is explicitly expressed by its real and imaginary parts. Note that $\Delta\vec{k} = 0$ indicates phase is automatically matched in this process. Since E_0 is complex amplitude which contains phase information, it can be expressed by

$$\mathrm{E}_0(z) = \mathrm{A}(z)e^{i\Phi(z)} \qquad (2.15)$$

By applying Equation 2.15, Equation 2.14 can be separated into two equations:

$$\frac{d}{dz}\mathrm{A(z)} = -\frac{\omega_1}{8nc}\mathrm{Im}(\hat{\chi}^{(3)}_{xxxx})\mathrm{A}^3(\mathrm{z})$$
$$\frac{d}{dz}\Phi(\mathrm{z}) = \frac{\omega_1}{8nc}\mathrm{Re}(\hat{\chi}^{(3)}_{xxxx})\mathrm{A}^2(\mathrm{z}) \qquad (2.16)$$

in this case, we assume the input is a plane wave; and the material is thin with respect to the linear and nonlinear beam propagations (i.e. no self-action for input wave).

Taking into account the irradiance of the incident light field as

$$I(z) = \frac{1}{2} c_0 n \varepsilon_0 \mathrm{A}(z)^2 \tag{2.17}$$

The first equation of Equation 2.16 can be transformed into

$$\frac{dI}{dz} = -\alpha_2 I^2 \tag{2.18}$$

where α_2 is called as the degenerate two-photon absorption coefficient of the material which is determined by

$$\alpha_2 = \frac{\omega_1}{2n^2 \varepsilon_0 c^2} \mathrm{Im}(\hat{\chi}^{(3)}_{xxxx}(-\omega_1; \omega_1, \omega_1, -\omega_1)) \tag{2.19}$$

The second equation of Equation 2.19 reveals the extra phase shift of the propagating beam modulated by the irradiance of the input field and related to the real part of $\chi^{(3)}$. The nonlinear refractive index n_2 is then defined as

$$\frac{d\Phi}{dz} = k_0 \Delta n = k_0 n_2 I(z) \tag{2.20}$$

Hence by applying Equation 2.17, we obtain

$$n_2 = \frac{1}{4n^2 \varepsilon_0 c} \mathrm{Re}(\hat{\chi}^{(3)}_{xxxx}(-\omega_1; \omega_1, \omega_1, -\omega_1)) \tag{2.21}$$

In the molecular system, to characterize the averaged 2PA of an individual molecule, the definition of 2PA crosses section, δ_{2PA}, is conventionally introduced by [45]

$$\frac{dn_p}{dt} = \delta_{2PA} \psi^2 \tag{2.22}$$

where n_p is the number of photons absorbed per unit volume of the medium by 2PA and ψ is the incident photon flux. δ_{2PA} is usually given in units of 1×10^{-50} cm^4 s photon^{-1} molecule^{-1}, which is called "Göppert-Mayer", or "GM" in honor of the author of Ref. 3.

The relation between δ_{2PA} and α_2 can be expressed by Ref. 12:

$$\delta_{2PA} = \frac{\hbar\omega\alpha_2}{N} = \frac{\hbar\omega^2}{2n^2c^2\varepsilon_0 N}\,\mathrm{Im}(\hat{\chi}^{(3)}_{xxxx}(-\omega_1;\omega_1,\omega_1,-\omega_1)) \qquad (2.23)$$

where N is the number of molecules per unit volume of the medium.

Similarly the definition of nonlinear refraction cross section, δ_{NLR}, is also introduced recently to characterize the NLR of an individual molecule [42], which is defined in the same units of Goppert-Mayer which we refer to as "refractive Goppert-Mayer" (RGM), or 1×10^{-50} cm^4 s photon^{-1} molecule^{-1} as

$$\delta_{NLR} = \frac{\hbar\omega}{N}kn_2 = \frac{\hbar\omega^2}{4n^2c^2\varepsilon_0 N}\,\mathrm{Re}(\hat{\chi}^{(3)}_{xxxx}(-\omega_1;\omega_1,\omega_1,-\omega_1)) \qquad (2.24)$$

It is advisable to define a figure of merit (FOM) between NLR and 2PA as

$$FOM = \frac{\delta_{NLR}}{\delta_{2PA}} = \frac{1}{2}\left|\frac{\mathrm{Re}(\hat{\chi}^{(3)}_{xxxx})}{\mathrm{Im}(\hat{\chi}^{(3)}_{xxxx})}\right| \qquad (2.25)$$

2.3 Bound Electronic Nonlinearity of an Isolated Molecular System

2.3.1 Introduction of Models to Describe the Bound Electronic Nonlinearity

To model the bound electronic nonlinearity of the material, there are generally two physical approaches: the classical anharmonic oscillator model and the "sum over states" model based on quantum mechanical perturbation theory. The anharmonic oscillator model, similar to the treatment derived by Owyoung [46], considers electron being bound to the nuclei via a "spring" parabolic potential, which is perturbed by a small anharmonicity under the presence of a strong incident electric field. The resonant frequency of the oscillator, corresponding to the transition

frequency of a molecular system, is thus determined by the "spring" constant and the electron mass. The strong electric field induces a nonlinearity of the restoring force on the electron with respect to its displacement from its equilibrium position, resulting in a nonlinear response of the material which couples back to the incident electric field, or generates new electric field frequencies. This approach provides an intuitive insight of the material nonlinearity without the necessity of involving wavefunctions and transition dipole moments. However, the anharmonic oscillator model can only provide a maximum of three resonance frequencies corresponding to x, y, and z coordinates, which is generally not physical in reality. In a molecular system, the electronic structure is usually characterized by a set of discrete states with different energetic positions as is described by Jabłoński diagrams [47], hence there are a set of resonant frequencies corresponding to transitions between these states. Thus a quantum mechanical perturbation approach, as known as the "Sum Over States" (SOS) model, was proposed by Ward in 1965[48] and further corrected by Orr and Ward in 1971 [43]. Given a molecular system with discrete energy states, the SOS model considers all electric dipole allowed transitions from ground state to the excited states, and between excited states. By repeatedly applying first order perturbation theory to calculate the probability of the electron being excited into possible states, the induced polarization by the incident electric field is determined, yielding the linear and nonlinear material susceptibility. The calculation of transition dipole moment requires a knowledge of the wavefunction of each state, and the SOS model summarizes the contributions of transitions between all possible states; therefore, the SOS model is much more computationally accurate comparing to the anharmonic oscillator model. , The SOS model is generally accepted by researchers as a fundamentally correct model to describe the complicated nonlinear susceptibilities of a molecular system. Furthermore, often times the material nonlinearities are

mainly linked with a few excited states (essential states), so the SOS model can be further simplified to describe the dispersion of the material nonlinearities without necessarily performing lengthy calculations.

By applying the SOS model, the $\chi^{(3)}$ of a molecular system can be written in SI units as [1,43]:

$$\chi^{(3)}_{ijkl}(-[\omega_p+\omega_q+\omega_r];\omega_p,\omega_q,\omega_r)=\frac{N}{\varepsilon_0\hbar^3}f^{(3)}\sum\nolimits'_{v,n,m}$$
$$\{\frac{\bar{\mu}_{gv,i}(\bar{\mu}_{vn,l}-\bar{\mu}_{gg,l})(\bar{\mu}_{nm,k}-\bar{\mu}_{gg,k})\bar{\mu}_{mg,j}}{(\bar{\omega}_{vg}-\omega_p-\omega_q-\omega_r)(\bar{\omega}_{ng}-\omega_q-\omega_p)(\bar{\omega}_{mg}-\omega_p)}+$$
$$+\frac{\bar{\mu}_{gv,j}(\bar{\mu}_{vn,k}-\bar{\mu}_{gg,k})(\bar{\mu}_{nm,i}-\bar{\mu}_{gg,i})\bar{\mu}_{mg,l}}{(\bar{\omega}^*_{vg}+\omega_p)(\bar{\omega}^*_{ng}+\omega_q+\omega_p)(\bar{\omega}_{mg}-\omega_r)}+\frac{\bar{\mu}_{gv,l}(\bar{\mu}_{vn,i}-\bar{\mu}_{gg,i})(\bar{\mu}_{nm,k}-\bar{\mu}_{gg,k})\bar{\mu}_{mg,j}}{(\bar{\omega}^*_{vg}+\omega_r)(\bar{\omega}_{ng}-\omega_q-\omega_p)(\bar{\omega}_{mg}-\omega_p)}$$
$$+\frac{\bar{\mu}_{gv,j}(\bar{\mu}_{vn,k}-\bar{\mu}_{gg,k})(\bar{\mu}_{nm,l}-\bar{\mu}_{gg,l})\bar{\mu}_{mg,i}}{(\bar{\omega}^*_{vg}+\omega_p)(\bar{\omega}^*_{ng}+\omega_q+\omega_p)(\bar{\omega}^*_{mg}+\omega_p+\omega_q+\omega_r)}\}$$
$$-\frac{N}{\varepsilon_0\hbar^3}f^{(3)}\sum\nolimits'_{n,m}\ \{\frac{\bar{\mu}_{gn,i}\bar{\mu}_{ng,l}\bar{\mu}_{gm,k}\bar{\mu}_{mg,j}}{(\bar{\omega}_{ng}-\omega_p-\omega_q-\omega_r)(\bar{\omega}_{ng}-\omega_r)(\bar{\omega}_{mg}-\omega_p)}$$
$$+\frac{\bar{\mu}_{gn,i}\bar{\mu}_{ng,l}\bar{\mu}_{gm,k}\bar{\mu}_{mg,j}}{(\bar{\omega}^*_{mg}+\omega_q)(\bar{\omega}_{ng}-\omega_r)(\bar{\omega}_{mg}-\omega_p)}+\frac{\bar{\mu}_{gn,l}\bar{\mu}_{ng,i}\bar{\mu}_{gm,j}\bar{\mu}_{mg,k}}{(\bar{\omega}^*_{ng}+\omega_r)(\bar{\omega}^*_{mg}+\omega_p)(\bar{\omega}_{mg}-\omega_q)}$$
$$+\frac{\bar{\mu}_{gn,l}\bar{\mu}_{ng,i}\bar{\mu}_{gm,j}\bar{\mu}_{mg,k}}{(\bar{\omega}^*_{ng}+\omega_r)(\bar{\omega}^*_{mg}+\omega_p)(\bar{\omega}^*_{ng}+\omega_p+\omega_q+\omega_r)}\} \qquad (2.26)$$

where g indicates the ground state; v, m, n indicate all possible excited states; $\mu_{\upsilon m}$ indicates the transition dipole moment from state υ to state m ($\mu_{\upsilon m}=\mu_{\upsilon m}^*$), and μ_{gg} is the ground state permanent dipole moment; $\bar{\omega}_{\upsilon m}=\omega_{\upsilon m}-i\Gamma_{\upsilon m}$, $\omega_{\upsilon m}$ is the resonant frequency between the state υ and state m, and $\Gamma_{\upsilon m}$ is a phenomenological damping factor which is related with the linewidth of the transition; and $i, j, k, l = x, y, z$. $\sum'$ indicates that the summation is taken over all possible

electronic states except the ground state. $f^{(3)}$ is a local field correction factor which can be written as:

$$f^{(3)} = \left[\frac{\varepsilon_i^r(\omega_p+\omega_q+\omega_r)+2}{3}\right]\left[\frac{\varepsilon_j^r(\omega_p)+2}{3}\right]\left[\frac{\varepsilon_k^r(\omega_q)+2}{3}\right]\left[\frac{\varepsilon_l^r(\omega_r)+2}{3}\right] \qquad (2.27)$$

where $\varepsilon^r = n^2$ is the relative dielectric constant of the material assuming no linear loss.

Note that $\chi^{(3)}$ is related with selected sequence of input frequencies ω_p, ω_q, and ω_r, i.e. different sequential combination of ω_p, ω_q, and ω_r yields different expression of $\chi^{(3)}$. However, if ω_p, ω_q, and ω_r are *extremely far below* any resonance frequencies, the frequency dependence of $\chi^{(3)}$ can be neglected, these $\chi^{(3)}$s are only related to the transition dipole moments and the transition frequencies and thus equal to each other which is so called Kleinman's symmetry.

2.3.2 Three-level Model – a Simplified SOS Model

The fact that the SOS model includes all possible transitions between the ground state and possible excited states makes it an extremely cumbersome task to calculate $\chi^{(3)}$. Therefore to find an approximation to simplify the SOS model it is necessary to conceptually demonstrate the spectral dispersion behavior of $\chi^{(3)}$. Fortunately, the formalism of the SOS model allows considering only a few essential states which contributes most significantly to the $\chi^{(3)}$. The simplest 2-level model is presented to show the dispersion behavior of NLR and 2PA with a single resonant frequency corresponding to a dominating transition between the ground and 1st excited state [49]. The 2-level model showing a 2PA resonance requires a permanent dipole moment difference ($\Delta\mu$) between the ground ($1A_g$) and 1st excited state ($1B_u$), and predicts a possible enhancement of n_2 near the one- and degenerate two-photon resonance, depending upon

the magnitude of the transition dipole moment (μ_{01}) and $\Delta\mu$, which also determines the sign and magnitude of off- and non-resonant n_2. The 2-level model can predict the spectral dispersion behavior of molecules with permanent dipole moments, e.g. linear molecule with strong charge transfer groups such as Donor-π-Acceptor structure; but it fails with symmetrical molecules since they possess negligible permanent dipole moments. Including another excited state (mA_g) is necessary to describe the spectral dispersion behavior of $\chi^{(3)}$ for symmetrical molecules. Such a 3-level model was proposed by Kuzyk *et al.* [50]. In this simplified approach, only three states are involved in the calculation: the ground state with *gerade* (*g*) symmetry ($1A_g$, labeled as *g*), the 1st excited state with *ungerade* (*u*) symmetry ($1B_u$, labeled as *e*), and another excited state with *gerade* symmetry (mA_g, labeled as *e'*) corresponding to a 2PA final state. The energy structure of the 3-level model is shown in Figure 2.1. The transition between the *g* state to *e* state, and between *e* to the 2PA final state, *e'*, are electric dipole allowed due to selection rule ($g \rightarrow u$); while the direct transition between ground state to 2PA final state with the same symmetry, $g \rightarrow g$, is forbidden. The expression of $\hat{\chi}^{(3)}_{xxxx}(-\omega;\omega,\omega-\omega)$, *with only resonant terms*, can be written as

$$\tilde{\chi}^{(3)}_{xxxx} =$$

$$\frac{Nf^{(3)}}{\hbar^3\varepsilon_0}\left\{\begin{array}{ll}\dfrac{\left|\mu^x_{ge}\right|^2\left|\Delta\mu^x\right|^2}{(\bar{\omega}_{eg}-\omega)(\bar{\omega}_{eg}-2\omega)(\bar{\omega}_{eg}-\omega)} & \text{D Term}\\ +\dfrac{\left|\mu^x_{ge}\right|^2\left|\Delta\mu^x\right|^2}{(\bar{\omega}^*_{eg}-\omega)(\bar{\omega}_{eg}-2\omega)(\bar{\omega}_{eg}-\omega)} & \text{D Term}\\ +\dfrac{\left|\mu^x_{ge}\right|^2\left|\bar{\mu}^x_{ee'}\right|^2}{(\bar{\omega}_{eg}-\omega)(\bar{\omega}_{e'g}-2\omega)(\bar{\omega}_{eg}-\omega)} & \text{T Term}\\ +\dfrac{\left|\mu^x_{ge}\right|^2\left|\bar{\mu}^x_{ee'}\right|^2}{(\bar{\omega}^*_{eg}-\omega)(\bar{\omega}_{e'g}-2\omega)(\bar{\omega}_{eg}-\omega)} & \text{T Term}\end{array}\right\}$$

$$-\frac{Nf^{(3)}}{\hbar^3\varepsilon_0}\left\{\begin{array}{ll}\dfrac{\left|\mu^x_{ge}\right|^4}{(\bar{\omega}_{eg}-\omega)(\bar{\omega}_{eg}-\omega)(\bar{\omega}_{eg}-\omega)} & \text{N Term}\\ \dfrac{\left|\mu^x_{ge}\right|^4}{(\bar{\omega}_{eg}-\omega)(\bar{\omega}^*_{eg}-\omega)(\bar{\omega}_{eg}-\omega)} & \text{N Term}\end{array}\right\} \qquad (2.28)$$

where $\Delta\mu^x$ is the permanent dipole moment difference between the excited state *e* and ground state *g*: $\Delta\mu^x = \mu^x_{ee} - \mu^x_{gg}$; while μ_{ge} and $\mu_{ee'}$ are the transition dipole moment between *g* and *e*, and *e* and *e'*, respectively. The full expression of $\tilde{\chi}^{(3)}_{xxxx}(-\omega;\omega,\omega-\omega)$ for symmetrical molecules contains 24 terms including both resonant and nonresonant terms. It is derived in detail in APPENDIX A. Nevertheless, the resonant terms written in Equation 2.28 have the most significant contribution to the overall $\tilde{\chi}^{(3)}_{xxxx}(-\omega;\omega,\omega-\omega)$, when the input frequency, ω, is close to a resonant transition frequency. The 6 terms in Equation 2.28 can generally be classified into three categories. The first two terms are called dipolar terms, or D terms, which are non-zero only when the molecule possesses a finite $\Delta\mu^x$. The D terms are derived from the 2-level model, which corresponds to an electron excited from the ground state (*g*) into the 1st excited state (*e*). For symmetrical molecules with negligible $\Delta\mu^x$, the D term is essentially zero, indicating a forbidden 2PA transition between g and e states. The third and fourth terms are called two-

photon terms, or T terms, which correspond to an electron being excited from the g state into the 2PA final state, *e'*, via an intermediate state, *e*. The transition dipole moment between *e* and *e'*, $\mu_{ee'}^{x}$, is thus important to enhance T terms. Another important enhancement of T terms originates from $(\overline{\omega}_{eg} - \omega)$ and $(\overline{\omega}_{eg}^{*} - \omega)$ in the denominator. A smaller energy difference between the input photon energy and the absorption gap of the material, called the detuning energy, would enhance the T term. This is called intermediate state resonance enhancement (ISRE), which is successfully demonstrated by Hales *et al*. [51]. However, this ISRE effect also competes with the last two terms, which are called negative terms, or N terms, due to its negative contribution to the $\hat{\chi}_{xxxx}^{(3)}(-\omega;\omega,\omega-\omega)$. N terms resonate between *g* and *e* states, and shows significant contribution when the input photon energy approaches the absorption gap of the material. This is term is also called the quadratic AC Stark effect as described in ref. 40. In some cases it is also referred to ground-state bleaching [52] since it turns into this resonant effect when the photon energy becomes resonant with the linear absorption. *For symmetrical dyes, only the T and N terms survive and compete against each other*. The dispersion behavior of $\hat{\chi}_{xxxx}^{(3)}(-\omega;\omega,\omega-\omega)$ is related with various factors, i.e. the transition dipole moments between states, and the resonance frequencies corresponding to the positions of each state. A detailed discussion about the dispersion relations of bound electronic nonlinearities for symmetrical molecules is in Section 2.3.3 by using a simplified 3-level model.

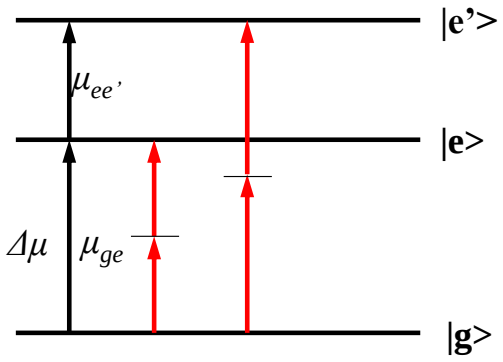

Figure 2.1: Energy structure of 3-level model

It is worth noting that in the simplified 3-level model, we assume the transition dipole moments, μ_{ge} , $\mu_{ee'}$ and $\Delta\mu$, are parallel to each other along the main molecular conjugation chain. If there is an angle between the dipole moments, an effective transition dipole moment should be calculated by

$$\mu_{ee'}^{eff} = \mu_{ee'}\sqrt{\frac{2\cos^2(\theta)+1}{3}} \qquad (2.29)$$

where θ is the angle between μ_{ge} and $\mu_{ee'}$ [53].

Another important assumption here made for the 3-level model is that $\tilde{\chi}^{(3)}_{xxxx}(-\omega;\omega,\omega-\omega)$ is calculated along the main molecular conjugation chain. In isotropic media, e.g. solution based samples, the molecules are randomly oriented, therefore, the overall $\tilde{\chi}^{(3)}_{xxxx}(-\omega;\omega,\omega-\omega)$ should be divided by a factor of 5 [54]. The corresponding δ_{2PA} and δ_{NLR} can be written as:

$$\delta_{2PA} = \frac{\hbar\omega\alpha_2}{N} = \frac{\hbar\omega^2}{10n^2c^2\varepsilon_0 N}\mathrm{Im}(\tilde{\chi}^{(3)}_{xxxx}(-\omega_1;\omega_1,\omega_1,-\omega_1)) \qquad (2.30)$$

and

$$\delta_R = \frac{\hbar\omega}{N} k n_2 = \frac{\hbar\omega^2}{20 n^2 c^2 \varepsilon_0 N} \mathrm{Re}(\tilde{\chi}^{(3)}_{xxxx}(-\omega_1;\omega_1,\omega_1,-\omega_1)) \quad (2.31)$$

If we consider only the T- and D-terms of Equation 2.28, the δ_{2PA} near the resonance frequency can be further simplified into Equation 2.32. Details of the derivation of Equation 2.32 can found in APPENDIX B.

$$\delta_{2PA}(\omega) = \frac{1}{5c^2\hbar n^2 \varepsilon_0^2} \frac{(\hbar\omega)^2}{(\hbar\omega_{eg} - \hbar\omega)^2 + \Gamma_{eg}^2} \left[\frac{|\mu_{eg}|^2 |\Delta\mu|^2 \Gamma_{eg}}{(\hbar\omega_{eg} - 2\hbar\omega)^2 + \Gamma_{eg}^2} + \frac{|\mu_{eg}|^2 |\mu_{ee'}|^2 \Gamma_{e'g}}{(\hbar\omega_{e'g} - 2\hbar\omega)^2 + \Gamma_{e'g}^2} \right] \quad (2.32)$$

Equation 2.32 can also be derived from a 2PA tensor approach [35], which is very useful to determine the molecular $\mu_{ee'}$ from a δ_{2PA} spectrum. Note that no local field correction is considered here.

2.3.3 Dispersion of Bound Electronic Nonlinearity of a Symmetrical Molecule Using the 3-level Model

Using the 3-level model for linear symmetrical molecules, it is instructive to simulate the dispersion behavior of the bound electronic $\tilde{\chi}^{(3)}_{xxxx}(-\omega;\omega,\omega-\omega)$. Shown in Figure 2.2 is the dispersion of the real and imaginary parts of the total $\tilde{\chi}^{(3)}_{xxxx}(-\omega;\omega,\omega-\omega)$, given that $\omega_{e'g}/\omega_{eg}=1.2$, $\Gamma_{eg}=\omega_{eg}/200$, $\Gamma_{e'g}=10\Gamma_{eg}$, $|\mu_{ge}|=|\mu_{ee'}|$. The dispersion curve of each $\chi^{(3)}_{xxxx}$ component is described in detail in APPENDIX A. A peak of the imaginary part of $\tilde{\chi}^{(3)}_{xxxx}(-\omega;\omega,\omega-\omega)$, corresponding to a 2PA resonance, is observed at $\omega_{e'g}/2$. Since for a linear symmetrical molecule, the permanent dipole moment difference, $\Delta\mu^x$, is negligible, no D terms are presented in $\tilde{\chi}^{(3)}_{xxxx}(-\omega;\omega,\omega-\omega)$. This 2PA resonance is from the T terms in Equation 2.28. The real part

of $\tilde{\chi}^{(3)}_{xxxx}(-\omega,\omega,\omega,-\omega)$, corresponding to the bound electronic n_2, initially increases gradually from a small negative value (at the DC limit, $\omega\rightarrow 0$) to a positive peak slightly red-shifted from the 2PA peak; it then decreases dramatically becoming negative as the incident photon energy passes the 2PA peak. This n_2 spectral shape near the two-photon resonance is the signature of the Kramers-Kronig (KK) relations described in ref 39,40. As the incident photon energy approaches the absorption gap of the material, corresponding to $\omega\rightarrow\omega_{eg}$, the N terms in Equation 2.28 start to dominate all other nonlinear contributions. A large negative n_2 is thus observed. Note that the imaginary part of $\tilde{\chi}^{(3)}_{xxxx}(-\omega,\omega,\omega,-\omega)$ also shows negative resonance as the incident photon energy approaches the absorption gap due to the presence of the tail of the transition linewidth, $\Gamma_{e'g}$ and Γ_{eg}, which is related to the lifetime of the states. This negative resonance of the imaginary part of $\tilde{\chi}^{(3)}_{xxxx}(-\omega,\omega,\omega,-\omega)$ can be perceived as a reduction of the overall absorption coefficient near the 1PA resonance wavelengths range, a so called ground-state bleaching effect [52].

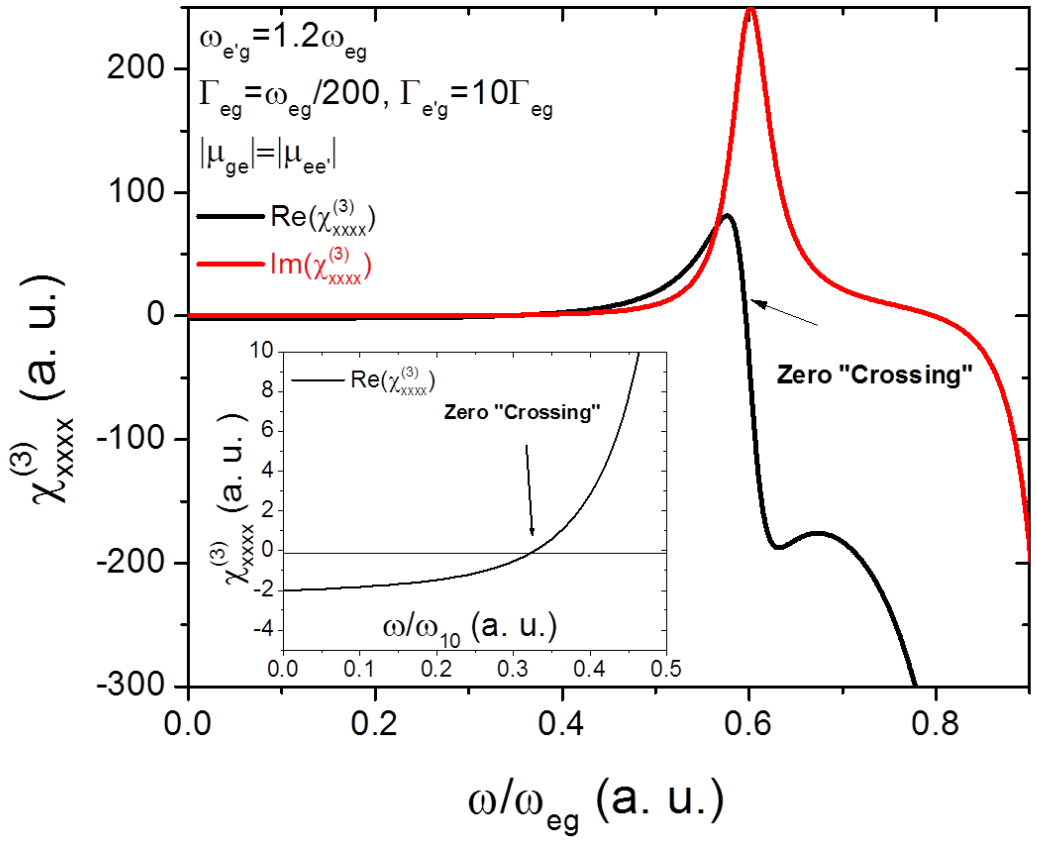

Figure 2.2: The dispersion of real (black) and imaginary (red) part of $\tilde{\chi}^{(3)}_{xxxx}$ as the function of normalized incident photon energy ω/ω_{eg}; inset: zero cross of real part of $\tilde{\chi}^{(3)}_{xxxx}$.

It is interesting to study $\tilde{\chi}^{(3)}_{xxxx}(-\omega,\omega,\omega,-\omega)$ at the DC limit, which determines the magnitude and sign of the nonresonant n_2. The expression of $\tilde{\chi}^{(3)}_{xxxx}|_{DC}$ is shown in Equation A1.13 in APPENDIX A. The sign of the nonresonant n_2 is determined by the ratio $(\overline{\omega}_{eg}|\mu_{ee'}|^2)/(\overline{\omega}_{e'g}|\mu_{ge}|^2)$, i.e. if $(\overline{\omega}_{eg}|\mu_{ee'}|^2)/(\overline{\omega}_{e'g}|\mu_{ge}|^2)>1$, the sign of nonresonant n_2 is positive; otherwise it is negative (or zero). In Figure 2.2 with $\omega_{e'g}=1.2\omega_{eg}$ and $|\mu_{ge}|=|\mu_{ee'}|$,

$(\overline{\omega}_{eg}\left|\mu_{ee'}\right|^2)/(\overline{\omega}_{e'g}\left|\mu_{ge}\right|^2)-1=-0.167$; hence nonresonant n_2 is negative. Therefore, the dispersion of the real part of $\hat{\chi}^{(3)}_{xxxx}(-\omega,\omega,\omega,-\omega)$ has two "zero-crossing" points in the vicinity of the two-photon resonance, corresponding to the electronic n_2 changing sign twice.

The governing elements for the dispersion behavior of the bound electronic $\hat{\chi}^{(3)}_{xxxx}$ are the relative strengths of the transition dipole moments, $\left|\mu_{ee'}\right|^2/\left|\mu_{eg}\right|^2$, and the ratio of transition frequencies: $\omega_{e'g}/\omega_{eg}$, *etc*., as discussed in the following paragraphs.

Shown in Figure 2.3 is the dispersion curve of the real and imaginary part of $\hat{\chi}^{(3)}_{xxxx}(-\omega,\omega,\omega,-\omega)$ with respect to $\left|\mu_{ee'}\right|^2/\left|\mu_{eg}\right|^2=0.25,0.5,1,2,4$ respectively. An increase of $\left|\mu_{ee'}\right|^2/\left|\mu_{eg}\right|^2$ leads to a more pronounced contribution from the two-photon resonance (T terms), hence a strong 2PA peak, and stronger n_2 peak near the 2PA resonance. Note that the sign of the real part of $\hat{\chi}^{(3)}_{xxxx}(-\omega,\omega,\omega,-\omega)$ is also related to $\left|\mu_{ee'}\right|^2/\left|\mu_{eg}\right|^2$. A small $\left|\mu_{ee'}\right|^2/\left|\mu_{eg}\right|^2$ indicates the N terms, proportional to $\left|\mu_{ge}\right|^4$, dominate the T terms ($\left|\mu_{ge}\right|^2\left|\mu_{ee'}\right|^2$), thus leading to a negative n_2 within all spectral ranges.

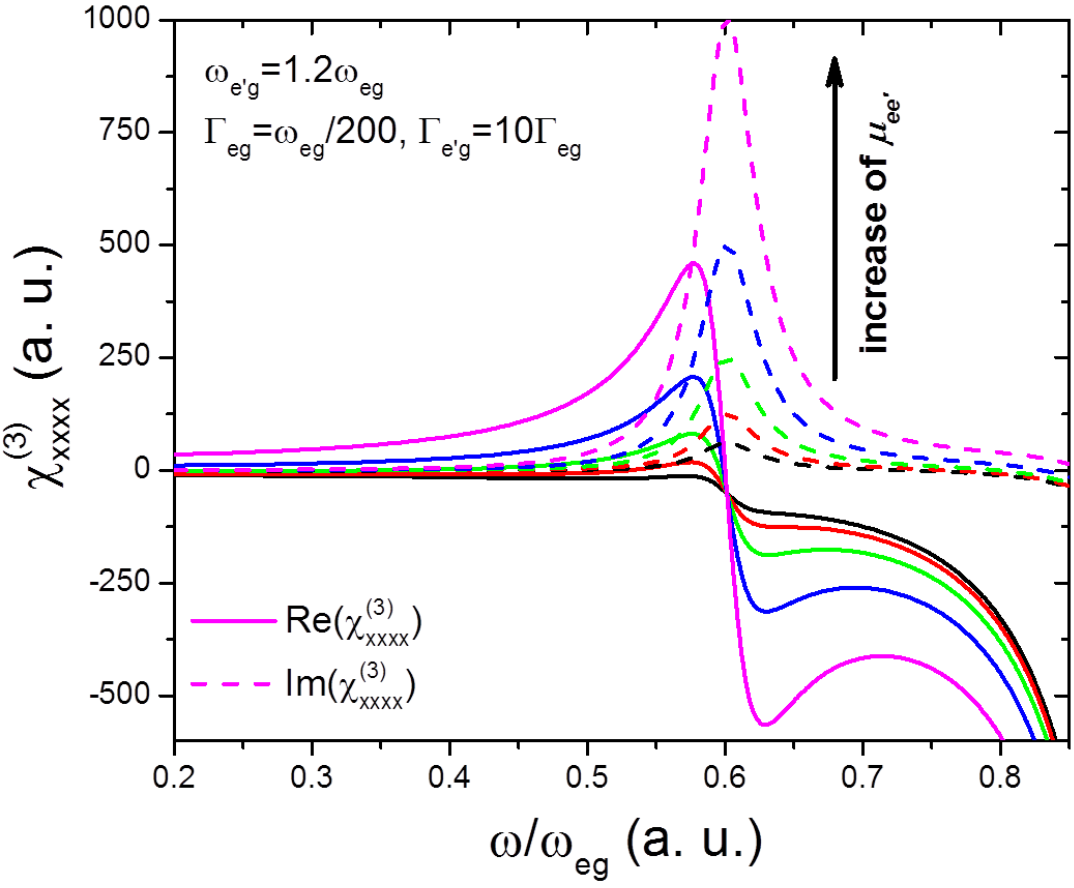

Figure 2.3: Dispersion of real (solid) and imaginary (dash) part of $\hat{\chi}^{(3)}_{xxxx}$ at $|\mu_{ee'}|^2 / |\mu_{eg}|^2 = 0.25, 0.5, 1, 2, 4$ respectively

The effect of relative position of the one-photon and two-photon transitions, represented by $\omega_{e'g}/\omega_{eg}$ on the dispersion curve of the real and imaginary part of $\hat{\chi}^{(3)}_{xxxx}(-\omega,\omega,\omega,-\omega)$ is illustrated in Figure 2.4, where $\omega_{e'g}/\omega_{eg} = 0.75, 1, 1.25, 1.5, 1.65, 1.84, 1.9$, respectively. An enhancement of the peak 2PA transition is observed in Figure 2.4a as a result of the increase of $\omega_{e'g}/\omega_{eg}$. This enhancement is due to the double resonance of the T terms induced by a small

detuning energy between the two-photon transition ($\omega_{e'g}/2$) and the intermediate state (ω_{eg}) (ISRE). However, as the 2PA final state approaches twice the intermediate state ($\omega_{e'g}/\omega_{eg} \to 2$), the 2PA spectrum may not be fully resolved due to the linewidth of ω_{eg} and $\omega_{e'g}$.

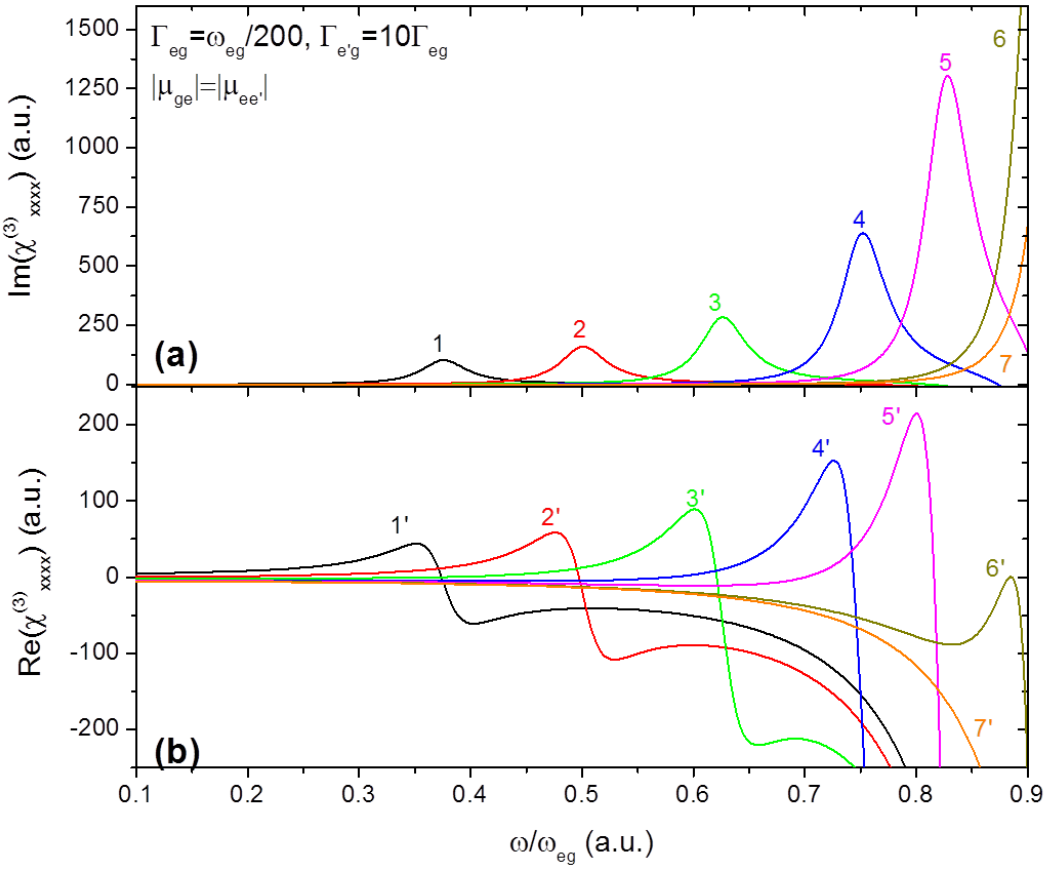

Figure 2.4: Dispersion of the imaginary (1, 2, 3, 4, 5, 6, 7) and real (1', 2', 3', 4', 5', 6', 7') part of $\hat{\chi}^{(3)}_{xxxx}$ at $\omega_{e'g}/\omega_{eg} = 0.75, 1, 1.25, 1.5, 1.65, 1.84, 1.9$, respectively

More interesting is the dispersion of n_2 corresponding to the real part of $\hat{\chi}^{(3)}_{xxxx}(-\omega,\omega,\omega,-\omega)$ presented in Figure 2.4b. When $\omega_{e'g}/\omega_{eg}$ is considerably less than 2, the increase of $\omega_{e'g}/\omega_{eg}$ again leads to the enhancement of a positive n_2 peak due to ISRE (curve 1'

to 5' in Figure 2.4b); however, as $\omega_{e'g}/\omega_{eg}$ approaches 2, the N terms start to compete and eventually dominates the T terms, as shown in curve 6' and 7'. As a result, the positive peak of n_2 cannot be resolved; n_2 is negative and its absolute value monotonically increases as the incident photon energy approaches ω_{eg}.

Shown in Figure 2.5 is the effect of linewidth Γ_{eg} of the one-photon transition on the dispersion of the real and imaginary parts of $\tilde{\chi}^{(3)}_{xxxx}(-\omega,\omega,\omega,-\omega)$, where $\omega_{eg}/\Gamma_{eg} = 400,200,100$, respectively. An increase of linewidth leads to a reduced 2PA peak, with wider spectral bandwidth as well as a less pronounced variation of n_2 near the 2PA resonance.

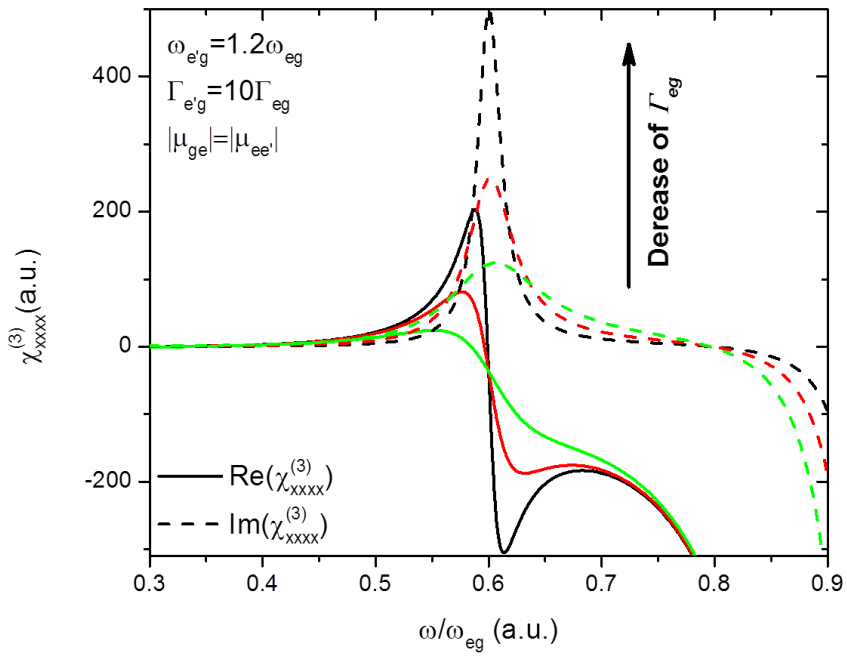

Figure 2.5: Dispersion of real (solid) and imaginary (dash) part of $\tilde{\chi}^{(3)}_{xxxx}$ at $\omega_{eg}/\Gamma_{eg} = 400,200,100$ respectively

In summary, a simple 3-level model can predict the spectral dispersion behavior of the real and imaginary parts of $\tilde{\chi}^{(3)}_{xxxx}(-\omega,\omega,\omega,-\omega)$, corresponding to the n_2 and 2PA spectrum, which will be very useful for the analyses in the following sections.

CHAPTER 3 EXPERIMENTAL METHODOLOGIES FOR LINEAR AND NONLINEAR SPECTROSCOPIC CHARACTERIZATION

To experimentally investigate the nonlinear optical properties of organic molecules, various spectroscopic characterization techniques are developed to measure different types of samples with liquid solution form or solid state phase. An intense but stable excitation source is essential for all the nonlinear optical measurements. Since both the magnitude and temporal response of nonlinearity are of vital interest for analysis, a systematic experimental methodology is implemented to extract the optical properties of the molecule.

While this chapter is mainly focused on a description of the nonlinear spectroscopic characterization techniques, i.e. Z-scan, 2PA induced fluorescence (2PF), and pump-probe, involved in this dissertation; a complete understanding of the linear optical properties is necessary on top of all nonlinear measurements. Therefore, we start with a brief introduction of linear spectroscopic characterization techniques, followed by a description of the excitation source and a detailed explanation of related nonlinear spectroscopic characterization techniques.

3.1 Linear Spectroscopic Characterizations

Linear optical properties of dyes include linear absorption (1PA) and fluorescence (1PF) spectra, the fluorescence quantum yield, and fluorescence excitation anisotropy. The significance of linear optical measurements is that they not only give the basic properties of the molecule, but also provide the necessary guidelines to select appropriate techniques for nonlinear optical measurements and their excitation parameters, e.g. wavelength, *etc*.

The linear absorption spectrum is the essential first step to characterize the optical properties of the molecules. The 1PA spectrum can reveal the absorption gap of the material and

identify other 1PA transitions of some higher lying energy states. For linear π-conjugated molecules, the strongest 1PA peak is usually located at the longest wavelength (lowest energy state), which reflects the position of a π→π* transition. Along with a delicate molar absorptivity measurement, the electronic transition strength, i.e. ground-to-excited state transition dipole moment μ_{ge} can be calculated in Equation 3.1 in ***CGS units*** [27,55].

$$\mu_{ge} = \sqrt{\frac{1500(\hbar c)^2 \ln(10)}{\pi N_A E_{01}} \int \varepsilon_{ge}(\nu) d\nu} \qquad (3.1)$$

Where $\varepsilon_{ge}(\nu)$ (in wavenumber cm^{-1}) is the molar absorbance spectrum of the corresponding 1PA band, N_A is Avogadro's number, and E_{ge} is the peak energy. Note that the transition dipole moment calculated here contains influence of local field from the solvent environment. The absorption peaks at short wavelength region also indicate higher lying one-photon allowed energy states which are useful in the following quantum chemical calculations.

Linear absorption measurements can also be used to check the photochemical stability of the molecule, since nonlinear optical measurements could induce significant photo-chemical damage of the sample. A comparison of the 1PA spectrum of the same sample before and after nonlinear optical measurement can verify if it did not decompose. Note that for certain organic molecules, aggregation is a common feature for concentrated solutions; therefore a concentration dependent linear absorption measurement, based upon the Beer-Lambert's law, is suggested to study the possible aggregation effects. A correct linear absorption spectrum should be measured at the concentration below the aggregation threshold. In this dissertation, the linear absorption spectrum is measured using a Cary500 spectrophotometer; a differential measurement is utilized to separate the linear absorption of the solute molecules from the solvent background.

The fluorescence spectrum, having a Stokes shift from the corresponding peak of 1PA band, could reveal the vibrational structure of the molecular states and the effect of solvent environment (e.g. solvent polarity). By Kasha's rule, fluorescence usually occurs from the lowest excited state (S_1), with exceptions for molecules with relatively complex end groups [56,57]. Another important molecular parameter extracted from fluorescence measurements is the fluorescence quantum yield (Φ_F), which is defined as the ratio between the numbers of emitted photons and absorbed photons. The fluorescence quantum yield is usually measured by comparing the fluorescence from the sample against a reference molecule with known Φ_F. Depending upon the fluorescence wavelength, various reference molecules are selected. At the emission wavelength range of 350-650 nm, commercial dyes, such as Anthracene in ethanol (Φ_F=0.27) [58], Rhodamine 6G in ethanol (Φ_F=0.95) [59], and Cresyl Violet in methanol (Φ_F=0.54) [60] are commonly used in this dissertation. At emission wavelengths longer than 650 nm, no commercial dye is available for reference, thus a photochemically stable cationic polymethine dye: 3-ethyl-2-[7-(3-ethyl-1,1-dimethyl-1,3-dihydro-2H-benzo[e]indol-2-ylidene)hepta-1,3,5-trienyl]-1,1-imethyl-1Hbenzo[e]indolium-4-methylbenzenesulfonate (labeled as PD 2631), with Φ_F=0.11±0.01 in ethanol and with fluorescence peak at 809 nm [57]. This dye is proposed as a fluorescence quantum yield reference for NIR range. The Φ_F of PD 2631 was repeatedly measured using Cresyl Violet dye in methanol as a reference.

From the absorption-fluorescence and quantum yield measurements, the fluorescence lifetime (τ_F) can be calculated by Strickler-Berg's equation in ***CGS units*** [61].

$$\tau_F = \Phi_F \tau_N$$

$$1/\tau_N = 2.88\times10^{-9} n^2 \varepsilon^{\max} [\frac{\int F(\nu)d\nu \times \int \frac{\varepsilon(\nu)}{\nu} d\nu}{\int \frac{F(\nu)}{\nu^3} d\nu}] \quad (3.2)$$

Where τ_N (s) is the natural lifetime (the lifetime in the absence of any nonradiative processes), n is the refractive index of the solvent, ε^{max} (cm^{-1} M^{-1}) is the molar absorbance at the peak of the absorption band, and $F(\nu)$ and $\varepsilon(\nu)$ are the normalized absorption and fluorescence spectra of the corresponding band with respect to photon frequency in wavenumbers (cm^{-1}). This calculated fluorescence lifetime for many polymethine dyes is shown to be equal to the lifetime of the corresponding excited state obtained by the pump-probe experiments discussed in .Section 3.3.4.

Another important linear optical measurement is fluorescence excitation anisotropy, which can identify the positions of the higher lying excited states and the orientation angles between their absorption transition dipole moments and fluorescence emission dipole moment. The value of anisotropy, $r(\lambda)$, is obtained by $r(\lambda) = [I_{//} - I_{\perp}]/[I_{//} + 2I_{\perp}]$, where $I_{//}$ and $I_{\perp}$ are intensities of fluorescence signal polarized parallel and perpendicular to the excitation light respectively [47]. The sample should be prepared in high viscous solvent to avoid molecular reorientation, and kept in low concentration (10^{-6} M) to avoid reabsorption. The relation between anisotropy value and the angle (ϕ) between absorption and emission dipole is written in Equation. 3.3:

$$r = \frac{2}{5}\left(\frac{3\cos^2\phi - 1}{2}\right) \quad (3.3)$$

Based on Equation 3.3, anisotropy value should have the range from 0.4 to -0.2, corresponding to parallel and perpendicular orientation between absorption and emission dipole moments.

The fluorescence spectrum, quantum yield, and excitation anisotropy in this dissertation are measured by a PTI Quantamaster spectrofluorometer with T format excitation-detection geometry. The monochromator with two gratings (1200 lines/mm and 600 lines/mm) is used to select wavelengths from the visible to NIR. Three detection channels (i.e. three PMT detectors) can be selected to measure the fluorescence wavelength range from 300 nm to 1.7 μm. The three PMT detectors are Hamamatsu R1527P (for blue channel, maximum detection wavelength λ^{max}=700 nm), Hamamatsu R928P (for red channel, maximum detection wavelength λ^{max}=800 nm) and liquid-nitrogen cooled Hamamatsu R5509-73 (for NIR channel, maximum detection wavelength λ^{max}=1700 nm). As an example, a typical fluorescence excitation anisotropy spectrum of a squaraine dye is shown in Figure 3.1 including the 1PA/1PF spectra. The flat area across 1PA main band has the anisotropy value near 0.35, indicating almost parallel orientation between absorption and emission dipoles, suggesting allowed 1PA transition. In contrast, valleys at 425 nm, 350 nm, and 305 nm in the spectrum indicate the large angles between these two dipoles, suggesting small transition dipole moments thus forbidden 1PA transitions. Therefore, excitation anisotropy can identify the higher lying energy states which are otherwise not accessible by the linear absorption spectrum. Due to selection rules of symmetrical cyanine-like dyes, the valley of the anisotropy spectrum could indicate a possible 2PA transition.

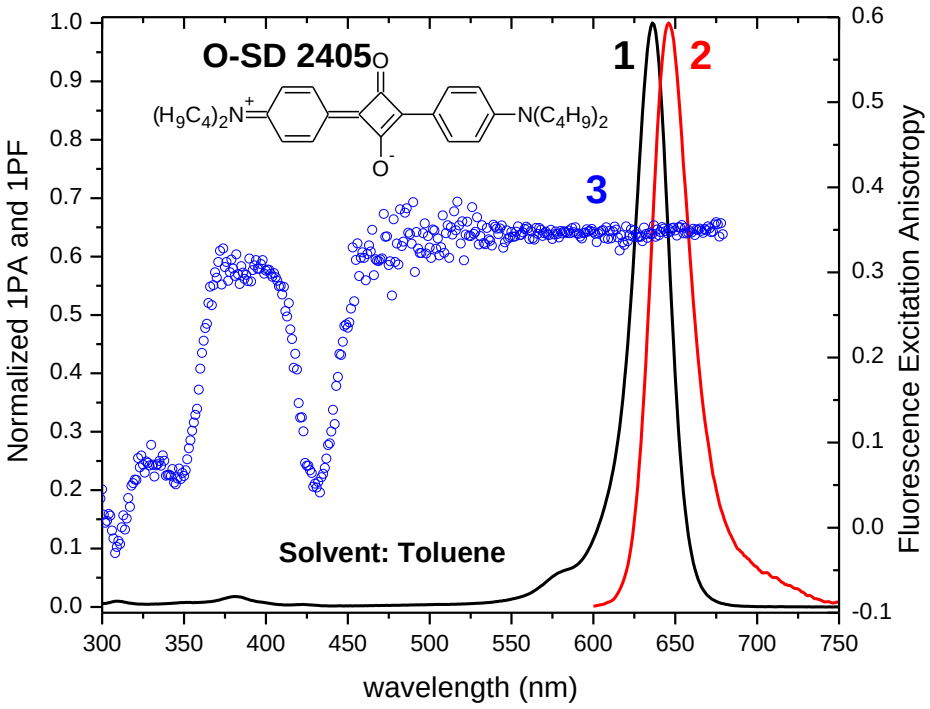

Figure 3.1: Linear absorption (1), fluorescence (2) and fluorescence excitation anisotropy (3) spectra of a squaraine dye (O-SD 2405) in toluene

The more detailed experimental procedure of the linear optical measurements is described in APPENDIX C.

3.2 Nonlinear Spectroscopic Characterizations

3.2.1 Excitation Source

Since nonlinear spectroscopic characterization measures the response of the material with its optical properties "modified" by the incident light, the material should be exposed to a strong excitation source with sufficient irradiance or fluence. A tunable laser source is thus a necessity. In this dissertation, the nonlinear spectroscopic characterization is mainly performed using a

femtosecond laser system with optical parametric generators/amplifiers (OPA/OPG). Picosecond and nanosecond laser systems are also involved in some experiments.

The femtosecond laser systems are Ti: Sapphire based regenerative amplifier systems (CPA-2210 and CPA-2010, CLARK-MXR), which operate at 775 nm with a repetition rate at 1k Hz and pulsewidth of ~140 fs (FWHM), delivering 1.6mJ and 1mJ pulse, respectively. The fs seed pulse is provided by an Erbium doped fiber ring laser (operating at 1550 nm), pumped by a 980 nm semiconductor laser diode, and frequency doubled to 775 nm by a periodically poled lithium niobate (PPLN) crystal. It is then stretched to ~200 ps by a multi-pass reflecting diffraction grating before being injected into the regenerative amplifier by a Pockels cell. This is a typical practice of chirped pulse amplification (CPA) technique, which is aimed to amplify an ultrashort pulse without extremely high peak power to avoid damage of optics [62]. After injection, the seed is then amplified in the gain medium (Ti: Sapphire crystal), which is pumped by a Q-switched frequency-doubled Nd: YAG Pump Laser operating at 532 nm. After several passes inside the gain medium to reach saturation, the amplified pulse is switched out by the same Pockels cell and compressed by a multi-pass transmission grating before being delivered to the output. The bandwidth of the laser is ~7 nm (FWHM)

The wavelength tunablity of the excitation source is provided by two types of traveling-wave optical parametric amplifiers, TOPAS-C and TOPAS-800 from Light Conversion, pumped by CPA-2010 and CPA-2210 respectively. They share generally the same working principle however with different setup layouts. Here we take TOPAS-C as an example.

TOPAS-C is a two-stage parametric amplifier of white-light continuum (WLC), as shown in Figure 3.2. A small portion of pump (~1-3 μJ, shown as ③ in Figure 3.2) from CPA2010 is focused on a sapphire plate (WLG in Figure 3.2) to generate a broadband stable WLC (⑤) as

seed pulse. It is then temporally chirped by a dispersive plate (ZnSe, TD) to introduce sufficient group velocity dispersion (GVD) so that different wavelength components can be separated by delays stages in the following pre-amplification. The WLC and another portion (~30-50 μJ, ④) of the pump are then focused onto a $\chi^{(2)}$ crystal (pre-amplification crystal, NC1) in a non-collinear manner, where parametric amplification takes place. After spatial separation, the pre-amplified signal beam (⑥) is collimated and delivered to another $\chi^{(2)}$ crystal (NC2), overlapping collinearly with the bulk part of the pump beam (②) to achieve power amplification. In both amplification processes, the crystal angle is optimized by rotational stages at phase-matching condition for maximum conversion efficiency. The output of the TOPAS-C thus contains two collinear signal and idler beams with orthogonal polarizations. The wavelength tuning range is 1.1-1.6 μm for the signal beam, and 1.5- 2.6 μm for the idler. At 1.3 μm for the signal beam, the output energy is ~200 uJ. Further extension of the wavelength tuning range can be achieved by second harmonic generation (SHG) of the signal or idler, or sum frequency generation of the signal and the pump. The total tuning range of the TOPAS-C is 510 nm to 2.6 um. For TOPAS-800, a five-pass system using superfluorescence as the seed pulse, extra tuning range (280 nm to 10 μm) is obtained by using forth harmonic generation and difference frequency generation (DFG). In both OPG/OPA systems, the output pulsewidth is 100-200 fs (FWHM).

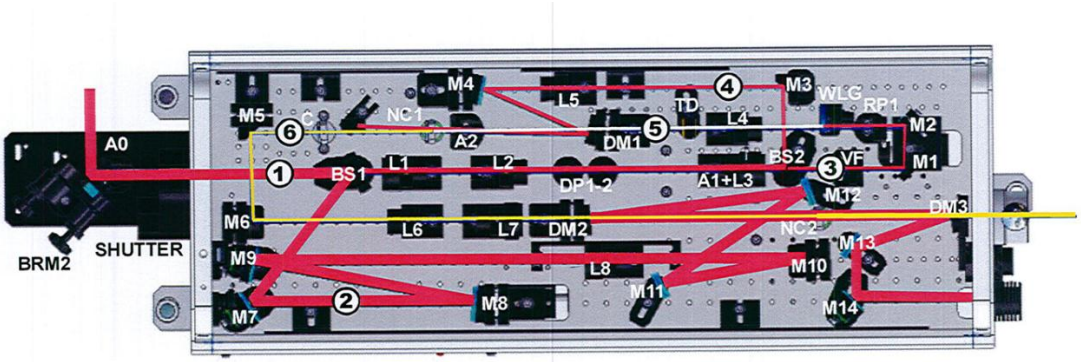

Figure 3.2: Setup schematic of TOPAS-C (from TOPAS-C manual). M-Mirror, L-lens, BS-beam splitter, DP-Delay plates, A-aperture, VF-variable ND filter, DM-dichroic-mirror, WLG-sapphire plate C-compensator, TD-temporal delay (ZnSe)

The picosecond system is composed by an optical parametric generator/amplifier (OPG/OPA, EKSPLA, Model PG401 DFG) and a pumping Nd:YAG mode locked laser (EKSPLA, model PL2143, ~30 ps FWHM pulsewidth operating at 1064 nm with 10 Hz repetition rate) which is frequency tripled. The wavelength range of picosecond system can be tuned from 400 nm to 16 μm. The nanosecond system is an externally frequency tripled 10 Hz seeded Nd:YAG laser (Continuum, Powerlight 9010) pumping optical parametric oscillator (OPO, Continuum Sunlite EX) with wavelength range tunable from 445 to 1750 nm. The pulsewidth is between 2.5-16.5 ns (FWHM).

3.2.2 Two-Photon Absorption Induced Fluorescence (2PF) Spectroscopy

With molecules with significant fluorescence quantum yield, two-photon absorption induced fluorescence (2PF) is a typical experimental technique to obtain a degenerate 2PA spectrum. After simultaneous absorption of two photons, the electron is promoted to an excited

state (S_n), followed by a rapid relaxation to the zero vibrational level of the 1st excited state (S_1). The number of fluorescence photons, emitted by the electron relaxing from S_1 to the ground state (S_0), is thus an indication of the population of the excited electrons during the excitation, which is proportional to the 2PA coefficient. Note that since the 2PA is proportional to the square of the input irradiance, such dependence also holds for the fluorescence signal; therefore it is a standard criterion to distinguish 1PF and 2PF by verifying the quadratic dependence of the fluorescence signal on input irradiance. 2PF was first used by Kaiser et al in 1961 [4], and then developed by Xu et al in 1996 [63] to measure 2PA spectra. A direct measurement of the fluorescence signal to determine 2PA is a relatively difficult experimental task, due to uncertainty on various experiment parameters, e.g. pulsewidth, pulse energy, collection geometry and efficiency, *etc*. With the knowledge of a reference molecule with known 2PA spectrum, a relative optical measurement, similar to the fluorescence quantum yield measurement, is thus feasible.

The experimental schematic is shown in Figure 3.3. The PTI Quantamaster spectrofluorometer is used for 2PF measurement with a tunable femtosecond pulse instead of the conventional Xenon lamp as the excitation source. A combination of half-wave plate and calcite polarizer is used as a beam energy attenuator; a telescope is used to expand the beam; an iris is placed afterward to select center part of the beam. The resulting clean flat top beam is then focused onto the sample solution in a 1cm cuvette to generate upconverted fluorescence, which is collected in a 90 ^{o} geometry with respect to the excitation beam by a collecting lens. The fluorescence spectrum is recorded by a computer-controlled monochromator and a low noise PMT detector. To minimize strong re-absorption of the fluorescence signal due to high

concentrations of the sample solution, the excitation beam is focused near the wall of the cuvette close to the collecting lens. The recorded fluorescence spectrum should be corrected by the spectral sensitivity of the detector and re-absorption by the solution itself due to the strong inner filter effect. To determine the 2PA spectrum of the sample solution, the integrated fluorescence signal is then compared against a reference molecule with known 2PA cross section under identical measuring condition. The 2PA cross section for the sample can be calculated from Equation 3.4:

$$\delta_{2PA\,sample} = \frac{\langle F \rangle_{sample} \Phi_{F\,ref} C_{M\,ref} \langle P \rangle_{ref}^{2}}{\langle F \rangle_{ref} \Phi_{F\,sample} C_{M\,sample} \langle P \rangle_{sample}^{2}} \delta_{2PA\,ref} \qquad (3.4)$$

where <F> is the integrated fluorescence and <P> is the average pump power which is proportional to pulse energy, C_M is the concentration of the solution measured by 1PA spectrum and Φ_F is the fluorescence quantum yield measured by 1PF. The typical error in our 2PF measurement is ~15%.

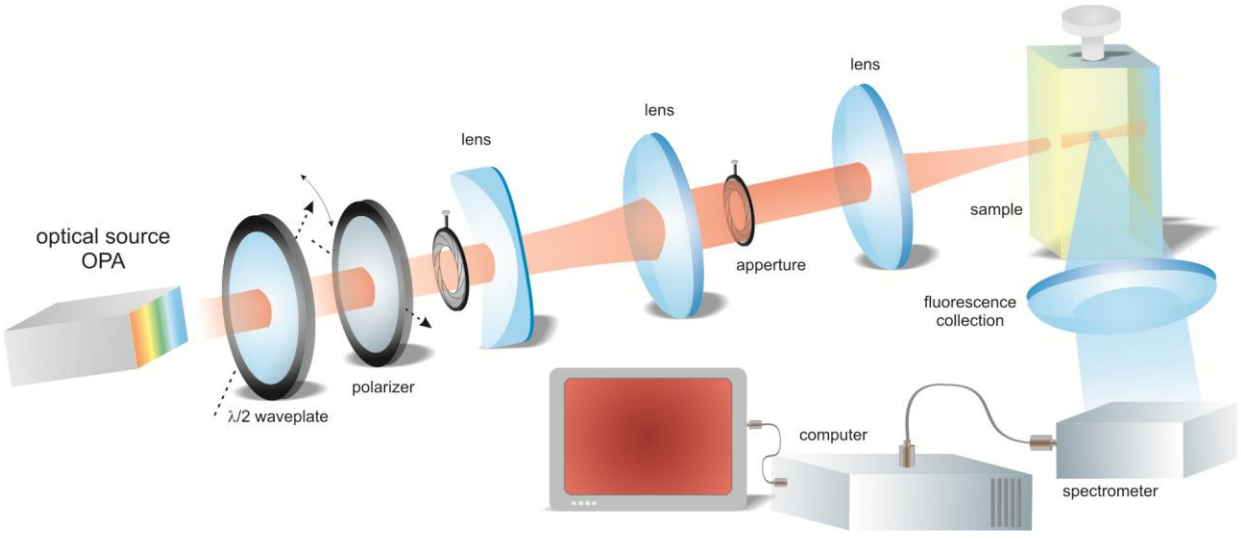

Figure 3.3: Experiment schematics for the two-photon fluorescence measurements

There are several important factors contributing to a successful and accurate 2PF measurement. The concentration of the solution should be as high as possible (but below the aggregation threshold) to increase the probability of 2PA; a typical concentration of solution for 2PF measurement is usually more than 10^{-4} M. The re-absorption of the fluorescence signal due to high concentration of the solution and small Stokes shift should be carefully considered. Assuming the fluorescence spectrum and quantum yield is independent upon concentration of the solution and the type of excitation (i.e. 1PA or 2PA), the 2PF spectrum can be fitted against 1PF spectrum measured at low concentration (with peak OD < 0.1) to obtain a correct spectral contour to eliminate inner filter effect [64]. The selection of reference molecule is based on the spectral range of the fluorescence of sample and reference molecule. A large overlap of the fluorescence spectrum could minimize the measurement error induced by spectral sensitivity of the detector. Several 2PF standards have been published with emission wavelengths ranging from 390 to 1000 nm and excitation wavelength from 500 to 1600 nm [63,65,66]. In this dissertation, we mainly use Rhodamine B in methanol ($\Phi_F=0.7$) as the reference molecule since the dye of interest is mainly fluorescent at red wavelengths.

The 2PF technique has several advantages. It is a rapid experimental technique to measure 2PA spectrum in comparison to other commonly adopted technique, e.g. Z-scan. It is not sensitive to 2PA followed by ESA, since ESA in this case doesn't contribute to the fluorescence process, although 1PF should be carefully excluded as discussed above. The sensitivity of 2PF is fairly high thanks to the high responsitivity of the PMT detector and zero background of fluorescence signal: a 2PA cross section less than 10 GM can be measured given a sample solution with large fluorescence quantum yield and high concentration.

On the other hand, the requirement that the sample solution be fluorescent is the main limitation of the 2PF technique. Another disadvantage is that it can only determine 2PA cross sections of liquid solutions; a solid state sample would be difficult to accommodate in the current setup due to lack of reference, although the relative spectral shape of 2PA might be determined. In our current laboratory condition, the 2PF wavelength range is limited to wavelengths shorter than 800 nm for a 2PA cross section spectrum due to limitations of the PMT detector. Finally, the 2PF technique can only measure 2PA, i.e. imaginary part of $\chi^{(3)}$; the nonlinear refractive index, n_2, has to be measured by other experimental techniques.

3.2.3 Z-scan

Z-scan, as proposed by Sheik-Bahae *et al*, is the most commonly adopted technique in NLO community to measure the material optical nonlinearities [67]. It is a simple but powerful single beam technique which only requires sample to translate through the focus of a Gaussian beam along its propagation direction. To measure the nonlinear absorption of the sample, one simply puts the detector behind the sample collecting all the transmitted light. An irradiance (which is dependent on z position) dependent transmittance is thus recorded (called as open-aperture Z-scan) as shown in Figure 3.4a. On the other hand, the nonlinear refraction of the sample can be measured by placing an aperture at far field of the beam, forming a closed-aperture Z-scan. Due to irradiance dependent refractive index of the sample, a "Kerr lens" is imposed on the sample near the focus inducing an extra phase front distortion of the incident beam (called self-phase modulation), which interferes at the aperture plane. For a positive "Kerr lens" formed by a positive n_2, if sample is placed before the focus of the beam, it would "pull"

the focus towards the sample due to extra focusing power, resulting in a further beam expansion on aperture plane and thus a decrease of aperture transmittance; while if the positive "Kerr lens" pass through the focus of the beam, it reduces beam expansion at the far field, and thus leading to an increase of aperture transmittance. Therefore, a valley-peak shape of Z-scan trace is the signature of a positive n_2 as shown in Figure 3.4b. A negative n_2 would have an opposite effect and thus resulting in a peak-valley Z-scan trace. Note that the Z-scan trace shown in Figure 3.4b assumes no nonlinear absorption (NLA). With the presence NLA, it will distort the closed-aperture Z-scan trace; however, a simple division with closed-aperture and open-aperture Z-scan trace, although without any physical significance, can be treated as a "pure" closed-aperture Z-scan trace to fit with appropriate n_2. But such treatment might be misleading if NLA is overwhelmingly large compared to NLR, an erroneous n_2 might be extracted [68].

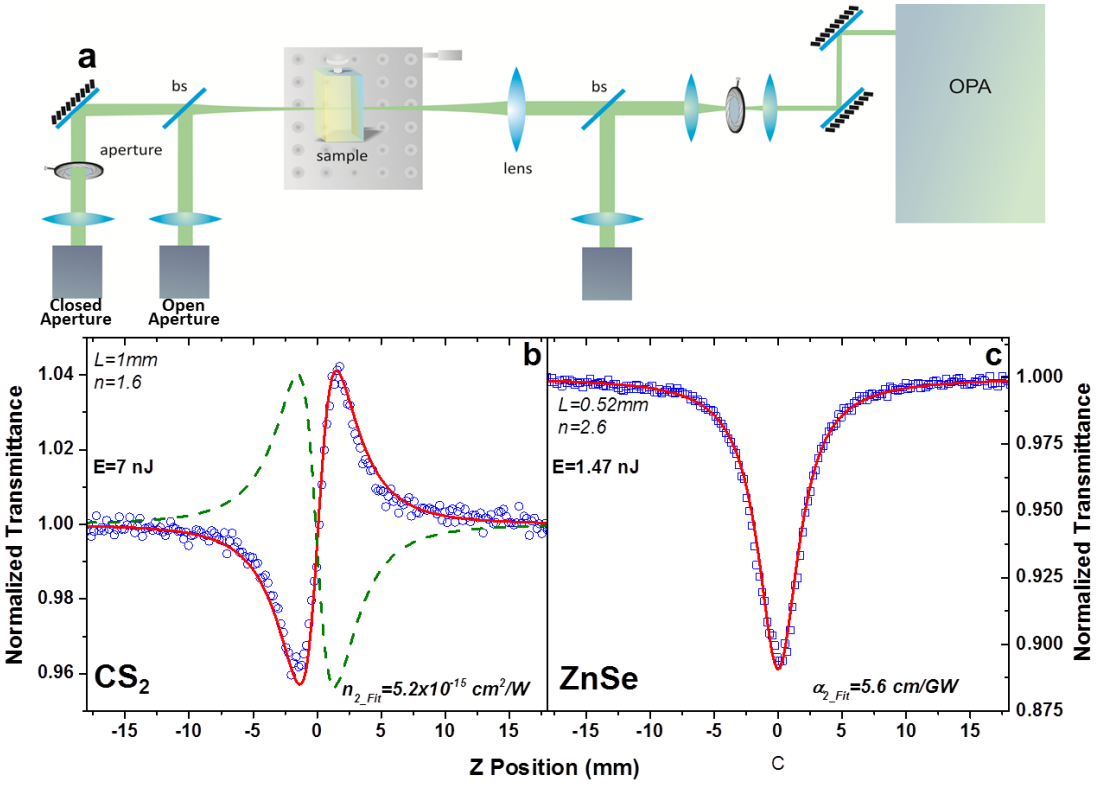

Figure 3.4: (a) Schematic of a single wavelength single arm Z-scan setup; (b) Experimental (blue dot) and fitted (red solid) closed-aperture Z-scan traces of CS_2 with a positive n_2=5.2 ×10^{-15} cm^2/W and simulation of Z-scan trace (green dash) with the same magnitude but negative n_2; (c) Experimental (blue dot) and fitted (red solid) open-aperture Z-scan traces of ZnSe with α_2=5.6 cm/GW. Note that the wavelength is 700 nm, spot size is 19.8 ±2 μm (HW1/e^2M) and pulsewidth is 143 ± 14 fs (FWHM)

There are several important factors leading to a successful Z-scan experiment. The exact knowledge of beam parameter is critical, i.e. the pulsewidth, and beam waist. The incident beam should be close to the ideal beam model assumed in the fitting program. In most cases, a TEM_{00} Gaussian beam is desirable since it is the simplest and easiest beam to generate in the laboratory condition. The beam waist and its quality can be measured independently by a knife-edge scan. The pulsewidth can be measured by auto-correlation technique; however, it might not be reliable when the pulsewidth is very short (<70 fs) where a change of optics might induce different GVD

thus altering pulsewidth. Another typical practice to obtain beam parameters is to use a reference material such as bulk semiconductor [40], fused silica [69] with their nonlinearity (2PA and n_2) well documented and perform a Z-scan on the current setup. The beam waist and pulsewidth is thus calibrated by fitting the corresponding Z-scan traces. CS_2 is also a popular reference material to calibration the Z-scan setup; however, since its n_2 is dependent upon input pulsewidth especially below ps pulsewidth, it is not a good reference material to determine the pulsewidth. More details about pulsewidth dependent n_2 will be discussed in CHAPTER 5. The sample quality is also important, especially for solid state samples or films with many surface defects, a low energy scan is necessary to probe the background, followed by a high energy scan. The background can possibly be canceled by dividing of high energy trace over low energy trace [40]. To reduce the noise of Z-scan trace, a correct reference arm should be in identical geometry as the closed-aperture arm, so that the fluctuation of the laser in both energy and pointing direction could be monitored and canceled.

There are two assumptions for most Z-scan traces to fit to a relatively simple mathematical model. The first assumption is that sample is "thin", with sample thickness, L, less than the Rayleigh range of the beam in the sample, which assures that the beam waist can be considered as a constant through the sample. The second assumption is that the induced nonlinear phase perturbation is small so no significant change of propagation behavior through the sample. For Z-scan traces with open-aperture signal, or with closed-aperture signal without any presence of NLA, a simple Gaussian-decomposition is the most efficient approach to extract nonlinear parameter [67]. However, for the closed-aperture signal coupled with NLA, a numerical code (written in Matlab) is developed, which assumes the incident beam has a plane wavefront with a Gaussian irradiance profile to simulate the Gaussian beam input. It numerically simulates

the beam "propagating" through each "slice" of the sample assuming cylindrical symmetry of the beam at each temporal "slice", and use Fresnel-Huygens diffraction formulism to propagate in free space from the exit of the sample to the closed-aperture plane before integration over the whole temporal and spatial domain to calculate the transmittance [70]. The typical absolute measurement error of nonlinearity measured by Z-scan is ~±25%, which is determined by the error of beam waist (10%), input energy (10%) and pulsewidth (10%).

Another important issue related with open-aperture Z-scan, despite its simplicity, is the complexity to find a correct physical model to interpret the experimental data. In various experimental conditions, different physical mechanisms would contribute to similar Z-scan traces. For example, when the incident photon energy is closed to the 1PA gap of the material, a 2PA process, or an ESA following the linear absorption in the tail of its absorption edge (a $\chi^{(1)}$: $\chi^{(1)}$ process) could yield to similar Z-scan trace. To distinguish these two physically distinctive phenomena, an additional experiment revealing the temporal response of the sample (i.e. pump-probe experiment) is necessary. This will be discussed in the next section. Another examples is the selection of input pulsewidth for Z-scan, the instantaneous process (e.g. 2PA) is preferably investigated by ultra-short pulse excitation, i.e. <100 fs-pulses, due to large irradiance but relatively small fluence; using long pulse (ns-, ps-pulse) might lead to over-estimation of the 2PA cross section by orders of magnitude, because the ESA will contribute to nonlinear absorption due to large fluence of the pulse and thus significant population built up in the excited state within the pulse duration [15].

In terms of investigation of D-2PA of the sample, Z-scan and 2PF are independent but complimentary techniques. 2PF is a rapid relative optical measurement which requires sample be fluorescent and a reference molecule with known 2PA; Z-scan is an absolute measurement

which can be performed on any sample without referring to a 2PA standard, but it needs a delicate alignment which is thus much less efficient than 2PF. Since 2PA is a material parameter, these two techniques should yield to the same result, if the experiments are performed carefully, and the Z-scan fitting models correctly reflect the nonlinear mechanisms [66]. Therefore, Z-scan and 2PF are two complementary techniques which can be utilized as a cross examination to each other. This will also be verified in pump-probe technique discussed in the following chapter.

3.3.4 Pump-probe Technique

Although Z-scan technique is proved to be versatile in measuring material optical nonlinearities, it measures the response only within the pulse duration but can't determine how material responses temporally after excitation. Another experimental approaches called pump-probe is thus developed. It uses a strong beam as a pump to excite the sample to change its optical properties; a weak probe, with its energy low enough not to perturb the sample, is then delivered in the overlap of the excitation area to measure the transmittance/ reflectance of the sample. By temporally delaying the delivery of the probe pulse using a retro-reflector mounted on a translation stage, the response of the sample after excitation can be investigated. The temporal accuracy is determined by the pulsewidth of the pump and probe pulse and the spatial resolution of the translation stage.

By choosing appropriate pump and probe wavelengths, the pump-probe technique can be used to investigate ESA or 2PA process of the material. To demonstrate the ESA process of the material in pump-probe experiment, a three level model based upon Jabłoński diagram is considered here as a standard physical model. The pump wavelength is usually set within the

1PA band of the sample (usually corresponding to the S_1 state). Before the pump pulse hits the sample, the linear transmittance of the probe pulse can be determined by Beer-Lambert's law

$$\begin{aligned} &\ln(T_0) = -\alpha_0 L \\ &\alpha_0 = -\sigma_{01} N \end{aligned} \qquad (3.5)$$

where N is the total population of electrons which sits at S_0 state. The excitation of pump pulse promotes a significant fraction of electrons into S_1 state (assuming $N_{S1}(0)$), which then relax back to S_0 state by exponential decay at a rate corresponding to the lifetime of the S_1 state (τ_F). Here we assume no population built up in the higher excited states, Sn, and the excitation is a δ function for simplicity. The rate equation after excitation at delay τ can be written as:

$$\begin{aligned} &\frac{dN_0}{d\tau} = \frac{N_{s1}}{\tau_F} \\ &\frac{dN_{s1}}{d\tau} = -\frac{N_{s1}}{\tau_F} \\ &N_0 + N_{S1} = N \end{aligned} \qquad (3.6)$$

where N_0 is the population of S_0; N_{S1} is the population of S_1. By solving Equation 3.6, N_0 and N_1 at delay τ after excitation can be written as

$$\begin{aligned} &N_{S1}(\tau) = N_{S1}(0) e^{-\tau/\tau_F} \\ &N_0(\tau) = N - N_{S1}(0) e^{-\tau/\tau_F} \end{aligned} \qquad (3.7)$$

Note that they follow a single exponential decay if no other excitation or other decay channel involved. The absorption of the probe pulse, after delay τ, can be written as:

$$\begin{aligned} &\frac{dI_p(\tau)}{dz} = -\alpha_p(\tau) I_p(\tau) \\ &\alpha_p(\tau) = \sigma_{01} N_0(\tau) + \sigma_{s1n} N_{s1}(\tau) \end{aligned} \qquad (3.8)$$

where $\alpha_p(\tau)$ is the transient absorption coefficient. By integrating the irradiance over the sample thickness, the transient transmittance of the probe can be written as

$$\ln[T(\tau)] = \ln\left[\frac{I_p(z=L)}{I_p(z=0)}\right] = -\alpha_p(\tau)L \qquad (3.9)$$

By subtracting Equation 3.9 from Equation 3.5, it yields

$$\ln(T_{norm}) = \ln\left[\frac{T(\tau)}{T_0}\right] = -(\alpha_p - \alpha_0)L = -\Delta\alpha(\tau)\cdot L \qquad (3.10)$$

Note that $T_{norm}=T(\tau)/T_0$ is the normalized transmittance trace of the pump we measured in the experiment. By applying Equations 3.5, 3.9 and 3.10, $\Delta\alpha(\tau)$ can be transformed to

$$\Delta\alpha(\tau) = (\sigma_{s1n} - \sigma_{01})N_1(\tau) \qquad (3.11)$$

Therefore, the *logarithm* of the normalized transmittance trace is proportional to the population at the S_1 state, which shows an exponential decay with a constant equal to the lifetime of S_1 as shown in Equation 3.7. Another important observation is that at a specific delay τ, $\Delta\alpha$ is proportional to the difference between ESA cross section σ_{s1n} and ground state absorption cross section σ_{01} which can be utilized to measure ESA spectrum of the sample. By changing probe wavelength and measure T_{norm} at the same delay under identical pump, one can build a "spectrum" showing difference between σ_{s1n} and σ_{01} in arbitrary units. However, to quantify σ_{s1n} in absolute values, we need to either quantify the exact parameter of the pump beam (i.e. irradiance and fluence) to calculate the population of S_1, or perform another independent experiment (ps Z-scan) to determine the absolute cross section at one wavelength (λ_{ESA}). The absolute ESA spectrum can then be expressed as [71]

$$\sigma_{S1n}(\lambda) = \sigma_{01}(\lambda) - [\sigma_{01}(\lambda_{ESA}) - \sigma_{S1n}(\lambda_{ESA})] \times \frac{\ln(T_{norm}|\lambda)}{\ln(T_{norm}|\lambda_{ESA})} \qquad (3.12)$$

To investigate the 2PA process, the pump wavelength is chosen below the absorption gap of the material to avoid any 1PA, or preferably below the half of the absorption gap of the

material to avoid D-2PA of the pump. As the pump and probe pulse overlap in time and space, the material will have a chance to simultaneously absorb two photons, one from pump and the other from probe, and promote an electron to a higher excited state. This is a non-degenerate 2PA (ND-2PA) process, since *two* independent beams are involved and the pump and photon usually have *different* photon energies [1], and the ND-2PA coefficient, α_2^{ND}, can be defined as

$$\frac{dI_p}{dt} = -2\alpha_2^{ND} I_E I_p \qquad (3.13)$$

Where I_E is the irradiance of the pump beam. Note that the coefficient 2 is the result of permutation parameter due to the presence of two input beams. By making 3 assumptions: (1) both pump and probe pulses are transform-limited Gaussian pulses; (2) no broadening is induced during the propagation of both pulses; (3) no depletion of the pump irradiance due to NLA, the analytical equation to describe the transmittance dynamics of the probe due to ND-2PA in this pump-probe scenario including the temporal walk-off mismatch between pump and probe (due to GVD) can be written as [72]:

$$Q(\sigma,\tau_d,W,\rho,\Gamma) = \frac{e^{-2\sigma}}{W\sqrt{\pi}}\int_{-\infty}^{+\infty}\exp\left\{-\left(\frac{\tau+\tau_d-\rho}{W}\right)^2 - \frac{\Gamma\sqrt{\pi}}{\rho}\left[erf(\tau)-erf(\tau-\rho)\right]\right\}d\tau \qquad (3.14)$$

where Q is transmittance of probe, σ is 1PA coefficient, τ_d is delay time between the pump and probe pulses, W is the ratio of the transform limited probe pulsewidth to pump pulsewidth. ρ is the parameter related to group velocity mismatch between pump and probe pulse. Γ is the parameter related to α_2^{ND} $\Gamma = LI_E\alpha_2^{ND}$, and L is sample length. A typical pump-probe trace for ESA and ND-2PA process is shown in Figure 3.5 a and b, respectively.

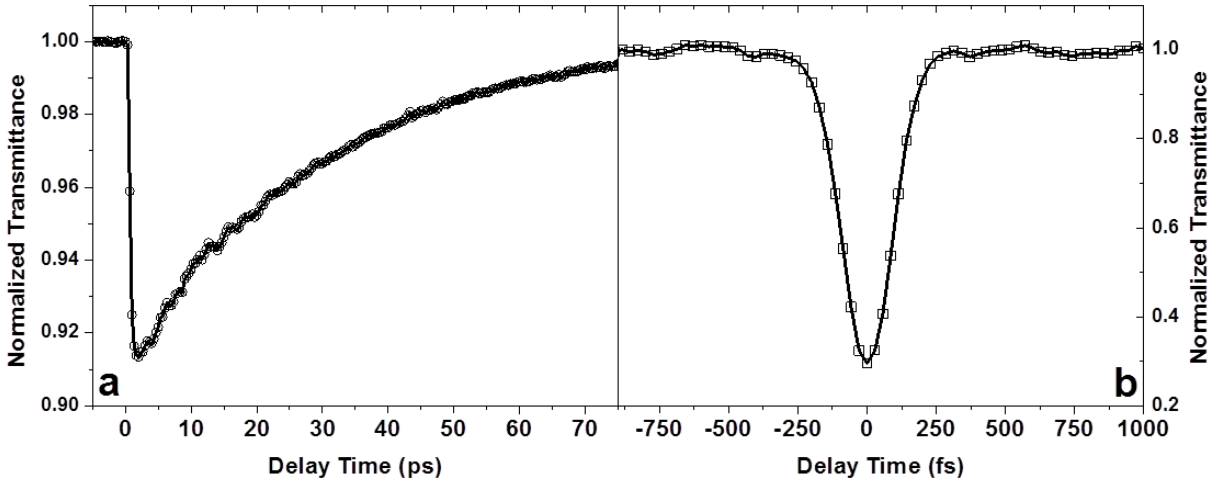

Figure 3.5: Typical pump-probe trace for ESA (a) and 2PA (b) process. The decay time of ESA is ~28 ps. The pulsewidth of excitation is ~140 fs (FWHM)

The difference in response time performed by pump-probe experiment is the most direct experimental approach to differentiate 2PA from ESA when the incident photon energy is close to the absorption edge (or actually within the linear absorption edge) of the material, which otherwise is almost indistinguishable in Z-scans [73].

In our laboratory, we use white light continuum (WLC) pump-probe technique as shown in Figure 3.6. The pump beam is generated by the wavelength tunable OPA/OPG (TOPAS-800 or TOPAS-C), pumped by the femtosecond laser system. A weak portion of fundamental laser, picked up from a beam sampler and then delayed by the retro-reflector, is focused onto a 1cm water cell with appropriate energy to generate a stable and broadband WLC serving as the probe beam. There are two approaches to utilized WLC as a probe. The first approach is to use WLC to probe the sample, and use a spectrometer with a high-resolution CCD camera to measure the spectrum of the transmitted WLC in comparison to the original WLC spectrum. This is conceptually a single-shot experiment to obtain the ESA and ND-2PA spectrum at one scan.

However the strong chirp of the WLC complicates the determination of the zero-delay point between pump and probe, which is essential for a pump-probe experiment; and the spectral overlap between fluorescence of the sample and the probe WLC will induce stimulated emission, which significantly modifies the population dynamics of the material [25]. Therefore, the second approach is adopted here despite a relatively poor spectral resolution: we use a spike filter in front of the sample to select the wavelength of the probe, and another identical spike filter in front of the detector to block the background pump. Hence the spectral resolution is determined by the number of spike filters available. The bandwidth of the spike filter is broad enough to pass the probe pulse without significantly changing its pulsewidth (~140 fs FWHM close to the pulsewidth of pump laser). The spot size of the pump is usually 5 × larger than the probe pulse to make sure the probe beam "sees" a homogenous irradiance which will simplify the modeling, and the angle between pump and probe is less than 5 º. To further improve the signal to noise ratio of the detection system, a mechanical optical chopper, synchronized with the repetition (1k Hz) of the laser, is introduced to modulate the pump beam at ~285 Hz. A lock-in amplifier (SR830, Stanford) is employed to record the signal. The utilization of the lock-in amplifier system in combination with the spike filter dramatically improves the signal to noise ratio of the detection system. In our current laboratory condition, for a non-degenerate pump-probe (pump and probe wavelengths are different), the smallest measurable change in transmittance is less than 0.05%; but it deteriorates to ~0.5% for a degenerate pump-probe due to the inefficiency of blocking the scattering from the pump.

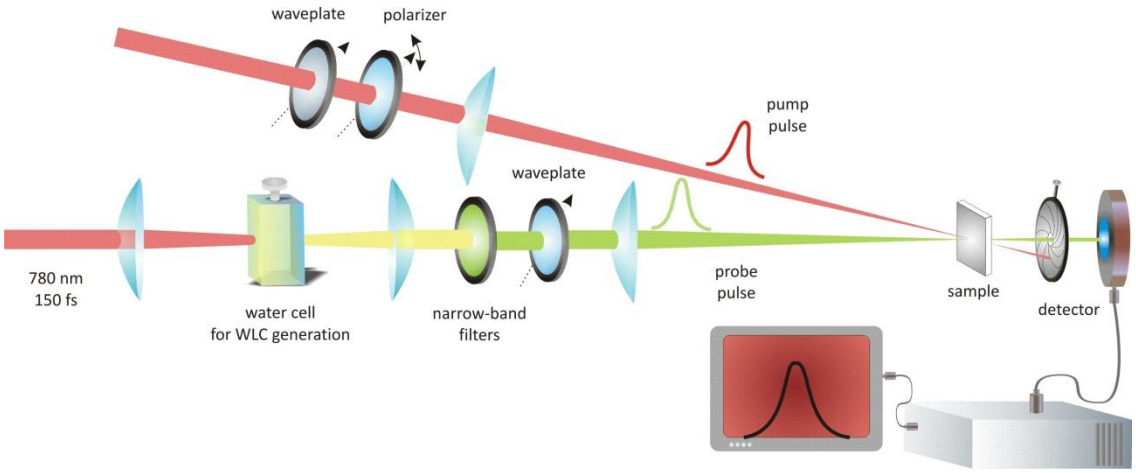

Figure 3.6: Experimental schematic of white light continuum (WLC) pump-probe setup

The polarization of the pump and probe is also an important factor to be considered in the pump-probe experiment. For ESA investigation, due to selective excitation of the linear molecule and the subsequent rotational randomization in an isotropic solution, the re-orientational lifetime of the molecule, usually over 100 ps for polymethine and squaraine dyes [25], will show contributions to the decay kinetics of the pump-probe data if the lifetime of S_1 state is close to or longer than the re-orientational lifetime. Therefore, the polarization angle between pump and probe beam is set at a "magic angle", 54.7 º, to eliminate re-orientation effects [74,75]. For 2PA investigation, the relative polarization of pump and probe determines the involvement of different $\chi^{(3)}_{ijkl}$ components of which *i, j, k,* and *l* are related with the beam polarization. Usually, a parallel polarization is employed to ensure measuring only $\chi^{(3)}_{1111}$. Half-wave plates are thus placed in front to the sample to control the polarization angle of pump and probe respectively without any lateral displacement of the beam on the sample. As will be shown in the next chapter, this is very useful to measure the polarization dependent nonlinearity of the

solid state material, which will reveal the anisotropic nature without complication due to sample inhomogeneity.

CHAPTER 4 STRUCTURE-PROPERTY RELATIONSHIPS OF NEAR INFRARED TWO-PHOTON ABSORBING MOLECULES

The spectroscopic techniques described in the previous chapter provide the capability to characterize the linear and nonlinear optical properties of molecules in either liquid solution or solid-state forms. By conducting these measurements, this chapter is mainly focused on the study of structure - 2PA property relationships of two-photon absorbing molecules. Previously, we investigated the structure - 2PA property relationships of fluorene-based molecules [64], polymethine (Donor-π-Donor) and squaraine ((Donor-π-Acceptor-π-Donor)) molecules [12] in terms of molecular symmetry, conjugation length, the donor or acceptor strength, solvism, *etc*. In this dissertation, we study the 2PA properties of four series of linear π conjugated NIR molecules with different molecular structural combinations. This chapter is organized as follows: A molecular design strategy is explained as the guideline for designing NIR molecules by extending the main conjugation length (and thus reducing the absorption gap) without the cost of photochemical instability. The four groups of NIR dyes are then introduced with their unique structural features as the motivation for its NLO investigation. The first two groups of dyes are: (1) Symmetrical Acceptor-π-Acceptor dyes with different conjugation length. (2) Asymmetrical Donor-π-Acceptor dyes. The study of these two groups of dyes, in combinations with D-π-D polymethine dyes (PDs), D-π-A-π-D squaraine dyes studied previously[12,64], further enriches the database of structure-2PA properties of cyanine-like molecules in order to develop a comprehensive strategy to enhance 2PA cross sections of organic molecules in various solvents. Furthermore, a single crystal, composed by a Donor-π-Acceptor dye, is also investigated extensively to reveal its large nonlinearity and strong anisotropy, which extends our scope from liquid solution forms to solid-state materials. The next two groups of dyes introduced in this

chapter focus on some interesting properties due to their specific structural features. The third dye group, a type of polymethine dye with very long conjugation length and small absorption gap, is presented to study the symmetry breaking effects. The last group of dyes, the pairs of oxygen-squaraine and sulfur-squaraine, is compared to study the role of sulfur atom on its optical nonlinearities. The linear and two-photon absorption properties of each group of dye are described in detail using various spectroscopic techniques. The results of quantum chemical calculations are also presented to explain the connection between structural modifications and nonlinear optical properties.

4.1 Extending the Linear Absorption into NIR Wavelengths

It is well known for linear π-conjugated molecular system, the linear absorption gap is mainly determined by its π-conjugation length. Lengthening of the main π-conjugation chain leads to a red-shift of the linear absorption peak, thus a decrease of absorption gap. Another great benefit for the lengthening of conjugation chain is the increase of nonlinear polarizability due to increased transition dipole moment (electron can transfer a longer distance), and reduced resonance frequency (smaller detuning energy), and thus the enhancement of 2PA cross section. Since the polymethine chain is the main conjugation bridge for a linear π-conjugated molecule, a straightforward molecular design approach is increasing the length of polymethine chain. An extension of conjugation length by one vinylene group (-C_2H_2-) usually leads to ~100 nm red shift of linear absorption peak [33]. This approach, although effective in decreasing the absorption gap of the molecule, is accompanied with a large problem of reduced photochemical stability, which complicates the investigation of the optical properties and limits its potential applications. An incorporation of a partial cyclization bridge on the center of the polymethine chain can

remedy the photochemical stability issue; however, it also somehow decreases the 2PA cross section compared to the molecule with similar conjugation length [33]. To overcome this difficulty, an alternative designing approach is preferred for NIR molecules. Instead of increasing the length of main conjugation chain, the end group is designed specifically to possess its own π-conjugation system which strongly interacts with the main conjugation chain. The result of such interaction is an "effective" increase of the conjugation length of the molecule without lengthening its polymethine chains. Shown in Figure 4.1 is the comparison of linear absorption spectra between two molecules (visible PD 2630 and NIR PD 2658) with the same main conjugation chain but different end groups. Note that the linear absorption peak of PD 2658 is ~1000 nm compared to ~700 nm for PD 2630. This 300 nm red-shift is connected with a substitution of benzoindolium groups for PD 2630 by benzofuroindolium groups for PD 2658, which is equivalent to the extension of conjugation chain by three vinylene groups.

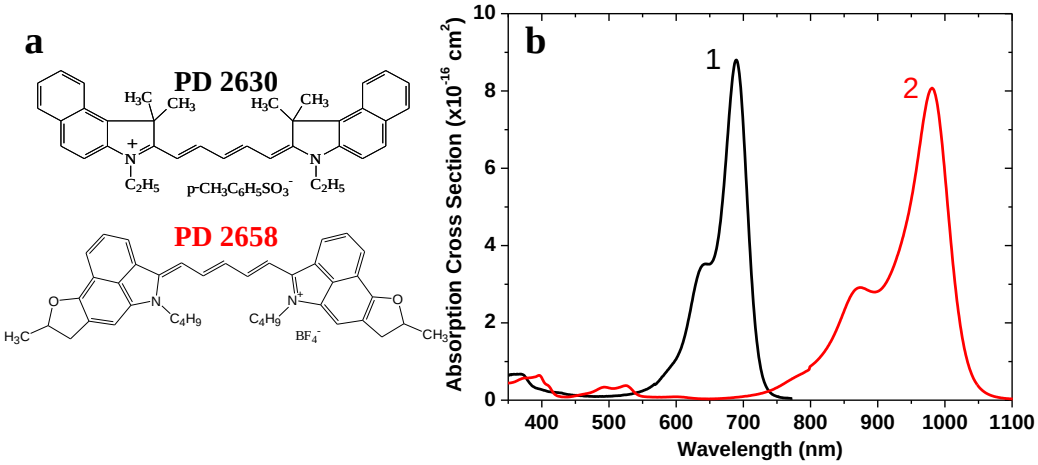

Figure 4.1: (a) Molecular structure and (b) linear absorption spectra of PD 2630 (1) in ethanol and PD2658 (1) in butanol

The detailed comparison of nonlinear optical properties of these two molecules can be found in ref 56. Nevertheless, development of end groups with their own π-conjugation system strongly interacting with the main polymethine chain to increase the "effective" conjugation length is the main design strategy to synthesize the NIR molecules shown in the following sections.

4.2 Introductions of Four Groups of Dyes

All the dyes involved in this dissertation are synthesized in Institute of Organic Chemistry, National Academy of Science, Kiev, Ukraine. By their unique features in molecular structure, they are classified into four groups.

Group1: Symmetrical Acceptor-π-Acceptor Anionic Dyes

This set of four dyes (labeled as G37, G38, G74 and G152) are featured with the two diethylamino-coumarin-dioxaborine (DOB) acceptors (A) connected via linear π conjugation chain with increasing length to form an anionic A-π-A structure shown in Figure 4.2. The presence of acceptor end groups leads to a negatively charged π-conjugation chain at the ground state, which is the mirror image of previously D-π-D dye [76]. The structure of DOB group possesses a strong donor diethylamino-group at the end of the end group, allowing us to suppose that this series of dyes can be represented as D-A-π-A-D quadrupolar-like structure. The presence of its own π conjugation system of the end group significantly increases the overall π conjugation length of the system. Differing in the length of vinylene chain, G37 is the shortest dye with n=1, and G152 is the longest, n=4. A bridge group is introduced at the center of the π-conjugation chain for G152 in order to increase the photochemical stability of the molecule. The

synthesis of G37, G38 and G74 can be found in ref. 77, and G152 in ref. 78. Note that the results for this group of dyes have been published in Ref. 78.

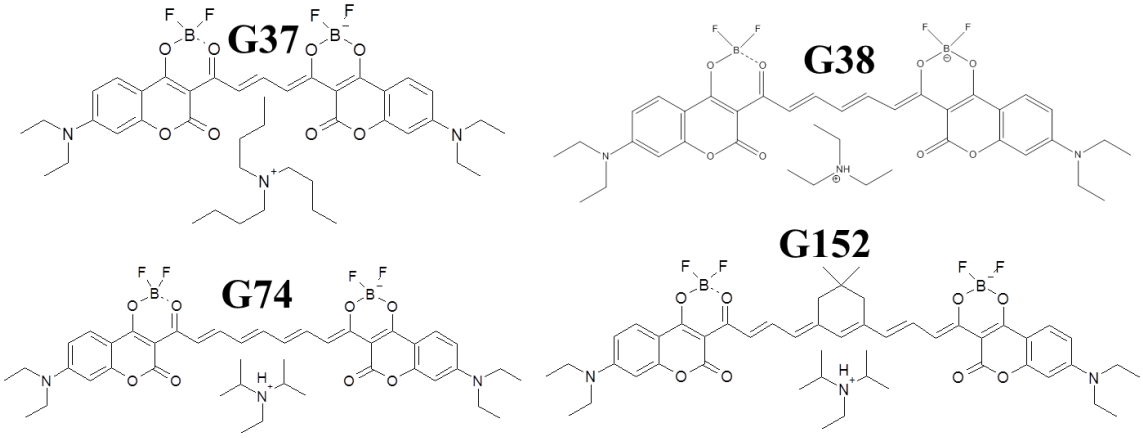

Figure 4.2: Molecular structures of G37 (n=1), G38 (n=2), G74 (n=3), and G152 (n=4)

Group 2: Asymmetrical Donor-π-Acceptor Dyes

This set of D-π-A dyes (G19, G40, G188) contains a DOB acceptor group and a trimethylindolin donor group at the ends of linear π-conjugation chain (Figure 4.3). Differing in the length of vinylene chain, G19 is the shortest dye with n=1, and G188 the longest one (n=3). The synthesis of G19 and G40 can be found in ref. 77 and G188 in ref. 79. Due to asymmetrical structure of this set of dyes, the study has been focused on the role of solvent polarity on their linear and nonlinear optical properties. Note that linear and nonlinear optical properties of this group of dyes in solution have been published in Ref 79.

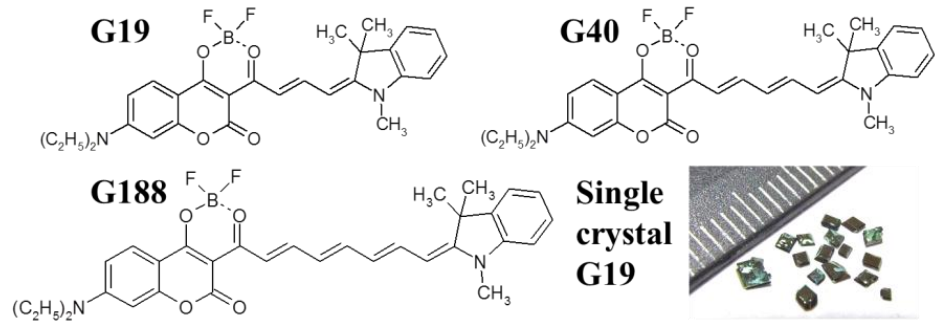

Figure 4.3: Molecular Structures of G19 (n=1), G40 (n=2), and G188 (n=3), and image of single crystal made from G19

In addition to the solution form of these D-π-A dyes, single crystals are grown from the sub-saturated G19 solution in acetonitrile (Figure 4.3). Due to high density and directional molecular packing, the single crystal shows large nonlinearity and strong anisotropic behavior. An X-ray diffraction analysis is necessary to determine the structure of single crystal cell and understand its linear and nonlinear optical property in consequence. Note that the result of this organic single crystal has been published in Ref 80.

Group 3: NIR linear polymethine dyes for symmetry breaking effect

Although the lengthening of the conjugation chain of linear molecules leads to an enhancement of 2PA cross section due to the increase of ground-to-excited-state transition dipole moment (μ_{01}), it is not the case for very long symmetrical polymethine dyes of which the linear absorption peak reaches ~1 μm. The ground state symmetry breaking (SB) effect in polar solvent leads to an appearance of asymmetrical charge distribution along the conjugation chain at the ground state [81]. A group of polymethine dyes with conjugation chain of different length connecting two 2-azaazulene end groups is thus developed [82-84] as shown in Figure 4.4. The

interaction of the heterocycles of 2-azaazulene end group with the main molecular chain increases the "effective" conjugation length, leading to a large red-shift of absorption peak into NIR. We performed linear, 2PA and ESA measurement of the dye with n=3 in different solvents to study the symmetry breaking effect upon nonlinear optical properties and the role of solvent polarities.

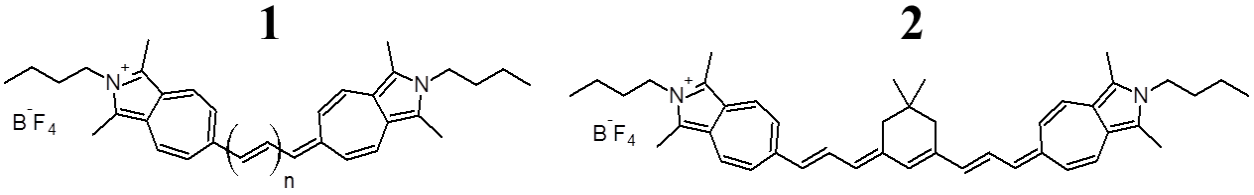

Figure 4.4: Molecular structures of JB7-08 (1, n = 1), JB9-08 (1, n = 2), JB17-08 (1, n = 3), and JB5-09 (2, n = 4)

Group 4: Sulfur-squaraine dyes v.s. oxygen-squaraine dyes

Squaraine dye is featured with an electron acceptor group at the center of its π-conjugation chain, making the dye essentially a D-π-A-π-D structure. The electron acceptor for oxygen-squaraine (O-SD) is the fragment C_4O_2; while in sulfur-squaraine (S-SD) or Sulfur-Oxygen squaraine (SO-SD), one or both oxygen atoms are replaced with sulfur, forming either C_4S_2 or C_4SO. Shown in the Figure 4.5 are a pair of O-SD2405 and S-SD 7805; and another pair of O-SD 2053 and SO-SD 7517. Each pair of dyes shares the same end group and conjugation length, but different electron acceptor. It is known that O-SD shows relatively large 2PA cross section, due to its large transition dipole moment and narrow absorption band allowing small detuning energy [32]. It will be interesting to investigate the 2PA properties of S-SD, and the intermediate structure SO-SD in comparison to its corresponding O-SD to understand the role of sulfur atom replacement in acceptor group.

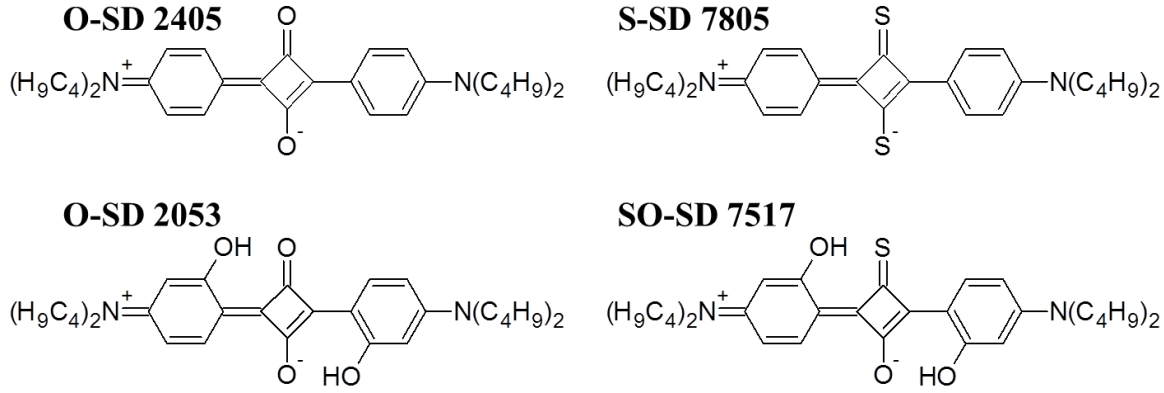

Figure 4.5: Molecular structures of O-SD 2405 *v.s.* S-SD7508; and O-SD-2053 *v.s.* SO-SD 7517

Note that the comparison of 2PA properties of O-SD 2405 and S-SD7508 has been published in Ref. 85.

4.3 Symmetrical Anionic Acceptor-π-Acceptor Dyes

4.3.1 Linear Absorption and Fluorescence Properties for A-π-A Dyes

The linear absorption and fluorescence spectra of this series of dyes, from G37 (n=1) to G152 (n=4) measured in dichloromethane (DCM) and acetonitrile (ACN), are shown in Figure 4.6. For all four dyes, linear absorption is composed by an intense cyanine-like band, corresponding to the $S_0 \rightarrow S_1$ transition and a few relatively weak absorption bands at visible and ultraviolet wavelengths, corresponding to the $S_0 \rightarrow S_n$ transitions. The increase of the main conjugation length by one vinylene group leads to a red shift of linear absorption peak by ~100 nm, which is also observed for D-π-D polymethine dyes [33]. The increase of solvent polarity from DCM to ACN leads to only a small hypsochromic shift of linear absorption peak by 3-7 nm, which is the indication of a small ground state stabilization effect in polar solvent. All dyes

show larger solubility and better photochemical stability in ACN than in DCM. Note that for linear absorption in DCM, a small broadband absorption feature is observed between 400-600 nm which is not stable and gradually increases. This is due to formation of a product of photo- or chemical-decompositions. Therefore the nonlinear measurement is only done in ACN. Additionally for G152, we observed a significant broadening of its main absorption band in both two solvents, which is connected with ground state symmetry breaking effect, as described in detail in ref. 86. This effect will be discussed in more detail in Section 4.7.

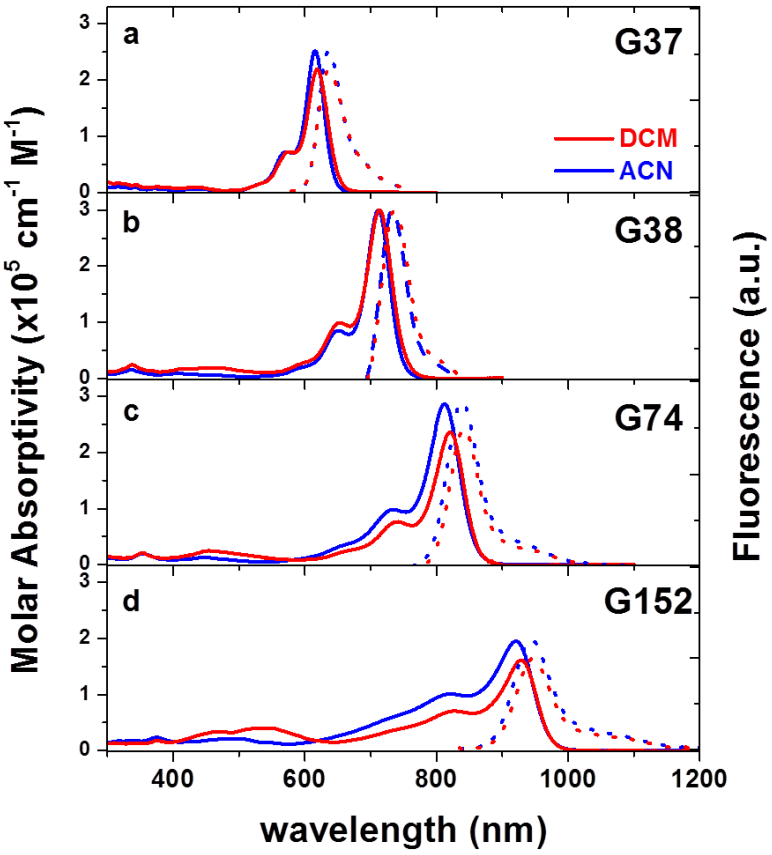

Figure 4.6: Linear absorption (solid) and fluorescence (dot) of G37 (n=1), G38 (n=2), G74 (n=3) and G152 (n=4) in DCM (red) and ACN (blue)

Figure 4.6 also shows the fluorescence spectra of this series of dyes. Similar to its absorption, fluorescence shows little solvatochromic effect with different solvent polarity. For G37 and G38, the fluorescence quantum yield is measured against Cresyl Violet in methanol, while G74 and G152, with significant red shift of linear absorption peaks, are measured against PD 2631 in ethanol. By using Equation 3.2, we can calculate the fluorescence lifetime of these dyes, which is verified by a picosecond degenerate pump-probe experiment. The main linear parameters of this series of dye, along with the ground state transition dipole moment (μ_{ge}) calculated from Equation 3.1 in two solvents are listed in Table 4.1. The main feature of this series of dyes is their relatively large fluorescence quantum yield (Φ_F). For G37 and G38 in ACN, Φ_F is 86% and 66%, respectively. Even for G152 with linear absorption peak > 900 nm, a 2% Φ_F is measured. There values are among the most efficient fluorescent chromophore in NIR range, which is desirable in fluorescence imaging and sensing application.

Table 4.1: Linear spectroscopic parameters of G37, G38, G74 and G152 in DCM and ACN; λ_{abs}^{max} and λ_{FL}^{max}: peak absorption and fluorescence wavelengths in nm; ε^{max} peak extinction coefficient in 10^5 M^{-1} cm^{-1}; Φ_F : fluorescence quantum yield ; $\tau_{F,1}$ and $\tau_{F,2}$: fluorescence lifetime time calculated by equation 3.2 and measured by pump-probe technique in ns; μ_{ge} ground–to-excited state transition dipole moment in Debye (D)

Dye (Solvent)	λ_{abs}^{max}	λ_{FL}^{max}	ε^{max}	Φ_F	$\tau_{F,1}$	$\tau_{F,2}$	μ_{ge}
G37(DCM)	618	637	2.19	0.89±0.05	2.2±0.2		14
G37 (ACN)	615	636	2.52	0.86±0.05	2.3±0.2	1.8±0.3	14
G38(DCM)	713	735	3.00	0.57±0.03	1.4±0.2		17
G38(ACN)	711	733	3.00	0.66±0.03	2.0±0.2	1.8±0.3	16
G74(DCM)	820	842	2.36	0.17±0.02	0.75±0.15		16
G74 (ACN)	812	839	2.86	0.18±0.02	0.65±0.13	0.7±0.1	18
G152 (DCM)	928	947	1.61	0.02±0.01	0.15±0.07		16
G152 (ACN)	921	945	1.95	0.02±0.01	0.12±0.06	0.12±0.02	20

4.3.2 Excitation Anisotropy and 2PA Absorption Spectra for A-π-A Dyes

To determine the spectral positions of higher transitions and its orientations with respect to fluorescence transition dipole, fluorescence excitation anisotropy is performed for this series of dyes. The solvent is chosen to be ethylene glycol due to its high viscosity to hinge its rotational reorientation. Shown in Figure 4.7, are the excitation anisotropy spectra (r) of this series of dyes with the emission wavelengths fixed at the corresponding fluorescence peaks. For all four dyes, a flat anisotropy value of r~0.35 is observed across the main linear absorption band, indicating a near parallel configuration between absorption and fluorescence transition dipoles, which is the indication of a $S_0 \rightarrow S_1$ transition. The anisotropy value shows large variation at shorter wavelength. For example, for G37, a broad minimum of r~ - 0.05 is observed at 390-460 nm range, corresponding to a large angle (~50-60 °) between absorption and fluorescence transition dipole. This is the indication of one-photon forbidden transition (or groups of transtions) not obvious from linear absorption spectrum. Between 320-370 nm, the anisotropy value again increases to ~0.3, followed by the trend of another rapid decrease at shorter wavelength. The anisotropy spectra of G38 and G74 follow the same trace, however, being red-shifted and with a reduced minimum value due to the increase of conjugation length. More interesting is the anisotropy spectrum of G152, where the broad minimum of anisotropy split into two minima at 470 nm and 550 nm, respectively. This is the indication, which is also confirmed by quantum chemical calculation, that the broadband minima observed for G37, G38 and G74 correspond to the overlapping of several 1PA forbidden (thus 2PA allowed) transitions which are gradually separated as the conjugation length increases. The fluorescence excitation anisotropy gives a good hint to predict 2PA transitions as discussed in the following paragraphs.

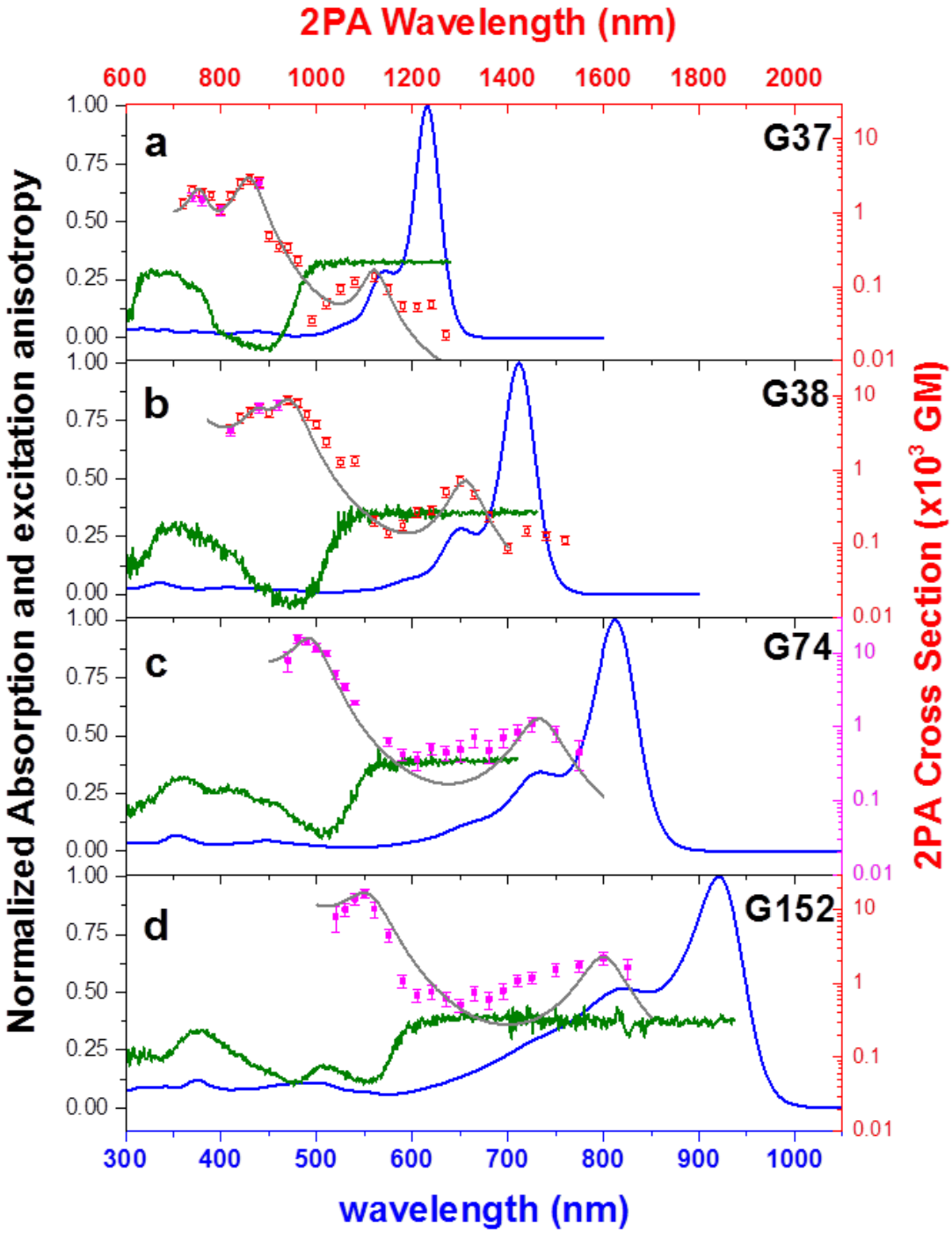

Figure 4.7: Linear absorption (blue solid), fluorescence excitation anisotropy (green solid, in ethylene glycol), 2PA spectra measured by 2PF (red dot), Z-scans (pink dot) and the fitting calculated by Equation 2.32 (gray solid) of G37 (a), G38 (b), G74 (c) and G152 (d) in ACN

The degenerate 2PA spectra of G37 and G38 are measured by 2PF technique as discussed in Section 3.2.2. For G37, 2PF technique is used to measure both the shape and magnitude of 2PA against a reference of Rhodamine B in methanol; additional Z-scans are performed as a cross check of 2PF experiment. However, for G38, 2PF can only give a 2PA spectral shape due to the limitation of detector calibration (below 800 nm only); it is then rescaled by performing Z-scans at certain wavelengths. For G74 and G152, because the fluorescence spectrum is beyond the detection limit of our detection system, only Z-scan is used to obtain the 2PA spectra.

Shown in Figure 4.7 are the 2PA cross section (δ_{2PA}) spectra for all dyes in ACN. The independent 2PF and Z-scan results show excellent agreement to each other for G37, which indicates that the re-scaling procedure, performed for G38 to obtain 2PA spectrum, is reasonable and accurate. For all four dyes the 1st 2PA band is relatively weak compared to a more intense 2PA band at shorter wavelength, and located on the vibrational shoulder, blue-shifted by ~1000-1200 cm^{-1} from its corresponding 1PA main absorption peak, covered by a constant excitation anisotropy value. The lengthening of conjugation chain leads to an increase of the peak δ_{2PA} value from G37 (140 GM at 2PA excitation wavelength of 1120 nm, n=1) to G152 (2200 GM at 1600 nm, n=4). This 2PA band is a common feature for all symmetrical cyanine dyes (including D-π-D cationic polymethine dyes and D-π-A-π-D squaraine dyes [32,33,73,87]), which originates from the vibrational coupling between S_1 and its vibrational modes inducing a small permanent dipole moment ($\Delta\mu$). Note that this vibrational-assisted 2PA band for G152 is relatively broadened compared to other dyes in this group. A 2200 GM peak δ_{2PA}, observed at ~1600 nm, is one of the largest values for a single organic molecule with 2PA excitation wavelength at the telecommunication range (1300-1600 nm). This large δ_{2PA} of G152 and relative broadening of 2PA band is connected with the large μ_{ge} (=20 D) and a symmetry breaking effect [33,86].

The second 2PA band for all four dyes, coincides with the minimum of the excitation anisotropy, is the most intense 2PA band corresponding to a 2PA allowed transition $S_0 \rightarrow S_2$. This is the first electronically allowed 2PA transition. Similar to the first 2PA band, the peak δ_{2PA} increases with the increase of conjugation length: δ_{2PA}=~2900 GM at 2PA excitation wavelength of 860 nm for G37, ~8800 GM at 940 nm for G38, ~15000 GM at 1100 nm at 960 nm for G74, and ~17000 GM at 1100 nm for G152. The third 2PA band for G37, located at 740 nm with peak δ_{2PA} of 2000 GM, matches with a small shoulder of its excitation anisotropy, presumably corresponding to a mixture of 2PA allowed $S_0 \rightarrow S_4$ and $S_0 \rightarrow S_6$ transitions. For G38, the third 2PA band, located at 880 nm with peak δ_{2PA} of 6800 GM, becomes less separated comparing to G37. Note that the third 2PA band is not resolved in G74 and G152, due to the presence of linear absorption tail at the corresponding wavelengths.

To understand the origin of the large δ_{2PA} observed for this series of symmetrical A-π-A dyes, we also use 3-level model proposed in Chapter 2 to fit the 2PA spectra. We can use Equation 2.32 to fit the 2PA spectra of these four dyes, assuming S_1 state is considered as the intermediate state. For G37 and G38, three 2PA bands are considered (one originated from vibronic coupling, connecting to $\Delta\mu$, and the two from electronic states, connecting to $\mu_{ee'}$) in the fitting program; while for G74 and G152, two 2PA bands are considered. The molecular parameters corresponding to the strongest 2PA band based on the fitting in Figure 4.7 are shown in Table 4.2. We can conclude that the extremely large δ_{2PA} can be attributed to the combination of extremely large μ_{ge} =13-20 D and $\mu_{ee'}$= 9- 13 D

Table 4.2: Molecular parameters corresponding to the strongest 2PA band of the molecule: the peak wavelength (λ_{2PA}^{max}) of 2PA band with the corresponding energy of final 2PA state $\omega_{ee'}$; the peak 2PA cross section (δ_{2PA}^{max}); and the excited state transition dipole moment ($\mu_{ee'}$)

Dye	λ_{2PA}^{max} (nm)	$\omega_{ee'}$ (eV)	δ_{2PA}^{max} (GM)	$\mu_{ee'}$ (D)
G37	860	2.88	2900±500	11
G38	940	2.62	8800±1300	12.8
G74	960	2.5	15000±2300	10.5
G152	1100	2.23	17000±2500	9.1

4.3.3 Quantum-Chemical Approach for A-π-A Dyes

Quantum chemical calculation is also performed by Dr. Olga Przhonska and colleagues at the Institute of Physics and the Institute of Organic Chemistry, National Academy of Sciences in Kiev, Ukraine, with the goal to understand the 2PA spectra and the origin of large 2PA cross section of this series of symmetrical anionic A-π-A dyes. Typically applied ZINDO/S method cannot be used for this series of molecules due to the lack of parameterization for the boron (B) atom. The wavefunctions of the excited states are built with the single configuration interaction technique taking into account of 9 molecular orbitals (MOs), of which 6 MOs are occupied and 3 unoccupied. Thus a total of 18 configurations are taken into account which is sufficient to model the 1PA and 2PA properties of the molecule spanning from near-UV to NIR wavelength range. The ordering of MOs is checked by ab initio method (6-31G** basis), and the calculation are performed for isolated molecules in vacuum condition. More detailed description of quantum-chemical approaches should be referred in ref. 76. The shapes of MOs for G37 are shown in Figure 4.8. The highest occupied MO (HOMO) of this anionic polymethine represents a specific

orbital (so-called solitonic level) with charge distributed within the chain only, which the mirror image of cationic polymethines, whose solitonic level corresponds to the lowest unoccupied MO (LUMO) [73]. HOMO-3 is a delocalized orbital, whereas HOMO-4 and HOMO-5 are localized orbitals with charge exclusively concentrated at the end groups. The intense cyanine-like absorption band, corresponding to $S_0 \rightarrow S_1$ transition, is purely originated from intense transition from HOMO to LUMO. Higher excited $S_0 \rightarrow S_n$ transitions are mixed. The $S_0 \rightarrow S_2$ transition, corresponding to the second 2PA band in G37, is separated by ~0.7 eV from $S_0 \rightarrow S_1$ transition, matches with the minimum of the excitation anisotropy. Several following transitions are strongly overlapped with their similar oscillator strengths due to contributions from localized MOs, leading to a broad anisotropy valley as shown in Figure 4.7. Therefore, the third 2PA band in G37 presumably corresponds to the mixture of $S_0 \rightarrow S_4$ and $S_0 \rightarrow S_6$ transitions. Note that the large excited-state transition dipole moment ($\mu_{ee'}$) can be explained by the effective charge transfer processes over large distance: e.g. HOMO-1 to HOMO as shown for G37 in Figure 4.8.

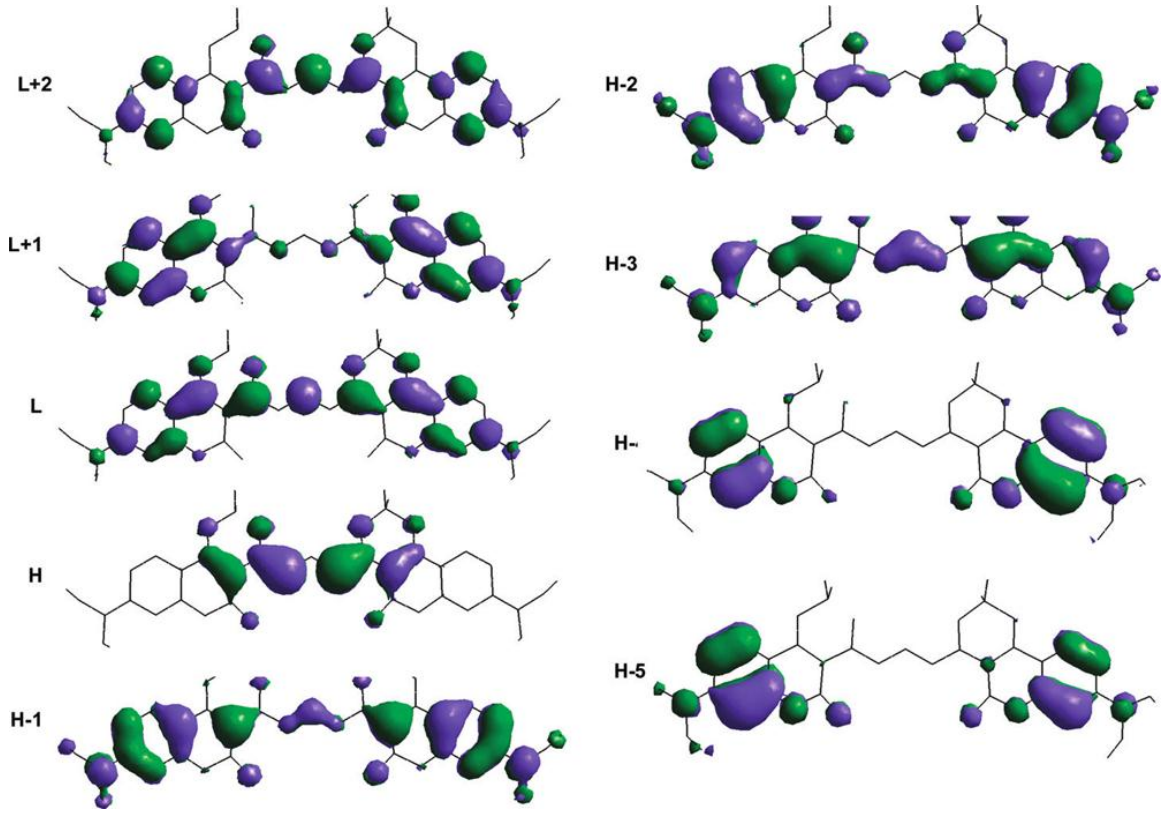

Figure 4.8: Molecular orbitals for G37 calculated in the framework of the standard semiempirical AM1 Hamiltonian (HyperChem Package). Reprinted with permission from ref. 78. Copyright 2010 American Chemical Society

4.4 Asymmetrical Donor-π-Acceptor Dyes

4.4.1 Linear Properties and Solvatochromism for D-π-A Dyes

Differing from previous group of symmetrical molecules, the substitution of one acceptor group by a donor group makes G19 (n=1), G40 (n=2) and G188 (n=3) essentially a class of asymmetrical Donor-π-Acceptor (D-π-A) molecules, frequently referred to as "push-pull" polyenes. Due to opposite charge affinity of the end group, asymmetrical D-π-A dye possess

large permanent dipole moment (μ). As a result, their optical properties can be significantly influenced by the solvent polarities [88-91]. It is known that the polarity of solvents can be characterized by their orientational polarizability, which is given by $\Delta f = (\varepsilon - 1)/(2\varepsilon + 1) - (n^2 - 1)/(2n^2 + 1)$, where ε is the static dielectric constant and n is the refractive index of the solvent [47]. Two solvents are chosen here with distinctive Δf values: toluene, a nonpolar solvent (Δf=0.013), and ACN, strong polar solvent (Δf=0.31). The linear absorption spectra in these two solvents are shown in Figure 4.9. Similar to symmetrical A-π-A dye, the absorption spectra for all three dyes are composed of an intense cyanine-like absorption band, corresponding to the 1PA allowed $S_0 \rightarrow S_1$ transition, which is systematically red-shifted by ~100 nm by adding one vinylene group in the main conjugation chain. The relatively weak linear absorption bands are also observed at visible and UV region responsible for 1PA transition into S_n state. The linear absorption peaks, with their molar absorbances and the corresponding ground-to-excited-state transition dipole moments (μ_{ge}) for each dye, are shown in Table 4.3. The most remarkable difference from symmetrical A-π-A dyes is the strong solvatochromic effect observed in toluene and ACN. Increasing solvent polarity from toluene to ACN leads to a bathochromic shift of the main absorption peak, ~11 nm for G19, ~28 nm for G40, and ~65 nm for G188. This strong solvatochromic behavior is connected with the large ground state and excited state permanent dipole moments of the dyes, as demonstrated previously for merocyanine dyes [92]. If the excited state has larger permanent dipole moment compared to the ground state, it is preferentially stabilized in the polar solvent (i.e. ACN), leading to a decrease of energy gap between these two states, thus a red-shift of linear absorption peak. Another feature more pronouncedly observed for G188 is the substantial spectral broadening in less polar solvent, toluene, evidenced by the increase of the shoulder of the main absorption band.

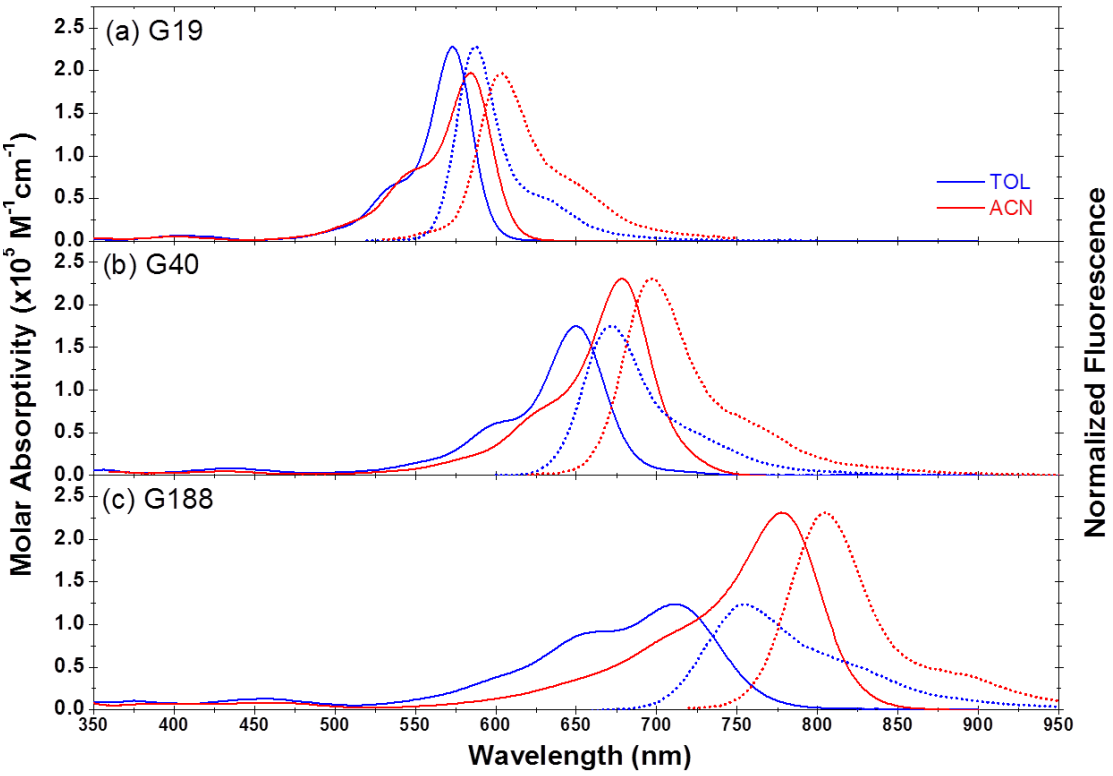

Figure 4.9: Linear absorption (solid) and fluorescence (dot) spectra of G19 (a), G40 (b), and G188 (c) in toluene (blue) and ACN (red)

We also measured the fluorescence spectra of all dyes as shown in Figure 4.9, and the corresponding fluorescence quantum yields (Φ_F) in two different solvents. Cresyl Violet in methanol is used as a fluorescence reference for G19 and G40, and PD 2631 in ethanol for G188. The results of quantum yield measurements for all dyes in toluene and ACN, with the calculated fluorescence lifetimes using Equation 3.2, are shown in Table 4.3. As shown, polarity of the solvent significantly affects not only the positions of absorption and fluorescence spectra but also the fluorescence quantum yields. An 8× decrease of Φ_F is observed for G19 in ACN (Φ_F=12.5%) compared to Φ_F=100% in toluene.

Table 4.3: Linear spectroscopic parameters of G19, G40, G188 in toluene and ACN; λ_{abs}^{max} and λ_{FL}^{max}: peak absorption and fluorescence wavelengths in nm; ε^{max} peak extinction coefficient in 10^5 M^{-1} cm^{-1}; $\tau_{F,1}$, $\tau_{F,2}$ and $\tau_{F,3}$: fluorescence lifetime (ns) calculated by Equation 3.2 , measured by time resolved fluorescence technique, and measured by pump-probe technique in ns; μ_{ge} ground-to-excited-state absorption transition dipole moment in D

Dye (Solvent)	λ_{abs}^{max}	λ_{FL}^{max}	ε^{max}	Φ_F	$\tau_{F,1}$	$\tau_{F,2}$	$\tau_{F,3}$	μ_{ge}
G19(toluene)	572	587	2.28	1.0±0.1	2.0±0.4	1.9±0.4		12.6
G19 (ACN)	583	603	1.95	0.12±0.01	0.3±0.1	0.5±0.2		13.1
G40(toluene)	650	672	1.75	0.81±0.08	2.3±0.5	1.9±0.4	1.7±0.3	13.1
G40(ACN)	678	698	2.31	0.52±0.05	1.6±0.3	1.5±0.5	1.5±0.3	15
G188(toluene)	712	754	1.24	0.34±0.03	1.2±0.2	1.1±0.2	1.0±0.2	14.7
G188 (ACN)	777	805	2.32	0.19±0.02	0.7±0.3	1.1±0.2	1.0±0.2	17.1

In order to investigate the effect of solvent polarity in more detail, we performed linear absorption peak and quantum yield measurements in the mixtures of toluene and ACN, which allows us to continuously change solvent polarity in the range of 0.013 (pure toluene) to 0.306 (pure ACN). The static dielectric constant (ε) and refractive index (n) of the mixture is calculated by averaging each ε and n value of toluene and ACN using the corresponding volume percentage as weighing factor. For example, if we mix the toluene and ACN by a volume percentage of 10% of toluene and 90% of ACN, the corresponding $\varepsilon_{mix} = 10\% \cdot \varepsilon_{toluene} + 90\% \cdot \varepsilon_{ACN}$ and *etc*. Polarity dependent absorption peaks and quantum yields for G19 are presented in Figure 2.1a. The increase of solvent polarity from 0.013 to 0.26 leads to a constant red-shift of the linear absorption peak from 572.5 nm to 585.5 nm; however, this red-shift is reversed by ~2 nm for Δf from 0.26 to 0.306. Similar effect is also observed in fluorescence spectra. This reproducible result has been meticulous studied by the following

procedures: (1) premixing toluene and ACN followed by the addition of G19; (2) dissolving G19 in toluene followed by the appropriate dilution of ACN; and (3) dissolving G19 in ACN followed by the appropriate dilution of toluene. All dye concentrations in toluene-ACN mixtures were kept similar, confirmed by measuring the absorbance and maintaining a constant optical density (1.0 ± 0.1). Although we do not understand the nature of this shift, we presume it is related to the reversal of permanent dipole moment difference between excited and ground states.

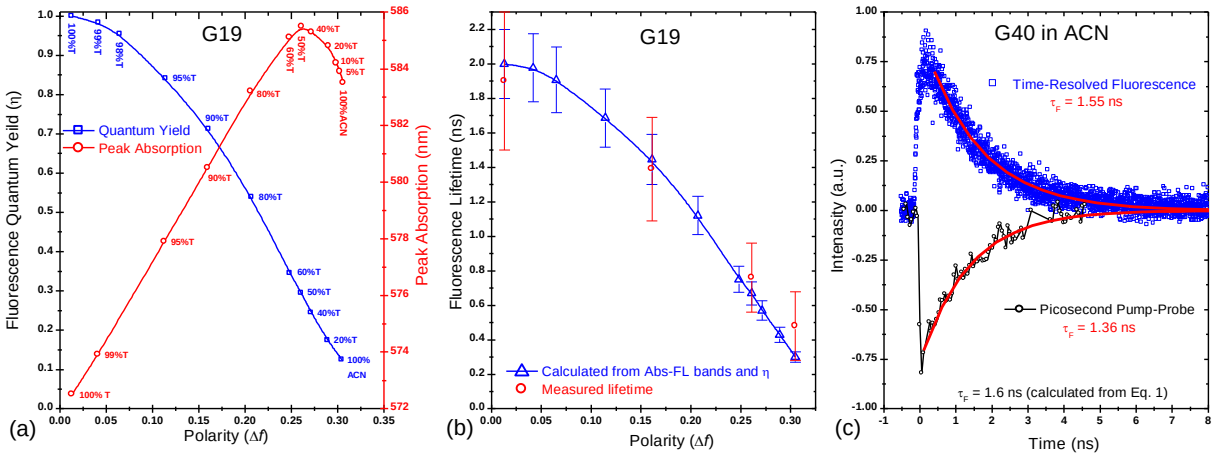

Figure 4.10: (a) Fluorescence quantum yield (blue squares) and peak position of ground state absorption (red circles) as function of solvent polarity for G19. Note: a reversal trend in peak absorption positions starting at 60% ACN and 40% toluene mixtures, presumably is connected with a dominant specific interaction between the dye molecule and polar solvent shell. (b) Comparison of fluorescence lifetime (blue triangles), calculated from Eq. 1, and measured by time-resolved fluorescence (red circles) as function of solvent polarity for G19. (c) Time-resolved fluorescence (blue squares) and picosecond pump-probe measured at 532 nm (black circles) for G40. [79] – Reprodcued by permission of The Royal Society of Chemistry, Copyright (2009).

The polarity dependent quantum yield, one the other hand, shows a monotonic decrease as the solvent polarity increases, as shown in Figure 4.10a. The calculated fluorescence lifetime (τ_F) using Equation 3.2, is shown in Figure 4.10b. To verify these calculated values, another

time-resolved fluorescence lifetime measurement is performed by a time-correlated single photon counting system (PicoQuant, PicoHarp300) collecting the complete fluorescence spectrum with an instrument response time of ~200 ps, as shown in Figure 4.10c. The samples were pumped by linearly polarized, 100 fs (FWHM) laser pulses at a wavelength of 390 nm from a frequency doubled Ti:sapphire femtosecond laser (Coherent Inc., Mira). The excitation polarization was oriented at the magic angle (54.7 °) with respect to the detected emission polarization. The time resolved fluorescence measurement results for G19, G40 and G188 are listed in Table 4.3. Additionally, we also measured the excited state lifetime using pump-probe technique in comparison to fluorescence lifetime measurements as shown for G40 in Figure 4.10c. In general, experimental results for all dyes agree to within 30% of the values calculated from the fluorescence quantum yield. The largest discrepancy between measured and calculated values is observed for G19 for the shortest lifetime (in pure ACN) measured by time-resolved fluorescence lifetime measurements; however, in this case the fluorescence signal is very weak (Φ_F=12.5%) and the response time of the system is comparable to the calculated lifetime (~300 ps). Based on these results, we can conclude that G19 is very sensitive to solvent polarity and can be used as an efficient probe to test the polarity of microenvironments.

4.4.2 Excitation Anisotropy and 2PA Spectra for D-π-A Dyes

The excitation anisotropy for all dyes, measured in polytetrahydrofuran (pTHF, averaged molecular weight of 1000), is shown in Figure 4.11. We observe that the excitation anisotropy spectra reveal the large alternation of peak and valley features for all molecules, in spite of their asymmetrical structure, which is quite an unusual result. This large alternation of anisotropy

values indicates that the molecules can be characterized by one-photon allowed and symmetry-forbidden transitions, which is opposite to the behavior of asymmetrical dyes studied previously [33], of which the states doesn't show distinctive type of symmetries. As shown in Figure 4.11, the excitation anisotropy function $r(\lambda)$ is constant ($r \approx 0.35$) in the broad spectral range 450–600 nm for G19, 500–700 nm for G40, and 600–850 nm for G188, indicating a nearly parallel orientation of the absorption (within the band $S_0 \rightarrow S_1$) and the emission transition dipole moments. In the shorter wavelength region, the anisotropy spectra show two minima at ≈430 nm and ≈350 nm for G19, at ≈470 nm and ≈380 nm for G40, and three minima at ≈510 nm, 380 nm and ≈305 nm for G188, corresponding to one-photon forbidden transitions $S_0 \rightarrow S_n$ forming 40–60 ° angles with the emission dipole moment. Based on quantum-chemical calculations, we conclude that the first minimum in the excitation anisotropy spectra (430 nm, 470 nm and 580 nm) correspond to the transition $S_0 \rightarrow S_2$ in the linear absorption and indicate the possible positions of the final states in 2PA spectra for these dyes. In addition to the excitation anisotropy, we also did emission anisotropy for G188 by fixing the excitation wavelength at the linear absorption peak and scan the emission intensity across its fluorescence bands in parallel and perpendicular polarizations with respect to excitation polarization. A constant emission anisotropy spectrum, shown in Figure 4.11c, indicates that no molecular vibrational depolarization is present at the emission wavelength range.

The degenerate 2PA spectra of all dyes in toluene and ACN, measured by 2PF technique and verified independently by Z-scans, are shown in Figure 4.11 along with their absorption spectra and excitation anisotropy. Note that the absolute value of 2PA cross sections can be obtained by 2PF technique for G19 and G40 using Rhodamine B in methanol as the reference,

while 2PF only measures a relative 2PA spectrum for G188 due to the lack of calibration of detector at the emission wavelengths.

As shown in Figure 4.11, the 2PA spectrum for G19 in both solvents presents two well-separated bands and the edge of a third 2PA band. Surprisingly, we do not observe a band corresponding to two-photon excitation into the peak of the $S_0 \rightarrow S_1$ transition in spite of the asymmetrical structure of G19 and the existence of permanent dipole moments in the ground and excited states, which is in contrary to asymmetrical dyes discussed in ref.33. The first 2PA band occurs at an energy shifted to the "blue" range at ≈1000-1200 cm^{-1} as compared to the peak of the $S_0 \rightarrow S_1$ transition with a constant anisotropy value across the whole band, which is typical for the symmetrical cyanine-like molecules (D-π-D and A-π-A structure, *etc*.). The origin of this 2PA band, which includes 2 peaks separated by ≈1000 cm^{-1} with cross-sections δ_{2PA} ≈400-500 GM, in general can be associated with vibrational coupling and the lowest 2PA-allowed band positioned close in energy to the 1PA-allowed band as was determined previously for some cyanine-like dyes [33,87]. A detailed quantum-chemical analysis allows us to conclude that the nature of the first 2PA band for all dyes can be attributed to the vibrational coupling between the first excited electronic state S_1 and its vibrational modes.

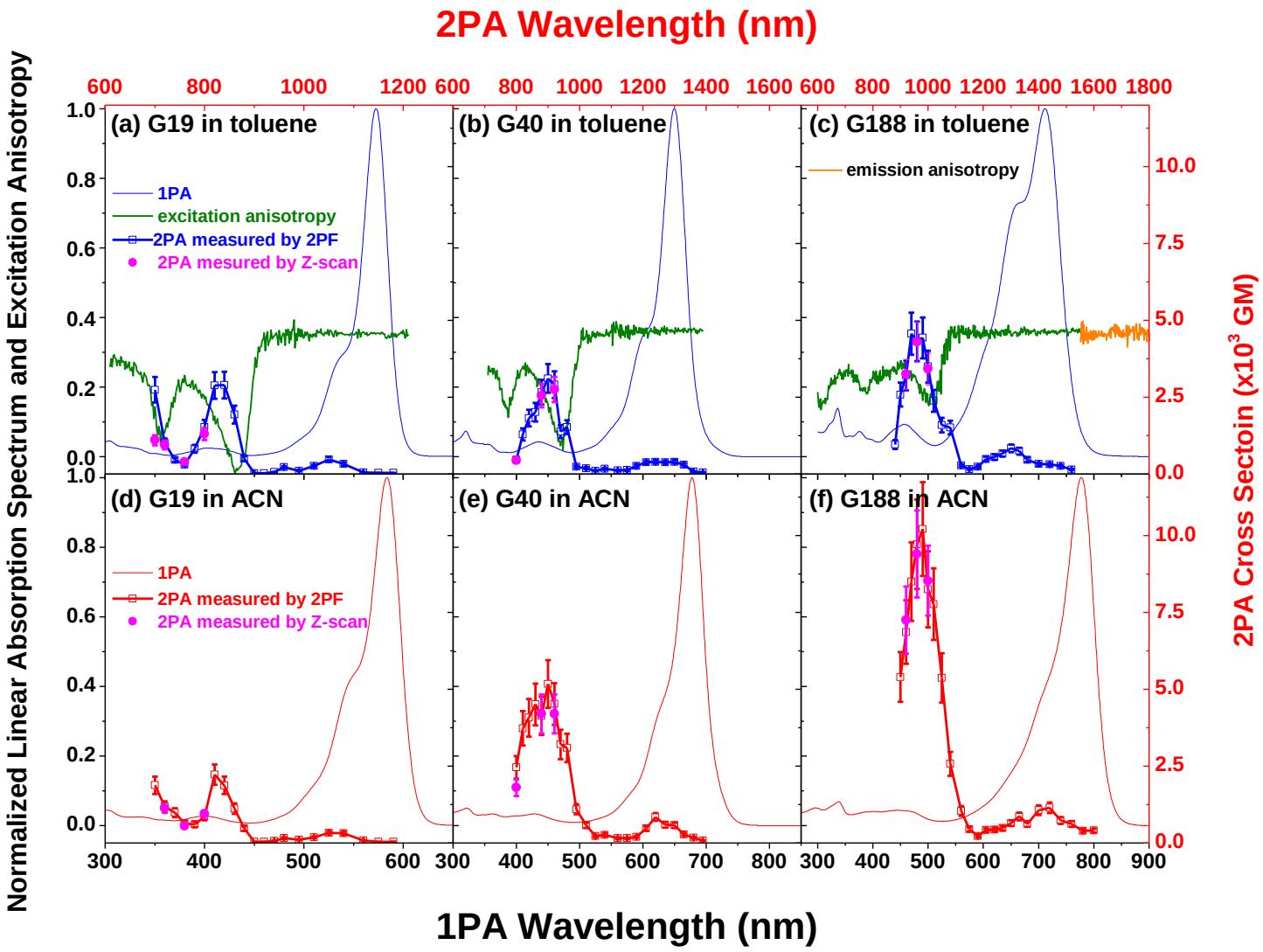

Figure 4.11: Linear absorption spectra, excitation anisotropy (measured in pTHF 1000) and 2PA spectra measured by 2PF and Z-scan of G19, G40 and G188 in toluene and ACN; additionally, and emission anisotropy of G188 is shown in c

Our calculations show that for G19, the lowest 2PA-allowed electronic state corresponds to the second observed 2PA band with the peak position ≈830-840 nm; δ_{2PA} ≈3000 GM in toluene and ≈2400 GM in ACN. The final state for this 2PA-allowed band corresponds to the S_2 state which is confirmed by the minimum in excitation anisotropy measurements. The edge of a third 2PA band is observed by tuning the excitation wavelength closer to the 1PA band, $S_0 \rightarrow S_1$. The peak of this third 2PA band, placed by calculation at ≈700 nm, cannot be reached due to the influence of the linear absorption edge. The reason of the absence of a 2PA band corresponding to $S_0 \rightarrow S_1$ transition, which is typical for asymmetrical dyes, will be discussed in further detail in the following quantum chemical calculation part.

The 2PA spectrum of G40, as shown in Figure 4.11, is composed of two well-separated bands. The first band corresponding to two-photon excitation from S_0 into the vibrational sub-levels of S_1, is similar to G19, however, slightly broader in toluene than in ACN. The second 2PA band, corresponding to an electronically allowed 2PA transition $S_0 \rightarrow S_2$ with peak position ≈900-910 nm in both solvents, shows δ_{2PA} ≈5000 GM in ACN and ≈3400 GM in toluene. This enhancement is more pronounced in G188 in ACN compared to its toluene solution. Despite the positions of the second 2PA band ($S_0 \rightarrow S_2$) for G188 in *both* toluene and ACN solutions are located at 2PA wavelength 960–970 nm (corresponding to incident photon energy ω~1.285 eV), we observe a larger than 2× enhancement of δ_{2PA} for G188 in ACN (δ_{2PA} ≈10000 GM) than that in toluene solution (δ_{2PA} ≈4700 GM). Considering the position of S_1 state of G188 in toluene ω_{eg} =1.742 eV, corresponding to 1PA peak of at 712 nm, and ω_{eg} =1.596 eV in ACN at 777 nm, the detuning energy between S_1 state and incident photon for G188 in toluene is $\Delta\omega|_{toluene} = \omega_{eg} - \omega = 0.457eV$, compared to $\Delta\omega|_{ACN} = 0.311eV$ in ACN solution. Based on 3-

level model and equation 2.31, δ_{2PA} is reversely proportional to $\Delta\omega^2$. This leads to an enhancement of δ_{2PA} by a factor of $(\Delta\omega|_{toluene} / \Delta\omega|_{ACN})^2 = 2.16$ in ACN compared to toluene solution, which agrees very well with experimental observation. Therefore, this enhancement can be explained by the result of a strong intermediate state resonance enhancement (ISRE), due to the large solvatochromic shift (65 nm) of the linear absorption band $S_0 \rightarrow S_1$, despite a relatively un-shifted 2PA band. Hence the selection of solvent polarity in asymmetrical D-π-A dyes provides another simple but effective strategy to enhance the δ_{2PA}.

4.4.3 Two-state Model and Quantum Chemical Calculations for D-π-A Dyes

This section, performed by Dr. Olga Przhonska and colleagues at the Institute of Physics and the Institute of Organic Chemistry, National Academy of Sciences in Kiev, Ukraine, is intended to explain the strong solvatochromic effect of this set of asymmetrical D-π-A Dyes, and the absence of 2PA band in the main 1PA band.

Since this group of dyes can be classified as a quasi-one-dimensional D-π-A push-pull dye, a well-developed two-state model can be used to explain the linear properties of the dye [36,93]. The structure of these molecules can be presented in two opposite resonance forms: neutral (D – π – A) and ionic (or zwitterionic) with the separated charges (D^+ – π – A^-), which is mostly determined by bond length alternation (BLA, defined as the difference of bond length between neighboring carbon atoms). The neutral form, usually called a "polyene-like" structure, is characterized by a large BLA with the minimized charge alternation along neighboring carbon atoms [94]; while the ionic form, usually called a "polymethine-like" structure, has a minimized BLA (also called "cyanine-limit" [36]) with the large charge alternation. These two forms,

exhibiting distinctive linear optical properties, in principle can be controlled by applying an electric field across the polarizable π-conjugated system. The influence of solvent polarity is equivalent to this applied electric field; hence it can affect the charge transfer from donor to acceptor, connected with the transition from "polyene-like" structure to a "polymethine-like" structure. Our understanding is that for the molecule G19 with the shortest conjugated chain, the donor-acceptor properties of the end groups in both solvents dominate over the properties of the polyenic chain, and the ground state can be represented by a "polymethine-like" structure. This is confirmed by very similar shapes of the absorption bands in ACN and toluene (Figure 4.9) and X-ray crystallography measurements, which were performed in monocrystal at 293 K on a Bruker Smart Apex II Diffractometer. The molecular geometry for the single orthorhombic crystal of G19 was determined from X-ray diffraction data using the CRYSTALS program package [95] and is presented in Figure 4.12a. BLA within the chain from C1 to C14 is larger than that for typical symmetrical polymethine dyes. However, their difference is much smaller than for the typical polyenic structure (≈0.1 Å) [76,96], which is determined by the properties of the end groups. The observed large differences in the fluorescence quantum yields and lifetimes in different polarity solvents are probably connected with the large geometry changes and reorganization of the solvent shells in the polar solvent due to "recharging" of carbon atoms in the excited state. As a result of the electron transition $S_0 \rightarrow S_1$, charge is transferred to the neighboring carbon atom leading to their "recharging" within the conjugated chain. Changes in solvent polarity typically do not significantly affect the linear and nonlinear properties of symmetrical cyanines.

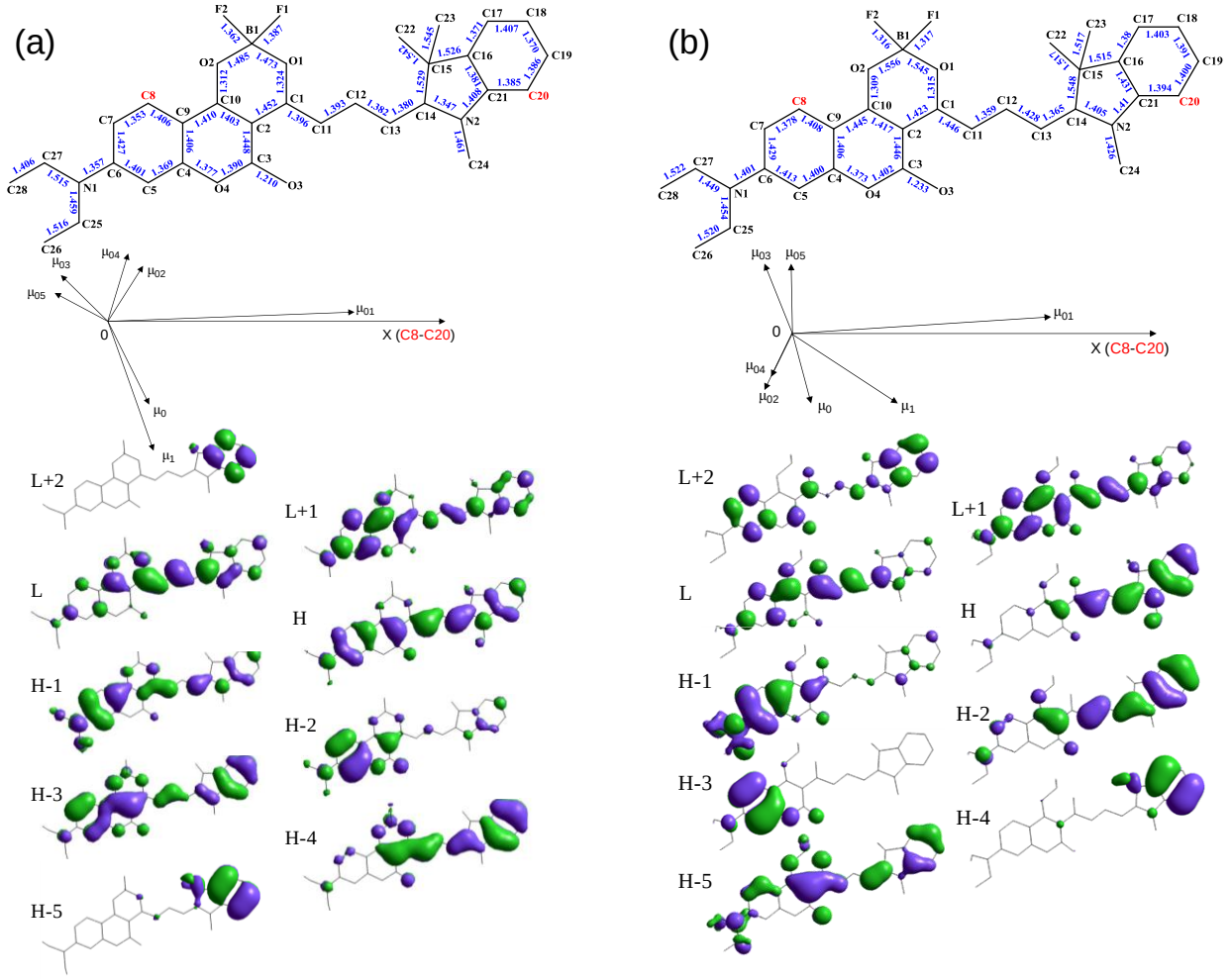

Figure 4.12: Molecular geometries for G19 obtained from X-ray measurements (a) and AM1 quantum chemical calculations (b), and related orientation of transitions, state dipole moments, and molecular orbitals. [79] – Reprodcued by permission of The Royal Society of Chemistry, Copyright (2009)

For the dye G188 with the longest conjugated chain, we suppose that the ground state represents a mixture of a "polymethine-like" structure, connected with the donor-acceptor properties of the end groups, and a "polyene-like" structure, mainly determined by a polyenic-type of conjugated chain with strong BLA. The relative contribution of these two resonance structures to the ground state is controlled by the polarity of the solvent: a more polar solvent can increase the ground-state polarization and make the charge-separated ("polymethine-like"

structure) form dominant. The neutral polyenic form dominates in less polar toluene resulting in a change of the absorption shape (growth of the short wavelength shoulder), clearly seen in the Figure 4.9c. Presumably, G40 represents an intermediate case between the shortest G19 and the longest G188 based on linear absorption data and quantum-chemical analysis. Analyzing the shift of the absorption peaks with the lengthening of the chromophore, we note that an increase in the conjugation length from G19 to G188, leads to a shift of ≈100 nm in ACN and ≈70 nm in toluene, which is in accord with the presented model of a co-existence of "polyene-like" and "polymethine-like" forms.

Due to the co-existence of two resonance forms, the quantum chemical calculation is performed for isolated molecules based on two geometries separately: one based upon X-ray measurement (refer to X-ray geometry) corresponding to "polymethine-like" structure of equalized BLA, another one based upon optimal geometry (refer to BLA geometry) with "polyene-like" structure of large BLA. For BLA geometry, the procedure of geometry optimization is stopped when the energy gradient reaches 0.01 kcal/mol. The energies of molecular orbitals, electronic transitions and oscillator strengths are calculated in the framework of the standard semiempirical AM1 method. 6 occupied and 3 unoccupied MOs (thus a total of 18 configurations) are taken into account to calculate the wavefunctions of excited state with single configuration interaction. For G19 (n=1), the MOs are displayed in Figure 4.12b. Similar to A-π-A dyes described in the previous section, these configurations are sufficient to model the one- and two-photon absorption spectra covering NIR, visible and near UV spectra measured experimentally. The calculations show that for G19, the positions of electronic transitions for both X-ray and BLA geometries are very close to each other within 5-7 nm, corresponding to a relatively small red-shift of 1PA peak in ACN compared to DCM. The major difference of two

geometries is the behavior of charge transfer between HOMO to LUMO corresponding to $S_0 \rightarrow S_1$ transition. For X-ray geometry, charge is transferred from the donor to acceptor part of the molecule; while for BLA geometry, charge is transferred to the neighboring carbon atoms within the conjugated chain. This observation is consistent to the difference between "polyene-like" and "polymethine-like" structures. Calculations show a large energy difference (≈160 nm) and a large angle ($\approx 60^0$) between the $S_0 \rightarrow S_1$ and $S_0 \rightarrow S_2$ transitions, contributing to large variations of excitation anisotropy value. For G40 (n=2), the difference in the calculated position of electronic transitions shows much larger difference (up to 60 nm) depending on the geometries. However, the experimental data indicates the molecule is more probably arranged in the "polymethine-like" structure, especially in ACN solutions. Similar large energy difference and large angle between the $S_0 \rightarrow S_1$ and $S_0 \rightarrow S_2$ transitions are also observed in G40. For G188 (n=3), the calculated positions of transition based on BLA model show a good agreement with experimental result in toluene, which confirms the "polyene-like" structure in less polar solvent. Meanwhile, the calculated $S_0 \rightarrow S_2$ transition from X-ray geometry approximately matches within ~100 nm error to the first valley of excitation anisotropy (at @520 nm). This again confirms our postulation of dynamic interplay of contributions from two resonance structures in different solvent polarities.

Another interesting observation from quantum chemical calculation based on X-ray geometry ("polymethine-like" structure), taking G19 for example, is the large angle of 70-75 ^{o} between permanent dipole moment difference between ground and excited state ($\Delta\mu=\mu_{ee}-\mu_{gg}$) and the ground to 1st excited state transition dipole moment (μ_{ge}), as shown in Figure 4.12a. Based on the Equation 2.29, this results in a dramatic decrease of $\Delta\mu$ by a factor of 2.6. This is the main

reason of the absence of a 2PA band under the 1PA peak for G19 as shown in Figure 4.11a and d, which is typically observed for D-π-A dipolar dyes [33].

4.5 Strategy to Enhance 2PA Cross Sections of Organic Molecules in Solutions

The study of A-π-A and D-π-A dyes, as discussed in previous sections, further enriches our knowledge of structure-2PA property relations of organic molecules, which helps us to formulate a general strategy to enhance 2PA cross sections of cyanine-like molecules. Based on the previously studied properties of D-π-D and D-π-A-π-D dyes [12,64], as well as D-π-A and A-π-A dyes studied in this chapter, and taking into account the three-level model described in Chapter 2, we propose the following strategies to enhance 2PA cross sections for organic dyes.

(1) Increase the ground-to-excited-state and excited-excited state transition dipole moments (μ_{ge} and $\mu_{ee'}$). The increase of μ_{ge} can be achieved by lengthening the π-conjugation, which increases the distance of charge transfer process. For linear conjugated molecules, 10^5 - 3×10^5 $M^{-1}cm^{-1}$ molar absorbance usually corresponds to μ_{ge} of 12-18 D of S_0 to S_1 transition. However, such increase of conjugation length may have two problems: first, it could induce photochemical instability as discussed above, which however can be remedied by designing a more complex end groups. Second, μ_{ge} can be saturated as the absorption peak goes into ~1000 nm, where symmetry breaking effect occurs. This will be discussed in Section 4.7. The increase of $\mu_{ee'}$ can be achieved by incorporation of a strong acceptor group into the conjugated bridge leading to a quadrupolar type arrangement of molecular structure (e.g. D-π-A-π-D), which again stimulates charge transfer over

large distance [73] for excited state transitions. Up to 30,000 GM cross section is observed for certain squaraines [24].

(2) Arrange the state levels to optimize the configuration of transition frequencies (ω_{eg}, $\omega_{e'g}$). A reduced detuning energy (ω_{eg}-ω) can leads to strong ISRE, which can be realized by making the main transition $S_0 \rightarrow S_1$ narrower (e.g. squaraines) allowing incident photon energy approaching the absorption edge. Another important strategy is arrange the position of $\omega_{e'g}$ to reach "double resonance" as discussed in Section 2.3.2, where both (ω_{eg}-ω) and ($\omega_{e'g}$-2ω) reaches minimum simultaneously (as discussed for T term in Section 2.3.2). For D-π-A asymmetrical dyes, by controlling the solvent polarity to decrease the tuning energy of $S_0 \rightarrow S_1$ transition (ω_{eg}-ω) is a simple yet effective way to enhance 2PA cross sections, as discussed for G188 in Section 4.4.2.

4.6 Single crystal of Donor-π-Acceptor Dye

Although the strategy proposed in the previous section provides a general guideline in molecular design for large 2PA cross section (δ_{2PA}) for individual organic molecules, there is an frequently ignored but very important issue, related to the overall 2PA coefficient (α_2) of a specific material (e.g. solutions): concentration. Most nonlinear optical measurements are performed in solutions with certain concentration of the samples. For cyanine-like dyes with relatively large molecular size, the maximum concentration is ~10^{-2} M (typically 10^{-4}-10^{-3} M), which is several orders of magnitude less than that for neat material (e.g. neat CS_2 16.5 M). Although aggregation may complicate the nonlinear optical measurement, increasing the concentration of the nonlinear organic molecule is still a straightforward and effective way to

enhance the overall nonlinearity of the material. Ionic liquid is a promising field to increase the concentration [97], but needs further investigations. Another approach to increase the concentration is switching the scope from liquid solution to solid-state material, i.e. organic single crystals. The main problem related with organic single crystal is its fabrication process. In spite of difficulties in growing single organic crystals of the size and optical quality required for nonlinear characterization, there are quite a few reports on the 2PA properties of organic materials in the solid phase. One of very few examples of single crystals of a conjugated polymer, is poly[bis(p-toluene sulfonate) of 2,4-hexadiyne-1,6-diol] or PTS, where the extremely large 2PA coefficient (up to 700 cm/GW) originates from the long π-conjugation chain, making it essentially a molecular quantum wire [98]. Another report presented the two-photon excited emission properties of a single crystal made of cyano-substituted oligo(p-phenylenevinylene) [99], which shows strong anisotropy of the single crystal due to directional molecular packing. Similar polarization-dependent anisotropy in two-photon excited fluorescence and second-harmonic generation is also observed for single organic nanocrystals, which show enhanced optical nonlinearities [100-102]. However, no direct measurement of the 2PA spectrum of a single crystal cyanine-dye has been reported. With the success of crystal growth technique, we report the 2PA spectrum, both linear and nonlinear anisotropy, and X-ray diffraction analysis with supporting quantum chemical calculations of an organic single crystal comprised of an asymmetrical cyanine-like D-π-A molecule, G19.

4.6.1 Crystal Growth Technique and Image of Single Crystals

We use a simple solvent slow cooling technique by self-nucleation of a sub-saturated hot solution of ACN to promote single crystal growth from its sub-saturated monomer solution. Unlike single polymetric crystal growth, described in ref. 98, no polymerization process is involved, which will also induce defects or multi-domains of the crystal. Such crystal growth process without polymerization allows for a valid comparison between single crystal form and the monomeric form in solution to identify the differences in the nonlinear spectroscopic properties. To obtain the single crystal of G19 molecule, a slightly sub-saturated G19 in ACN solution is prepared with a temperature just below the solvent boiling points (82 ℃). It is then sealed and placed in a hot water bath inside a vacuum Dewar to allow for slow cooling to room temperature in order to form single crystals. Shown in Figure 4.13a, is the image of several crystals obtained from this technique. We choose one with the best quality to investigate its linear and nonlinear optical properties. Figure 4.13b and c show optical micrographs of a single crystal captured by a standard microscope (Olympus BX51, working in reflection mode) with a digital camera; dimension scales are calibrated against a standard micrometer. The lateral dimensions is 1.5×1 mm with thickness of ~370 μm. These images show the sharp facets and parallel surfaces suitable for optical measurements. The defect on the upper left corner of (Figure 4.13b) was damaged during mounting the sample before measurements.

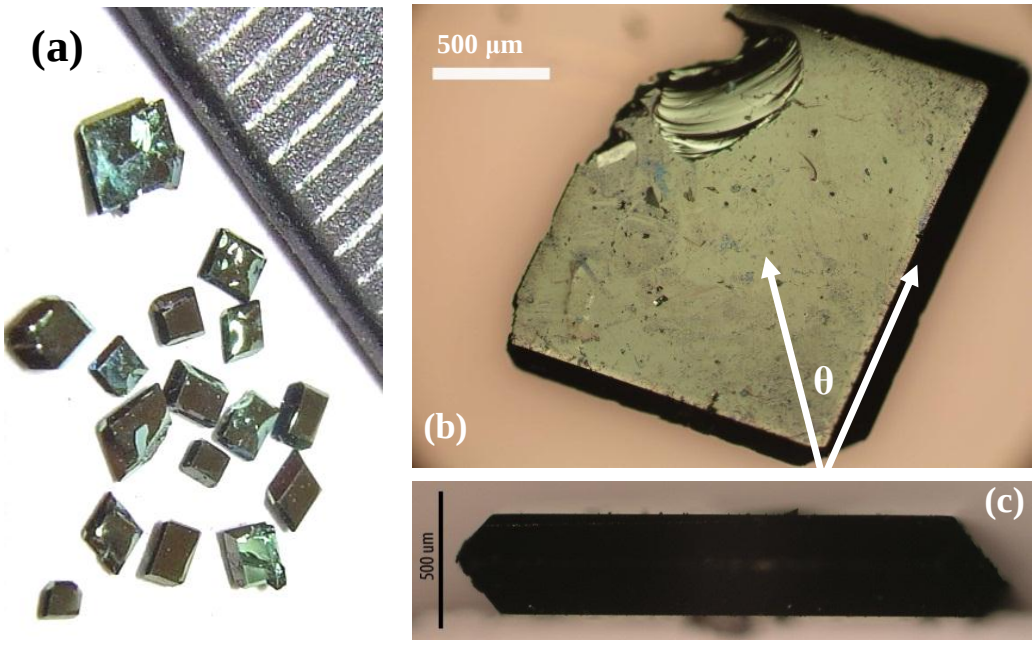

Figure 4.13: Photograph (a) of G19 single crystals; microscopic image (b) of a G19 single crystal; and (c) photograph of facet of the same single crystal of (b)

4.6.2 Linear Absorption and Reflection Spectra

The linear transmittance of the G19 crystal under unpolarized illumination is measured by an Ocean Optics spectrometer USB4000-UV-VIS with a tungsten–halogen white light source Oriel 66184. Due to small size of the single crystal, the light beam is first focused down to ~300-500 µm to under-fill the sample. The transmitted light is then re-collimated and focused onto a multi-mode fiber connecting to the spectrometer. The polarization angle dependent linear transmittance spectra are measured by placing an uncoated calcite polarizer in front of the sample. The linear transmittance spectrum of the single crystal using unpolarized light is shown in the inset of Figure 4.14 in comparison of linear absorption spectrum in toluene solution (also

shown in Figure 4.14). The one-photon absorption (1PA) edge is ~1.55 eV (800 nm). We also measured the linear transmittance spectra of this single crystal using polarized light with polarization angle θ indicated in Figure 4.13b. We observed a large variation of transmittance and a slight shift of the 1PA edge with θ. Between 1.38 and 1.46 eV (850 – 900 nm), where the single crystal has a relatively small absorption, the lowest transmittance (~50%) is observed at θ=45º whereas the highest transmittance (~70%) at θ=135º. We assume that the variation of transmittance within the transparency range (<1.46 eV, or >850 nm) is mainly due to a polarization angle dependent refractive index leading to different reflection losses on both front and rear (100) surfaces of the single crystal; however, since there are inhomogeneities on the crystal surface, we can't exclude the possibility that a slight displacement of the probing spot position caused by rotation of a calcite polarizer, which may also induce transmittance change. Assuming no scattering loss, the reflection loss on each surface is ~21% determined by unpolarized light at 1.30 eV (950 nm) at normal incidence. We can estimate the averaged refractive index of the crystal to be ~2.7. The linear absorption peak for the crystal cannot be resolved due to the extremely large absorption coefficient and sample thickness.

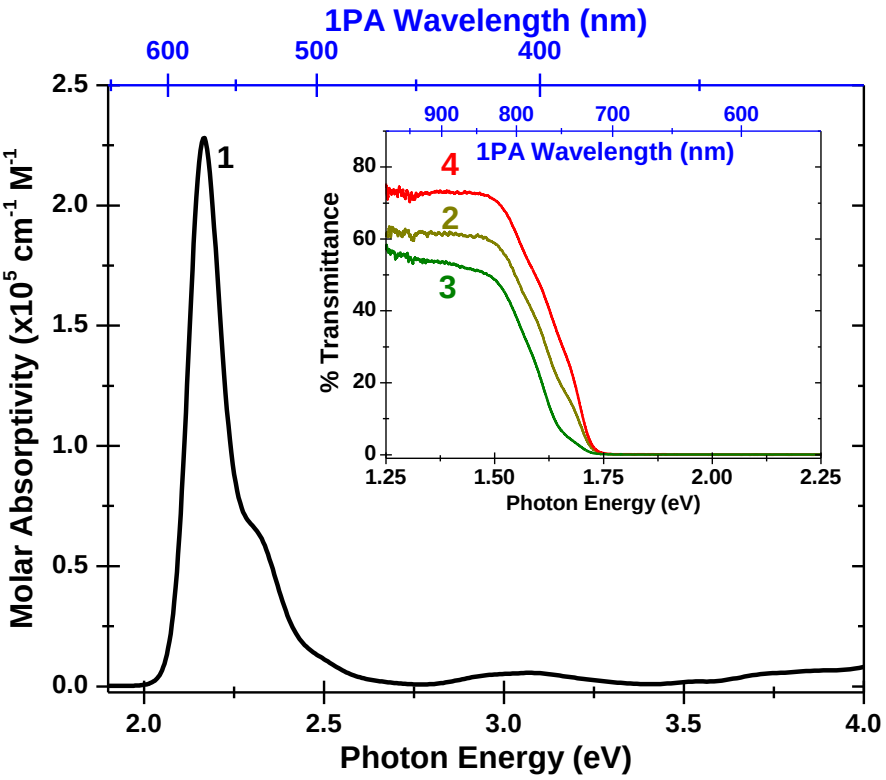

Figure 4.14: Molar absorptivity of G19 in toluene (1) measured at ~ 10^{-6} M using a 1 cm cell, and linear transmittance of the G19 crystal (inset) using unpolarized light (2), and with light polarized at θ = 45 º(3), corresponding to a calculated refractive index of 3.2; and light polarized at θ = 135 º(4), , corresponding to a calculated refractive index of 2.3, both based on Fresnel reflections. Reprinted with permission from ref. 80. Copyright 2012 American Chemical Society

To study the optical properties of the single crystal in the visible wavelength range (450-700 nm) where the transmittance is extremely small, we measured the reflection spectrum of the crystal using polarized incident light. The same microscope was used to measure the polarization dependent reflection spectrum of the single crystal. A linear rotatable polarizer (U-AN360-3 Olympus) was inserted to generate polarized light and to control the incident polarization angle, θ, as indicated in Figure 4.13b. The setup was calibrated against a standard

silicon wafer with known reflection coefficient. The spot size of the probe beam was 20 ± 2 μm. The reflection spectra at different locations on the sample are similar to the spectral shape shown in Figure 4.15, however, there are some variations in reflectivity which can be connected with the surface defects and irregularities. The reflection spectra of the single crystal are measured at θ = 45 ± 5°, 90 ± 5°, and 135 ± 5°. At θ = 45 ± 5°, the reflectivity is much stronger than at θ = 135 ± 5°. This is probably due to a stronger absorption, corresponding to a larger imaginary part of the refractive index along this polarization angle at this wavelength range. However, it is relatively difficult to decouple the real and imaginary part of the refractive index based only on a reflection spectrum. Note that only at 45 ± 5° and 135 ± 5° the polarization of the reflected light is maintained. This indicates the alignment of the optic axis. The polarization angle dependent reflectivity at 525 nm is shown in the inset of Figure 4.15. The variation of reflectivity can be fit with a sinusoidal curve with a maximum at 45° and minimum at 135°, as shown in the inset of Figure 4.15. Additionally, reflection microscopy and micro-ellipsometery measurements were unsuccessful in determining the peak of linear absorption and refractive index of the single crystal due to its small size and complicated reflection spectrum possibly containing real and imaginary parts of the linear permittivity.

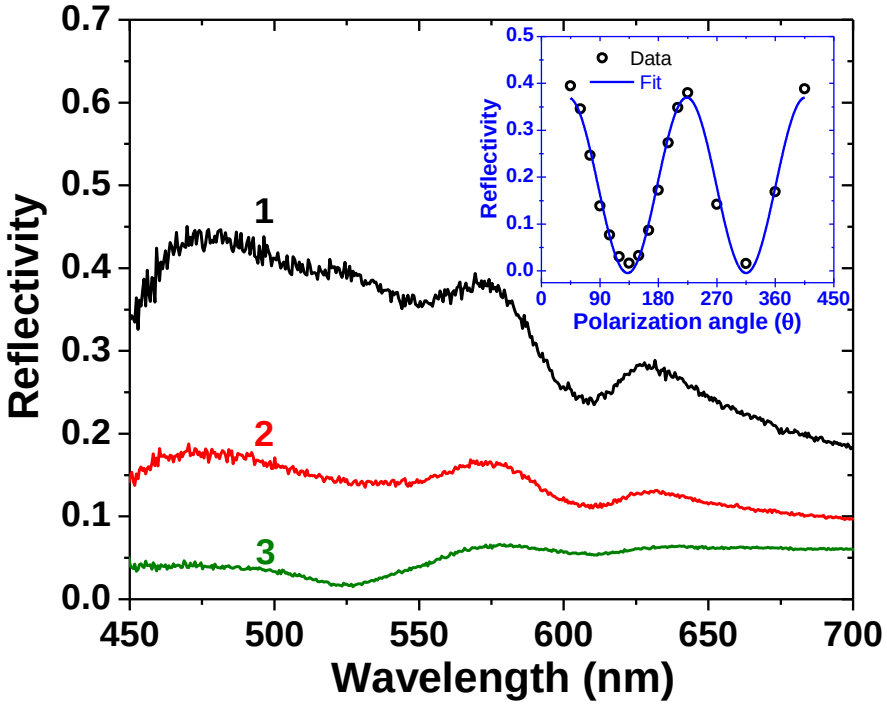

Figure 4.15: The reflection spectrum of the single crystal measured with polarization angle, θ, at 45 º(1), 90º (2) and 135º (3); inset is the reflectivity at 525.5 nm as a function of θ with experimental data (dot) and sinusoidal fitting (curve). Reprinted with permission from ref. 80. Copyright 2012 American Chemical Society.

4.6.3 Non-degenerate 2PA and Degenerate 2PA Spectra

To demonstrate the strong anisotropy of the spectroscopic characteristics of single crystal, we measured the polarization dependent non-degenerate 2PA (ND-2PA) by a femtosecond co-polarized pump-probe technique with the excitation and probe photon energy of 1.46 eV (corresponding to an excitation wavelength of 850 nm) and 1.30 eV (probe at 950 nm) respectively. The polarization angle was determined by rotating a half-wave plate in front of the

sample. Both excitation and probe beams were kept co-polarized, i.e. they were linearly polarized at the same angle θ. Both the excitation and probe photon energies are below the linear absorption edge of the crystal. The corresponding ND-2PA coefficient, α_2^{ND}, is calculated from: $\frac{dI_p}{dz} = -2\alpha_2^{ND} I_{ex} I_p$, where, I_{ex} and I_p are the irradiances of the excitation and probe beams, respectively. To measure the polarization angle dependence of the linear transmittance of the crystal, the excitation beam was blocked and the transmitted probe beam at 1.30 eV (950 nm) was measured. We record the linear transmittance (T_L) of the probe beam in the absence of excitation, and compare it with the nonlinear transmittance change (defined as $\frac{T_L - T_{NL}}{T_L}$) of the probe beam as a function of its polarization angle θ (see Figure 4.13 b) at zero temporal delay. Since the polarization angle is adjusted by rotating the half-wave plate placed in front of the crystal, no translation of the probe and pump beam is induced. Figure 4.16 shows the angular dependence of the linear transmittance and nonlinear transmittance change of the single crystal at probe photon energy 1.30 eV (950 nm), ~0.25 eV below the absorption edge. The linear transmittance reaches a minimum at ~45 °, and a maximum at ~135 ° with respect to the long crystal growth facet as shown in Figure 4.13b. Since the linear absorption at the probe wavelength 950 nm is small (the losses of linear transmittance are due to Fresnel reflection and scattering), the minimum of the linear transmittance at $\theta \approx 45°$ suggests the largest refractive index, *i.e.* the largest linear polarizability of the crystal. The maximum nonlinear transmittance change is observed at $\theta = 45 \pm 5$ °, and corresponds to $\alpha_2^{ND} = 50 \pm 8$ cm/GW, while the minimum, corresponding to $\alpha_2^{ND} = 14 \pm 1.6$ cm/GW, is observed at $\theta = 135 \pm 5$ °. This observation is similar to the polarization angle dependent two-photon excited fluorescence of the single crystal

made of cyano-substituted oligo(p-phenylenevinylene), discussed in ref. 103, where the fluorescence intensity is proportional to the 2PA coefficient at the corresponding polarization angle. Although the linear and nonlinear transmittance may vary with different spot positions on the sample due to surface defects, the coincidence of the angle for maximum nonlinear transmittance change with the angle for minimum linear transmittance of the probe beam reconfirms the orientation of the optic axis of the G19 crystal along the $\theta \approx 45°$ direction, which is also the direction of largest optical nonlinearity.

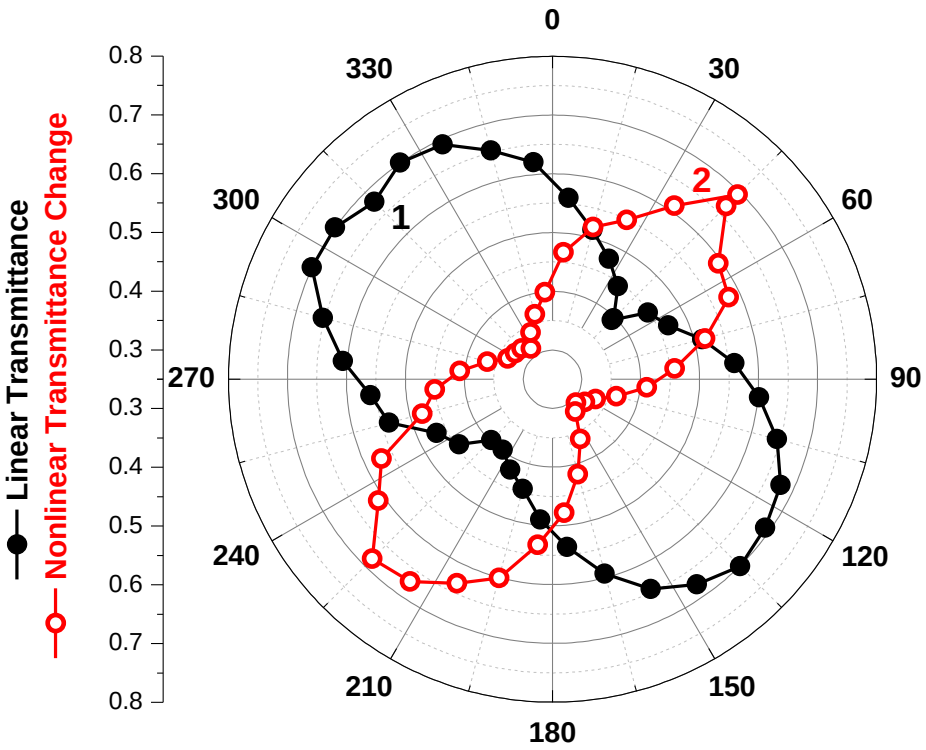

Figure 4.16: Linear transmittance (1) and nonlinear transmittance change at zero delay (2) for the G19 single crystal with respect to the polarization angle of the incident light. The scale is magnified, so that the transmittance begins at the center with 0.25 and the outer ring is 0.8. Reprinted with permission from ref. 80. Copyright 2012 American Chemical Society.

The ND-2PA pump-probe data (θ = 45 °) are shown in Figure 4.17a. The excitation and probe pulse widths were 140 ± 15 fs (FWHM), and spot size of the excitation beam was 410 ± 40 μm (HW1/e^2M) measured by the knife-edge technique. Given the pump energy of 0.27 μJ, the peak irradiance at the sample is 0.54 GW/cm^2 taking into account the Fresnel reflection. We note that ~17% of the excitation energy is absorbed by the sample due to the strong 2PA at this wavelength, which may lead to an underestimation of the α_2^{ND} value of 3-5 cm/GW; however, the anisotropic nature of the α_2^{ND} remains the same. As shown in Figure 4.17a, the transmittance of the probe beam decreases only when the pump and probe pulses temporally overlap to each other at -250 fs to 250 fs delay range, and shows full recovery at longer delay. Therefore, no excited state absorption is present. By changing the probe wavelength but keeping the pump photon energy fixed at 1.46 eV (850 nm), we also measured the ND-2PA spectrum at θ = 45 ° shown in Figure 4.18. A 2PA band is resolved with a peak transition at ~2.76 eV (excitation at 900 nm), which is to be discussed in detail with the following experiments.

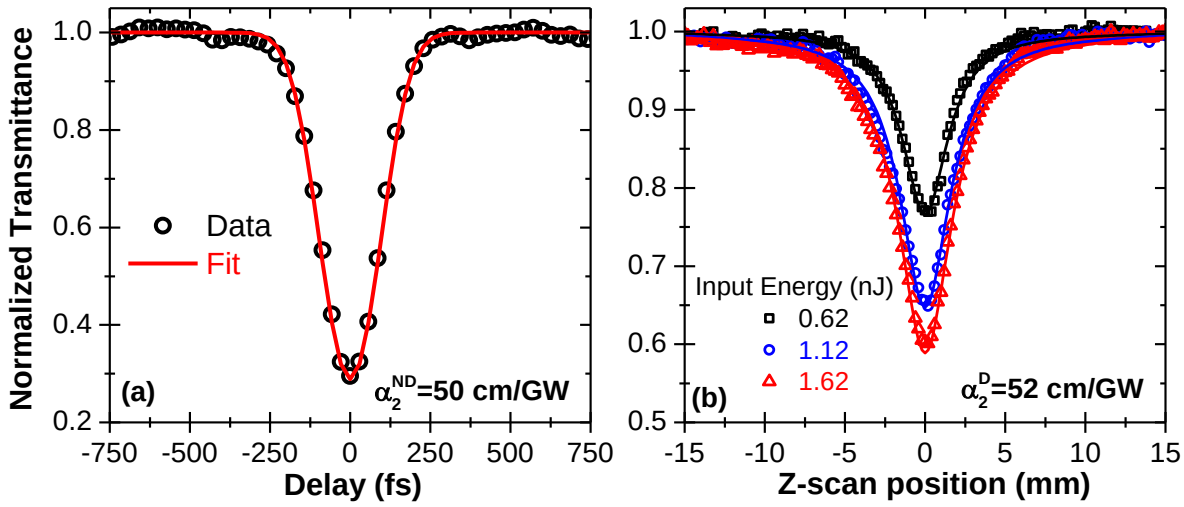

Figure 4.17: (a) ND-2PA pump-probe data of G19 crystal at θ = 45 °polarization angle; (b) D-2PA Z-scan data of the G19 single crystal at 900 nm and θ = 45 °polarization angle. Reprinted with permission from ref. 80. Copyright 2012 American Chemical Society.

The frequency degenerate D-2PA spectrum of the G19 single crystal is measured by open-aperture Z-scan with femtosecond pulses over the photon energy range from 0.87 eV to 1.44 eV (860 – 1425 nm), corresponding to two-photon transitions between 1.74 eV and 2.88 eV. The beam is polarized at θ=45 ± 5 ° to the crystal edge (as indicated in Figure 4.13b) for maximizing angle the 2PA and the polarization state of the transmitted light is observed to be linear for all wavelengths studied. To characterize and verify the setup and accuracy, bulk semiconductors of CdSe and CdTe were used as reference samples [40]. Special care was taken to make sure that the laser beam was exciting the same spot on the crystal for all Z-scan measurements. The Z-scan curves showed a background due to sample inhomogeneities and/or surface irregularities that were subtracted using the technique described in detail in Ref. 67. The beam is polarized at θ=45 ±5 °to the crystal edge (as indicated in Figure 4.13b) to maximize the 2PA, and the polarization state of the transmitted light is observed to be linear for all

wavelengths studied. Figure 4.18 shows the resulting 2PA spectrum. We observe the strongest 2PA band from 2.61 to 2.88 eV (excitation from 860 to 950 nm) (marked as (1) in Figure 4.18) with a peak D-2PA coefficient (α_2) of 52 $\pm$ 9 cm/GW at the summed photon energy of 2.76 eV (corresponding to a D-2PA excitation at 900 nm). The D-2PA spectral shape over this wavelength range is consistent with the ND-2PA spectrum measured by the pump-probe technique. The Z-scan data at 2.76 eV (excitation at 900 nm) is shown in Figure 4.17b. The spot size is 20 $\pm$ 2 μm (HW1/e^2M), and the pulsewidth 140 $\pm$ 15 fs (FWHM), both verified by performing Z-scans on the bulk semiconductor CdSe used as a reference material. The successful fitting at multiple energies using the same D-2PA coefficient (α_2^D) assured no significant excited-state absorption. It is well known that the D-2PA coefficient of semiconductors can be *universally* scaled with E_g^{-3}, where E_g is the bandgap of the solid [40]. Therefore, to demonstrate the strong nonlinearity of the organic single crystal we compare the G19 single crystal, with an absorption edge of 1.55 eV (800 nm), to CdTe with a bandgap of 1.44 eV (861 nm) [104]. The D-2PA coefficient is ~2.5× larger than the bulk semiconductor CdTe (α_2 = 21 $\pm$ 3 cm/GW at an excitation of 900 nm) [40]. The largest 2PA band for the crystal is red-shifted by ~0.25 eV (~70 nm) compared to that of the corresponding toluene solution (also redrawn in Figure 4.18). By estimating the number density of the G19 molecules of the crystal, determined by X-ray analysis (see unit cell deduced in Figure 4.19a), the average D-2PA cross section of an individual molecule in the single crystal at 2.76 eV is ~ 690 GM, which is approximately 4× smaller than the 2PA peak in the solution. Given that the 2PA cross section in isotropic solution is averaged by a factor of five due to the random orientation of solute molecules [54], the reduction of the 2PA cross section in the crystal is ~20×. This is presumably due to strong molecular

interactions between the closely-spaced molecules in the crystal, as well as the different orientations of molecules inside the crystal unit cell (see Figure 4.19a). The positions of the next two lower energy 2PA bands (see Figure 4.18 labeled (2) and (3)) in the crystal are located at ~2.05 eV (excitation at ~1210 nm) and ~1.86 eV (excitation at ~1330 nm) with a peak α_2 of 5.5 $\pm$ 1.5 cm/GW and 3 $\pm$ 0.6 cm/GW, respectively. Figure 4.18 compares the spectral positions of the 2PA bands in the monomeric form to that of the single crystal. Note that we measure a 2PA cross section for the solution, and a bulk 2PA coefficient for the crystal, so direct comparison of the 2PA magnitudes is avoided here due to the complex relative molecular orientation pattern in crystal (see Figure 4.19a). The D-2PA spectrum of the monomeric form in toluene, a low polarity solvent, exhibits three 2PA bands as shown in Figure 4.18: (1) the first 2PA band between 2.75 - 3.31 eV (labeled as (1') in Figure 4.18) with peak cross-section of $\approx$ 3000 GM corresponding to a 2PA allowed transition into the S_2 state; (2) a smaller 2PA band is observed between 2.25 - 2.61 eV (labeled as (2') in Figure 4.18) with a peak cross-section $\approx$ 500 GM that is due to the vibrational coupling between S_1 and its vibrational mode; and (3) the strongest 2PA band related with a 2PA allowed transition into higher-lying excited states (>3.5 eV) which cannot be fully resolved due to the onset of the 1PA edge. The origins of these 2PA bands in toluene is described in more detail in Section 4.4.2

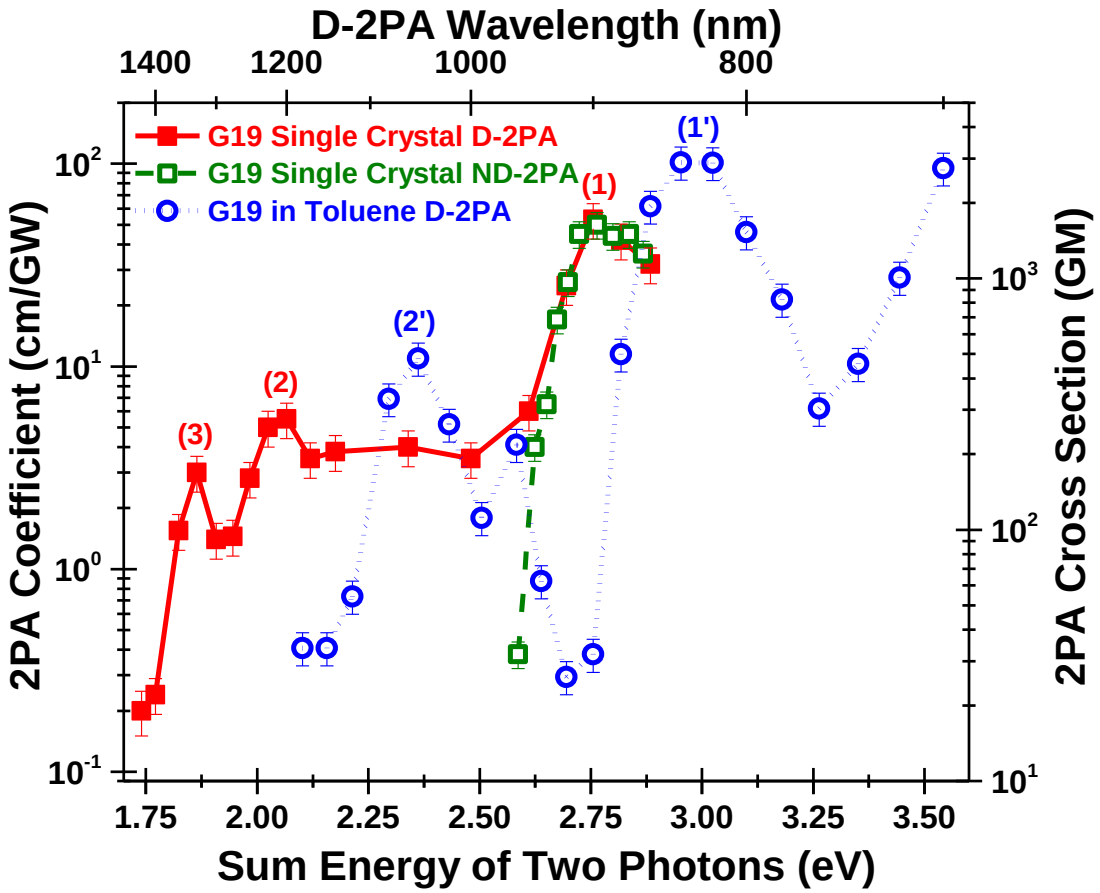

Figure 4.18: Comparison of D-2PA (red solid squares) and ND-2PA (green open squares) spectrum of G19 single crystal and its toluene solution (blue open circles) measured at the concentration of 8×10^{-5} M. Reprinted with permission from ref. 80. Copyright 2012 American Chemical Society.

.

4.6.4 X-ray Diffraction and Quantum Chemical Calculations

To explain the origin of the 2PA bands in the single crystal, we analyze its structure with X-ray diffraction analyses at ~100 K. The experiment and data analysis was performed by Dr. Titiana V. Timofeeva and her colleagues in Department of Chemistry, New Mexico Highlands

University, Las Vegas, NM. The crystal is orthorhombic, with space group *Pbca*, and unit cell parameters a = 15.861(2), b = 16.382(2), c = 18.465(2) Å (Figure 4.19a). Crystallographic evaluation of the G19 morphology revealed that the most developed face of the crystal (shown in Figure 4.13 b) corresponds to (100), i.e. perpendicular to crystallographic axis *oa*, also shown in Figure 4.19 a. By counting the number of molecules in the unit cell and calculating the volume of the unit cell, we estimate the number density of molecules of the crystal is ~1.7×10^{21} cm^{-3} (2.8 Mol L^{-1}). All the molecules in the crystal are symmetrically equivalent. They form centrosymmetric π-stacking dimers (one is shown on Figure 4.19 a) with a separation between the molecular planes of $\approx$ 3.38 Å. It has been shown that intermolecular interactions can alter the spectral properties significantly [105,106], and that the crystalline environment, in turn, may enhance the intermolecular interactions [107,108]. In order to understand the optical properties of the crystal, we perform quantum chemical calculations using the standard TD-B3LYP/6-31G** method as implemented in Gaussian 2003 suite of programs [109]. This calculation was performed by Dr. Artëm E. Masunov in NanoScience Technology Center, University of Central Florida. Our calculations indicate strong electronic coupling (c.a. 0.32 eV) between the molecules in one dimer (Figure 4c). Each unit cell in the crystal contains four such dimers in different orientations. Our calculations also show that the electronic coupling between the molecules in the adjacent dimers are only 3% compare to that inside the dimer (c.a. 0.01 eV). Therefore, the optical properties of the crystal are expected to be similar to the properties of the molecular dimers, slightly perturbed by the crystalline environment. In order to predict the absorption anisotropy, the angular dependence of the absorption by the molecular dimer needs to be averaged over the four specific orientations observed in the unit cell. However, this extends beyond the scope of the present work.

Quantum chemical calculations also reveal a different origin of the 2PA in the solid state as compared to its monomeric form in solution. Results are shown schematically in Figure 4.19c and presented in Table 4.4. In the monomeric form, the main linear absorption peak is dominated by the HOMO→LUMO transition, and the strongest 2PA band (labeled (1') in Figure 4.18) corresponds to the HOMO-1→LUMO transition. Dimerization around the center of symmetry (C_i) leads to a splitting of each electronic energy level into two: in-phase and out of phase giving linear combinations with opposite parities ($HOMO_+$ and $HOMO_-$; $LUMO_+$ and $LUMO_-$; etc.) as shown in Figure 4.19c. As a result, all electronic transitions in the dimer become mixed and split (mixed meaning "+" and "-" combinations and split referring to an energy separation between these two combinations). According to our calculations (see Table 4.4), there are four transitions in the dimer generated by 1PA transitions $S_0 \rightarrow S_1$ in each monomer: two allowed $A_g \rightarrow B_u$ (with different oscillator strengths) and two forbidden $A_g \rightarrow A_g$ transitions with zero oscillator strength. Both allowed transitions $A_g \rightarrow B_u$ are formed by "+" and "-" combinations of $HOMO_+ \rightarrow LUMO_-$ and $HOMO_- \rightarrow LUMO_+$ transitions. Both forbidden transitions $A_g \rightarrow A_g$ are formed by "+" and "-" combinations of $HOMO_+ \rightarrow LUMO_+$ and $HOMO_- \rightarrow LUMO_-$ transitions. These transitions (with final states A_{g-} and A_{g+}) are red-shifted relative to the monomeric absorption peak $S_0 \rightarrow S_1$ and may be allowed in 2PA transitions due to the same parity of these two states as defined by selection rules. We suggest that these calculated $A_g \rightarrow A_g$ transitions correspond to the experimental 2PA bands with peak positions at 2.05 eV (excitation at 1210 nm) and 1.86 eV (excitation at 1330 nm), labeled as (2) and (3) in Figure 4.18. The next four transitions shown in Table 4.4 are derived from 1PA transitions, $S_0 \rightarrow S_2$, in each monomer. They correspond to two allowed $A_g \rightarrow B_u$ (also with different oscillator strengths) and two

forbidden $A_g \rightarrow A_g$ transitions. In our 2PA measurements, we can observe only one band at longer wavelengths with a final state of A_{g-} symmetry. The $A_g \rightarrow A_g$ transition (with a final state of A_{g+} symmetry) corresponding to the shorter wavelength cannot be observed due to the close proximity of the 1PA edge.

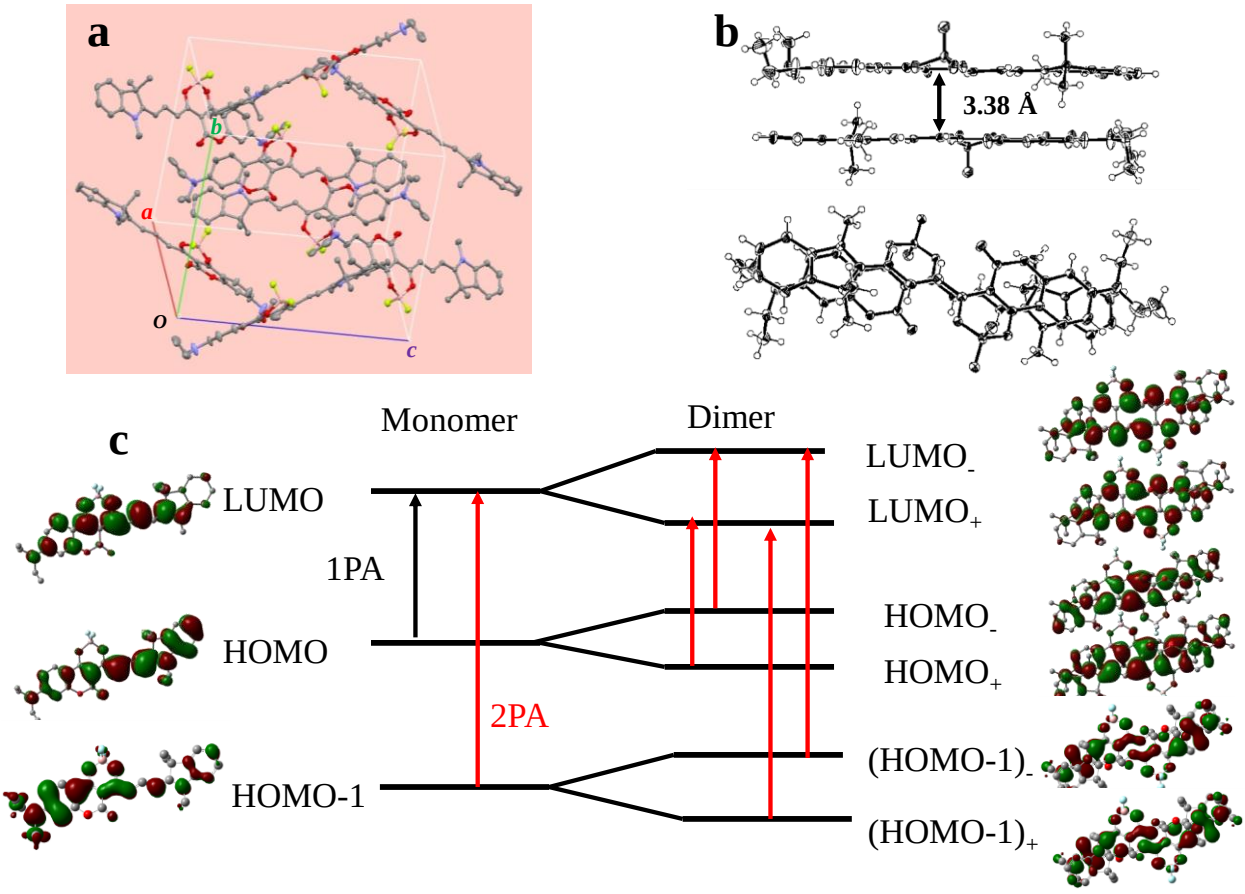

Figure 4.19: (a) Molecular packing in G19 single crystal ; (b) formation of molecular π-stacking dimers aligned in an anti-parallel mode; (c) schematic of formation of molecular orbitals in dimer from the molecular orbitals in monomer. The red and black arrows in the monomer illustrate 1PA and 2PA transitions, respectively. The red arrows in dimer illustrate the 2PA transitions (see explanation in the text). Reprinted with permission from ref. 80. Copyright 2012 American Chemical Society.

Based on the quantum chemical calculations, we conclude that the dimer's three transitions $S_0 \rightarrow S_1$, $S_0 \rightarrow S_3$, and $S_0 \rightarrow S_6$ are 2PA allowed given that the parities of the states are the same. They are labeled as (1), (2), and (3) in Figure 4.18 respectively. Note that the 2PA transition $S_0 \rightarrow S_6$ in the dimer is the combination of $(HOMO\text{-}1)_+ \rightarrow LUMO_+$ and $(HOMO\text{-}1)_- \rightarrow LUMO_-$, similar to the strongest 2PA transition ($S_0 \rightarrow S_2$) in the monomer corresponding to HOMO−1→LUMO. Therefore, the 2PA transition in the dimer (labeled as 1 in Figure 4.18) adopts the same configuration, but slightly red-shifts in spectral position with respect to the monomer 2PA transition (labeled as 1' in Figure 4.18). The two other 2PA transitions of the dimer (labeled as 2 and 3 in Figure 4.18) are different and correspond to the combination of $HOMO_- \rightarrow LUMO_-$ and $HOMO_+ \rightarrow LUMO_+$. These 2PA bands are strongly red-shifted with respect to the HOMO→LUMO transition in the monomer. Thus, while the pi-stacking dimers are similar to H-aggregates, they lead to a red shift in 2PA transition, which is opposite to the well-known blue shift in linear spectra upon formation of H-aggregates [110].

Table 4.4: TD-B3LYP/6-31G** calculations for transitions of the monomer G19 and corresponding dimer. Reprinted with permission from ref. 80. Copyright 2012 American Chemical Society.

Transitions	Oscillator Strengths	Final State Symmetry	Main configurations Weighing factors | Involed MOs
Monomer G19			
$S_0 \rightarrow S_1$	1.76	B_u	0.69 | HOMO→LUMO>
$S_0 \rightarrow S_2$	0.04	A_g	0.68 | HOMO-1→LUMO>
Dimer G19 Transitions generated by $S_0 \rightarrow S_1$ transitions of monomer molecules			
$S_0 \rightarrow S_1$	0	A_g-	0.60 | $HOMO_+ \rightarrow LUMO_+$> – 0.36 | $HOMO_- \rightarrow LUMO_-$>
$S_0 \rightarrow S_2$	0.07	B_u-	0.44 | $HOMO_+ \rightarrow LUMO_-$> – 0.56 | $HOMO_- \rightarrow LUMO_+$>
$S_0 \rightarrow S_3$	0	A_{g+}	0.35 | $HOMO_+ \rightarrow LUMO_+$> + 0.60 | $HOMO_- \rightarrow LUMO_-$>
$S_0 \rightarrow S_4$	3.08	B_{u+}	0.53 | $HOMO_+ \rightarrow LUMO_-$> + 0.41 | $HOMO_- \rightarrow LUMO_+$>
Dimer G19 Transitions generated by $S_0 \rightarrow S_2$ transitions of monomer molecules			
$S_0 \rightarrow S_5$	0.09	B_u-	0.32 | $(HOMO-1)_+ \rightarrow LUMO_-$> – 0.60 | $(HOMO-1)_- \rightarrow LUMO_+$>
$S_0 \rightarrow S_6$	0	A_g-	0.53 | $(HOMO-1)_+ \rightarrow LUMO_+$> – 0.46 | $(HOMO-1)_- \rightarrow LUMO_-$>
$S_0 \rightarrow S_7$	0.2	B_{u+}	0.61 | $(HOMO-1)_+ \rightarrow LUMO_-$> + 0.29 | $(HOMO-1)_- \rightarrow LUMO_+$>
$S_0 \rightarrow S_8$	0	A_{g+}	0.43 | $(HOMO-1)_+ \rightarrow LUMO_+$> + 0.29 | $(HOMO-1)_- \rightarrow LUMO_-$>

4.7 NIR 2-Azaazulene Polymethine Dye with a Broken-Symmetry Ground State

4.7.1 Introduction of Ground-state Symmetry Breaking

The symmetrical polymethine dyes (PDs), cationic or anionic, usually have the general molecular structure as $R^{\pm}-(CH=CH)_n-CH=R$, where R represents a specific end group. According to traditional triad theory [111], symmetrical PDs exhibit two distinctive features: the equalization of the single and double bond length (so called cyanine limit [36]), and large alternation of the positive and negative charges on the neighboring carbon atoms within the polymethine chain. These features are responsible for the intense narrow linear absorption band of PDs, corresponding to $S_0 \rightarrow S_1$ transition, with an unresolved vibrational shoulder on the shorter wavelength ("blue") side of the absorption peak. Such absorption feature is also observed for anionic polymethine series as discussed in Section 4.3. Additionally, since the charge distribution is symmetrical with respect to the molecular structure which is relatively independent on solvent polarity, very small solvatochromic effect is observed for symmetrical PDs in different polar solvents, as demonstrated in linear absorption spectra of G37 and G38 in Figure 4.6. However, as the conjugation length progressively increases, an unexpected spectral feature is observed for long PDs, as described by Tolbert *et al* [112]: a remarkably feature-less broad absorption band shows up on the "blue" side of $S_0 \rightarrow S_1$ band, which is accompanied by a substantial decrease of the peak molar absorptivity. The authors of ref 112 concluded that the symmetry for short PDs could not be maintained for long PDs, and hence the system properties of long PDs could not be extrapolated from its short analogues. More remarkable is the strong solvatochromic effect observed in solvents with different polarity: this feature-less absorption

band can be significantly enhanced in polar solvent, as was observed by Lepkowicz *et al* [81]. This phenomenon, so called ground-state symmetry breaking (SB) effect, contradicts to triad theory predicting that the bandgap of symmetrical polymethine should eventually vanish at infinite conjugation length. This SB effect is the indication of the appearance of a molecular form with an asymmetrical charge distribution in the ground state and, thus, leading to an asymmetrical bond-length alternation (BLA), which can be stabilized in polar solvent.

Generally there are two main approaches utilized by different research groups to explain this peculiar phenomenon. One is based upon so called "soliton model" [113-118]. It was found that the total charge distribution of the π-conjugated system is not delocalized uniformly along the π-conjugation chain but as a wave of alternating positive and negative partial charges, i.e. as a solitonic wave with electrons and holes respectively. If the conjugation length of symmetrical PDs is longer or comparable to the dimension of soliton, the peak of the solitonic wave could be shifted to one of the end groups, leading to the rearrangement of BLA (molecular geometry) breaking its original symmetry with respect to π center. As a result, the linear absorption spectra show dramatic changes with strong contribution from asymmetrical charge distribution. Semi-empirical quantum chemical calculation methods can be used to demonstrate the evolution of BLA under the influence of solitonic waves.

Another approach is called essential-state model proposed by Terenziani and Painelli, *et al* [86,119,120]. For symmetrical PDs with D-π-D quadrupolar structure, the charge resonance is among three structures D^{+}-π-D ↔ D-$π^{+}$-D ↔ D-π-D^{+}. These three resonant structures are chosen as the *basis states* to form the three essential-states. These three essential states, corresponding to the ground state, the one-photon allowed (but two-photon forbidden, S_1) state and two-photon allowed (but one-photon forbidden, S_n) state, are the three most important states which

dominates the low-energy (i.e. energy lower than the two-photon allowed S_n) physics of the PDs. It is shown that for long polymethine PDs, the one-photon allowed (S_1) and two-photon allowed (S_n) state are stable, featured by a single minimum in potential energy surface (PES); while the ground state exhibits double minimum PES, and thus is bistable, corresponding to a broken ground-state symmetry. Note that according to essential-state model, symmetry breaking can also happen to 1st excited state of certain type of chromophores (e.g. fluorene [121,122]). Another feature of essential-state model is its capability to take into account the influence of solvent polarity on the linear and nonlinear optical properties of the chromophore by introducing only one parameter, i.e. solvent relaxation energy. The great advantage of essential state model is that only 7 adjustable parameters (6 of them are solvent independent plus solvent-dependent relaxation energy) are needed for the modeling, while for its counterpart, the well-known Marcus-Hush model [123], the number of adjustable parameters is much larger: for example, a fit of just the absorption spectrum in a *single solvent* would require a minimum of 6 adjustable parameters. An additional set of 6 adjustable parameters is needed to fit the 2PA spectrum in *one solvent*.

In this section, we experimentally study a specific class of NIR linear PDs, 2-azaazulene dye (as shown in Figure 4.4), to demonstrate the influence of ground-state symmetry breaking upon its linear optical properties. More importantly, for one dye from this series, 2-butyl-6-[7-(2-butyl-1,3-dimethylcyclo-hepta[*c*]pyrrol-6(2*H*)-ylidene)hepta-1,3,5-trien-1-yl]-1,3-dimethyl cyclohepta[*c*] pyrrolium tetrafluoroborate, labeled as JB17-08, we also measured the 2PA and ESA spectra in two different solvents of different polarity to study the SB effect on its nonlinear optical properties. The conclusion of two approaches, quantum chemical analysis and essential-

state model developed by other groups, are briefly introduced to explain the origin of ground-state SB effect on long PDs.

4.7.2 Linear Optical Properties of the NIR 2-Azaazulene Polymethine Dye

The linear absorption spectra of this series of dyes from JB7-08 (n=1) to JB5-09 (n=4) are shown in Figure 4.20a in two solvents: a relatively low polar solvent DCM and highly polar solvent ACN (for JB7-08, JB9-08, and JB17-08) or ethanol (for JB5-09). Note that the linear absorption spectra was obtained with concentration of the solution less than 10^{-5} M; further dilution of solution didn't change the spectral shape, i.e. no aggregation was observed. For JB7-08 (n=1), the linear absorption peak is located at 825 nm in DCM, ~300 nm red shifted compared to traditional polymethine dyes with indolium or thiazolium end groups and the same chain length [33]. Therefore, the effect of these 2-azaazulene end groups is equivalent to the extension of polymethine chain by approximately three vinylene groups. The increase of conjugation length by one vinylene group leads to ~100 nm red shift of main absorption peak ($S_0 \rightarrow S_1$), which is typical for polymethine dyes. The linear absorption at visible and UV range is due to absorption into higher excited states ($S_0 \rightarrow S_n$). More interesting is the solvatochromic behavior of this set of dyes in solvents with different polarity. For JB7-08 (n=1), the linear absorption peak shows small hypsochromic shift in ACN (814 nm), compared to the 825 nm in DCM, which indicates a small reduction of the permanent dipole moment from ground state to excited state [47]. Both main absorption bands show relatively narrow bandwidth in both solvents with similar peak molar absorptivity, which is the indication of symmetrical charge distributions in both excited and ground states. In contrast, the absorption spectra of JB17-08, despite its symmetrical molecular

structure, show a remarkable change in spectral shape at changing of solvent polarity, featured by a substantial band broadening and reduction of peak molar absorptivity in ACN compared to DCM. This is a strong indication of polar solvatochromism which is typical for asymmetrical (push-pull) dyes exhibiting ground state charge localization and a large ground state permanent dipole moment (as shown in Section 4.4.1). Therefore, the linear absorption of JB17-08 in ACN can be considered as the co-existence of the symmetrical charge distribution form (SF) and asymmetrical charge distribution form (ASF). If we assume that in DCM, JB17-08 molecules still maintain its symmetrical charge distribution, i.e. 100% SF; we can virtually separate the contribution from SF and ASF forms in its linear absorption in ACN as shown in Figure 4.20b.

This virtual separation is presented in Figure 4.20b for low concentrated solutions (C<10 μM) to avoid aggregation. The black curve shows the total linear absorption spectrum of JB17-08 in ACN, while the blue shaded area corresponds to absorption in DCM (presumably representing absorption of the molecules in SF form only), blue shifted by ~20 nm to coincide with the absorption peak in ACN. The close overlap of the two absorption contours on the red side of the spectrum indicates that the absorption peak in ACN at 1043 nm is mainly due to the contribution from the SF form. We can extract the absorption contribution of the ASF form by subtracting the blue shaded area (contribution from the SF form) from the total absorption spectrum (black curve). This contribution, situated on the blue side of the total spectrum, is shown as the red shaded area in Figure 4.20b. As a result, by the ratio of the peak molar absorptivities, the concentration of the SF form in ACN can be estimated as ~42%, and the contribution of the ASF form can be estimated as ~58%.

For JB5-09 (n=4), the linear absorption shows a broad main absorption band in both solvents, DCM and ethanol, suggesting that SB has already taken place in low polar solvent.

The $S_0 \rightarrow S_1$ transition dipole moments (μ_{ge}), estimated from the area beneath the linear absorption band, using Equation 3.1, are: 12 D for JB7-08, 15.6 D for JB9-08, 18 D for JB17-08 and 16 D for JB5-09.

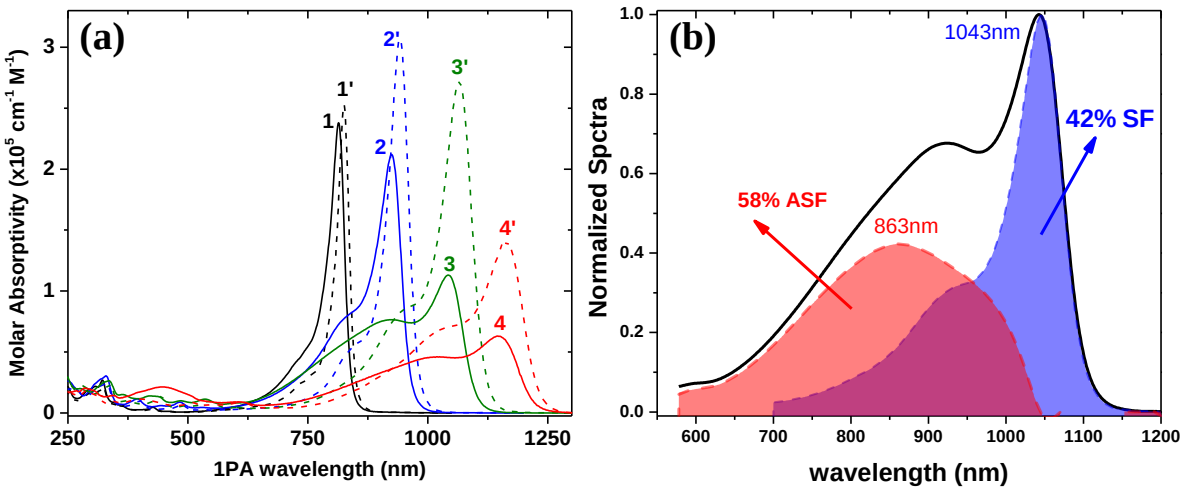

Figure 4.20: (a) Linear absorption of JB7-08 in DCM (1) and ACN (1'), JB9-08 in DCM (2) and ACN (2'), JB17-08 in DCM (3) and ACN (3') and JB5-09 in DCM (4) and ethanol (4'). Note the solubility of JB5-09 in ACN is poor; (b) virtual separation of SF and ASF from the total linear absorption spectrum of JB17-08 in ACN (black contour). The blue shaded area is the contribution from SF, and the red shaded area is the subtraction result corresponding to contribution from ASF.

To exclude the origin of such substantial spectral broadening from other trivial cause such as aggregation, the linear absorption of JB17-08 in DCM and ACN was measured at the concentration less than 10^{-5} M. Further dilution of solution doesn't lead to any change of the spectral shape. To further check the purity of JB17-08, high-performance liquid chromatography and mass spectrometry analysis was also performed in the Chemistry department, University of Central Florida. The purity of the dye including various isomers (all-trans, all-cis, and two possible cis, trans isomers) is ~90%, with the desired all-trans structure being somewhat less than 85%. This is consistent with our quantum chemical calculation which shows that only all trans-

form is the most energetically preferable in the ground state at the room temperature as the energy barriers for formation of other types of isomers (including rotation around the bonds placed in the middle of the chain) are much larger than *kT* energy. Additionally we performed calculation of the spectral positions and oscillator strengths for the electronic transitions in possible cis-forms. We found that the spectral peaks of the $S_0 \rightarrow S_n$ transitions in cis-isomers differs by only several nanometers from the corresponding transition peak in trans-form. Therefore, a broad shoulder in the absorption spectrum in polar ACN cannot be connected with $S_0 \rightarrow S_1$ transition in cis-form. It also cannot be connected with $S_0 \rightarrow S_2$ transition in cis-form as oscillator strength of this transition remains small and contradicts to experimentally measured anisotropy spectrum (shown in Figure 4.21).

The fluorescence spectra of JB9-08 (n=2) and JB17-08 (n=3) in DCM and toluene are shown in Figure 4.21 a and b. The fluorescence quantum yields of both dyes are no more than 5%. Note that no fluorescence could be measured for JB7-08 (n=1) and JB5-09 (n=4). Additionally, the fluorescence excitation anisotropy curves for JB9-08 in ethylene glycol and for JB17-08 in DCM and ACN are shown in Figure 4.21a and b. The anisotropy curve is noisy due to small fluorescence quantum yield and peaky spectrum of excitation lamp at NIR wavelength range. For JB17-08, fluorescence spectra in both solvents, DCM and ACN, are narrow with similar bandwidth, confirming that the emission occurs only from the SF form, in accord with previous reports [56]. The excitation anisotropy curves in both solvents show similar shape. It is flat within the main absorption band (up to ≈750 nm) and $r(\lambda)$ values are high (≈0.35) indicating a small angle between the absorption and emission transition dipoles. The decrease in the values of $r(\lambda)$ in the range from 700 nm to 550 nm locates the position of the next electronic state (or group of states) with a larger angle (≈30°) between the absorption and emission dipoles. The

deepest valley is observed in the range 430-470 nm indicating an angle up to 65° between these two dipoles. Magnitudes of anisotropy valleys in ACN are somewhat smaller, which could indicate to the influence of asymmetric form with slightly different orientation of transition dipole moments. Similar excitation anisotropy shape is also observed for JB9-08 in ethylene glycol but blue shifted compared to JB17-08.

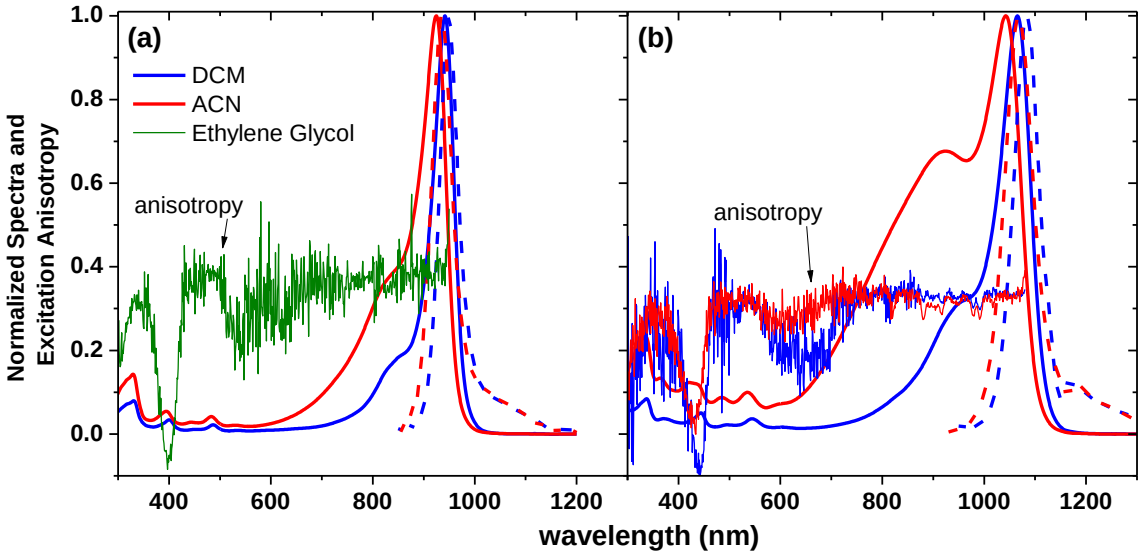

Figure 4.21: (a) Linear absorption (solid) and fluorescence (dash) of JB9-08 in DCM (blue) and ACN (red) with excitation anisotropy in ethylene glycol (green); (b) linear absorption (solid) and fluorescence (dash) of JB17-08 in DCM (blue) and ACN (red) with excitation anisotropy in both solvents

4.7.3 Two-photon Absorption and Excited State Absorption of JB17-08

The frequency-degenerate 2PA spectra of JB17-08 in DCM and ACN are measured by the open-aperture Z-scan technique [67] using femtosecond pulses. With this technique, δ_{2PA} are directly obtained without the need of reference samples, thus minimizing experimental errors. Pulsewidths at wavelengths of interest are 120-150 fs (FWHM), measured independently by the

second-harmonic autocorrelation technique. To verify the spot size at the focus, we also performed a Z-scan of the semiconductor GaAs at 1.5 μm. Both DCM and ACN solvents show significant absorption in the wavelength range of interest (1.3-2.1 μm), and their linear absorption is taken into account in the fitting procedure adopted to analyze the 2PA cross section values, δ_{2PA}. The resulting spectra are shown in Figure 4.22. In spite of the large variation of δ_{2PA} measured between 1800 nm and 2000 nm (absolute experimental error is ~± 20%), the measured data are reproducible.

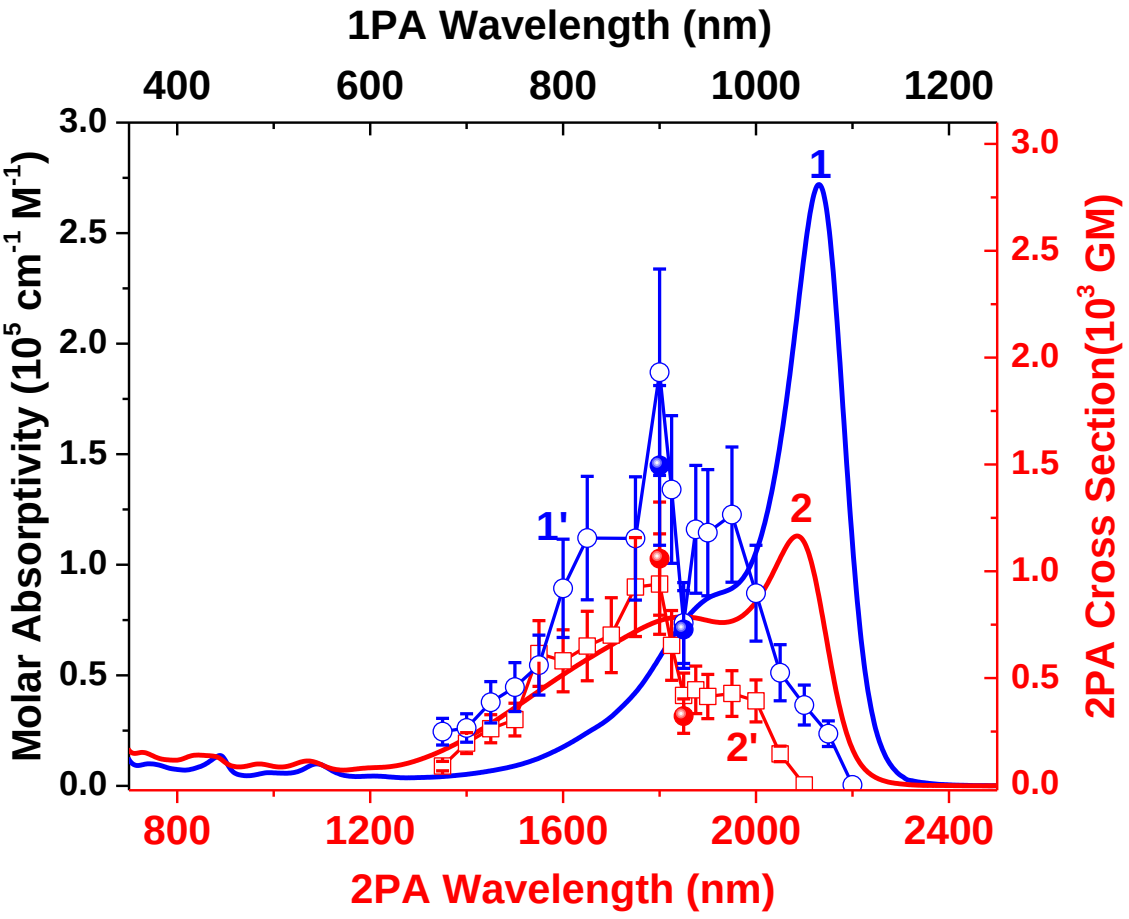

Figure 4.22: 1PA (1, 2) and 2PA (1', 2') spectra in DCM (1, 1') and ACN (2.2'), respectively. Top and left axes are related to 1PA, and bottom and right axes are related to 2PA. The solid dots (blue for DCM and Red for ACN solution) are experimental data repeated 24 hours later.

In DCM solution at the moderately high concentrations $C > 10^{-4}$ M, needed for 2PA measurements, hints of the presence of H-aggregates JB17-08 are recognized due to the increased absorption at the blue side of the spectrum. The linear absorption spectra of JB17-08 in DCM and ACN, measured at concentrations larger than 1 mM, are compared with corresponding spectra measured at concentrations less than 10 μM, as shown in Figure 4.23. No changes in absorption are observed at further dilution below 10 μM. In both solvents at high concentration, there is a slight increase of absorption on the blue side of the spectrum indicating the possible formation of H-aggregates [110,124]. This aggregation is stronger in lower polar DCM as compared to high polar ACN solution, as shown in Figure 4.23.

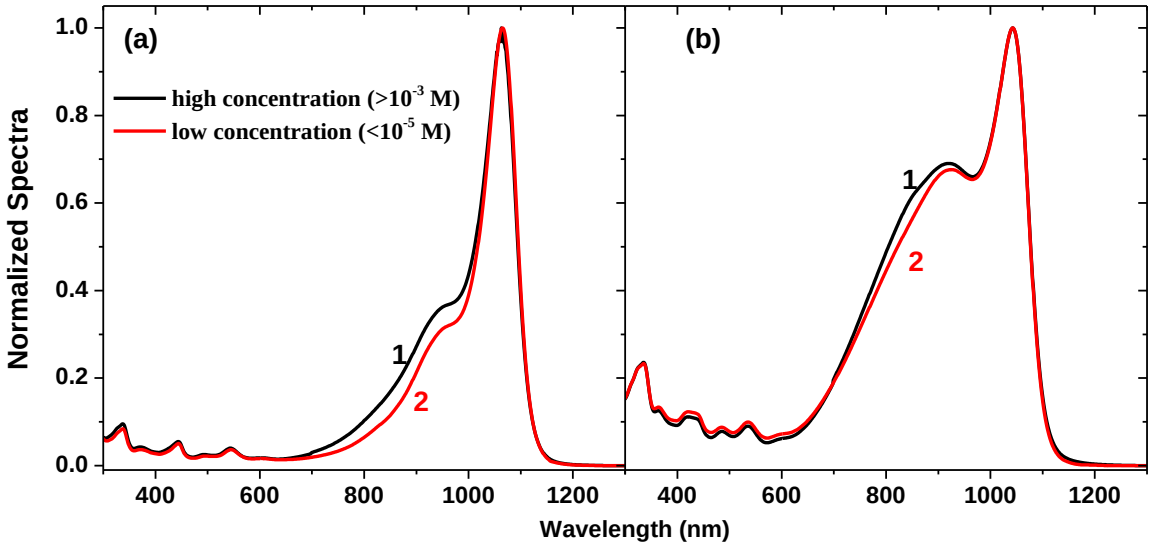

Figure 4.23: comparison of linear absorption of JB17-08 in DCM (a) and ACN (b): curves 1 in (a) and 1 in (b) correspond to high concentration C>1mM, and curves 2 in (a) and 2 in (b) correspond to low concentrations $C=4.4\times10^{-6}$ M and $C=6.6\times10^{-6}$ M, respectively

Aggregation hinders the accurate determination of the 2PA cross section in DCM solution; however, we can assume that the *shape of the 2PA spectrum* is not significantly

affected by aggregation for the following two reasons: 1) as was shown previously [125], 2PA for J- and H-aggregates at the excitation into their main absorption bands is only weakly allowed due to their symmetrical structures; 2) since the main absorption peak of H-aggregates is usually located at higher energies compared to the monomer, the detuning energy for aggregates is larger, thus reducing possible contributions of their 2PA [51] in the wavelength range of interest.

To precisely determine the δ_{2PA} in DCM, Z-scan measurements were performed on JB17-08 solutions at $C = 6.7 \times 10^{-5}$ M in DCM and $C = 6.4 \times 10^{-5}$ M in ACN, respectively. At this concentration no significant aggregation is observed in either solvent (Figure 4.24a). Measurements were run at 1800 nm, corresponding to the 2PA main peak, in 1 cm thick quartz cells. Based upon the maximum open-aperture Z-scan signal in DCM compared to that in ACN, as shown in Figure 4.24b, and the concentration of the solution, we estimate that δ_{2PA} in DCM is $1.6 \pm 0.2\times$ larger than that in ACN solution. Therefore, using the ratio of δ_{2PA} at 1800 nm obtained from diluted solutions, we rescaled the 2PA spectrum in DCM, obtained from Z-scan measurements in concentrated solution, as shown in Figure 4.22. Note that without taking into account the aggregation, δ_{2PA} in DCM can be under-estimated by a factor of 2.

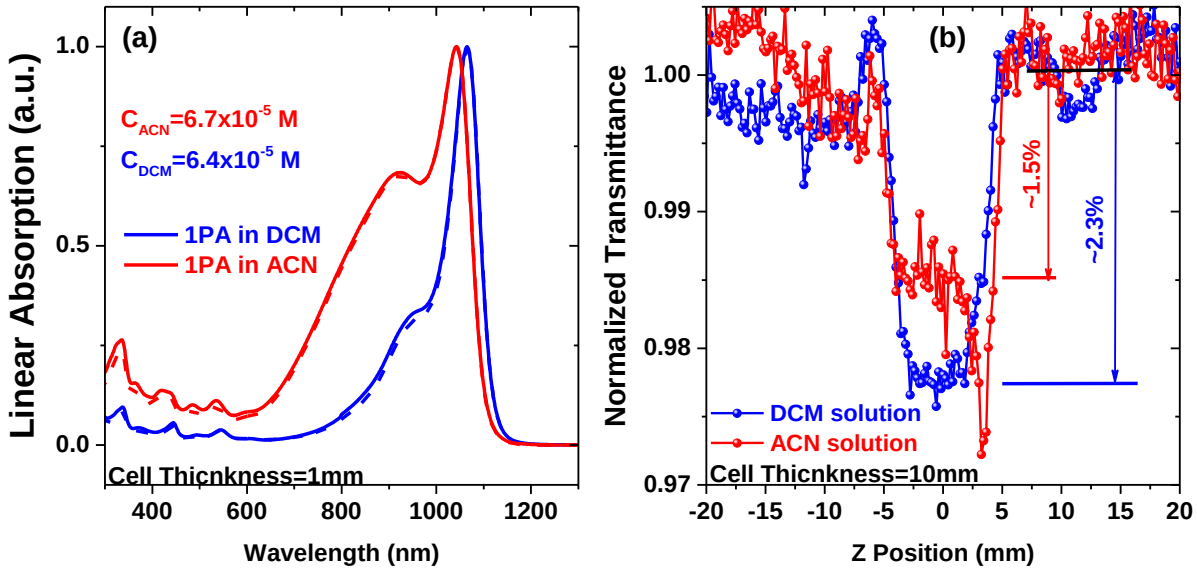

Figure 4.24: (a) Linear absorption of JB17-08 in DCM (blue solid, C=6.4×10^{-5}M) and ACN (red solid, C=6.7×10^{-5} M), in comparison to linear absorption (dash) measured at <10^{-5} M, where no aggregation. Note that the cell thickness is 1 mm; (b) Z-scan performed in 1cm cell filled with JB17-08 in DCM (blue, C=6.4×10^{-5}M) and ACN (red, C=6.7×10^{-5} M), respectively. Note that the wavelength is 1800 nm, energy is 110 nJ, pulsewidth 130 fs (FWHM), spot size is 19 μm (HW1/e^{2}M)

As seen from Figure 4.22, the one-photon $S_0 \rightarrow S_1$ absorption band in DCM shows a dominant contribution from the SF of the dye, for which a direct $S_0 \rightarrow S_1$ 2PA transition is not allowed by symmetry. Therefore, the main channel for the observed 2PA spectrum in the $S_0 \rightarrow S_1$ spectral region for DCM solutions can be attributed to electron-vibration coupling [126]. Accordingly, the experimental 2PA spectrum in DCM, shown in Figure 4.22, is blue-shifted with respect to twice the wavelength of the corresponding 1PA peak. The structure of the 2PA band is fairly complex, suggesting the possible involvement of several vibrational modes. There are 3 peaks in this 2PA spectrum; one roughly corresponds to a vibrational shoulder in the 1PA band (skeleton vibration of ≈1200 cm^{-1}), which is typical for polymethine molecules; and two

additional peaks corresponding to vibrational modes of 700–800 cm^{-1} not resolved in the 1PA spectrum.

Linear absorption spectrum of JB17-08 in ACN points to the dynamical co-existence in solution of the symmetric (SF) and asymmetric forms (ASF) of this dye, as shown in Figure 4.20 b. There are two leading factors responsible for the 2PA band observed in ACN. For SF form, the 2PA is originated vibronic-coupling, similar to that in DCM. For ASF, the lowered symmetry makes the 2PA transition allowed in the 1PA band of ASF (red area of Figure 4.20b), due to the variation of the permanent dipole moment ($\Delta\mu$), which is similar to dipolar dyes. Therefore, the 2PA band of JB17-08 in ACN has a mixed contribution from both SF and ASF.

The shape of ESA spectra is measured by the femtosecond white-light-continuum (WLC) pump-probe technique described in Section 3.3.4. To build a significant population in the first excited state in ACN solution, the pump wavelength is set at the peak of 1PA (peak of SF absorption). The lifetime of the 1^{st} excited state is measured to be 28 ± 2 ps (shown in the inset of Figure 4.25b). The shape of ESA spectrum in DCM is the same as that in ACN (not shown). In ACN solution, where JB17-08 shows the strongest SB effect, another ESA spectrum was also measured by pumping at 900 nm, i.e. in the peak of absorption corresponding to the ASF. To obtain quantitative values for the ESA cross section, additional independent Z-scan measurements at 600 nm are performed using a picosecond pump pulse as shown in Figure 4.25a. The pulsewidth is 13 ps (FWHM) measured independently by second-harmonic autocorrelation. A reference material, CS_2, is used via closed-aperture Z-scan to calibrate the spot size (12.25 μm, $HW1/e^2M$) in the focus and verify the pulsewidth of the Z-scan setup. For each sample, Z-scan measurements are performed with several different input energies, and the fitting is based on a three-level model using the rate and propagation equations shown below:

$$\frac{dI}{dz} = -\sigma_{01}N_0 I - \sigma_{1n}N_1 I$$
$$\frac{dN_0}{dt} = -\frac{\sigma_{01}N_0 I}{\hbar\omega} + \frac{N_1}{\tau_F}$$
$$\frac{dN_1}{dt} = \frac{\sigma_{01}N_0 I}{\hbar\omega} - \frac{N_1}{\tau_F} - \frac{\sigma_{1n}N_1 I}{\hbar\omega} + \frac{N_n}{\tau_{n1}} \qquad (4.1)$$
$$\frac{dN_n}{dt} = \frac{\sigma_{1n}N_1 I}{\hbar\omega} - \frac{N_n}{\tau_{n1}}$$

where I is the irradiance of the input pulse (Fresnel reflections included) as a function of the penetration depth z; τ_F and τ_{n1} are the lifetimes of the first and higher lying excited states; N_0, N_1, N_n are the population densities of the ground, first excited and higher-lying excited states, respectively. The fitting for different energies yield to a single set of parameters: σ_{1n}=77 ±10 ×10^{-17} cm^2, ~25× larger than ground state absorption cross section σ_{01} = 3.17 ×10^{-17} cm^2, with τ_{n1}=5 ±1 ps. The results of ESA cross section spectra and Z-scan traces are shown in Figure 4.25 a and b.

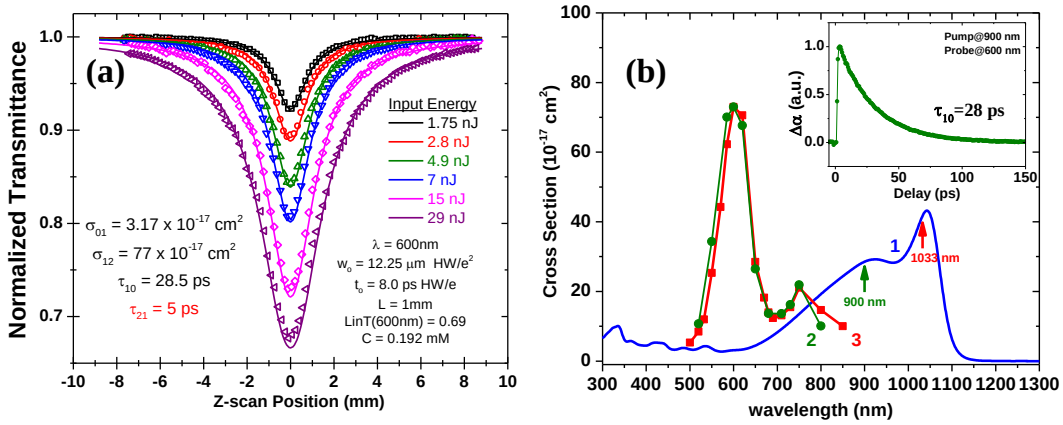

Figure 4.25: (a) Picosecond Z-scans of JB17-08 in ACN to determine the ESA cross section value at 600 nm. (b) Linear absorption (1) and ESA spectra of JB17-08 in ACN at the excitation into the peak of the ASF, 900 nm (2) and at the excitation into the peak of the SF, 1033 nm (3). The inset shows a decay of the first excited state: τ_F =28 ± 2 ps

ESA spectra measured in ACN upon excitation at the maximum of the ASF absorption band (curve 2 in Figure 4.25b) and at the maximum of the SF absorption band (curve 3) are practically coincident, confirming that the same *relaxed* excited-state geometry is reached after excitation to either the SF or ASF form.

4.7.4 Quantum Chemical Analysis for SB Effect

This section will summarize the quantum chemical calculation analysis, which is completely performed by Dr. Olga Przhonska and colleagues at the Institute of Physics and the Institute of Organic Chemistry, National Academy of Sciences in Kiev, Ukraine. The intent of this section is to demonstrate the influence of SB upon the BLA and charge alternations along the conjugation chain of the PDs. More details should refer to ref 127.

Calculations are performed for the series of dyes with n = 1 to 5 in *vacuum*. For simplicity, all molecular structures are considered with the open polymethine chains without bridges. As was shown by us earlier, cyclization of the part of the chain by a six-membered (trimethylene) bridge does not cause considerable distortion of the ground state geometry as compare to unsubstituted chromophore, and does not protect the dye structure from ground state symmetry breaking [128].

Ground state geometry optimization is performed by *ab initio* method (RHF/6-31G**) using the standard program package Gaussian 2003 [129]. The electronic transitions are calculated by semi-empirical ZINDO/S and, for comparison, by TD DFT methods. Both methods give a considerable divergence between the calculated and experimental data, which is known for the long linear conjugated systems, especially polymethine dyes absorbing in the NIR spectral

region [38,130]. However, both methods give the same order of the molecular orbitals (MOs) and same charge distributions within them resulting in the same order and same nature of the electronic transitions.

With optimized molecular geometry, the BLA, represented by the difference between the neighboring CC bonds, can be characterized by Δl_ν function: $\Delta l_\nu = (-1)^\nu (l_\nu - l_{\nu+1})$, where l_ν is a length of the ν-th carbon bond [115]. This parameter Δl_ν can be used for characterization of the shape and location of the BLA wave (also called as geometrical soliton [115]). Sometimes, it is convenient to describe these waves by their modulus (or scalar values): $|\Delta l_\nu| = |l_{\nu+1} - l_\nu|$. The calculated BLA functions for a series of 2-azaalulene dyes with n = 1 – 5 are presented in Figure 4.26.

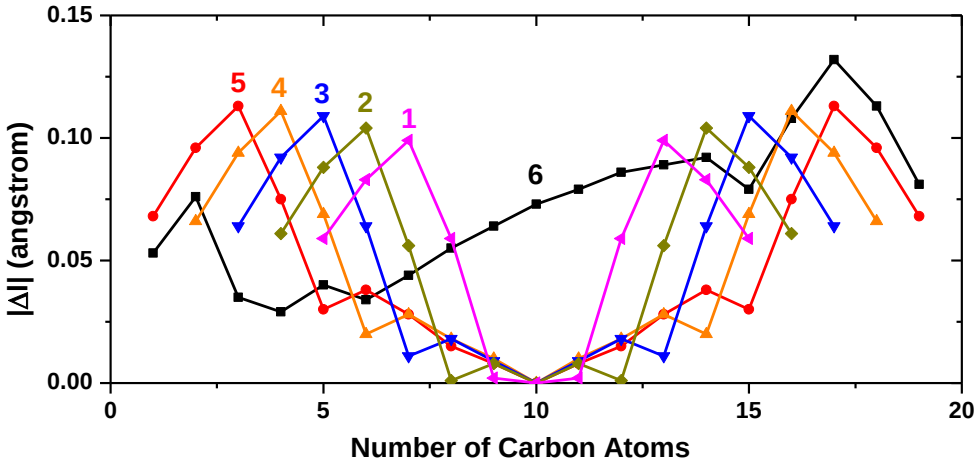

Figure 4.26: |Δl| functions for 2-azaalulene dyes with n = 1 (curve 1), 2 (curve 2), 3 (curve 3), 4 (curve 4) and 5 (symmetrical form - curve 5; asymmetrical form - curve 6). The bonds numbering corresponds to the longest chain n = 5. For comparison, all other molecules are placed into the center (labeled as 10)

It is seen that the difference in the bond lengths is minimal in the center of the chromophore; however the lengthening of the polymethine chain is accompanied by a regular

increase of the $|\Delta l_v|$ function near the end groups. Calculations indicate a significant degree of BLA within the heterocyclic end groups, which are similar in all dyes in this series. For n=1 to n=4, BLA is symmetrical with respect to the molecular center, indicating the absence of SB. However, at n = 5, calculation shows appearance of asymmetrical form with considerable BLA (curve 6, Figure 4.26) along the polymethine chain increasing from one end group to another, indicating dramatic change of molecular geometry, i.e. strong SB effect. Note that for the molecule with n=5, we compare asymmetrical form (curve 6 in Figure 4.26) with the symmetrical form (curve 5 in Figure 4.26), which is *hypothetically* constructed by introducing two additional CH-groups to the chain center into the optimized molecular geometry of previous vinilog with n=4 (without BLA). The practice is also repeated in the calculation of charge alternation along conjugation chain as discussed below. Similar BLA, which we observe for the dye with symmetrical molecular structure and n=5, is typically observed for the dyes with the different end groups, and in this case $|\Delta l_v|$ function increases from the end group with the stronger donor ability to the group with the weaker donor strength [131].

It is well known that all polymethine dyes are characterized by a considerable alternation of the charge magnitudes at neighboring carbon atoms within the conjugated chain [131]. For symmetrical 2-azaazulene dyes with n = 1 to n=3 it is confirmed experimentally with ^{13}C NMR spectroscopy. Similar to the BLA function, the difference of the electron densities at the neighboring carbon atoms μ and $\mu+1$ can be characterized by charge alternation function Δq_μ, which can be calculated as: $\Delta q_\mu = (-1)^\mu (q_\mu - q_{\mu+1})$, where q_μ is traditional Mulliken atomic electron density [116]. This parameter Δq_μ (or, sometimes, its scalar value $|\Delta q_\mu|$) presents a useful way to visualize the charge distribution in π-systems.

Figure 4.27a, represents the ground state charge alternation functions Δq for a series of 2-azaazulene dyes with n = 1 – 5. It is seen that for n=1 to n=4, the shapes of Δq functions show symmetrical structures, which are almost insensitive to a length of chromophore: there are constant Δq values along the chain, two degenerate maxima at the carbon atoms connecting each terminal residue with the polymethine chain, and essential decrease of Δq values within the end groups. Correspondingly, at n=5, calculation shows asymmetrical structure of Δq function (curve 6, Figure 4.27a), which changes considerably along the polymethine chain from one end group to another. Note that curves 5 in Figure 4.27a and b are constructed for the hypothetical symmetrical form for comparison purpose.

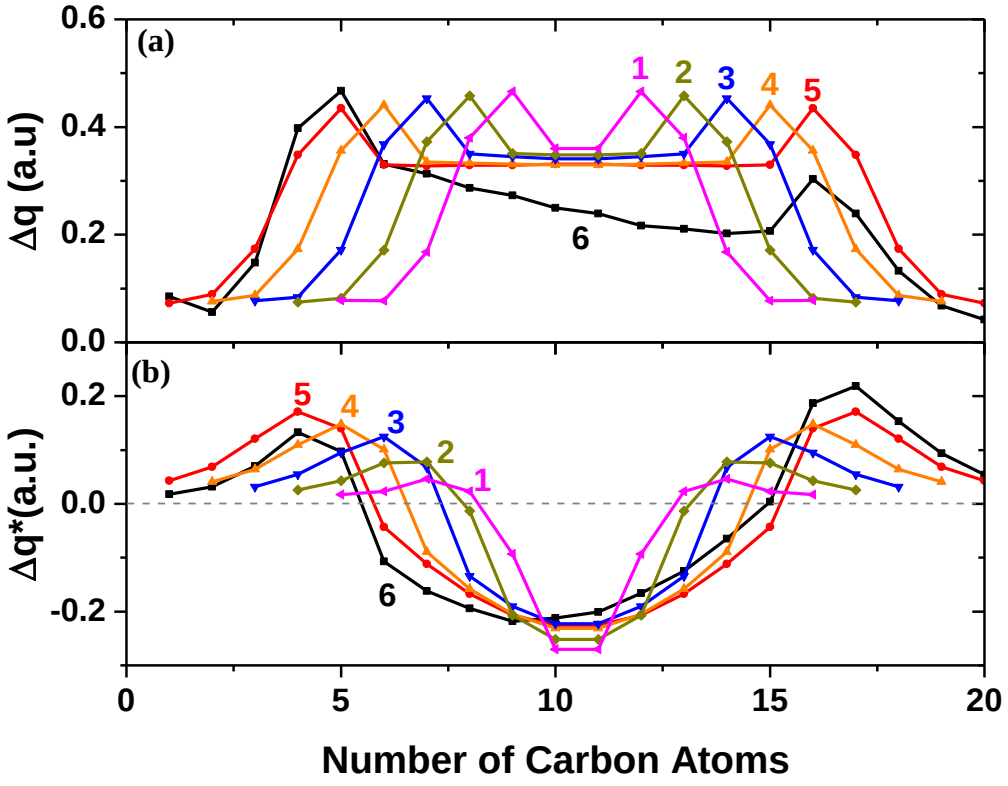

Figure 4.27: Δq functions of 2-azaalulene dyes with n = 1 (curve 1), 2 (curve 2), 3 (curve 3), 4 (curve 4) and 5 (symmetrical form - curve 5; asymmetrical form - curve 6) in the ground (a) and excited (b) states. The bonds numbering corresponds to the longest chain n = 5. For comparison, all other molecules are placed into the center (labeled as 10)

Figure 4.27b represents the excited state charge distribution functions Δq^* for a series of 2-azaazulene dyes with n = 1 – 5, while keeping Franck-Condon geometry corresponding to unchanged ground state geometry. It is seen that the molecular backbone can be divided into three parts accordingly to the order of the charge redistribution function after the excitation. Charge alternation within end groups is characterized by the same order as the ground state charge alternation, however, with a considerable decrease in charge alternation amplitude.

Charge alternation within the polymethine chain is characterized by the opposite order as compare to the ground state Δq function and also smaller charge alternation magnitude similar to traditional polymethine dyes [132]. More detailed analysis shows that the lengthening of the chain is accompanied by a regular increase of the part with the opposite charge alternation. It is important to compare the ground- and excited state charge distributions for asymmetrical form (dye with n = 5). If a ground state Δq function shows an asymmetrical behavior with a considerable change along the chain from one end group to another (Figure 4.27a, curve 6), the excited state Δq^* function (curve 6, Figure 4.27b) is almost symmetrical. Therefore, we can conclude that after the excitation, the difference between asymmetrical and symmetrical forms becomes much smaller. This effect of excited state symmetrization is confirmed experimentally by the narrow fluorescence shapes which are independent on the solvent polarity (see Figure 4.21b) and is in accord with the theoretical model proposed by F. Terenziani and A. Painelli for quadrupolar chromophores [86,119] as discussed in next section.

As a summary, quantum chemical calculations show that for dye in *vacuum* condition, the SB effect takes place at n=5; however, our experimental results demonstrate that in polar solvents symmetry breaks earlier, at n=3. Absorption spectrum shown in Figure 4.20a for the dye JB17-08 clearly reveals a coexistence of the forms with the symmetrical and asymmetrical charge distribution and bond length equalization and alternation, correspondingly.

4.7.5 Essential-state Model for SB Effect

This section will summarize the essential-state model analysis, which is completely performed by Drs. Francesca Terenziani and Anna Painelli from Dipartimento di Chimica GIAF

and INSTM UdR-Parma, Universit à di Parma, Parma, Italy. The intent of this section is to rationalize symmetry breaking of long PDs in polar solvents and allow their low-energy spectral features to be quantitatively reproduced in terms of a minimal set of model parameters. The detail of derivation is out of the scope of this dissertation. More detailed information should refer to ref. 119,133.

The main resonance structures for JB17-08 dye can be schematically represented as D^+-π-D ↔ D-π^+-D ↔ D-π-D^+, where D stands for the terminal (donor) group and π for the polymethine chain. The two equivalent structures with the charge located on either one of the two molecular end groups drive symmetry breaking in the ground state of PDs. The three main resonating structures, labeled as $Z_1 \leftrightarrow N \leftrightarrow Z_2$, are chosen as basis states in an essential state approach. The two degenerate states Z_1 and Z_2 are separated by an energy gap 2η from state N, and the resonance integral τ mixes Z_1 and Z_2 with N. Symmetry-adapted basis states are conveniently introduced as N, $Z_+ = \frac{1}{\sqrt{2}}(Z_1 + Z_2)$ and $Z_- = \frac{1}{\sqrt{2}}(Z_1 - Z_2)$. N and Z_+, to give the ground state $|g\rangle = \sqrt{1-\rho}|N\rangle + \sqrt{\rho}|Z_+\rangle$ and a totally-symmetric excited state $|e'\rangle = \sqrt{1-\rho}|Z_+\rangle - \sqrt{\rho}|N\rangle$, where ρ is the weight of Z_+ in the ground state, i.e. it represents the degree of symmetric quadrupolar charge separation in the ground state. The third antisymmetric state, $|e\rangle = |Z_-\rangle$, stays unmixed. Note that the $|e'\rangle$ state is higher in energy than the $|e\rangle$ state. Parameter ρ measures weight of Z_+ in the ground state, corresponding to quadrupolar character of the ground state. Explicit expressions for ρ and for the energies of these three electronic states as functions of η and τ are given in ref. 119. Since Z_1 and Z_2 represent two opposite resonance structures of the molecule, they have a large dipole moment of equal magnitude, μ_0, and opposite

direction, $\mu_0 = \langle Z_+ | \hat{\mu} | Z_- \rangle = \langle Z_- | \hat{\mu} | Z_+ \rangle$. The lowest-energy $g \rightarrow c$ transition (corresponding to $S_0 \rightarrow S_1$) is one-photon allowed with $\mu_{gc} = \mu_0 \sqrt{\rho}$ but is 2PA forbidden. The higher-energy transition $g \rightarrow e'$ ($S_0 \rightarrow S_n$) is allowed in 2PA, even if it is experimentally masked by coincidence with the 1PA resonance. The $e \rightarrow e'$ transition ($S_1 \rightarrow S_n$) is an ESA transition with a transition dipole moment $\mu_{ee'} = \mu_0 \sqrt{1-\rho}$.

In addition to these three electronic states, equally important is the coupling between electronic and vibrational degrees of freedom related to the readjustment of molecular geometry according to the charge distribution along the molecular backbone [119]. Therefore the proposed essential-state model also introduces two effective molecular coordinates, Q_+ and Q_-, which are taken into account for the relaxation of the molecular geometry upon excitation. These two coordinates have harmonic frequencies, $\omega_\pm$, and relaxation energies $\varepsilon_\pm$. Finally, polar solvation is described by the reaction electric field, F_{or}, whose equilibrium value is proportional to the dipole moment of the solute. It is generated at the solute location by the reorientation of polar solvent molecules around the solute. The total Hamiltonian H can be expressed as [119]:

$$H = \begin{pmatrix} 0 & -\sqrt{2}\tau & 0 \\ -\sqrt{2}\tau & 2\eta - \sqrt{\varepsilon_+}\omega_+ Q_+ & -\sqrt{\varepsilon_-}\omega_- Q_- - \mu_0 F_{or} \\ 0 & -\sqrt{\varepsilon_-}\omega_- Q_- - \mu_0 F_{or} & 2\eta - \sqrt{\varepsilon_+}\omega_+ Q_+ \end{pmatrix} + \frac{P_+^2 + \omega_+^2 Q_+^2}{2} + \frac{P_-^2 + \omega_-^2 Q_-^2}{2} + \frac{\mu_0^2 F_{or}^2}{4\varepsilon_{or}} \quad (4.2)$$

Where the first term is the Hamiltonian related to electronic transition, and the second and third terms are the harmonic oscillator Hamiltonians relevant to Q_+ and Q_- (P_+ and P_- are the conjugate momenta). The last term is the elastic energy associated with the reaction field. ε_{or}

measures the relaxation energy, i.e. the energy gained by solvent relaxation after the vertical excitation process. The stronger solvent polarity leads to larger ε_{or}.

By applying adiabatic approximation to F_{or}, whose dynamics are governed by the slow rotation of solvent molecules and associated with a thermal distribution, F_{or} becomes a classical variable and the Hamiltonian H in Equation 4.2 can be numerically solved on a grid of F_{or} values. For each F_{or} value, vibronic eigenstates can be obtained which is used to calculate the corresponding optical spectra [134]. A fixed intrinsic bandwidth 2Γ (FWHM) is assigned to each eigenstate (corresponding to a width $\sigma = \Gamma / \sqrt{2\ln 2}$ in the case of Gaussian bandshapes). Spectra measured in solution are finally obtained as thermal averages of spectra calculated for different F_{or}. Specifically, 1PA and 2PA spectra are averaged assuming a Boltzmann distribution based on the F_{or}-dependent ground state energy, while fluorescence and ESA spectra are averaged over the Bolzmann distribution related to the excited state. Details of the calculation should be referred to refs. 119 and 133.

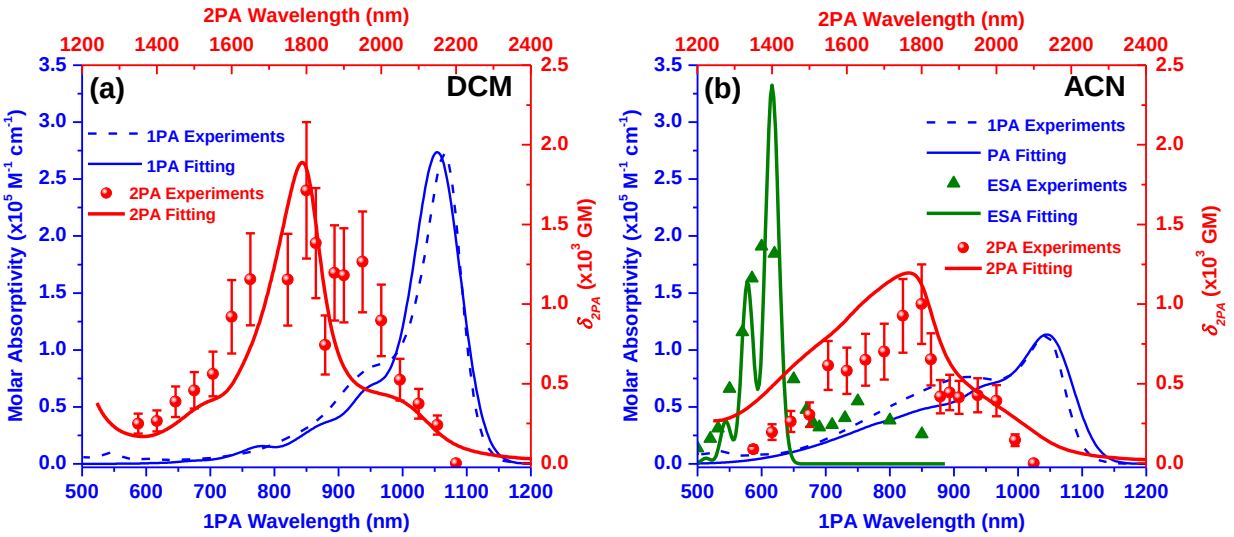

Figure 4.28: 1PA (blue), 2PA (red) and ESA (green, only for ACN solution) spectra calculated by essential-state model fitting using molecular parameters in Table 4.5 compared to the experimental results in DCM (a) and ACN (b)

The calculated spectra, presented in Figure 4.28a and b, are obtained with the optimized model parameters reported in Table 4.5. All molecular parameters, including the electronic parameters, η, τ and μ_0, the vibrational frequencies $\omega_{\pm}$, relaxation energies $\varepsilon_{\pm}$ and the bandwidth Γ, are strictly solvent-independent. Only the solvent relaxation energy, ε_{or}, is tuned to account for increasing solvent polarity from DCM to ACN. Calculated spectra quantitatively reproduce experimental spectra, a non-trivial result in view of the modest number of adjustable model parameters and of the complex spectral behavior of JB17-08.

Table 4.5: Parameters of the essential-state model for JB17-08

τ	η	ω_+	ω_-	ε_+	ε_-	$\varepsilon_{or}(DCM/ACN)$	Γ	μ_0
eV	eV	eV	eV	eV	eV	eV	eV	D
1.07	-0.32	0.13	0.18	0.37	0.45	0.23 / 0.35	0.04	24.5

The ground-state potential energy as the function of F_{or}, calculated with the model parameters in Table 4.5, is shown in Figure 4.29a and b in DCM and ACN. In DCM, the ground-state shows a single minimum at $F_{or}=0$; while in ACN, the ground state energy shows a double minimum located at finite (equal but opposite) F_{or} values. Due to thermal disorder, the solution can be described as a collection of solute molecules, each one being surrounded by different environment induced from solvent molecules, i.e. experiencing different F_{or}. Therefore, the probability distribution of F_{or}, as shown in Figure 4.29a and b, determines the position of ground state and hence the status of symmetry breaking of the solute molecules. In the hypothetical zero-temperature limit, for solution in DCM, all the molecules would be located in the single minimum of the energy curve, corresponding to all molecules in SF form at $F_{or}=0$, i.e. no symmetry breaking. The calculated main 1PA band, as shown in Figure 4.29c, is dominated by the 0-0 transition, which is strictly forbidden by 2PA. Note that the small 1PA band at the blue side of the 1PA peak is due to symmetrical-vibrational mode (Q_+ in Equation 4.2). The 2PA band is originated from the vibronic-coupling into the anti-symmetrical vibrational mode (Q_- in Equation 4.2). For ACN solution, all molecules would be located in either one of the two minima, as shown in Figure 4.29b at zero-temperature, i.e. all molecules are ground state symmetry broken. The calculated 1PA bands, as shown in Figure 4.29d, demonstrate a well-resolved vibronic structure with maximum intensity for the 0-0 transition. Since all the molecules are in ASF form, D-term ($\Delta\mu\neq0$, Equation 2.28) is not zero and thus 2PA transition into 1PA main band is allowed.

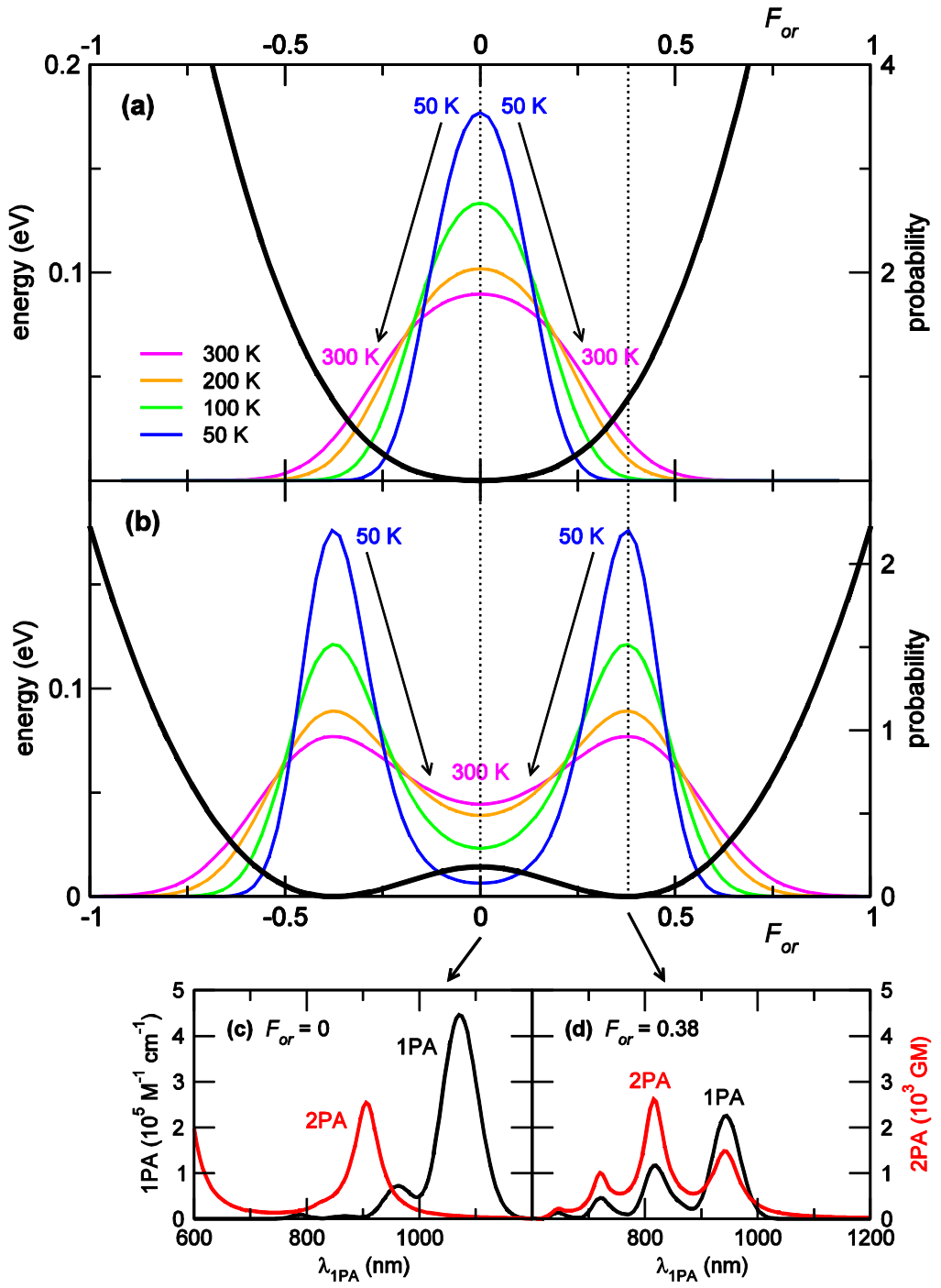

Figure 4.29: Top: Parts (a) and (b): calculated ground state energy (black thick line) vs the solvation reaction field F_{or} for the low-polarity solvent (a, ε_{or} = 0.23 eV) and for the high-polarity solvent (b, ε_{or} = 0.35 eV); Boltzmann probability distributions of the reaction field (based on the ground-state energy) at different temperatures (see legend). Bottom: 1PA (black) and 2PA (red) spectra calculated for (c) F_{or} = 0, and (d) for the F_{or} value corresponding to the energy minima of b

At any finite temperature, a *continuous* distribution of the reaction field is calculated according to the Boltzmann law for DCM and ACN solutions, respectively, and for a few selected temperatures, as shown in Figure 4.29a and b. The 1PA and 2PA spectra are calculated as the weighted sum of spectra relevant to different F_{or} (Figure 4.30). The increase of temperature leads to a broadening of the probability distribution of F_{or}. In DCM, the maximum probability is still at F_{or}=0, indicating no ground state symmetry breaking, except a slight increase of the population experiencing a sizable F_{or}. However, in ACN solution at 300 K, despite the maximum probability of F_{or} is found at the minimum ground state energy of finite F_{or} values (ASF), the relatively large probability at F_{or} = 0 indicates significant population of SF, confirming the coexistence of SF and ASF forms in ACN solution. This observation is also consistent with the temperature evolution of the calculated 1PA and 2PA spectra as shown in Figure 4.30. For DCM solution of which the ground state symmetry is still maintained for solute molecules, an increase of the temperature only induces slight spectral broadening of the 1PA and 2PA spectra (Figure 4.30a). In contrary, in ACN solution, the temperature increase leads to a significant red shift of the 1PA and 2PA spectra, and to the spectral bandwidth broadening (Figure 4.30b).

To explain the identical shapes of the ESA spectra in ACN with different excitation wavelengths, i.e. to the absorption peaks of SF and ASF form, respectively, Figure 4.30c shows the potential energy of the ground state, of the 1st excited state ($|e\rangle$, responsible for fluorescence and ESA), and of the higher-lying excited state ($|e'\rangle$, reached by ESA), calculated as a function of F_{or} for model parameters relevant to the ACN solution. Only the ground state energy shows double minimum at a finite F_{or} value, while for $|e\rangle$ and $|e'\rangle$, both energy curves show a single minimum at F_{or} = 0. As a result, the distribution probability of F_{or} shows a single minimum in

the 1st excited state $|e>$, despite the double peak distribution probability of F_{or} in the ground state. This calculation result indicates that the symmetry is maintained in the 1st excited and higher excited states, which explains the identical ESA spectra obtained at different excitation wavelengths and corresponding to 1PA transition between the single minimum of the 1st excited state $|e>$, and higher excited state $|e'>$.

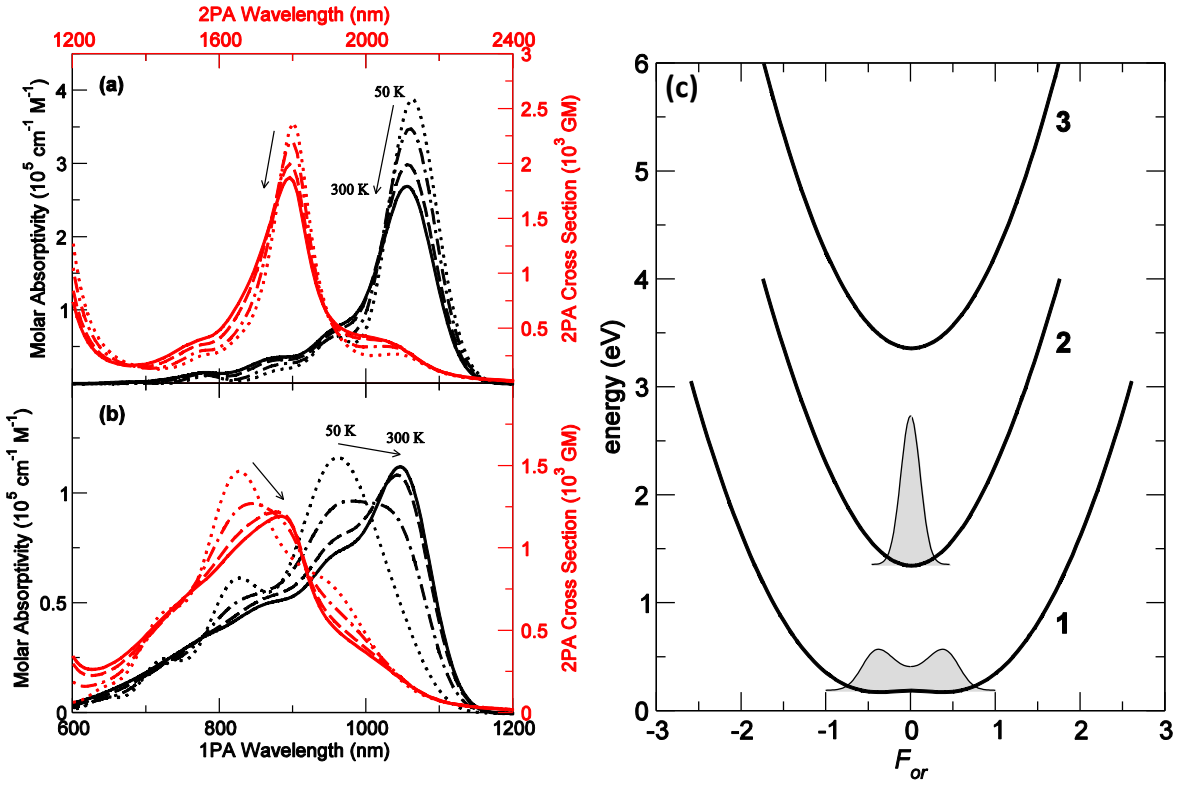

Figure 4.30: 1PA (black lines) and 2PA (red lines) spectra calculated at T = 300, 200, 100 and 50 K (in the order indicated by the arrows) in DCM (a, ε_{or} = 0.23 eV,) and ACN (b, ε_{or} = 0.35 eV). (c) calculated energies of the ground state (1), the 1st excited state (2), and higher excited state (3) as the function of F_{or} in ACN solution (ε_{or} = 0.35 eV). The shadowed areas represent the probability distribution of F_{or} according to the Boltzmann law.

4.8 From a Two-photon Absorber to a Two-photon Photosensitizer – Comparison of 2PA Properties between Oxygen-squaraines and Sulfur-squaraines

It is well known that oxygen-squaraine (O-SD), with an electron acceptor (C_4O_2) inserted into the center of the conjugation chain, is a good 2PA absorber. Up to 30,000 GM δ_{2PA} is observed for some extended squaraines [24]. The reasons for the large δ_{2PA} are: 1) the introduction of the acceptor group increases the density of states available for 2PA transitions; 2) the relatively narrow 1PA band allows tuning the incident photon energy close to the S_1 state, thus leading to strong ISRE [73]. However, as a common feature for polymethine (or polymethine-like) dyes, O-SDs usually have very small intersystem crossing (ISC) rate, leading to relatively small triplet quantum yield, Φ_T, defined by

$$\phi_T = \frac{k_{ISC}}{k_{S10} + k_{ISC}} \qquad (4.3)$$

where k_{ISC} (ISC rate) is defined as the rate of S_1 state to the 1st triplet state transition; and k_{S10} is the rate of S_1 to S_0 transition in the absence of intersystem crossing. This small Φ_T for the polymethine (-like) dyes is primarily due to a large splitting energy between 1st singlet excited state (i.e. S_1 state), and 1st triplet state, labeled as T_1 state [135,136], as shown in Figure 4.31a. To remedy this problem, a molecular design approach to enhance ISC is proposed by Webster *et al* [85] to insert a lower-lying n→π* transition under the singlet π→π* transitions (shown in Figure 4.31b) to reduce the *energy difference* between singlet and triplet states. Such inversion of low lying π→π* transition with n→π* transition can be realized by replacing the oxygen atoms in the electron acceptor bridge (C_4O_2) by sulfur atoms. This approach is successfully applied to synthesize a sufur-squaraine molecule S-SD 7805 as opposed to its oxygen-squaraine counterpart

O-SD 2405: a dramatic enhancement of Φ_T is observed from essentially zero (for O-SD 2405) to unity (for S-SD7805) measured by double pump-probe technique [85]. Similar practice is also applied to synthesize SO-SD 7517 (one oxygen and one sulfur atoms) as compared O-SD 2053: the increase of Φ_T is from zero (for O-SD 2053) to 0.64 (for SO-SD 7517). The molecular structures of O-SD 2405, S-SD7805, O-SD 2053 and SO-SD 7517 are shown in Figure 4.5. The large Φ_T in S- (or SO-) squaraines makes them excellent *photosensitizers* to generate singlet molecular oxygen O_2 (a $^1\Delta_g$), which is known to be important for many photochemical and photobiological processes, especially for photodynamic therapy (PDT) [137,138].

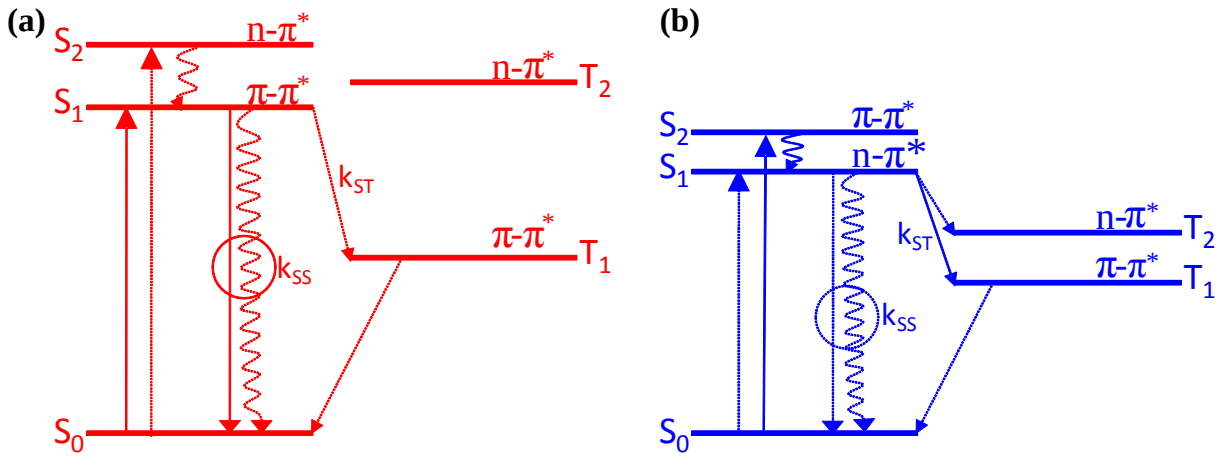

Figure 4.31: Schematic of energy level structures and transitions of O-SD (a) and S-SD (b). Reprinted with permission from ref. 85. Copyright 2010 American Chemical Society.

For two-photon PDT treatment, it is desirable to combine the large Φ_T (good photosensitizer) with the large δ_{2PA} (good 2PA absorber): in this case the effect can be achieved by illuminating a molecular sensitizer by an appropriate wavelength with a deep penetration depth [139]. In this section, we will compare of two groups of oxygen- and sulfur squaraine dyes: O-SD 2405 vs S-SD 7508, and O-SD 2053 vs SO-SD 7517, to study the role of the sulfur atom

replacements on the linear and 2PA properties. Note that the details about triplet state properties of these groups of dye can be found in the dissertation of Davorin Pecili from the NLO group.

4.8.1 The Comparison of Linear Optical Properties between O-SD and S-SD (SO-SD)

The comparison of linear absorption spectra of O-SD 2405 *vs* S-SD 7508, and O-SD 2053 *vs* SO-SD 7517 in toluene is shown in Figure 4.32a and b. The main linear molecular parameters are listed in Table 4.6. The replacement of both oxygen atoms by sulfurs leads to a red shift of the main absorption peak by 41 nm from O-SD 2405 to S-SD 7508; while only by 19 nm from O-SD 2053 to SO-SD 7517 (only one oxygen atom being replaced by sulfur). Both O-SDs show relatively large ground-to-excited-state transition dipole moments (μ_{ge}) of ~13 D. S-SD and SO-SD show slightly smaller μ_{ge} due to a reduced peak molar absorptivity. Compared to its counterpart O-SD 2405, S-SD 7508 shows relatively strong absorption peak at 400 nm and 490 nm, respectively. Similar absorption features at UV and visible wavelength range are also observed for SO-SD 7517 compared to O-SD 2053, however, with slightly smaller molar absorptivity.

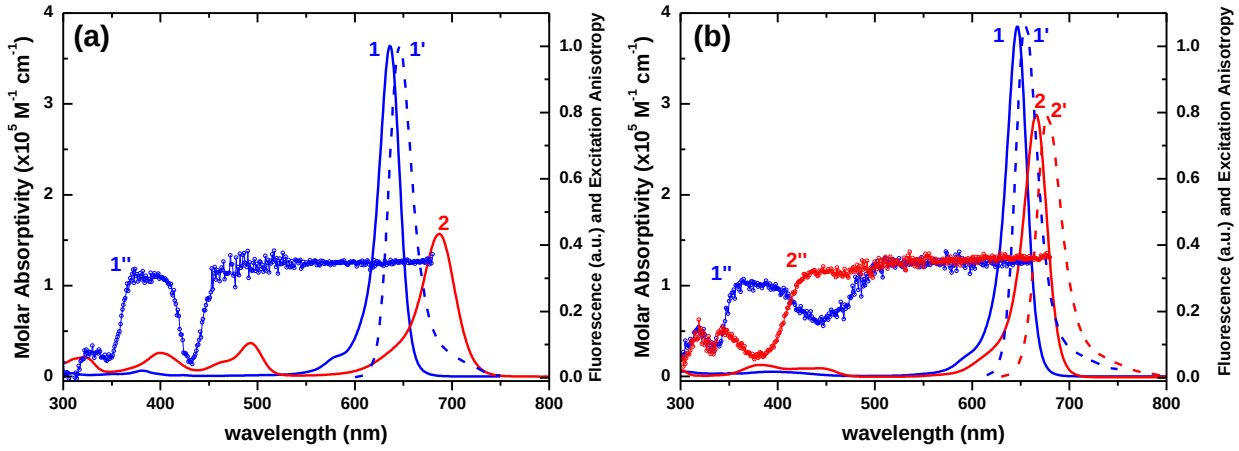

Figure 4.32: (a) Molar absorptivity (1) and fluorescence (1') spectra in toluene and excitation anisotropy (1'') of O-SD 2405 in pTHF, and molar absorptivity (2) spectrum of S-SD 7508 in toluene; (b) molar absorptivity and fluorescence spectra of O-SD 2053 (1, 1') and SO-SD 7517 (2, 2') in toluene; and their excitation anisotropy in pTHF (1'' for O-SD 2053 and 2'' for SD-SD 7517).

The fluorescence spectra of the O-SD 2405 and O-SD 2053 in toluene are shown in Figure 4.32a and b. Both two molecules show narrow fluorescence spectra, close to a mirror image of their corresponding linear absorption bands, with ~10 nm Stokes shifts. The quantum yields, Φ_F, measured against reference molecule Cresyl Violet in methanol (Φ_F =54%), for both two O-SDs are near unity (Φ_F =100%). This is consistent with the extremely small Φ_T for these O-SDs. In contrast, the fluorescence of S-SD 7508 in toluene is extremely small (i.e. Φ_F *<0.001*) beyond the detection limit of our spectrofluorometer, which is in accord with its near unity Φ_T. The fluorescence spectrum SO-SD 7517 in toluene (Φ_F ~28%) is shown in Figure 4.32 b.

Table 4.6: Linear spectroscopic parameters of O-SD 2405, S-SD 7508, O-SD 2053 and SO-SD 7517 in toluene; λ_{abs}^{max} and λ_{FL}^{max}: peak absorption and fluorescence wavelength; ε^{max} peak extinction coefficient; Φ_F : fluorescence quantum yield ; $\tau_{F,1}$: fluorescence lifetime time calculated by equation 3.2; μ_{ge} ground state absorption transition dipole moment calculated from equation 3.1

Dye	λ_{abs}^{max}	λ_{FL}^{max}	ε^{max}	η	$\tau_{F,1}$	μ_{ge}
	nm	*nm*	$10^5 M^{-1} cm^{-1}$		*ns*	*Debye*
O-SD 2405	636	646	3.64	0.95±0.05	2.3±0.2	13.2
S-SD 7508	687	NA	1.57	<0.001	NA	10.5
O-SD 2053	647	654	3.85	0.95±0.05	2.4±.2	13.3
SO-SD 7517	666	677	2.88	0.28±0.02	0.9±0.1	12.1

The fluorescence excitation anisotropy spectra, *r(λ)*, of O-SD 2405, O-SD 2053 and SO-SD 7517 in pTHF are shown in Figure 4.32a and b. For O-SD 2405, *r* is flat with a constant value ~0.35 across the main linear absorption band up to ~480 nm, a valley is observed at ~430 nm with minimum *r* value of ~0.046. The next minimum of *r* is at ~350 nm. Similar structure of anisotropy spectrum is also observed for O-SD 2053: the first minimum is located at 450 nm (*r~0.16*) and the next minimum is located at 335 nm. For SO-SD 7517, the same constant *r* of 0.35 is observed across the main absorption band up to ~450 nm. The first minimum is relative broad with *r*~0.063. It is interesting to note that below 350 nm the anisotropy spectra of O-SD 2053 and SO-SD 7517 overlap each other.

4.8.2 Comparison of 2PA Spectra and Discussions

Due to large Φ_F, the 2PA spectra of O-SDs in toluene can be measured by 2PF technique discussed in Section 3.2.2. Z-scans were also performed to verify the δ_{2PA} measured by 2PF and to complete the 2PA spectrum. However, 2PF technique is not successful in measuring 2PA

spectra of S-SD 7508 and SO-SD 7517 in toluene. For S-SD 7508, the zero Φ_F essentially eliminates the possibility to utilize 2PF technique. Furthermore, for both S-SD 7508 and SO-SD 7517, the dyes are *not* photochemically stable under strong laser irradiation. To overcome this obstacle, we performed single wavelength Z-scans in 1 mm flow cell filled with S-SD 7508 (or SO-SD 7517) solution. The flow rate, controlled by a tube-pump (Masterflex®), is set at ~350mL/min, which is fast enough to avoid dye molecules being exposed to multi-shot excitation. Note that since 2PA is an instantaneous process, the flowing schematic doesn't affect the 2PA signal.

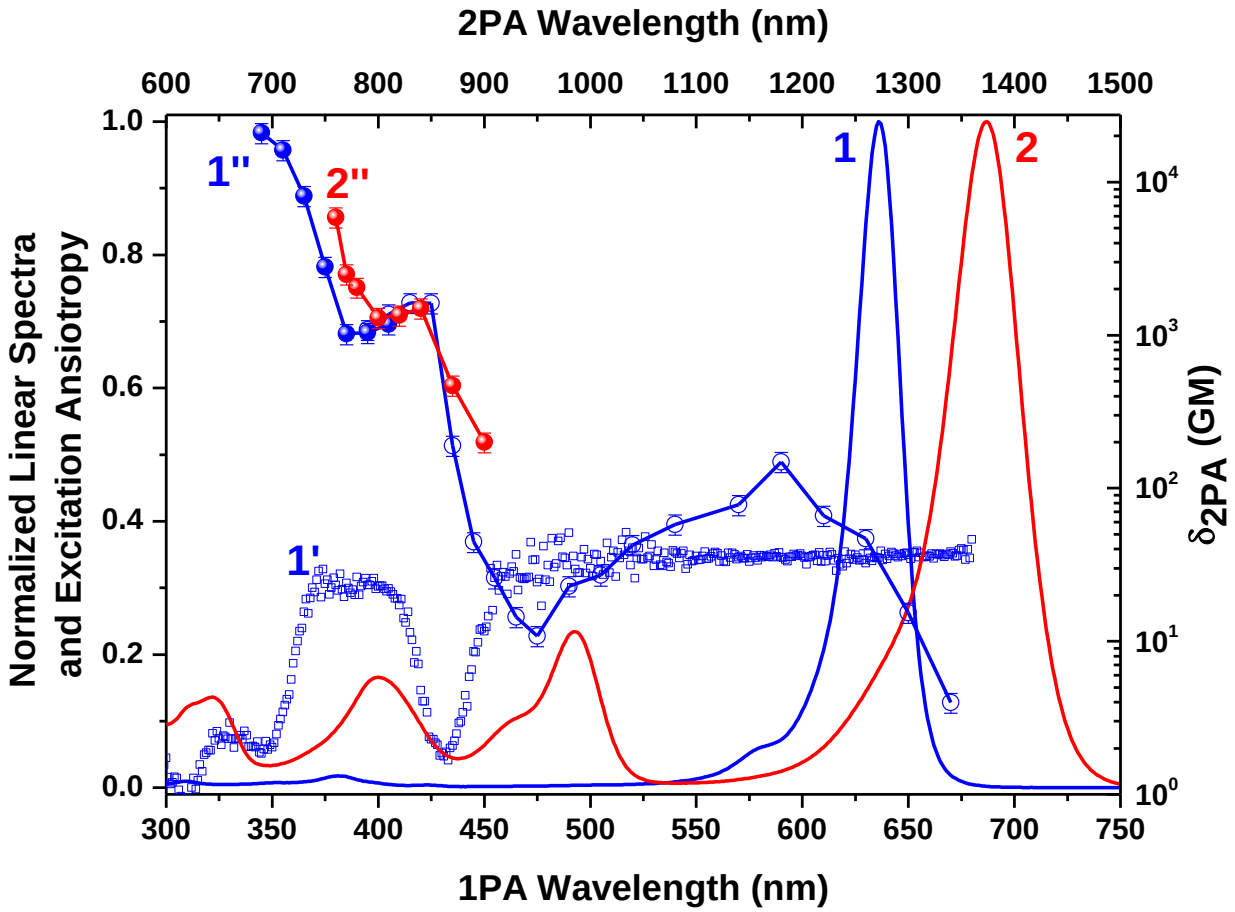

Figure 4.33: Normalized one-photon absorption (1, 2), excitation anisotropy in p-THF (1'), and two-photon absorption spectra (1", 2") for O-SD 2405 (1,1',1") and S-SD 7508 (2, 2"). 2PA data is obtained by both 2PF (blue open squares for SD-O 2405) and open-aperture Z-scan (solid blue circles for SD-O 2405and solid red circles for S-SD 7508)

The 2PA spectra of O-SD 2405 and S-SD 7508 in toluene are shown (in logarithmic scale) in Figure 4.33 along with their linear spectra. O-SD 2405 exhibits three 2PA bands. The first 2PA band (vibronic coupling band) with δ_{2PA}^{max} = 200 GM occurs at an energy "blue-shifted" by ≈1000-1200 cm^{-1} as compared to the peak of the $S_0 \rightarrow S_1$ transition. The positions of the second 2PA band with δ_{2PA}^{max} = 2000 GM (at 850 nm) and the third, strongest 2PA band, with δ_{2PA}^{max} = 15,000 GM (at 700 nm) corresponds to the S_2 and S_4 final states as indicated by anisotropy and

supported by quantum-chemical calculations. The 2PA spectrum of S-SD 7508 is similar to the shape for O-SD 2405 in the range of the second 2PA band; however, the high energy peak cannot be reached due to the ≈40 nm red shift and slight broadening of the linear absorption band. The largest δ_{2PA} = 7000 GM for S-SD 7508 was observed at 760 nm.

The 2PA spectra of O-SD 2053 and SO-SD 7517 in toluene are shown (in logarithmic scale) in Figure 4.34. O-SD 2053 exhibits similar 2PA structures as O-SD 2405: the first 2PA band is located on the vibrational shoulder of the linear 1PA band with δ_{2PA}^{max}= 200 GM. The second 2PA band with δ_{2PA}^{max} = 1200 GM at 840 nm, coincides with the valley of anisotropy, corresponding to the S_2 final state. The third 2PA band of O-SD 2053, however, cannot be resolved due to the presence of linear absorption edge. More interesting is the complete 2PA spectrum of SO-SD 7517 showing similar 2PA shape as O-SD 2053. The largest δ_{2PA}=1660 GM is observed at 760 nm. Incidentally, at wavelengths close to linear absorption edge, S-SD (or SO-SD) shows slightly larger δ_{2PA} than its O-SD counterpart. Assuming the S_1 state is the intermediate state for all dyes, this enhancement of δ_{2PA} can be attributed to the red-shift of the linear absorption peak leading to smaller detuning energy and thus ISRE.

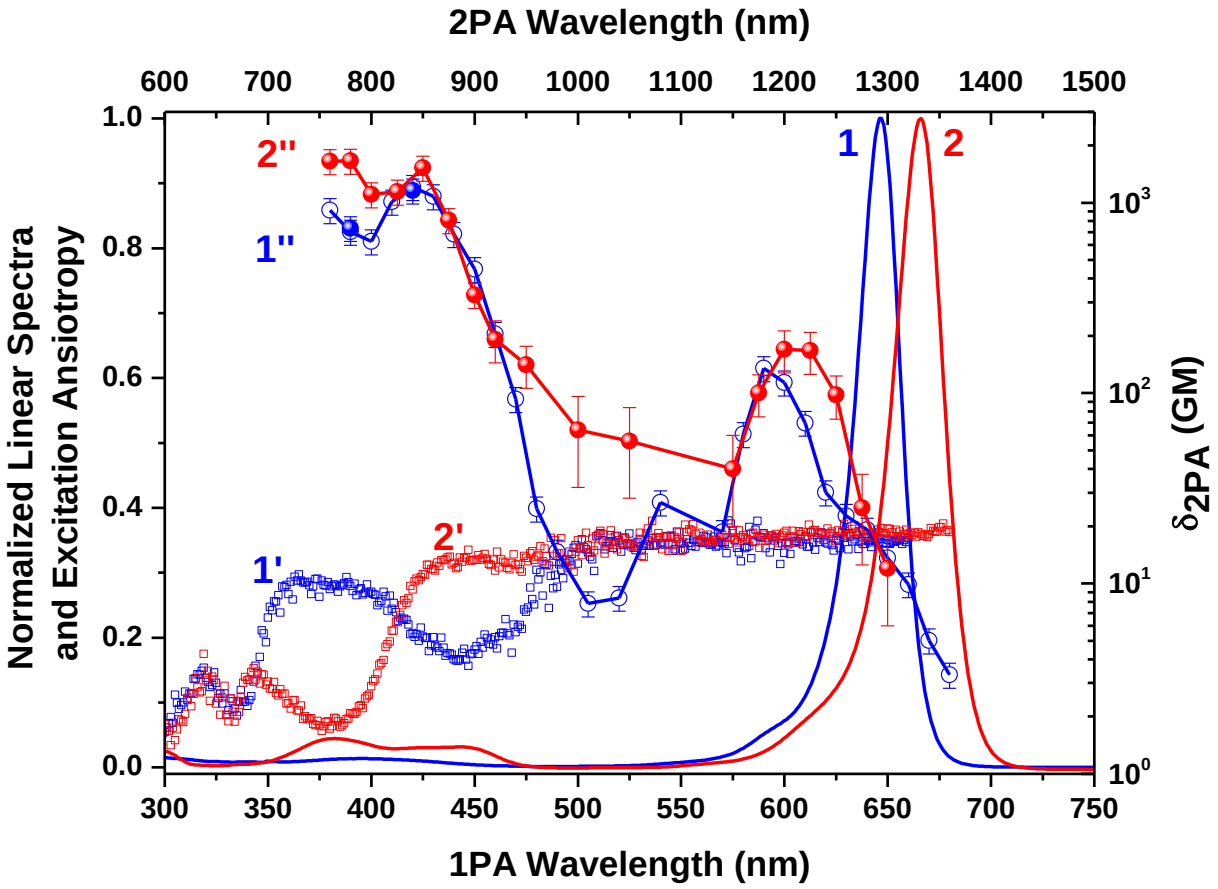

Figure 4.34: Normalized one-photon absorption (1, 2), excitation anisotropy in p-THF (1', 2'), and two-photon absorption spectra (1", 2") for O-SD 2053 (1,1',1") and SO-SD 7517 (2, 2', 2"). 2PA data is obtained by both 2PF (blue open circle for O-SD 2053) and open-aperture Z-scan (solid blue circles for O-SD 2053 and solid red circles for SO-SD 7517)

Based on quantum chemical calculations, it is known that a squaraine molecule consists of two *perpendicular* π-conjugated systems [85]: one is placed along the main conjugation backbone and the other is placed in the vertical plane between two oxygen (or sulfur) atoms. Although the replacement of oxygen atom by sulfur generates a low-lying n→π* transition below π→π* transition, which mixes singlet and triplet states of different nature and thus

effectively enhances the intersystem crossing rate; the direction of transition is orthogonal to the main conjugation chain [85]. It is known that the transitions along the main conjugation chain are responsible for the 2PA transition of squaraine dyes [32,73]; the replacement of oxygen by sulfur atoms on the central-bridge only affects the transitions which are perpendicular to the main conjugation chain and thus show minimum influence on the 2PA spectrum of S-SD (or SO-SD) compared to its O-SD counterparts. .

4.8.3 Singlet Molecular Oxygen Generation via Two-photon Absorption

It is well known that the generation of singlet O_2 can be visualized by a direct measurement of singlet O_2 luminescence at ≈1270 nm [140]. The experiment is performed in S-SD 7508 in air-saturated ACN solution at room temperature using PTI spectrofluorometer with a NIR PMT (discussed in Section 3.1) detector at steady-state regime. For the two-photon excited singlet oxygen luminescence, the pump is a 140 fs (FWHM) laser at 780 nm (fundamental laser) and 1kHz repetition rate. Figure 4.35 shows the dependence of the luminescence signal as a function of the pump energy. The linear fit for the 3 lowest pump energy (both in logarithmic scale) shows slope ~ 2.0 indicating the two-photon induced luminescence. The higher energy point falls below the fitting line due to saturation of the photomultiplier tube. The merit parameter for PDT, which describes the molecular ability to generate singlet O_2, is the product of the 2PA cross section and quantum yield of singlet O_2 generation (labeled as Φ_Δ), $\delta_{2PA} \times \Phi_\Delta$. For S-SD 7508, the measured Φ_Δ=1.0±0.2, yielding that merit parameter is 7000 at 780 nm, which is comparable to the largest reported values, published for porphyrin dimers [141]. For SO-

SD 7517 in ACN with Φ_Δ=0.7±0.15, the merit parameter is 1162. Note that the Φ_Δ is measured by comparing singlet O_2 luminescence with a known reference Acridine in ACN (Φ_Δ =0.82 [142]).

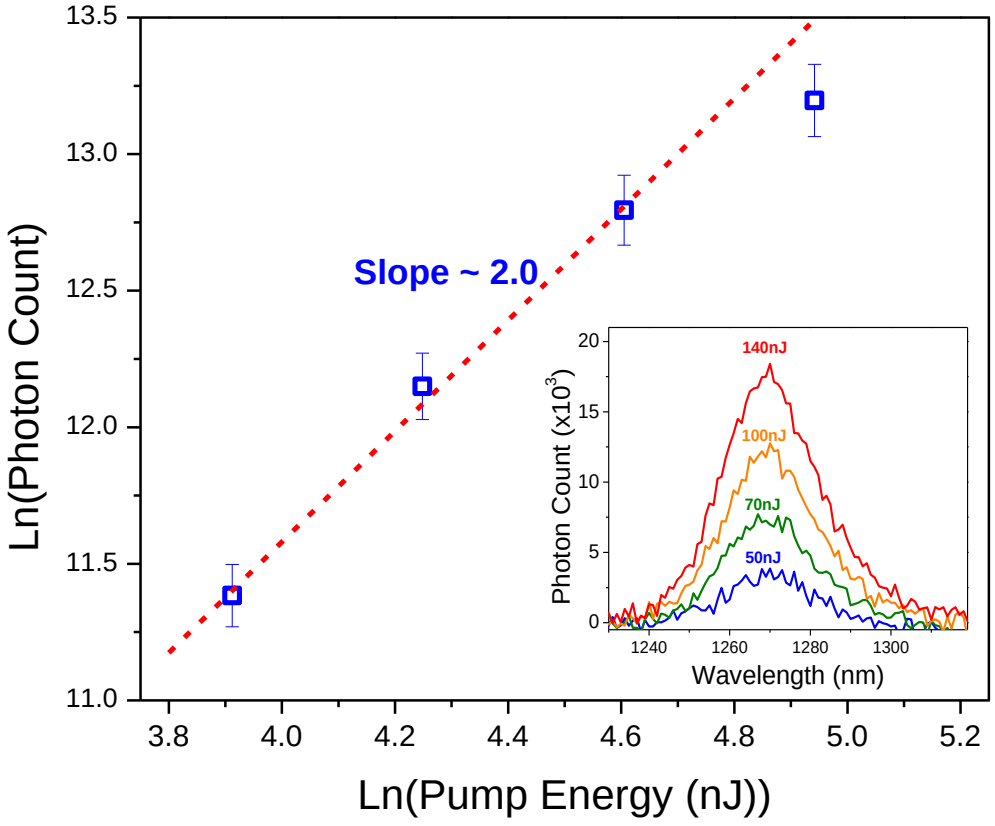

Figure 4.35: Pump energy dependence of the singlet oxygen luminescence. The inset shows the luminescence spectra at several pump energies. Reprinted with permission from ref. 85. Copyright 2010 American Chemical Society.

CHAPTER 5 NONLINEAR REFRACTION OF MOLECULES

The previous chapter is mainly focused on the 2PA properties, i.e. imaginary part of $\chi^{(3)}$, of organic molecules. The structure-property relationships of four groups of molecules are discussed in detail which further advances our understanding of 2PA enhancement in organics. However, there is another remaining important question: what are the properties of the molecules related to the real part of $\chi^{(3)}$, i.e. the nonlinear refraction, n_2? Furthermore, how to enhance the nonlinear refraction of the molecule? It is very desirable for all optical switching applications to have large nonlinear refractive index, n_2, but relatively small 2PA loss, α_2 [20]; therefore, significant effort is devoted in this dissertation to study the nonlinear refraction of the molecules. This chapter is organized as the following: an overview of nonlinear refraction is provided to reveal the complex origin of nonlinear refraction in the molecular systems, followed by a brief introduction of experimental techniques used to characterize both the temporal response and the tensor elements of $\chi^{(3)}$ of molecule. The spectral and pulsewidth dependent n_2 properties of a simple molecule, carbon disulfide CS_2, are investigated experimentally by pulsewidth-varying polarization resolved Z-scan technique. The n_2 spectrum of neat CS_2, measured by pulsewidth less than 70 fs, is then analyzed based on the three-level model discussed in Chapter 2. Finally, the n_2 of some organic molecules are measured and analyzed to provide a general guideline to enhance n_2 of organic molecules.

5.1 Origin of Molecular Nonlinear Refraction

Although the pure nonlinear refraction alters only the phase of the light propagating inside a nonlinear material without energy loss, various physical phenomena, e.g. self-focusing

or defocusing, soliton generation, four-wave mixing, *etc*, are related to nonlinear refractive index of the material. Opposite to 2PA, where the origin is mainly due to electronic transition between discrete energy states, the physical mechanisms of nonlinear refraction are much more complicated, mixed with the electronic contributions and nuclear responses. Because of huge mass mismatch between electron and nuclei, they have completely different response time; i.e. sub-fs response time for electron *vs* at least 100 fs for nuclei. As a consequence, the nonlinear refraction of the material shows significant dependence upon the duration of excitation source. For ultra-short pulse (<~50 fs), the nonlinear refraction of the material is mainly electronic. As the incident pulsewidth increases, the contribution from nuclei kicks in and weighs higher, which might eventually dominate over the total nonlinear response of the material.

The molecular nonlinear mechanisms, differing by their response time, could have the following physical origins:

1) n_2 due to bound electron response

Similar to the mechanism of 2PA, this part of nonlinearity is related to the transition dipole coupling between discrete molecular states. A strong incident electromagnetic wave distorts the bound electron distribution in the molecule, and thus leading to nonlinear change of polarizability of the molecule. Since the electron response is prompt within the femtosecond pulse (pulsewidth no less than 30 fs in our lab facility), the n_2, induced by electronic transition, can be considered as instantaneous. A classic perturbation theory by Orr and Ward [43], a so called "sum-over-states" model (SOS), is developed to describe the model of the electronic n_2. A simplified 3-level model derived from this perturbation theory is discussed in Chapter 2.

2) n_2 due to nuclei response

The coupling between light and vibrational modes of the Raman active molecule can also modulate the polarizability of the molecular, and thus give rise to a significant n_2, however, in a much slower time scale. As much as ~20% Raman contribution to n_2 is reported in fused silica by Hellwarth *et al* [143], given that the excitation pulse is long enough so the the vibration can build up (usually in ps) to show maximum contribution. However, for a 100 fs pulse, this contribution for fused silica is approximately 1%, as discussed by Santran *et al* [144].

Molecular reorientation can also lead to n_2 contribution, due to the nature of the anisotropic polarizablity of linear molecules. As the linear polarizability along the molecular axis is larger than that in perpendicular direction, the applied electric field tends to align the molecular axis along the field direction to minimize its potential energy, which will significantly change the macroscopic refractive index along the applied electric field, and thus leading to large positive n_2. As large as 60×10^{-13} cm^{-2}/W of n_2 value has been observed in liquid crystal materials [145]. However, due to the reorientation relaxation time, the response of the nonlinearity due to reorientation is relatively slow. For relatively small molecule such as neat Carbon Disulfide, CS_2, it is about 1.61-2.2 ps [146,147].

In a neat liquid, or when organic molecules are dissolved in a liquid solvent, the molecule cannot rotate freely but usually experiences a rapid damping "force" applied by the solvation structure. In this case, molecules can only "rock" around their initial orientation. Such a reorientational movement is called "libration", or hindered rotation. The n_2, induced by libration, usually decays in a short time scale, e.g. ~170 fs for CS_2 [146].

Another nuclear response in liquids originates from transient distortion of polarizability induced by inter-molecular interactions (*e.g.* collisions), a so called "interaction-induced"

response which is also observed in cryogenic atomic liquids [146]. The decay time constant is estimated to be 400-600 fs

Note that electrostriction and thermal nonlinearities are also slow but macroscopic nonlinearities of the material, which are connected with density changes of the material by either acoustic wave propagation or thermal effects. They are not discussed here due to their response on much longer time scales (usually ns or longer). Details of the analysis can be found in [148].

The complex physics of n_2 makes the de-coupling of electronic and nuclear n_2 much more difficult. In principle, there could be two approaches to examine the origin of optical nonlinearity of an isotropic material: by investigating its temporal response after the excitation to distinguish the different response times of the nonlinear mechanisms, or by probing the tensor elements of $\chi^{(3)}$.

The first approach can be implemented by a pump-probe experimental scheme. The time resolved optical Kerr effect (OKE) experiment is a typical setup to probe the nonlinear response of the material [146]. A pump pulse induces a nonlinear birefringence of the sample, which is examined by a delayed weak probe pulse polarized at 45° with respect to the pump pulse. By using a pair of crossed polarizers, a change of polarization state of the probe pulse can be detected by the transmittance change, which is related to the temporal response of the material nonlinearity. This experiment is further developed by using a pump pulse with a variable pulsewidth to study the interplay between different nonlinear responses [149]. In addition to the OKE experiment, other techniques are also developed in the frame of pump-probe scheme, such as femtosecond four-wave-mixing [150], two-beam energy transfer [151], collinear nonlinear interferometry [144], and femtosecond time division interferometry [152], *etc.*

The second approach is based on the fact that nonlinear mechanisms contribute differently to $\chi^{(3)}$ tensor elements, which can be distinguished by employing light with different polarization states. Hence a separation of $\chi^{(3)}$ tensor elements of the material can shed light on its intrinsic origins of the nonlinearities. A so called "ellipse-rotation" is the first experimental approach to distinguish $\chi^{(3)}$ tensor elements [46]. Recently, Z-scans with linear, circular and elliptically polarized light using similar principles has also been reported as a tool to investigate $\chi^{(3)}$ tensor elements [153] to separate the electronic and nuclear nonlinearities.

5.2 Nonlinear Refraction of CS_2

Carbon disulfide (CS_2) is one of the most widely-studied nonlinear optical (NLO) liquids, which, due to its relatively large n_2, is considered as a standard reference to calibrate the nonlinearity measurement of other unknown material. However, more than one order of magnitude increase of n_2 is observed by Ganeev *et al*. using conventional Z-scan technique with individual femto-, pico- to nano-second pulse at 532 nm, 795 nm and 1054 nm [154]. The time resolved optical Kerr experiment (OKE) [146] and femtosecond interferometry [152] reveal the complicated origins of optical nonlinearities with distinguishable response time: instantaneous electronic contribution, molecular libration (~170 fs), intermolecular interaction (~420 fs), and molecular re-orientation (~1.6-2.2 ps) [146,155]. Other approaches to separate electronic and nuclear contributions to the third order nonlinearity of CS_2 are proposed to use the polarization resolved Z-scan [153] and pump-probe technique [151] to determine the $\chi^{(3)}$ tensor elements. The nonlinear absorption at ~800 and 1064 nm of CS_2 is also reported in refs. 156,157, however, the origin is still controversial pending further discussion. Although the relevant information of the

nonlinearity of CS_2 is scattered through the scientific literature, a systematic study of the detailed pulsewidth and wavelength dependence of n_2 of CS_2 is lacking and thus it is of great interest.

In this section, we systematically investigate the spectral and temporal dependence of the optical nonlinearity of CS_2 by Z-scan. With the capability of continuously tuning the pulsewidth from 32 fs to 2.3 ps (FWHM), we investigate the evolution of n_2 with respect to the excitation duration to determine the relative contribution of electronic and nuclear polarizabilities to the total nonlinear response of CS_2. To separate the tensor element of $\chi^{(3)}$, Z-scan is performed with linear and circular polarized light, respectively. We also show the experimental results of several n_2 spectra measured by femto-, pico- and nano-second pulses, as well as a 2PA spectrum measured by femtosecond pulses.

5.2.1 Linear Properties of CS_2

The linear transmittance of neat CS_2, measured in a 1mm cell by the NLO group, is shown in Figure 5.1a. It shows a wide transparent window from the visible to NIR wavelength range except a small absorption peak at around 1383 nm. The linear absorption drops to ~10% at ~365 nm, suggesting the linear absorption edge of the material. The details of the linear absorption at UV range cannot be resolved in the neat liquid due to extremely high molecular density (16.5 M L^{-1}). To distinguish the absorption features in the UV range, we mixed CS_2 in methanol, for which the linear absorption in the UV range turns on below 200 nm (shown in Figure 5.1a). Shown in Figure 5.1b is the linear absorption of the CS_2/methanol mixture obtained by two separate concentrations of CS_2 measured by the NLO group. A relatively broadband linear absorption with ε^{max} of ~50.3 M^{-1} cm^{-1} (corresponding to linear absorption cross

section σ_{ge} of ~1.92×10^{-19} cm^2) is observed at 250-375 nm range at 0.2245 M. The relatively small ε^{max} indicates this band is forbidden (or quasi-forbidden). Literatures' studying the UV spectrum of CS_2 vapor shows that this weak broadband absorption possibly contains the mixture of several transitions with complicated origins [158,159]. By reducing the concentration of CS_2 to 0.445 mM, another linear absorption peak at ~207 nm (~6 eV) can be resolved with much stronger ε^{max} ~5.43×10^{4} M^{-1} cm^{-1} (σ_{ge}~2.07×10^{-16} cm^2). This band corresponds to a much stronger transition measured in CS_2 vapor with similar wavelength ($^1B_2\leftarrow{}^1\Sigma_g^+$, where $^1B_2$ correlates with the $^1\Sigma_u^+$ state of linear molecule) [158]. The transition dipole moment, ~5.5 D can be estimated by taking the integral of the linear absorption spectrum using Equation 3.1.

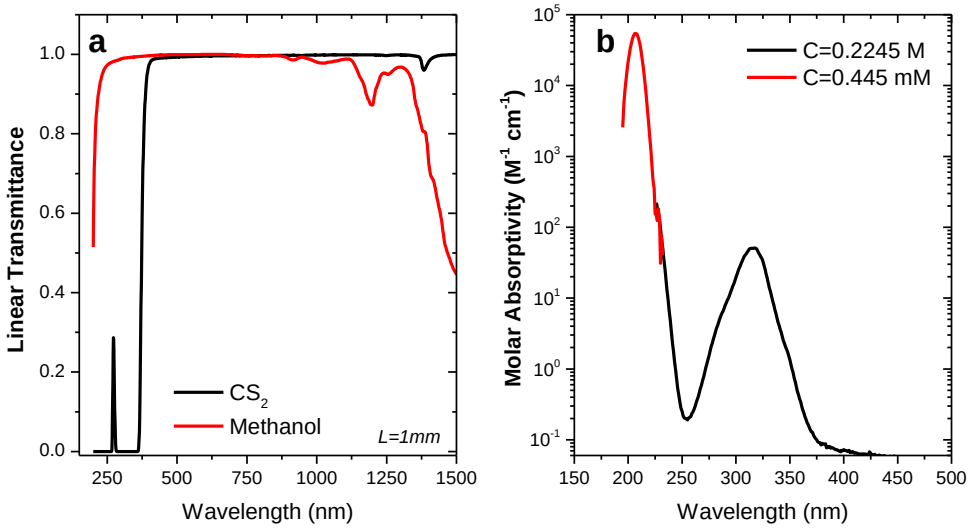

Figure 5.1: (a) Linear transmittance of neat CS_2 and methanol in 1mm cell; (b) Molar absorptivity of CS_2-methanol mixtures with two concentration (C=0.2245 M and C=0.445mM)

5.2.2 Control of Pulsewidth

The tunablity of the pulsewidth is achieved by a pair of high index prism (Newport SF10) compressor / stretcher as shown in Figure 5.2. The broadband pulsed laser beam is incident on prism 1 (usually near the apex) at a Brewster angle to minimize Fresnel loss; inside the prism 1, the beam undergoes normal group velocity dispersion (GVD) as well as an angular dispersion spatially separating different frequency components of the pulse. This angular dispersion leads to an anomalous GVD between prism 1 and prism 2. The beam then enters prism 2 which again exhibits normal GVD. The geometrical arrangement of prism 2 is symmetric with respect to prism 1 in order to re-collimate the angularly dispersed beam. A roof mirror is placed after the prism 2 to send the beam back into prism 2, which propagates along the same path but in a reversed direction. Hence the beam is reconstructed at the entrance of the compressor, which ideally is spatially identical to the incident beam. The detailed arrangement of the prism pair can be found in ref. 160. The normal GVD of the beam can be adjusted by inserting the amount of glass of prism 2 into the beam, while the anomalous GVD is controlled by the separation between prism 1 and prism 2. At 700 nm, the FWHM spectral bandwidth of TOPAS-C is ~22 nm (~13.5THz, FWHM) corresponding to a ~30 fs (FWHM) transform-limited pulsewidth. By changing the separation between prism 1 and prism 2, or controlling the amount of glass thickness which the beam passes in prism 2, the pulse can be shortened or stretched.

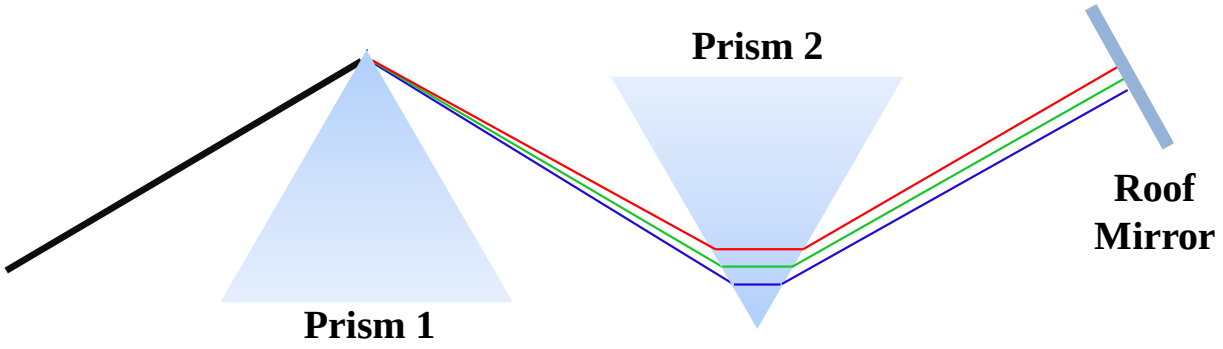

Figure 5.2: Schematic of the prism compressor / stretcher setup

The great advantage of the prism compressor / stretcher is its simplicity and convenience. The GVD of the pulse can be controlled continuously without misalignment of the setup, or significantly altering the spectrum of the input pulse. The pulsewidth is determined on the same Z-scan setup by performing open- aperture Z-scans on the bulky semiconductors ZnSe (for 700 nm) and CdSe (for 1064 nm) and closed aperture Z-scan on fused silica. The 2PA coefficient of semiconductors [70] and n_2 of fused silica [69] are well-characterized in the literature. All reference materials show consistent nonlinearities; therefore, the pulsewidth and focusing spot size of the excitation pulse of the Z-scan setup can be calibrated by the reference materials. The absolute error of pulsewidth is 30%, determined by the GVD of ZnSe and CdSe (~20% for shortest pulse), and the absolute error of Z-scan measurement (~25%); but the relative error is less than absolute error. Note that the pulsewidth can also be measured by auto-correlation setup; however, for the shortest pulsewidth (32 fs, FWHM), additional optics used in autocorrelation setup may induce some GVD which could slightly stretch the pulsewidth (estimated by ~10% assuming a 32 fs bandwidth-limited pulse passes through a ~10 mm optical path of fused silica).

By utilizing this pulsewidth control module, we successfully obtain a continuous change of pulsewidth from 32 fs up to 2.3 ps (FWHM) at 700 nm and from 65 to 350 fs (FWHM) at 1064 nm. The minimum pulsewidth is determined by the bandwidth of the pulse, while the maximum of the pulsewidth is restricted by the geometrical limitation of our setup, i.e. the size of the 1 inch prism and optical table (corresponding maximum separation between two prisms by ~2 m).

5.2.3 The n_2 Evolution of CS_2 from Femto- to Pico- Second Excitation Pulses

By using linearly polarized light, the n_2 of CS_2 measured by the femtosecond system with the prism compressor/stretcher is shown in Figure 5.2 as a function of input pulsewidth on a logarithmic scale. At 700 nm, where the photon energy is near half of the one photon absorption edge (1PA) of CS_2, no nonlinear absorption is observed with peak irradiance of up to 38 GW/cm^2 (negligible imaginary part of $\chi^{(3)}$). Below 65 fs, an approximately constant value of n_2 is observed at $2.6 \pm 0.5 \times 10^{-15}$ cm^2/W, corresponding to $\chi^{(3)}_{xxxx} = 2.4 \pm 0.5 \times 10^{-21}$ m^2/V^2 (Equation 2.21). The stretching of the input pulse leads to a monotonic increase of n_2 as the nuclear contributions show larger influence. At 110 fs, we observe an n_2 value of $4.1 \pm 0.6 \times 10^{-15}$ cm^2/W. This value is slightly larger (33%) but still agree in error range with reported values [161-163] at similar pulsewidth. At 2.3 ps, longer than the molecular reorientational time (1.6-2.2 ps), we obtained an n_2 value of $18 \pm 3 \times 10^{-15}$ cm^2/W ($\chi^{(3)}_{xxxx} = 16 \pm 2.4 \times 10^{-21}$ m^2/V^2) consistent with reported value [162], which is ~6.4 times larger than its value at shortest pulsewidth. We also obtain n_2 value of $40 \pm 6 \times 10^{-15}$ cm^2/W ($\chi^{(3)}_{xxxx} = 35 \pm 5.3 \times 10^{-21}$ m^2/V^2) at 9 ps (FWHM) measured by picosecond system at 700 nm. Similar results are also obtained at 1064 nm with

relatively smaller pulsewidth tunable range (65 to 350 fs) from femtosecond system shown in Figure 5.3. Note that the n_2 value at 32.5 ps (FWHM) of 1064 nm, is measured by our picosecond laser system. Thus, the relative error between this measurement and the fs measurement is larger than the relative errors among the fs measurements.

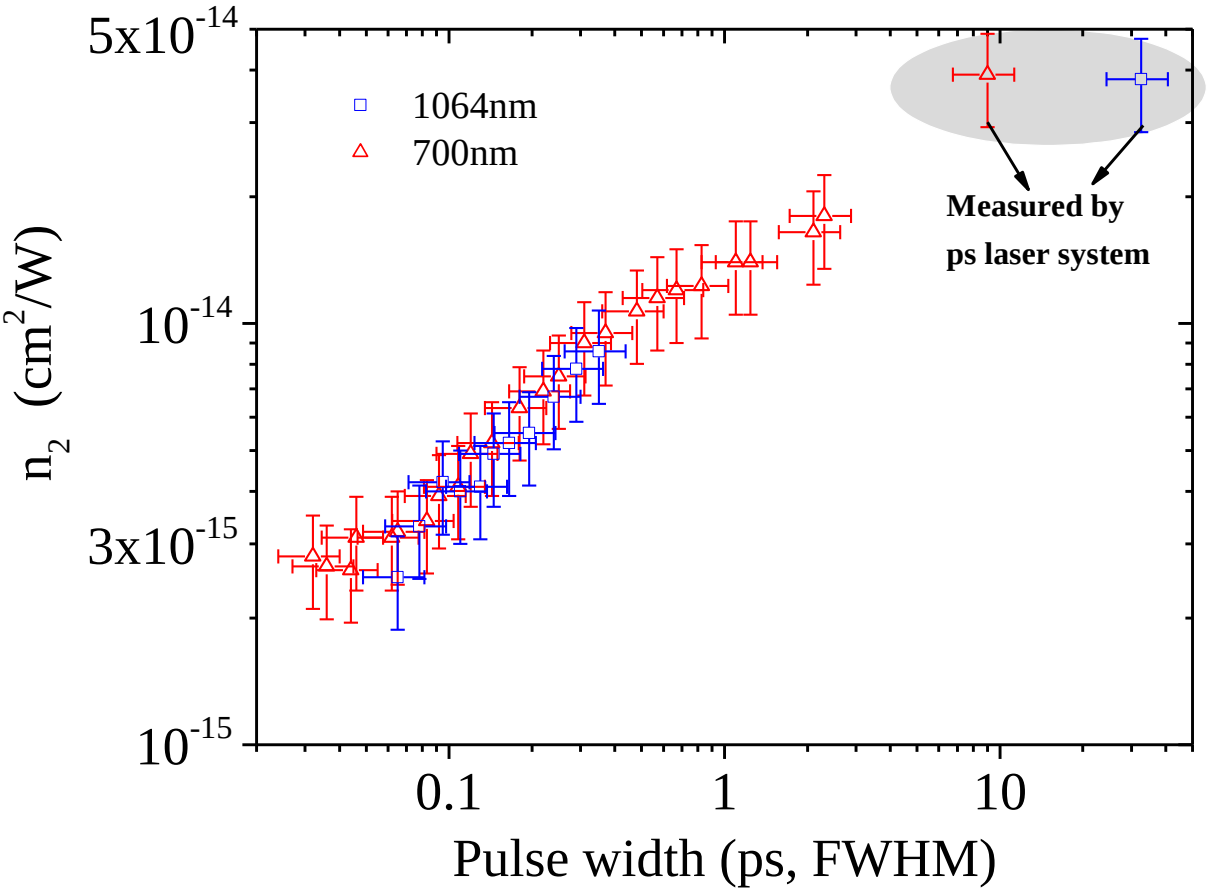

Figure 5.3: Measured n_2 of CS_2 as the function of incident pulsewidth at 700 nm and 1064 nm; the pulsewidth is controlled by a pair of prism compressor / stretcher. Note that data points in shadowed area are measured by picosecond laser system (EKSPLA, model PL2143)

In order to separate the tensor element of $\chi^{(3)}$, we also perform Z-scan using circularly polarized light. The circular polarized light is generated by placing a quarter-wave plate in front of the Z-scan focusing lens, with the optics axis oriented at 45 ° with respect to polarization of

incident light. More than 90% ellipticity is achieved for circular polarized light (an ideal circular polarized light corresponds to 100% of ellipticity) . The ellipticity is defined by the ratio of the minimum over the maximum electric field, which can be checked by placing a polarizer and measuring the energy of the pulse at difference polarization angles. Note that the energy of the pulse, measured by the energy meter, scales with the square of the electric field at this particular polarization angle. It is known that for an isotropic medium, the induced nonlinear polarization of the material can be written as [1,2]

$$\vec{\mathrm{P}}^{(3)}(\omega) = \varepsilon_0\{A\vec{\mathrm{E}}(\omega)\left|\vec{\mathrm{E}}(\omega)\right|^2 + \frac{1}{2}B[\vec{\mathrm{E}}(\omega)\cdot\vec{\mathrm{E}}(\omega)]\vec{\mathrm{E}}^*(\omega)\}$$
$$A = \frac{3}{4}[\hat{\chi}^{(3)}_{1122}(-\omega;\omega,-\omega,\omega) + \hat{\chi}^{(3)}_{1212}(-\omega;\omega,-\omega,\omega)],\ B = \frac{3}{2}\hat{\chi}^{(3)}_{1221}(-\omega;\omega,-\omega,\omega) \quad (5.1)$$

So for linear polarized light (i.e. $\mathrm{E_x}(\omega)$), $\mathrm{P}_i^{(3)}(\omega)$ can be written as

$$\mathrm{P}_i^{(3)}(\omega) = \varepsilon_0[A + \frac{1}{2}B]\left|\mathrm{E_x}(\omega)\right|^2\mathrm{E_x}(\omega)$$
$$A + \frac{1}{2}B = \frac{3}{4}[\hat{\chi}^{(3)}_{1122}(-\omega;\omega,-\omega,\omega) + \hat{\chi}^{(3)}_{1212}(-\omega;\omega,-\omega,\omega) + \hat{\chi}^{(3)}_{1221}(-\omega;\omega,-\omega,\omega)] \quad (5.2)$$
$$= \frac{3}{4}\hat{\chi}^{(3)}_{1111}(-\omega;\omega,-\omega,\omega)$$

which is consistent with Equation 2.9.

For circularly polarized light, the input electric field can be written in the base of unit vector of left ($\vec{\sigma}_+$) and right circular ($\vec{\sigma}_-$) polarized light as

$$\vec{\mathrm{E}} = \mathrm{E}_+\vec{\sigma}_+ + \mathrm{E}_-\vec{\sigma}_- \quad (5.3)$$

Where $\vec{\sigma}_+$ and $\vec{\sigma}_-$ can be written as

$$\vec{\sigma}_\pm = \frac{\sqrt{2}}{2}(\hat{e}_x \pm i\hat{e}_y) \quad (5.4)$$

It is easy to prove that $\vec{\sigma}_{\pm}^{*} = \vec{\sigma}_{\mp}, \vec{\sigma}_{\pm} \cdot \vec{\sigma}_{\pm} = 0, \vec{\sigma}_{\pm} \cdot \vec{\sigma}_{\mp} = 1$. Therefore $\left|\vec{\mathrm{E}}\right|^2$ and $\vec{\mathrm{E}} \cdot \vec{\mathrm{E}}$ can be written as

$$\begin{aligned} \left|\vec{\mathrm{E}}\right|^2 &= \vec{\mathrm{E}} \cdot \vec{\mathrm{E}}^* = \left|\mathrm{E}_+\right|^2 + \left|\mathrm{E}_-\right|^2 \\ \vec{\mathrm{E}} \cdot \vec{\mathrm{E}} &= 2\mathrm{E}_+\mathrm{E}_- \end{aligned} \tag{5.5}$$

Hence $\mathrm{P}_{\mathrm{i}}^{(3)}(\omega)$ can be written as

$$\begin{aligned} \vec{\mathrm{P}}^{(3)}(\omega) &= \varepsilon_0 \{ A\vec{\mathrm{E}}[\left|\mathrm{E}_+\right|^2 + \left|\mathrm{E}_-\right|^2] + \frac{1}{2} B[2\mathrm{E}_+\mathrm{E}_-]\vec{\mathrm{E}}^* \}] \\ &= \varepsilon_0 A(\left|\mathrm{E}_+\right|^2 + \left|\mathrm{E}_-\right|^2)(\mathrm{E}_+\vec{\sigma}_+ + \mathrm{E}_-\vec{\sigma}_-) + B\mathrm{E}_+\mathrm{E}_-(\mathrm{E}_+^*\vec{\sigma}_+^* + \mathrm{E}_-^*\vec{\sigma}_-^*) \end{aligned} \tag{5.6}$$

Separating $\mathrm{P}_+^{(3)}(\omega)$ and $\mathrm{P}_-^{(3)}(\omega)$, it is straight forward to get

$$\begin{aligned} \mathrm{P}_+^{(3)}(\omega) &= [A\left|\mathrm{E}_+\right|^2 + (A+B)\left|\mathrm{E}_-\right|^2]\mathrm{E}_+ \\ \mathrm{P}_-^{(3)}(\omega) &= [A\left|\mathrm{E}_-\right|^2 + (A+B)\left|\mathrm{E}_+\right|^2]\mathrm{E}_- \end{aligned} \tag{5.7}$$

Therefore a pure circular polarized light (e.g. left circular polarized light $\vec{\mathrm{E}} = \mathrm{E}_+\vec{\sigma}_+$) induces only the nonlinear polarization with the same parity as

$$\mathrm{P}_+^{(3)}(\omega) = \varepsilon_0 A\left|\mathrm{E}_+\right|^2 \mathrm{E}_+ = \frac{3}{4}\varepsilon_0[\hat{\chi}_{1122}^{(3)}(-\omega;\omega,-\omega,\omega) + \hat{\chi}_{1212}^{(3)}(-\omega;\omega,-\omega,\omega)]\left|\mathrm{E}_+\right|^2 \mathrm{E}_+ \tag{5.8}$$

Based on Equations 5.2 and 5.8, it is easy to conclude that in isotropic medium the nonlinearity induced by linear polarized light is proportional to *A+0.5B*, while the nonlinearity induced by circular polarized light is proportional to A^2. Therefore Z-scans with linearly and circularly polarized lights are sufficient to extract *B* and *A* values. The ratio of *B/A* can be expressed in terms of n_2 measured by linear and circular light as

$$\frac{B}{A} = 2\frac{n_2\big|_{linea} - n_2\big|_{circular}}{n_2\big|_{circular}} \tag{5.9}$$

If the nonlinearity originates from the electronic response of the material, the Kleinman symmetry leads to *B/A=1*, given that the incident photon energy is not resonant with the transition frequencies. On the other hand, *B/A=6* indicates that the nonlinearity is due to molecular reorientation [2]; however, the ratio of *B/A* is *not obvious* if the nonlinearity is related with other types of nuclear movement, e.g. molecular libration, vibration, intermolecular interaction, *etc*.

Shown in Figure 5.4, is n_2 measured by linear and circular polarized light and the ratio of *B/A* with respect to excitation pulsewidth at 700 nm. The increase of pulsewidth leads to an increase of both $n_2|_{circular}$ and $n_2|_{linear}$. *B/A*=1.1 is obtained at 34 fs, indicating that electronic response is the main mechanism of the nonlinearity at this pulsewidth. However, it seems that the nuclear response has already shown significant influence at 67 fs, evidenced by *B/A*=1.9. The increase of input pulsewidth leads to a further increase of *B/A*. At 120 fs, *B/A*=2.2, which is close to the value report by Yan *et al* [153], indicating larger influence of nuclear contribution to the nonlinear response. Although the reorentational time of CS_2 is within 1.6-2.2 ps, the fact that ratio *B/A*=4.5, i.e., 25% less than 6 at 9 ps suggests the origin of nonlinearity at this pulsewidth is probably still mixed with different mechanisms.

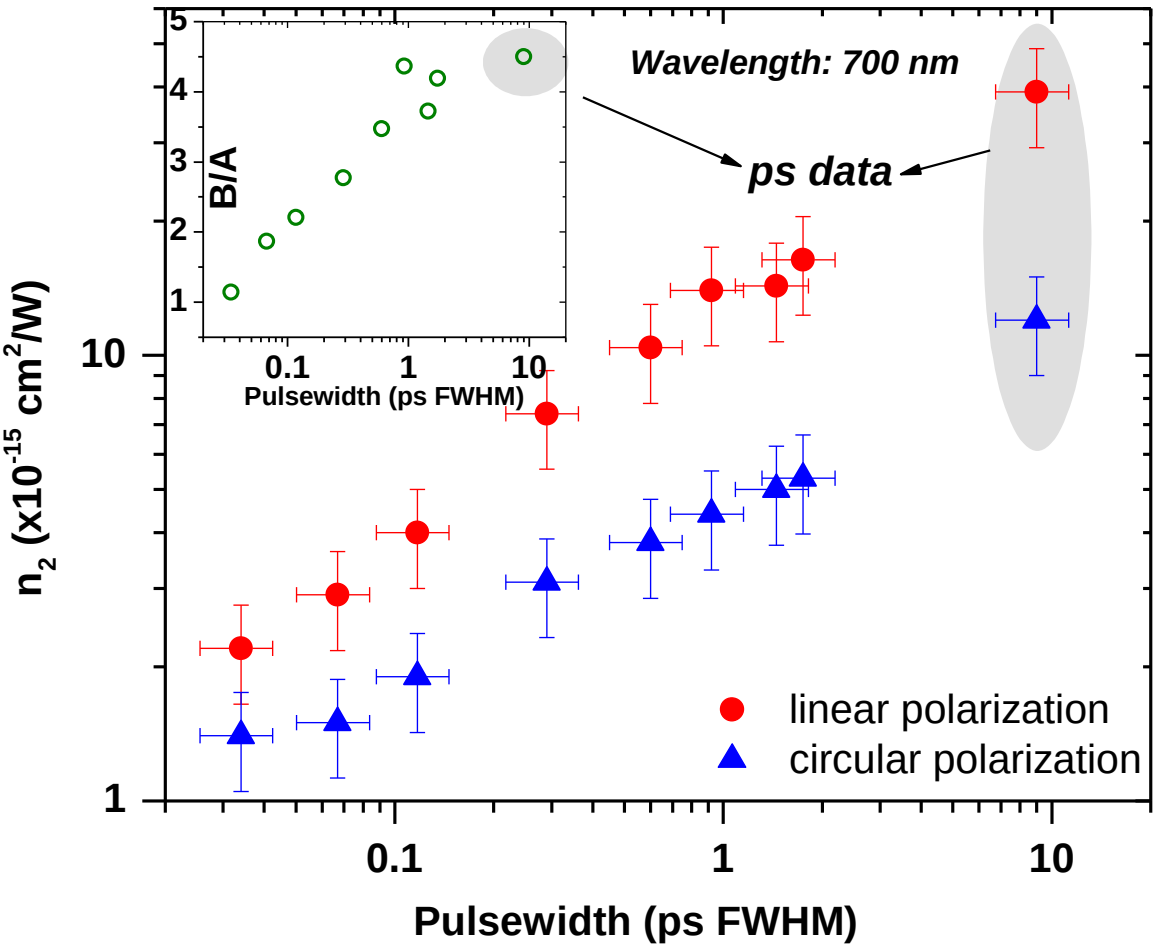

Figure 5.4: $n_2|_{circular}$ and $n_2|_{linear}$ as the function of incident pulsewidth; inset: the ratio of B/A *v.s.* pulsewidth. Note that data points in the shadowed area are measured by picosecond laser system (EKSPLA, model PL2143)

5.2.4 The n_2 Dispersion and 2PA Spectrum of CS_2 by Femtosecond Pulse

Since the n_2 response of CS_2 is strongly dependent upon the input pulsewidth in the femtosecond region, in order to minimize the nuclear contribution to the optical nonlinearity of CS_2, we measure the femtosecond n_2 spectrum of CS_2 with the minimum possible pulsewidth achieved by the prism compressor. Between 420 nm to 1064 nm, we successfully obtain

pulsewidths less than 70 fs (FWHM). The n_2 spectrum is shown in Figure 5.5, the n_2 value is approximately constant and equals $2.65 \pm 0.5 \times 10^{-15}$ cm^2/W at wavelength longer than 600 nm; at wavelength shorter than 600 nm, the n_2 increases up to its peak value of $7.3 \pm 1.4 \times 10^{-15}$ cm^2/W at 440 nm, following a relatively rapid decrease of n_2 when the wavelength gets shorter. Meanwhile, the 2PA starts to turn on at 500 nm and shows α_2 peak value of 2 ± 0.3 cm/GW at 410 nm, ~30 nm blue shifted with respect to the n_2 peak as shown in Figure 5.5. Note that at 403 nm and 390 nm, the input pulsewidth is 140-155 fs (FWHM) due to limitation of our prism compressor, we obtain n_2 of $5.0 \pm 0.7 \times 10^{-15}$ cm^2/W and $4.1 \pm 0.5 \times 10^{-15}$ cm^2/W, respectively (not shown in Figure 5.5). Based upon the trend of the n_2 spectrum shown in Figure 5.5, the n_2 of CS_2 measured by shorter pulsewidth (<70 fs) is estimated about 30-40% lower than that obtained by 140-155 fs pulses. However, the α_2 is relatively independent upon the input pulsewidth, as is evidenced by the same α_2 value measured at 410 nm with input pulsewidth of 50 fs and 165 fs (FWHM).

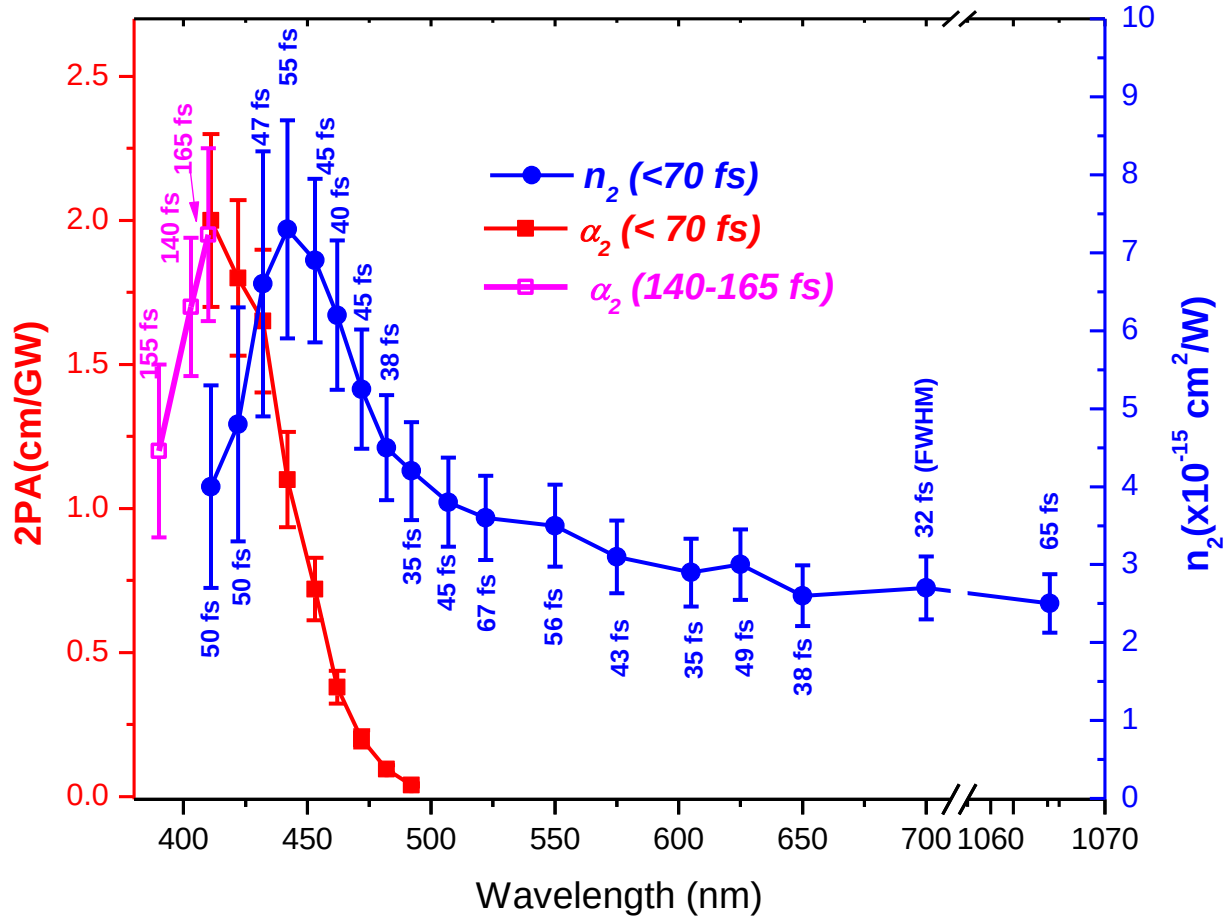

Figure 5.5: n_2 (blue) and 2PA (red) spectrum of CS_2 measured with pulsewidth less than 70 fs (FWHM), and 2PA (pink) spectrum measured with pulsewidth between 140 – 165 fs (FWHM)

In general, the spectral dispersion behavior of n_2 and 2PA of CS_2 measured by femtosecond pulse without significant contribution from nuclear response could be explained by "SOS" model discussed in Chapter 2. Since CS_2 is a symmetrical molecule, "SOS" model can be reduced into 3-level model described in Section 2.3. Here we only consider three states: the even symmetry ground state ($1A_g$), an one photon allowed state with odd symmetry ($1B_u$), and the 2PA final state corresponding to another state with even symmetry (mA_g). The transitions $1A_g \rightarrow 1B_u$, and $1B_u \rightarrow mA_g$ are strongly dipole allowed, corresponding to μ_{01} and μ_{12}, while the

direct transition between $1A_g$ and mA_g is forbidden. We identify that the intermediate state ($1B_u$) is located at the strong 1PA band (~6 eV) with linewidth of 0.17 eV and transition dipole moment μ_{01} of 5.5 D obtained from experimental spectrum (see Section 5.2.1); however, a local field enhancement factor, $f^{(1)}=(n^2+2)/3$, should be taken into account, which reduces the actual μ_{01} to ~3.6 D [2]. We also exclude the weak 1PA band at 250-375 nm as the intermediate state due to its extremely small molar absorptivity (ε^{max} ~50.3 M^{-1} cm^{-1}) corresponding to transition dipole moment only 0.3 D. The mA_g state is at 208 nm (5.95 eV with linewidth 0.4 eV), corresponding the 2PA final state at 420 nm shown in Figure 5.5. We postulate that the mA_g state lies very close to $1B_u$ state implies the strong electron correlation effect in CS_2 as it is observed in conjugated polymers as stated in ref. 164. By using 3-level model, described in Section 2.3, we fitted the experimental data as shown in Figure 5.6. Note that the experimental δ_{2PA} and δ_{NLR} of CS_2 is calculated assuming the molecular density of 16.5 M L^{-3}. Since the refractive index is ~1.6 (ε^r=2.56, assuming no dispersion), a local field correction factor $f^{(3)}$ of 5.33, obtained by Equation 2.26, is also included in the model. By fitting the 2PA spectrum of CS2, we obtain $\mu_{ee'}$ of 8.7 D, which is more than 2× larger than μ_{ge}. We are able to reproduce the NLR spectral shape calculated from fitting parameters obtained by 2PA spectrum, with fairly good accuracy in its peak position and the trend of variation; however, the magnitude of NLR cross section is systematically under-estimated by a factor of 2.0. The reason of disagreement between experimental n_2 value and fitting is probably due to either the contribution from nuclear responses, the contribution from other electronic states not included in the 3-level model, or molecular interactions between individual CS_2 molecules.

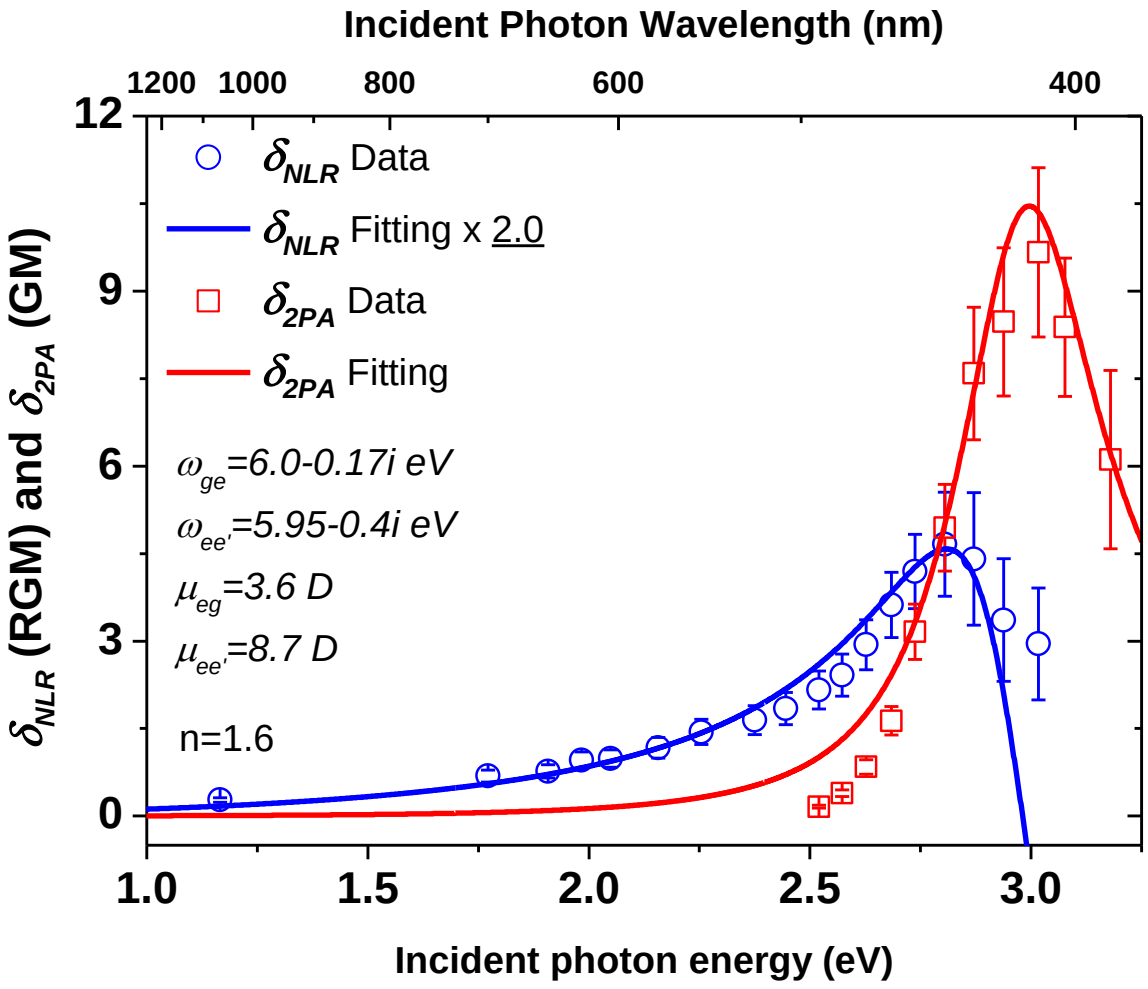

Figure 5.6: Experimental and 3-level model fitting of δ_{2PA} and δ_{NLR} spectrum of CS_2. Note that the fitting for δ_{NLR} is multiplied by a factor of 2.0

5.2.5 The n_2 Dispersion of CS_2 by Pico- and Nano-Second Pulse

The n_2 spectrum using 13-20 ps (FWHM) pulses (blue), measured by the NLO group, is presented in Figure 5.7a. The pulsewidth is measured independently by autocorrelation technique. This pulsewidth is 5-6× longer than the reorientation time of CS_2. The measured n_2

values of ~35 $\times 10^{-15}$ cm^2/W are approximately constant within a wide spectral range. They are more than an order of magnitude larger than the corresponding values using sub-70 fs laser pulses. This observation indicates that the reorientational nonlinearity is wavelength insensitive and dominates the nonlinear refraction.

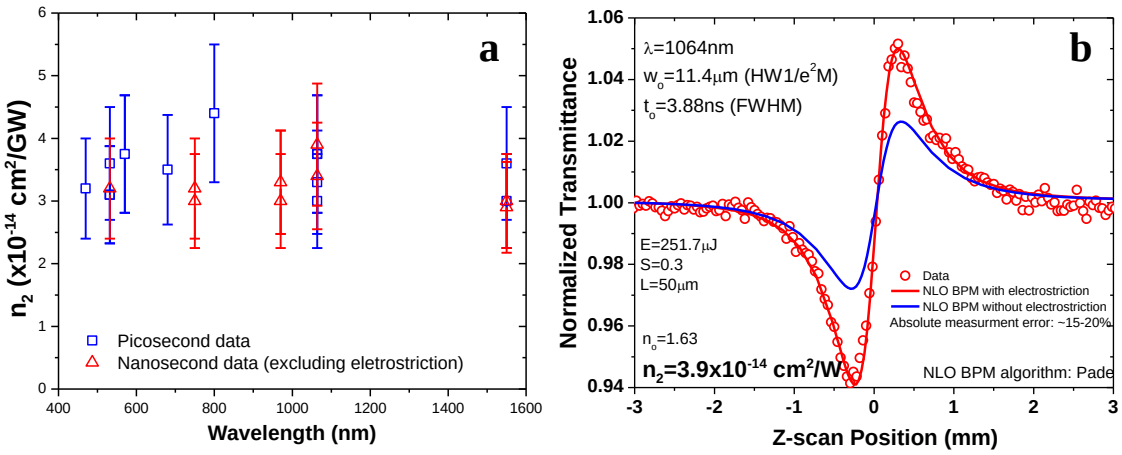

Figure 5.7: (a) n_2 spectrum of CS_2 measured by ps- and ns-pulse; (b) comparison of Z-scan fitting with/without taking into account the electrostriction effect.

We also present the n_2 of CS_2 measured by the NLO group using nanosecond pulsewidths 2.5-16.5 ns (FWHM) pulses (red), as shown in Figure 5.7a. The pulsewidth is measured by a fast silicon photodiode connected to the oscilloscope. For this pulsewidth range electrostriction needs to be accounted for since the photo-acoustic wave generated by the electric field of the nanosecond pulse has time to travel over a significant fraction of the spatial beam size [148]. Figure 5.7b shows the nanosecond Z-scan trace and numerical fittings, fit with a beam propagation code [148], with and without the electrostrictive contribution. This indicates that approximately 50% of the refraction is due to the electrostrictive effect. The observed n_2 (excluding electrostriction) is ~39 $\times 10^{-15}$ cm^2/W similar to the n_2 value measured by picosecond

pulses, indicating that the reorientational nonlinearity saturates as the pulsewidth increases from picoseconds to nanoseconds.

5.3 Nonlinear Refraction of Organic Molecules

We also extend the investigation of nonlinear refraction into linear π-conjugated organic molecules which have relatively large third order nonlinearities. Differing from neat CS_2, the n_2 measurement of organic molecules is usually conducted on its solution forms. Therefore, it is necessary to separate the n_2 contribution of the solute molecule from the solvent background, which can be realized by performing single wavelength or WLC Z-scans [42] sequentially on the solution and solvent to differentiate the slight difference of the nonlinear signal. Although the nonlinearity per solute molecule is usually much larger than that per solvent molecule, for a solution with 10^{-3}-10^{-4} M concentration, the much larger density of the solvent molecules yield to a nonlinear signal overwhelmingly stronger than the signal contributed from solute molecules. Therefore, the detection of differential nonlinear signal from the n_2 of solute by such sequential Z-scan procedure is limited by the noise on each Z-scan curve originating from shot-to-shot energy and beam pointing fluctuations of the excitation pulse. An alternative approach, proposed by Dr. Van Stryland *et al*, to further reduce noise is to perform Z-scans on both solution and solvent simultaneously. A dual-arm Z-scan method is being developed to construct two identical Z-scan arms [165]. The main challenge is to make sure both arms having exactly the same pulse energy, spot size; and the solution and solvent sample should sit on the same z position when doing Z-scan. In this case, the nonlinear signals from solvent in both arms can cancel each other. The schematic setup of dual-arm Zscan is shown in Figure 5.8

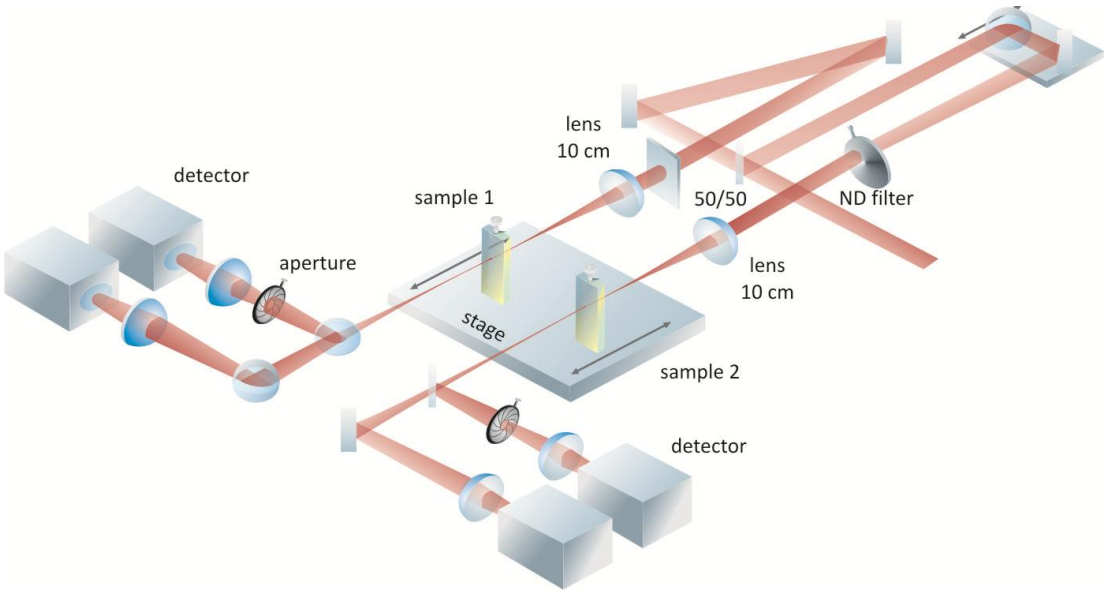

Figure 5.8: Schematic setup of dual-arm Z-scan; the solution and solvent sample are placed at the position of sample 1 and sample 2 of the setup.

There are several approaches to theoretically predict the n_2 spectrum of organic molecules. Since the 2PA properties of some types of linear π-conjugated organic molecules are discussed in refs. 32,64 and Chapter 4, a simple approach to estimate the dispersion of electronic n_2 of the molecule can be deduced from its 2PA spectrum by Kramers-Krönig relations [39]. Another approach to model the electronic n_2 of the molecule can be achieved by "Sum-Over-State" quantum mechanical perturbation theory as discussed in Section 2.3, given the knowledge of discrete electronic state structure and the corresponding transition dipole moments of the molecular system. Here we use simple 3-level model, deduced from "SOS" model, to describe general dispersion behavior of n_2 of a squaraine molecule O-SD 2405 and an extended bis(diarylaminostyryl) chromophore with heterocycle-vinylene bridge (SJZ-316)

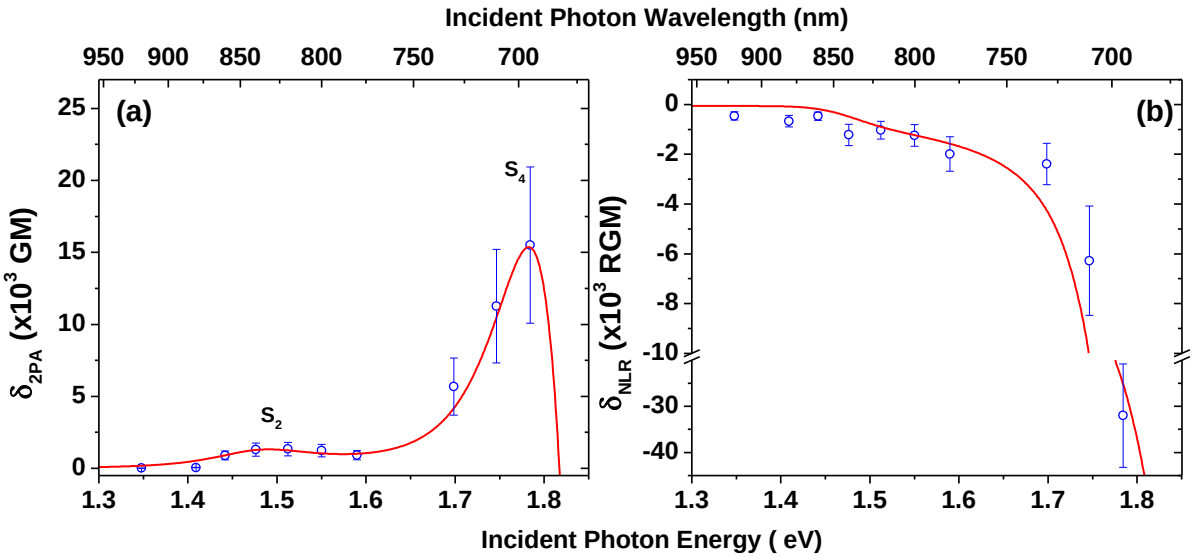

Figure 5.9: Experimental δ_{2PA} (a) and δ_{NLR} (b) spectrum (blue dot) and its 3-level model fitting (red solid) of O-SD 2405 in toluene. These data were taken with the dual-arm Zscan [165]

The 2PA spectrum of O-SD 2405 in toluene has been shown in Figure 4.33 in Section 4.8.2 in logarithmic scale. Three 2PA bands are observed and their origins are discussed in Section.4.8.2. Since the first 2PA band at ~1200 nm/1.03 eV is due to 2PA coupling into vibronic sub-states of the S_1 state and is much weaker than the two other 2PA bands, we only take into account the second 2PA state at 2PA wavelength of 840 nm (1.475 eV), corresponding to excitation into S_2 state at 2.95 eV, and the third 2PA band at 2PA wavelength of 700 nm (1.77 eV), corresponding to excitation into S_4 state at 3.54 eV. Both two 2PA final states share S_1 as the intermediate state, and we assume the transition between S_2 and S_4 states is forbidden due to the same type of symmetry of the states. By using 3-level model with multi 2PA final states, in Figure 5.9a we can fit the 2PA spectrum of O-SD 2405 with the fitting parameter shown in Table 5.1. Note that the position of S_1 state is determined by the 1PA peak (636 nm/1.95 eV), with its linewidth (0.04 eV) estimated by the Half-width-half-maximum (HWHM) of its S_1 band in

photon energy; the linewidth of the higher states is assume to be 0.15 eV (S_2) and 0.18 eV (S_4) for best fitting; the ground-to-excited state transition dipole moment (μ_{ge}), estimated from Equation 3.1, is 17 D, however, it is reduced to 12 D for local field correction, $f^{(1)}$=1.4, given the refractive index of toluene is 1.49. We also included the local field correction, $f^{(3)}$=4 into the fitting model.

Table 5.1: Fitting parameters for O-SD 2405 in Figure 5.9. Note that ω_{ge}, Γ_{ge} and μ_{ge} corresponds to S_0 to S_1 state; $\omega_{ge'}$, $\Gamma_{ge'}$ and correspond to S_2 and S_4 state; and $\mu_{ee'}$ corresponds to transition from S_1 to S_2 or S_4 state.

States	ω_{ge} or $\omega_{ge'}$ (eV)	Γ_{ge} or $\Gamma_{ge'}$ (eV)	μ_{ge} or $\mu_{ee'}$ (D)
S_1	1.95	0.04	12
S_2	2.95	0.15	6
S_4	3.54	0.18	11

The δ_{NLR} spectrum of O-SD2405, measured by the dual-arm single wavelength Z-scan procedure with pulsewidth ~130-140 fs (FWHM), is presented in Figure 5.9b. Note that we can only resolve δ_{NLR} value of O-SD2405 from solvent background at wavelengths relatively close to its linear absorption edge. Measurement of δ_{NLR} values at longer wavelengths is unsuccessful due to impossibility to distinguish the signals from solute from solvent molecules. As is shown in Figure 5.9b, the experimental δ_{NLR} value of O-SD2405 is negative with its magnitude increasing as the incident photon wavelength approaches the linear absorption edge of the molecule. The bandwidth of the pulse is ~20 nm (FWHM, ~0.05eV in photon energy). Assuming the origin of n_2 is electronic in nature, the trend of δ_{NLR} dispersion of O-SD2405 can be fitted with a 3-level model with multi-2PA-final-states using parameters listed in Table 5.1,

where two 2PA final states, corresponding to $\omega_{ge'}|_{S2}$=2.95 eV and $\omega_{ge'}|_{S4}$=3.54 eV, are taken into count in the fitting. The small variation of δ_{NLR} fitting at ~1.475 eV (840 nm) is originated from the weak S_2 state; however, it is relatively difficult to verify fitting by experimental data since the δ_{NLR} value is too small. Of particular interest is a result at 690 nm (1.8 eV), where the measured δ_{NLR} is -32,000 RGM, more than 10-fold larger compared to the value (-2100 RGM) at 730 nm (1.70 eV), despite a large 2PA band with maximum δ_{2PA} over 15,000 GM. No linear absorption or ESA absorption is observed at 690 nm. Because at 700 nm (corresponding to 2PA final state $\omega_{ge'}$=3.54 eV), the photon energy is very close to the 1PA peak at 636 nm (ω_{ge}=1.96 eV), i.e. $\omega_{ge'}/\omega_{ge}$=1.81 close to 2, the strong negative δ_{NLR} near linear absorption edge is due to dominating contribution from the negative (N) term as discussed in Section.2.3.3.

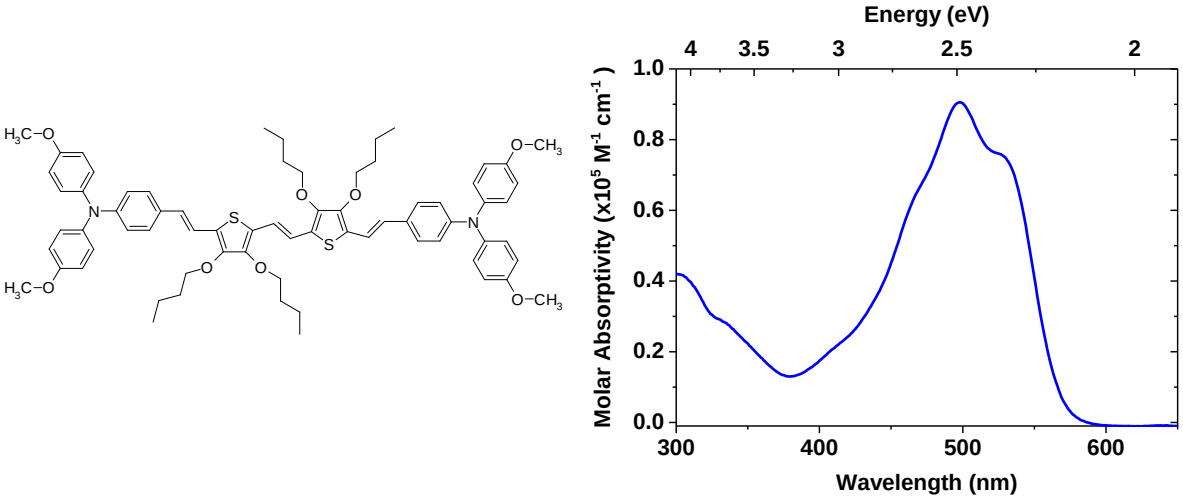

Figure 5.10: Molecular structure of SJZ-316 and its linear absorption spectrum in THF

The molecular structure of SJZ-316 is shown in Figure 5.10 with the linear absorption spectrum measured in THF. The linear absorption peak is observed at 496 nm (2.5 eV) with peak molar absorptivity 9.06×10^4 M^{-1} cm^{-1} [30]. The ground-to-excited-state transition dipole

moment (μ_{ge}) is set at ~12 D from quantum chemical calculation [30]. The 2PA spectrum, measured by 2PF and Z-scans (conventional and WLC), is shown in Figure 5.11a. The first 2PA band is observed at 800 nm (1.55 eV, responding to the 2PA final state at 3.1 eV) with peak δ_{2PA} of 500 GM; and the second 2PA at 650 nm (1.9 eV, 2PA final state at 3.8 eV) with peak δ_{2PA} of 3,900 GM. More interesting is the δ_{NLR} spectrum, measured by sequential WLC Z-scan procedure [42] as shown in Figure 5.11 b. A positive δ_{NLR} ~120 RGM, is observed at 710 nm (1.75 eV). It then increases to 730 RGM at 690 nm (1.8 eV). However, δ_{NLR} changes its sign from positive to -410 RGM at 670 nm (1.85 eV), followed by a dramatic increase of its *negative* magnitude as the photon energy approaches the linear absorption edge. Note that δ_{NLR} cannot be resolved at incident photon energy below 1.7 eV (wavelength > 730 nm) due to indistinguishable signal between solution and solvent measured by Z-scan. We fit both δ_{2PA} and δ_{NLR} spectra using 3-level model (Figure 5.11) quantitatively with the fitting parameter shown in Table 5.2. A local field correction, $f^{(3)}$=3, is applied to the model. Assuming the 1PA band at 496 nm (i.e. ω_{ge}=2.5 eV) is the intermediate state for both 2PA transitions, we are able to reproduce the trend of δ_{NLR} as shown in Figure 5.11 b. The small variation of δ_{NLR} fitting at ~1.55 eV (800 nm), originated from the first weak 2PA band (3.1 eV), is difficult to verify due to its small magnitude. The positive δ_{NLR} peak at 690 nm (1.8 eV), originated from the transition into the second 2PA band (3.8 eV), can be fitted with excited state transition dipole moment $\mu_{ee'}$=15 D, which is ~25% larger than μ_{ge}. Therefore, the positive δ_{NLR} peak is the result from (1) the large magnitude of $\mu_{ee'}$, and (2) the photon energy to this 2PA state far below the 1PA peak, i.e. $\omega_{ge'}/\ \omega_{ge}$=1.49 for SJZ-316 compared to $\omega_{ge'}/\ \omega_{ge}$=1.81 for O-SD 2405. Note that the linewidth for the transitions are chosen for the best fitting.

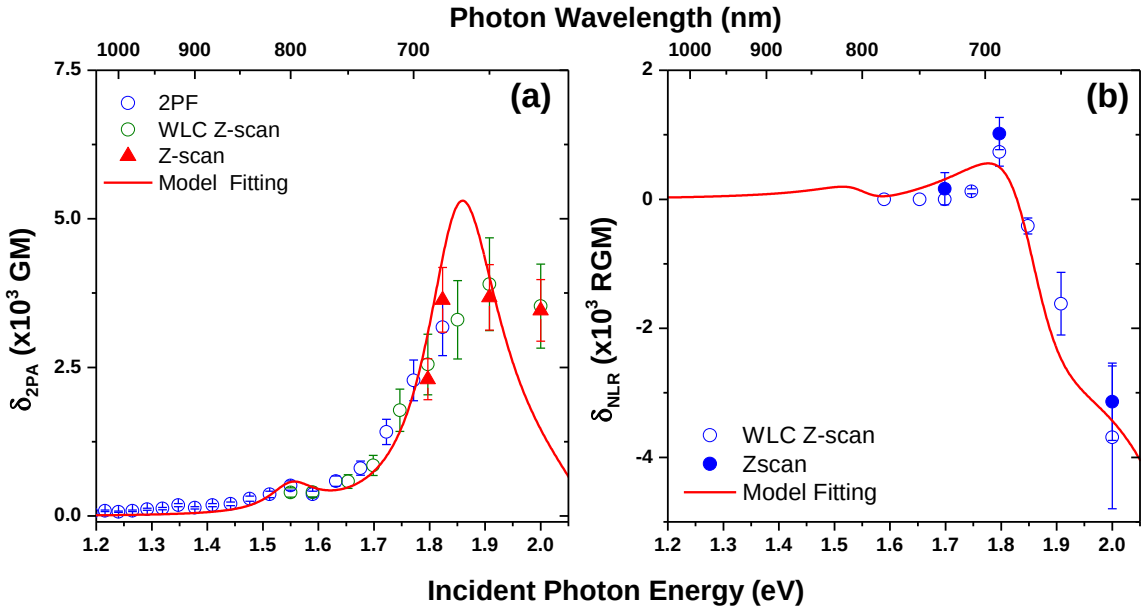

Figure 5.11: (a) Experimental δ_{2PA} (a) and δ_{NLR} spectrum (b) of SJZ-316 in comparison with a 3-level model fitting

Table 5.2: Fitting parameters for SJZ-316 in Figure 5.11. Note that ω_{ge}, Γ_{ge} and μ_{ge} corresponds to S_0 to 1PA state; $\omega_{ge'}$, $\Gamma_{ge'}$ and correspond to ground state to the two 2PA states; and $\mu_{ee'}$ corresponds to transition from 1PA state to the two 2PA states.

States	ω_{ge} or $\omega_{ge'}$ (eV)	Γ_{ge} or $\Gamma_{ge'}$ (eV)	μ_{ge} or $\mu_{ee'}$ (D)
1PA	2.5	0.05	12
$2PA_1$	3.1	0.1	6
$2PA_2$	3.7	0.16	15

5.4 Strategy to Enhance Electronic n_2 of Organic Molecules

With the excitation wavelength at 1550 nm and pulsewidth of ~100 fs (FWHM), we also measured n_2 and 2PA cross section of some squaraine and polymethine molecules as listed in

Table 5.3. The molecular structures of O-SD2878, O-SD2737 and S-SD7611 are shown in Figure 5.12. For all squaraine dyes, except O-SD2405 of which solute n_2 is undetectable, we observe a negative n_2 which is consistent with conclusion in ref. 166. However, it is difficult to predict the sign of n_2 at longer wavelengths since the incident photon energy (1550 nm / 0.8 eV) is only ~60% of the linear absorption peak. Quantum chemical calculation is necessary to estimate the $\mu_{ee'}$ and thus the sign of δ_{NLR} in the DC limit (*i.e.* $\omega << \omega_{ge}$). More interesting is that as the linear absorption peak red shifts, we observe an increase of the magnitude of δ_{NLR}, although they have similar μ_{ge}. This is the indication of increased contribution from the N-term resulting from the small detuning energy between the incident photon energy and the linear absorption peak. Note that for polymethine dye with the longest linear absorption peak (1043 nm in ACN), labeled as JB17-08 (Figure 4.4), magnitude of *negative* δ_{NLR} > 600 "RGM" is observed.

Table 5.3: List of nonlinear parameters of polymethine and squaraine dyes measured at 1550 nm with pulsewidth ~100 fs (FWHM).

molecule	solvent	1PA peak	ε_{abs}^{max}	concentration	total n_2	solvent n_2	solute n_2	solute δ_{NLR}	solute δ_{2PA}
		nm	$\times 10^5$ M^{-1} cm^{-1}	mM	$x10^{-15}$ cm^2/W	$x10^{-15}$ cm^2/W	$x10^{-15}$ cm^2/W	RGM	GM
G74	ACN	812	2.86	1.7	1.4	0.85	0.55	279	438
O-SD 2405	Toluene	636	3.64	2.3	1.5	1.5	-0.1	undetectable	0
S-SD 7611	DCM	901	1.36	8.7	0.55	0.95	-0.4	-40	49
O-SD 2737	DCM	931	1.97	8.6	0.35	0.95	-0.6	-60	42
O-SD 2878	Chloroform	970	1.71	2.55	0.75	1.05	-0.3	-102	66
JB 17-08	ACN	1043	1.13	1.055	0, or less than 0	0.8	~-0.8	-655	605

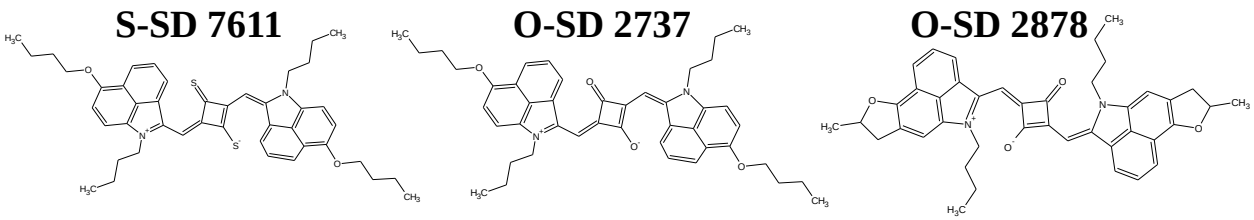

Figure 5.12: Molecular structures of S-SD 7611, O-SD 2737, and O-SD 2878

It is important to note that positive δ_{NLR} is also observed for some organic molecules. For symmetrical A- π-A dye G74 in ACN, we observe a positive δ_{NLR} of 279 ±150 RGM at 1550 nm, compared to ~180 RGM estimated by 3-level model, which is close to its peak value of δ_{NLR}. Positive δ_{NLR} is also observed for extended squaraine dyes [24] and extended bis(diarylaminostyryl) chromophore with additional heterocycle-vinylene bridge (discussed in Section 5.3). Since all these dyes show a strong 2PA peak (>3000 GM) which is located relatively far away from linear absorption edge, the positive n_2 is induced by a strong influence of T-term due to large excited state transition dipole moments ($\mu_{ee'}$).

Based on the experimental results and 3-level model, we can summarize the following basic strategies to increase the n_2 of the organic molecules.

1. A positive n_2 peak, originated from T-term of 3-level model, is usually observed near the 2PA peak on the low energy side ("red side"), as shown in Figure 2.2. Assuming a molecule which has a linear absorption peak at 1000 nm (ω_{eg}=1.24 eV) and linewidth of 0.04 eV; 2PA absorption peak at 1.6 μm ($\omega_{e'g}$=1.55 eV) with linewidth of 0.1 eV; and μ_{ge}=12 D and $\mu_{ee'}$=16 D, a δ_{2PA} peak of 3000 GM is expected at 1600 nm, with a positive δ_{NLR} peak of 410 RGM at 1700 nm in ACN (n=1.34). The increase of $|\mu_{ee'}|/|\mu_{ge}|$ is desirable to have a large positive δ_{NLR}; however, a small detuning energy may also increase the positive δ_{NLR}, given the condition that N-term is not overwhelmingly large, as is evidenced in Figure 2.4.
2. A large negative n_2 is connected with N-term, which shows dominating contribution when the incident photon approaches to linear absorption peak of the molecule. As large as -10, 000 RGM δ_{NLR} is expected at 1140 nm (1.09 eV photon energy) for the

molecule with the molecular parameters given in previous paragraph, provided no ESA is observed at this wavelength. Note that δ_{NLR} originated from N-term can be orders of magnitude larger than that from T-term, which is also confirmed in O-SD 2405 as shown in Figure 5.9. Since the N-term is also proportional to $|\mu_{ge}|^4$, a large ground-to-excited-state absorption transition dipole moment (μ_{ge}) is necessary to enhance a negative δ_{NLR}.

3. Another effective but often ignored approach to increase the *overall* n_2 contribution from solute is to increase the solubility of the organic dyes without significant aggregation to reach the high concentration larger than 10^{-2} M.

CHAPTER 6 CONCLUSIONS AND FUTURE WORK

6.1 Conclusions

In this dissertation, we investigate the third-order nonlinearity of organic molecules (also including data for inorganic molecule CS_2), which contains two aspects: two-photon absorption (2PA) and nonlinear refraction (NLR), corresponding to imaginary and real parts of the third-order susceptibility, $\chi^{(3)}$, of the material. Spectroscopic techniques are employed to experimentally characterize the linear and nonlinear optical properties of the molecules. The linear spectroscopic techniques include absorption (reflection), fluorescence, and fluorescence anisotropy; while the nonlinear spectroscopic techniques contain Z-scan, two-photon fluorescence, and white-light continuum transient absorption (pump-probe). The main conclusions of this dissertation can be divided into the following two parts.

6.1.1 Structure-2PA Properties of Organic Molecules

The first part of the dissertation is focused on studying the structure-2PA properties of organic dyes. Four groups of NIR dyes are introduced with different approaches on molecular structure modification to investigate the corresponding influence on 2PA properties. A molecular design strategy is then summarized to enhance the 2PA cross section. Additional to the solution-based study, we also measured 2PA properties of a single crystal made from one of the D-π-A dye which shows strong and anisotropic nonlinearity. All these studies are correlated with molecular structures and quantum chemical analysis to reveal the intra- and inter- molecular

interactions. The detailed conclusions for each group of dyes and the single crystal are summarized below:

(1) Acceptor-π-Acceptor Polymethine Dyes

Large fluorescence quantum yield is observed for this set of symmetrical dyes, which makes them among the most highly fluorescent NIR chromophores. Due to their symmetrical molecular structure, this set of dyes shows little solvatochromism. Very large peak δ_{2PA} is observed: from ~3000 GM for G37 (n=1) up to 17000 GM for G152 (n=4). At 1600 nm, G152 still exhibits ~2200 GM δ_{2PA} due to the presence of strong "vibrational coupling", which makes this dye one the strongest 2PA absorbers at the telecommunication window. The large δ_{2PA} of this set of dyes originates from the combination of extremely large ground-to-excited-state transition dipole moments (μ_{ge}) and large excited state transition dipole moments ($\mu_{ee'}$). This is one of the approaches to enhance δ_{2PA} by increasing the transition dipole moments between relevant states.

(2) Donor-π-Acceptor Dyes

Due to the asymmetrical molecular structure, this set of dyes shows strong solvatochromism. Both linear (absorption and fluorescence peaks, fluorescence quantum yields and lifetimes) and 2PA properties are strongly dependent upon the polarity of the solvent. This strong solvatochromism can be explained by the dynamic transition between two quantum structures: "polymethine-like" and "polyene-like" structures under the influence of solvent polarity. A 2× increase of δ_{2PA} is observed for G188 (n=3) in ACN (10000 GM) compared to toluene (4700 GM) at the sample spectral position. This enhancement can be explained by strong intermediate resonance enhancement induced by the large red-shift of its linear absorption

band $S_0 \rightarrow S_1$, which provides another approach to enhance δ_{2PA} by tuning the energy levels of intermediate and 2PA final states.

(3) Single Crystal made from a Donor-π-Acceptor Dye

Due to extremely high molecular packing density, organic single crystal made from G19 shows 2.5× larger peak 2PA coefficient (52±9 cm/GW) compared to inorganic semiconductor (CdTe) with a similar absorption edge. However, the optical properties, linear and nonlinear, are strongly dependent upon the incident polarization because of its anisotropic molecular packing pattern. X-ray diffraction analysis shows π-stacking dimers formation in the crystal, similar to H-aggregates. Confirmed by quantum chemical calculations, this dimerization leads to the splitting of the energy bands and the appearance of the new-shifted 2PA bands when compared to the monomer solution.

(4) NIR 2-Azaazulene Polymethine Dye

Due to the long conjugation length, this set of dyes shows the indication of ground state symmetry breaking, featured by an increase of linear absorption on its vibrational shoulder of main absorption band in polar solvents. Taking JB17-08 (n=3) as an example, the 2PA and ESA spectra of JB17-08 in DCM and ACN are investigated. Two quantum chemical approaches are introduced to analyze the linear and nonlinear optical properties with respect to the conjugation length and solvent polarity. Both experimental and quantum chemical analysis suggests that this molecule maintains its ground state symmetry in low polar solvent (e.g. DCM), but experiences strong symmetry-breaking in high polar solvent (e.g. ACN); however the symmetry of the excited state is still maintained in both solvents. The essential-state model, developed by Terenziani and Painelli *et al*, can well re-produce the linear, 2PA and ESA spectra of JB17-08 in

DCM and ACN with significant fewer amounts of fitting parameters compared to conventional Marcus-Hush model.

(5) Sulfur-squaraines and Oxygen-squaraines

Although the replacement of oxygen atom by sulfur atom in the electron acceptor (C_4O_2) at the center of the conjugation chain significantly enhances the intersystem crossing rate leading to a dramatic increase of the triplet quantum yield from oxygen-squaraine (O-SD) to sulfur- (or one-sulfur-one-oxygen-) squaraines (S-SD or SO-SD), the measured 2PA spectrum of S-SD (or SO-SD) is essentially the same as its O-SD counterpart. This observation indicates that while the 2PA transitions are mainly connected with the transitions along the main conjugation chain, the transitions related to sulfur atoms may not effectively influence the 2PA transition due to their orthogonality to the conjugation chain. Given that large δ_{2PA} and quantum yield of singlet O_2 generation, the S-SD and SO-SD can be a good candidate for two-photon photosensitizer for photodynamic therapy applications.

6.1.2 Nonlinear Refraction of Molecules

The second part of this dissertation investigates the NLR of molecules measured by the Z-scan technique. By utilizing a prism compressor/stretcher, the n_2 of a simple molecule (CS_2) is measured as the function of input pulsewidth. The n_2 and 2PA spectrum of neat CS_2, and other two organic molecules, an oxygen-squaraine and a bis(diarylaminostyryl) chromophore, are measured. The 3-level model, simplified from "Sum-over-states" model is used to analyze the dispersion of both n_2 and 2PA spectra of these molecules. The detailed conclusions are the following:

(1) Neat CS_2 shows strong pulsewidth dependent n_2. A continuous increase of n_2 is observed from 32 fs ($2.6 \pm 0.5 \times 10^{-15}$ cm^2/W), to 2.3 ps ($18 \pm 2.7 \times 10^{-15}$ cm^2/W) at 700 nm. The evolution of n_2 with respect to the incident pulsewidth demonstrates the increasing contribution from nuclei movement, which eventually dominates the NLR of CS_2 at 2 ps or longer pulsewidth. A polarization resolved Z-scan measurement confirms this trend.

(2) The n_2 spectra of neat CS_2 (obtained at pulsewidth less than 70 fs), and symmetrical oxygen-squaraine and bis(diarylaminostyryl) chromophores (obtained at pulsewidth ~140 fs), are investigated along with their 2PA spectra. Both 2PA and n_2 spectra can be fitted with the simple 3-level model under certain accuracy, which could help to develop molecular design approach to enhance NLR of organic molecules at certain operating wavelengths.

6.2 Future Work

On the basis of the conclusions listed in Section 6.1, a few potential research directions are proposed:

(1) While the current structure-2PA properties of organic molecules are getting richer and more diverse, there is still a long way to go to achieve the ultimate goal of developing a predictive capability for the nonlinear optical properties of organic molecules. More molecules with different structural modifications are still necessary in spite of the difficulty of molecular synthesis.

(2) Given the impressively strong nonlinearity of the G19 single crystal studied in this dissertation, synthesis and fabrication of solid-state organic single crystal of

sufficient optical quality is certainly a very promising direction. Fine quantum chemical analysis is also needed to study the inter-molecular interaction inside the crystal unit cell, to understand their optical properties and predict the spectral positions of 1PA and 2PA bands. Given the large 2PA coefficient of organic single crystals, a strong NLR is also expected and should be studied in more detail. To measure the NLR properties of the single crystal, the surface quality of the single crystal needs to be improved to reduce the scattering loss of the incident beam.

(3) Although sulfur-squaraine dyes shows a promising application as a two-photon photosensitizer, the photochemical stability needs to be improved which otherwise will limit their effectiveness. The toxicity of the chemicals and their solubility in water are also important issues for biomedical applications.

(4) Although this dissertation demonstrates the evolution of n_2 of neat CS_2 with respect to the input pulsewidth, the separation of the electronic and various nuclear contributions to n_2 is still a more difficult task. A convincing physical model is needed to decouple the physical mechanisms behind NLR of CS_2.

With the development of the dual-arm Z-scan, more NLR spectra of organic molecules should be measured and added into the database, which helps people to understand the structure-NLR property relations of organic molecules. A pulsewidth dependent study of their n_2 spectra will be an interesting topic to investigate.

APPENDIX A THE DERIVATION OF BOUND ELECTRONIC NONLINEAIRTY USING A SIMPLIED THREE-LEVEL MODEL FOR SYMMETRICAL MOLECULES

The formulism of SOS model can be found in Equation 2.26, where the *v*, *m*, *n* corresponds to all possible states excluding ground state. Therefore, $\chi^{(3)}_{ijkl}(-\omega;\omega,\omega-\omega)$, $\chi^{(3)}_{ijkl}(-\omega;\omega,-\omega,\omega)$, and $\chi^{(3)}_{ijkl}(-\omega;-\omega,\omega,\omega)$ can be written in Equations A.1 to A.3; and $\tilde{\chi}^{(3)}_{ijkl}(-\omega;\omega,\omega-\omega)$ is the summation of $\chi^{(3)}_{ijkl}(-\omega;\omega,\omega-\omega)$, $\chi^{(3)}_{ijkl}(-\omega;\omega,-\omega,\omega)$, and $\chi^{(3)}_{ijkl}(-\omega;-\omega,\omega,\omega)$.

$$
\begin{aligned}
&\chi^{(3)}_{ijkl}(-\omega;\omega,\omega,-\omega) = \frac{N}{\varepsilon_0\hbar^3} f^{(3)} \sum\nolimits'_{v,n,m} \\
&x\{\frac{\bar{\mu}_{gv,i}(\bar{\mu}_{vn,l}-\bar{\mu}_{gg,l})(\bar{\mu}_{nm,k}-\bar{\mu}_{gg,k})\bar{\mu}_{mg,j}}{(\bar{\omega}_{vg}-\omega)(\bar{\omega}_{ng}-2\omega)(\bar{\omega}_{mg}-\omega)} + \\
&+\frac{\bar{\mu}_{gv,l}(\bar{\mu}_{vn,i}-\bar{\mu}_{gg,i})(\bar{\mu}_{nm,k}-\bar{\mu}_{gg,k})\bar{\mu}_{mg,j}}{(\bar{\omega}^*_{vg}-\omega)(\bar{\omega}_{ng}-2\omega)(\bar{\omega}_{mg}-\omega)} + \frac{\bar{\mu}_{gv,j}(\bar{\mu}_{vn,k}-\bar{\mu}_{gg,k})(\bar{\mu}_{nm,i}-\bar{\mu}_{gg,i})\bar{\mu}_{mg,l}}{(\bar{\omega}^*_{vg}+\omega)(\bar{\omega}^*_{ng}+2\omega)(\bar{\omega}_{mg}+\omega)} \\
&+\frac{\bar{\mu}_{gv,j}(\bar{\mu}_{vn,k}-\bar{\mu}_{gg,k})(\bar{\mu}_{nm,l}-\bar{\mu}_{gg,l})\bar{\mu}_{mg,i}}{(\bar{\omega}^*_{vg}+\omega)(\bar{\omega}^*_{ng}+2\omega)(\bar{\omega}^*_{mg}+\omega)}\} \\
&-\frac{N}{\varepsilon_0\hbar^3} f^{(3)} \sum\nolimits'_{n,m} \{\frac{\bar{\mu}_{gn,i}\bar{\mu}_{ng,l}\bar{\mu}_{gm,k}\bar{\mu}_{mg,j}}{(\bar{\omega}_{ng}-\omega)(\bar{\omega}_{ng}+\omega)(\bar{\omega}_{mg}-\omega)} \\
&+\frac{\bar{\mu}_{gn,i}\bar{\mu}_{ng,l}\bar{\mu}_{gm,k}\bar{\mu}_{mg,j}}{(\bar{\omega}^*_{mg}+\omega)(\bar{\omega}_{ng}+\omega)(\bar{\omega}_{mg}-\omega)} + \frac{\bar{\mu}_{gn,l}\bar{\mu}_{ng,i}\bar{\mu}_{gm,j}\bar{\mu}_{mg,k}}{(\bar{\omega}^*_{ng}-\omega)(\bar{\omega}^*_{mg}+\omega)(\bar{\omega}_{mg}-\omega)} \\
&+\frac{\bar{\mu}_{gn,l}\bar{\mu}_{ng,i}\bar{\mu}_{gm,j}\bar{\mu}_{mg,k}}{(\bar{\omega}^*_{ng}-\omega)(\bar{\omega}^*_{mg}+\omega)(\bar{\omega}^*_{ng}+\omega)}\}
\end{aligned}
\qquad \text{(A. 1)}
$$

$$\chi^{(3)}_{ijkl}(-\omega;\omega,-\omega,\omega) = \frac{N}{\varepsilon_0\hbar^3} f^{(3)} \sum\nolimits'_{v,n,m}$$

$$x\{\frac{\overline{\mu}_{gv,i}(\overline{\mu}_{vn,l}-\overline{\mu}_{gg,l})(\overline{\mu}_{nm,k}-\overline{\mu}_{gg,k})\overline{\mu}_{mg,j}}{(\overline{\omega}_{vg}-\omega)(\overline{\omega}_{ng})(\overline{\omega}_{mg}-\omega)} +$$

$$+\frac{\overline{\mu}_{gv,j}(\overline{\mu}_{vn,k}-\overline{\mu}_{gg,k})(\overline{\mu}_{nm,i}-\overline{\mu}_{gg,i})\overline{\mu}_{mg,l}}{(\overline{\omega}^*_{vg}+\omega)(\overline{\omega}^*_{ng})(\overline{\omega}_{mg}-\omega)} + \frac{\overline{\mu}_{gv,l}(\overline{\mu}_{vn,i}-\overline{\mu}_{gg,i})(\overline{\mu}_{nm,k}-\overline{\mu}_{gg,k})\overline{\mu}_{mg,j}}{(\overline{\omega}^*_{vg}+\omega)(\overline{\omega}_{ng})(\overline{\omega}_{mg}-\omega)}$$

$$+\frac{\overline{\mu}_{gv,j}(\overline{\mu}_{vn,k}-\overline{\mu}_{gg,k})(\overline{\mu}_{nm,l}-\overline{\mu}_{gg,l})\overline{\mu}_{mg,i}}{(\overline{\omega}^*_{vg}+\omega)(\overline{\omega}^*_{ng})(\overline{\omega}^*_{mg}+\omega)}\}$$

$$-\frac{N}{\varepsilon_0\hbar^3} f^{(3)} \sum\nolimits'_{n,m} \quad \{\frac{\overline{\mu}_{gn,i}\overline{\mu}_{ng,l}\overline{\mu}_{gm,k}\overline{\mu}_{mg,j}}{(\overline{\omega}_{ng}-\omega)(\overline{\omega}_{ng}-\omega)(\overline{\omega}_{mg}-\omega)}$$

$$+\frac{\overline{\mu}_{gn,i}\overline{\mu}_{ng,l}\overline{\mu}_{gm,k}\overline{\mu}_{mg,j}}{(\overline{\omega}^*_{mg}-\omega)(\overline{\omega}_{ng}-\omega)(\overline{\omega}_{mg}-\omega)} + \frac{\overline{\mu}_{gn,l}\overline{\mu}_{ng,i}\overline{\mu}_{gm,j}\overline{\mu}_{mg,k}}{(\overline{\omega}^*_{ng}+\omega)(\overline{\omega}^*_{mg}+\omega)(\overline{\omega}_{mg}+\omega)}$$

$$+\frac{\overline{\mu}_{gn,l}\overline{\mu}_{ng,i}\overline{\mu}_{gm,j}\overline{\mu}_{mg,k}}{(\overline{\omega}^*_{ng}+\omega)(\overline{\omega}^*_{mg}+\omega)(\overline{\omega}^*_{ng}+\omega)}\} \qquad \text{(A. 2)}$$

$$\chi^{(3)}_{ijkl}(-\omega;-\omega,\omega,\omega) = \frac{N}{\varepsilon_0\hbar^3} f^{(3)} \sum\nolimits'_{v,n,m}$$

$$x\{\frac{\bar{\mu}_{gv,i}(\bar{\mu}_{vn,l}-\bar{\mu}_{gg,l})(\bar{\mu}_{nm,k}-\bar{\mu}_{gg,k})\bar{\mu}_{mg,j}}{(\bar{\omega}_{vg}-\omega)(\bar{\omega}_{ng})(\bar{\omega}_{mg}+\omega)} +$$

$$+\frac{\bar{\mu}_{gv,j}(\bar{\mu}_{vn,k}-\bar{\mu}_{gg,k})(\bar{\mu}_{nm,i}-\bar{\mu}_{gg,i})\bar{\mu}_{mg,l}}{(\bar{\omega}^*_{vg}-\omega)(\bar{\omega}^*_{ng})(\bar{\omega}_{mg}-\omega)} + \frac{\bar{\mu}_{gv,l}(\bar{\mu}_{vn,i}-\bar{\mu}_{gg,i})(\bar{\mu}_{nm,k}-\bar{\mu}_{gg,k})\bar{\mu}_{mg,j}}{(\bar{\omega}^*_{vg}+\omega)(\bar{\omega}_{ng})(\bar{\omega}_{mg}+\omega)}$$

$$+\frac{\bar{\mu}_{gv,j}(\bar{\mu}_{vn,k}-\bar{\mu}_{gg,k})(\bar{\mu}_{nm,l}-\bar{\mu}_{gg,l})\bar{\mu}_{mg,i}}{(\bar{\omega}^*_{vg}-\omega)(\bar{\omega}^*_{ng})(\bar{\omega}^*_{mg}+\omega)}\}$$

$$-\frac{N}{\varepsilon_0\hbar^3} f^{(3)} \sum\nolimits'_{n,m} \quad \{\frac{\bar{\mu}_{gn,i}\bar{\mu}_{ng,l}\bar{\mu}_{gm,k}\bar{\mu}_{mg,j}}{(\bar{\omega}_{ng}-\omega)(\bar{\omega}_{ng}-\omega)(\bar{\omega}_{mg}+\omega)}$$

$$+\frac{\bar{\mu}_{gn,i}\bar{\mu}_{ng,l}\bar{\mu}_{gm,k}\bar{\mu}_{mg,j}}{(\bar{\omega}^*_{mg}+\omega)(\bar{\omega}_{ng}-\omega)(\bar{\omega}_{mg}+\omega)} + \frac{\bar{\mu}_{gn,l}\bar{\mu}_{ng,i}\bar{\mu}_{gm,j}\bar{\mu}_{mg,k}}{(\bar{\omega}^*_{ng}+\omega)(\bar{\omega}^*_{mg}-\omega)(\bar{\omega}_{mg}-\omega)}$$

$$+\frac{\bar{\mu}_{gn,l}\bar{\mu}_{ng,i}\bar{\mu}_{gm,j}\bar{\mu}_{mg,k}}{(\bar{\omega}^*_{ng}+\omega)(\bar{\omega}^*_{mg}-\omega)(\bar{\omega}^*_{ng}+\omega)}\} \qquad \text{(A. 3)}$$

Noted that they have different denominators, $\chi^{(3)}_{ijkl}(-\omega;\omega,\omega-\omega)$, $\chi^{(3)}_{ijkl}(-\omega;\omega,-\omega,\omega)$, and $\chi^{(3)}_{ijkl}(-\omega;-\omega,\omega,\omega)$ are not equal to each other in general case, except when $\omega\rightarrow 0$ in DC limit. Another important observation for $\chi^{(3)}_{ijkl}(-\omega;\omega,\omega-\omega)$ is that in the first two terms contains $(\bar{\omega}_{ng}-2\omega)$ in denominator, corresponding to a two-photon transition, which is the origin of T terms (for 3-level model) and D terms (2-level model) in Equation 2.28. $\chi^{(3)}_{ijkl}(-\omega;\omega,-\omega,\omega)$ contains $(\bar{\omega}_{ng}-\omega)(\bar{\omega}_{ng}-\omega)(\bar{\omega}_{mg}-\omega)$ and $(\bar{\omega}^*_{ng}-\omega)(\bar{\omega}_{ng}-\omega)(\bar{\omega}_{mg}-\omega)$ terms in denominator for the fifth and sixth terms, hence it is the origin of N terms in Equation 2.28. $\chi^{(3)}_{ijkl}(-\omega;-\omega,\omega,\omega)$ contains no resonance term, it thus has minimum contribution at both one- and two-photon resonance.

For 3-level model indicated in Figure 2.1, there are six possibilities to assign *v, m, and n*. They are: 1) *m=n=e'*, *v=e*; 2) *m= e'*, *v=n=e*; 3) *v=e'*, *m=n=e*; 4) *v=n=e'*, *m=e*; 5) *n =e'*, *v=m=e*; 6) *v=m=e'*, *n=e*. For symmetrical dye considering $\mu_{e'e'}=\mu_{ee}=\mu_{gg}=0$ and $\mu_{ge}'=0$, it can be verified that only case 3) and case 5) show non-zero contributions.

For case 3), terms in $\sum_{v,n,m}^{'}$ are zero, the 3 $\chi_{xxxx}^{(3)}$ s can be expressed in:

$$\chi_{xxxx}^{\prime(3)}(-\omega;\omega,\omega,-\omega)=$$
$$-\frac{N}{\varepsilon_0\hbar^3}f^{(3)}\left|\mu_{ge}\right|^4\{\frac{1}{(\overline{\omega}_{eg}-\omega)(\overline{\omega}_{eg}+\omega)(\overline{\omega}_{eg}-\omega)}+\frac{1}{(\overline{\omega}_{eg}^{*}+\omega)(\overline{\omega}_{eg}+\omega)(\overline{\omega}_{eg}-\omega)} \quad \text{(A. 4)}$$
$$+\frac{1}{(\overline{\omega}_{eg}^{*}-\omega)(\overline{\omega}_{eg}^{*}+\omega)(\overline{\omega}_{eg}-\omega)}+\frac{1}{(\overline{\omega}_{eg}^{*}-\omega)(\overline{\omega}_{eg}^{*}+\omega)(\overline{\omega}_{eg}^{*}+\omega)}\}$$

$$\chi_{xxxx}^{\prime(3)}(-\omega;\omega,-\omega,\omega)=$$
$$-\frac{N}{\varepsilon_0\hbar^3}f^{(3)}\left|\mu_{\mathrm{ge}}\right|^4\{\frac{1}{(\overline{\omega}_{eg}-\omega)(\overline{\omega}_{eg}-\omega)(\overline{\omega}_{eg}-\omega)}+\frac{1}{(\overline{\omega}_{eg}^{*}-\omega)(\overline{\omega}_{eg}-\omega)(\overline{\omega}_{eg}-\omega)} \quad \text{(A. 5)}$$
$$+\frac{1}{(\overline{\omega}_{eg}^{*}+\omega)(\overline{\omega}_{eg}^{*}+\omega)(\overline{\omega}_{eg}+\omega)}+\frac{1}{(\overline{\omega}_{eg}^{*}+\omega)(\overline{\omega}_{eg}^{*}+\omega)(\overline{\omega}_{eg}^{*}+\omega)}\}$$

$$\chi_{xxxx}^{\prime(3)}(-\omega;-\omega,\omega,\omega)=$$
$$-\frac{N}{\varepsilon_0\hbar^3}f^{(3)}\left|\mu_{\mathrm{ge}}\right|^4\{\frac{1}{(\overline{\omega}_{eg}-\omega)(\overline{\omega}_{eg}-\omega)(\overline{\omega}_{eg}+\omega)}+\frac{1}{(\overline{\omega}_{eg}^{*}+\omega)(\overline{\omega}_{eg}-\omega)(\overline{\omega}_{eg}+\omega)} \quad \text{(A. 6)}$$
$$+\frac{1}{(\overline{\omega}_{eg}^{*}+\omega)(\overline{\omega}_{eg}^{*}-\omega)(\overline{\omega}_{eg}-\omega)}+\frac{1}{(\overline{\omega}_{eg}^{*}+\omega)(\overline{\omega}_{eg}^{*}-\omega)(\overline{\omega}_{eg}^{*}+\omega)}\}$$

For Case 5), terms in $\sum_{n,m}^{'}$ are zero, the 3 $\chi_{xxxx}^{(3)}$ s can be expressed in:

$$\chi''^{(3)}_{xxxx}(-\omega;\omega,\omega,-\omega) = \frac{N}{\varepsilon_0\hbar^3} f^{(3)}\left|\mu_{ge}\right|^2\left|\mu_{ee'}\right|^2\{\frac{1}{(\overline{\omega}_{eg}-\omega)(\overline{\omega}_{e'g}-2\omega)(\overline{\omega}_{eg}-\omega)}+\frac{1}{(\overline{\omega}^*_{eg}+\omega)(\overline{\omega}^*_{e'g}+2\omega)(\overline{\omega}_{eg}+\omega)} + \frac{1}{(\overline{\omega}^*_{eg}-\omega)(\overline{\omega}_{e'g}-2\omega)(\overline{\omega}_{eg}-\omega)}+\frac{1}{(\overline{\omega}^*_{eg}+\omega)(\overline{\omega}^*_{e'g}+2\omega)(\overline{\omega}^*_{eg}+\omega)}\} \quad \text{(A. 7)}$$

$$\chi''^{(3)}_{xxxx}(-\omega;\omega,-\omega,\omega) = \frac{N}{\varepsilon_0\hbar^3} f^{(3)}\left|\mu_{ge}\right|^2\left|\mu_{ee'}\right|^2\{\frac{1}{(\overline{\omega}_{eg}-\omega)(\overline{\omega}_{e'g})(\overline{\omega}_{eg}-\omega)}+\frac{1}{(\overline{\omega}^*_{eg}+\omega)(\overline{\omega}^*_{e'g})(\overline{\omega}_{eg}-\omega)} + \frac{1}{(\overline{\omega}^*_{eg}+\omega)(\overline{\omega}_{e'g})(\overline{\omega}_{eg}-\omega)}+\frac{1}{(\overline{\omega}^*_{eg}+\omega)(\overline{\omega}^*_{e'g})(\overline{\omega}^*_{eg}+\omega)}\} \quad \text{(A. 8)}$$

$$\chi''^{(3)}_{xxxx}(-\omega;-\omega,\omega,\omega) = \frac{N}{\varepsilon_0\hbar^3} f^{(3)}\left|\mu_{ge}\right|^2\left|\mu_{ee'}\right|^2\{\frac{1}{(\overline{\omega}_{eg}-\omega)(\overline{\omega}_{e'g})(\overline{\omega}_{eg}+\omega)}+\frac{1}{(\overline{\omega}^*_{eg}-\omega)(\overline{\omega}^*_{e'g})(\overline{\omega}_{eg}-\omega)} + \frac{1}{(\overline{\omega}^*_{eg}+\omega)(\overline{\omega}_{e'g})(\overline{\omega}_{eg}+\omega)}+\frac{1}{(\overline{\omega}^*_{eg}-\omega)(\overline{\omega}^*_{e'g})(\overline{\omega}^*_{eg}+\omega)}\} \quad \text{(A. 9)}$$

Based on Equation 2.10, the $\tilde{\chi}^{(3)}_{xxxx}(-\omega;\omega,\omega,-\omega)$ can be expressed in form of summation of Equation A. 4 through A. 9 which possesses a total of 24 terms, and then divided by a factor of 3. The analytical expression of $\tilde{\chi}^{(3)}_{xxxx}(-\omega;\omega,\omega,-\omega)$ is extremely complicated, nevertheless possible [1]. Presented in Figure A. 1 is the dispersion curve of each $\chi^{(3)}_{xxxx}$ component in its real and imaginary part, as well as their summations. Evidently, the 2PA resonance, located at $\omega_{e'g}/2$, is attributed to $\chi^{(3)}_{xxxx}(-\omega;\omega,\omega,-\omega)$; whereas $\chi^{(3)}_{xxxx}(-\omega;\omega,-\omega,\omega)$ shows dominating contribution when the photon energy is approaching to absorption gap, ω_{eg}, corresponding the N term. $\chi^{(3)}_{xxxx}(-\omega;-\omega,\omega,\omega)$ doesn't contain any strong resonant terms in denominator, and thus is almost a constant across the whole spectrum except close to absorption gap, showing minimum contribution to the overall nonlinearity.

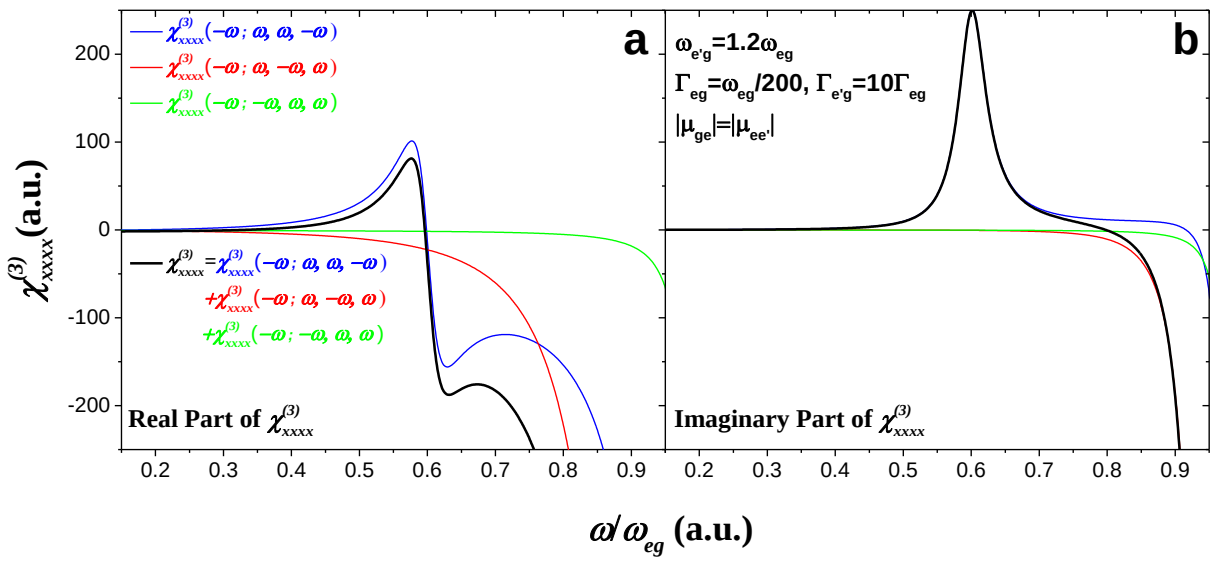

Figure A. 1: Dispersion of real (a) and imaginary (b) part of different $\chi^{(3)}_{xxxx}$ components

To estimate the bound electronic n_2 in DC limit ($\omega \to 0$), All $\chi'^{(3)}_{xxxx}$ components converge to

$$\chi'^{(3)}_{xxxx}|_{DC} = -\frac{N}{\varepsilon_0 \hbar^3} f^{(3)} |\mu_{ge}|^4 \{\frac{1}{(\bar{\omega}_{eg})^3} + \frac{1}{|\bar{\omega}_{eg}|^2 \bar{\omega}_{eg}} + \frac{1}{|\bar{\omega}_{eg}|^2 \bar{\omega}^*_{eg}} + \frac{1}{(\bar{\omega}^*_{eg})^3}\} \quad \text{(A. 10)}$$

All $\chi''^{(3)}_{xxxx}$ components converge to

$$\chi''^{(3)}_{xxxx}|_{DC} = \frac{N}{\varepsilon_0 \hbar^3} f^{(3)} |\mu_{ge}|^2 |\mu_{ee'}|^2 \{\frac{1}{(\bar{\omega}_{eg})^2 \bar{\omega}_{e'g}} + \frac{1}{|\bar{\omega}_{eg}|^2 \bar{\omega}^*_{e'g}} + \frac{1}{|\bar{\omega}_{eg}|^2 \bar{\omega}_{e'g}} + \frac{1}{(\bar{\omega}^*_{eg})^2 \bar{\omega}^*_{e'g}}\} \quad \text{(A. 11)}$$

Therefore, we can write $\hat{\chi}^{(3)}_{xxxx}|_{DC}$ as

$$\hat{\chi}^{(3)}_{xxxx}\,|_{DC} = \chi'^{(3)}_{xxxx}\,|_{DC} + \chi''^{(3)}_{xxxx}\,|_{DC}$$

$$= \frac{N}{\varepsilon_0 \hbar^3} f^{(3)} \left|\mu_{ge}\right|^2 \frac{(\overline{\omega}_{eg} + \overline{\omega}^*_{eg})}{\left|\overline{\omega}_{eg}\right|^4} \left\{ \frac{(\overline{\omega}_{eg}\overline{\omega}_{e'g} + \overline{\omega}^*_{eg}\overline{\omega}^*_{e'g})}{\left|\overline{\omega}_{e'g}\right|^2} \left|\mu_{ee'}\right|^2 - \frac{[(\overline{\omega}^2_{eg} + (\overline{\omega}^*_{eg})^2]}{\left|\overline{\omega}_{eg}\right|^2} \left|\mu_{ge}\right|^2 \right\} \quad \text{(A. 12)}$$

If we assume that $\Gamma_{eg} << \omega_{eg}$, $\Gamma_{eg} << \omega_{eg}$. Equation A. 12 can be further simplified to

$$\hat{\chi}^{(3)}_{xxxx}\,|_{DC} = \frac{4N}{\varepsilon_0 \hbar^3} f^{(3)} \frac{\left|\mu_{ge}\right|^2}{\omega^3_{eg}} \left\{ \frac{\omega_{eg}}{\omega_{e'g}} \left|\mu_{ee'}\right|^2 - \left|\mu_{ge}\right|^2 \right\} \quad \text{(A. 13)}$$

It is also important to note that here we consider only one 2PA final state; the 3-level model can be easily extended to multi- 2PA final states, if all these 2PA final states share the same intermediate state. For each 2PA final state, equation A. 7-A. 9 should be repeated to each 2PA final state with different $\omega_{e'g}$ and $\mu_{ee'}$. The overall $\hat{\chi}^{(3)}_{xxxx}$ is the summation of all these terms.

APPENDIX B DERIVATION OF 2PA CROSS SECTION FROM RESONANCE TERMS OF THREE-LEVEL MODEL

The T terms in Equation 2.28 can be written as

$$\widehat{\chi}^{(3)}_{xxxx,T-term} = \frac{N}{\hbar^3 \varepsilon_0}\left(\frac{\left|\mu^x_{ge}\right|^2 \left|\overline{\mu}^x_{ee'}\right|^2}{(\overline{\omega}_{eg}-\omega)(\overline{\omega}_{e'g}-2\omega)(\overline{\omega}_{eg}-\omega)} + \frac{\left|\mu^x_{ge}\right|^2 \left|\overline{\mu}^x_{ee'}\right|^2}{(\overline{\omega}^*_{eg}-\omega)(\overline{\omega}_{e'g}-2\omega)(\overline{\omega}_{eg}-\omega)} \right) \quad \text{(B. 1)}$$

where $\overline{\omega}_{eg} = \omega_{eg} - i\Gamma_{eg}$, $\overline{\omega}_{e'g} = \omega_{e'g} - i\Gamma_{e'g}$. Note that the local field correction is not considered here.

Pluging complex expression for resonance frequencies, $\widehat{\chi}^{(3)}_{xxxx,T-term}$ can be written as

$$\widehat{\chi}^{(3)}_{xxxx,T-term} = \frac{N}{\hbar^3 \varepsilon_0}\left|\mu^x_{ge}\right|^2 \left|\overline{\mu}^x_{ee'}\right|^2 \frac{1}{(\omega_{eg}-\omega-i\Gamma_{eg})(\omega_{e'g}-2\omega-i\Gamma_{e'g})}\left(\frac{1}{(\omega_{eg}-\omega-i\Gamma_{eg})} + \frac{1}{(\omega_{eg}-\omega+i\Gamma_{eg})} \right) \quad \text{(B. 2)}$$

$$= \frac{N}{\hbar^3 \varepsilon_0}\left|\mu^x_{ge}\right|^2 \left|\overline{\mu}^x_{ee'}\right|^2 \frac{(\omega_{eg}-\omega+i\Gamma_{eg})(\omega_{e'g}-2\omega+i\Gamma_{e'g})}{\left[(\omega_{eg}-\omega)^2+\Gamma^2_{eg}\right]\left[(\omega_{e'g}-2\omega)^2+\Gamma^2_{e'g}\right]} \frac{2(\omega_{eg}-\omega)}{\left[(\omega_{eg}-\omega)^2+\Gamma^2_{eg}\right]}$$

Separating real and imaginary part of the Equation B.2 leads to

$$\mathrm{Im}(\widehat{\chi}^{(3)}_{xxxx,T-term}) = \frac{2N}{\hbar^3 \varepsilon_0}\frac{1}{\left[(\omega_{eg}-\omega)^2+\Gamma^2_{eg}\right]} \frac{\left|\mu^x_{ge}\right|^2 \left|\overline{\mu}^x_{ee'}\right|^2 \Gamma_{e'g}}{\left[(\omega_{e'g}-2\omega)^2+\Gamma^2_{e'g}\right]} \cdot K \quad \text{(B. 3)}$$

where K is expressed as

$$K = \frac{[(\omega_{eg}-\omega)\Gamma_{e'g} + \Gamma_{eg}(\omega_{e'g}-2\omega)](\omega_{eg}-\omega)}{\left[(\omega_{eg}-\omega)^2+\Gamma^2_{eg}\right]\Gamma_{e'g}} \quad \text{(B. 4)}$$

Assuming the incident photon energy is off-resonant with the 1PA transition, *i.e.* $\omega_{eg}-\omega >> \Gamma_{eg} \rightarrow (\omega_{eg}-\omega)^2+\Gamma^2_{eg} \approx (\omega_{eg}-\omega)^2$, K can be simplified as

$$K \approx 1 + \frac{(\omega_{e'g}-2\omega)}{(\omega_{eg}-\omega)}\frac{\Gamma_{eg}}{\Gamma_{e'g}} \quad \text{(B. 5)}$$

At near 2PA resonance, $(\omega_{e'g}-2\omega) << (\omega_{eg}-\omega)$, $K \approx 1$.

Applying Equation B.3 into Equation 2.30, we can get

$$\delta_{2PA}(\omega)\Big|_{T-term} = \frac{1}{5c^2\hbar n^2\varepsilon_0^2}\frac{(\hbar\omega)^2}{(\hbar\omega_{eg}-\hbar\omega)^2+\Gamma_{eg}{}^2}\left[\frac{\left|\mu_{eg}\right|^2\left|\mu_{ee'}\right|^2\Gamma_{e'g}}{(\hbar\omega_{e'g}-2\hbar\omega)^2+\Gamma_{e'g}{}^2}\right] \quad \text{(B. 6)}$$

Note that the term in "**[]**" follows the Lorenzian shape, which shows minimum contribution when ω is off resonance from $\omega_{e'g}$. Since D-term in Equation 2.28 shows the same formulism as T-term, we can get the same result in "**[]**" except $\hbar\omega_{e'g}$ is replaced by $\hbar\omega_{eg}$, and $\mu_{ee'}$ is replaced by $\Delta\mu$. Summation of D- and T-term leads to Equation 2.32.

APPENDIX C IMPORTANT PROCEDURES TO MEASURE FLUORESCENCE OF SOLUTION-BASED SAMPLES

The purpose of this appendix is to make user be aware of some important steps in using the PTI spectrofluorometer for a successful fluorescence measurement. It is still necessary that user need to refer to the manual written by Dr. Jie Fu in powerpoint (stored in the shared drive) for procedures in detailed graphs.

(1) Introduction of Fluorometer

Fluorometer is a device which can measure the fluorescence properties of a sample. Shown in Figure C. 1 is the photograph of a PTI Quantamaster spectrofluorometer used in this dissertation. It essentially contains two major parts: excitation source and detection system. The broadband excitation is provided by the Xenon lamp, with the excitation wavelength selected by the excitation monochromator. The sample, usually in solution form filled in 1 cm cuvette, is placed in the sample compartment. The two detection systems are placed at 90 ° in T-format geometry with respect to the excitation to minimize the excitation scattering (shown in Figure C. 1). Three PMT detector systems are adopted in the fluorometer. They are Hamamatsu R1527P (for emission channel A, maximum detection wavelength λ^{max}=700 nm), Hamamatsu R928P (for emission channel B, maximum detection wavelength λ^{max}=800 nm) and liquid-nitrogen cooled Hamamatsu R5509-73 (for NIR channel, maximum detection wavelength λ^{max}=1700 nm). Channel A and B can be scanned simultaneously, while the NIR channel shares the same detection channel with channel B. For each channel (A and B), there is a monochromator used to select detection wavelength. The monochromator has two set of reflective grating; one has 1200 lines/mm with blaze wavelength λ_b=400 nm, and the other has 600 line/mm with blaze wavelength λ_b=1.25 μm. It is recommended that for wavelengths shorter than 600 nm, 1200 lines/mm grating is more effective than 600 line/mm grating, and otherwise, 600 line/mm grating is better. The selection of the grating can be achieved by rotating the knob on the top of the

monochromator. Note that it is a *one-way* knob, which can be turn in only one direction. For channel B monochromator, there is a switch knob to control the mirror deflecting fluorescence signal to either channel B PMT or NIR PMT detectors. Note that user needs to *press* and *then turn* in order to make the switch work. The resolution of the monochromator is determined by the width of the entrance and exit slit. For 1200 line/mm grating, every half turn of the micrometer equals to 1 nm wavelength resolution (FWHM), while for 600 line/mm grating, every half turn of the micrometer equal to 2 nm wavelength resolution. The channel A and B PMT detectors have two working mode: digital and analog. In digital mode, the detectors are biased at high voltage (≤1000 V) for maximum sensitivity. Digital mode is used in one-photon fluorescence (1PF) measurement. During two-photon fluorescence (2PF) experiment, the detectors are set at analog mode for minimum dark current. There are three major components not shown in Figure C. 1: a Brytebox for electronic control, a step motor control box and a liquid nitrogen cooling system for NIR PMT.

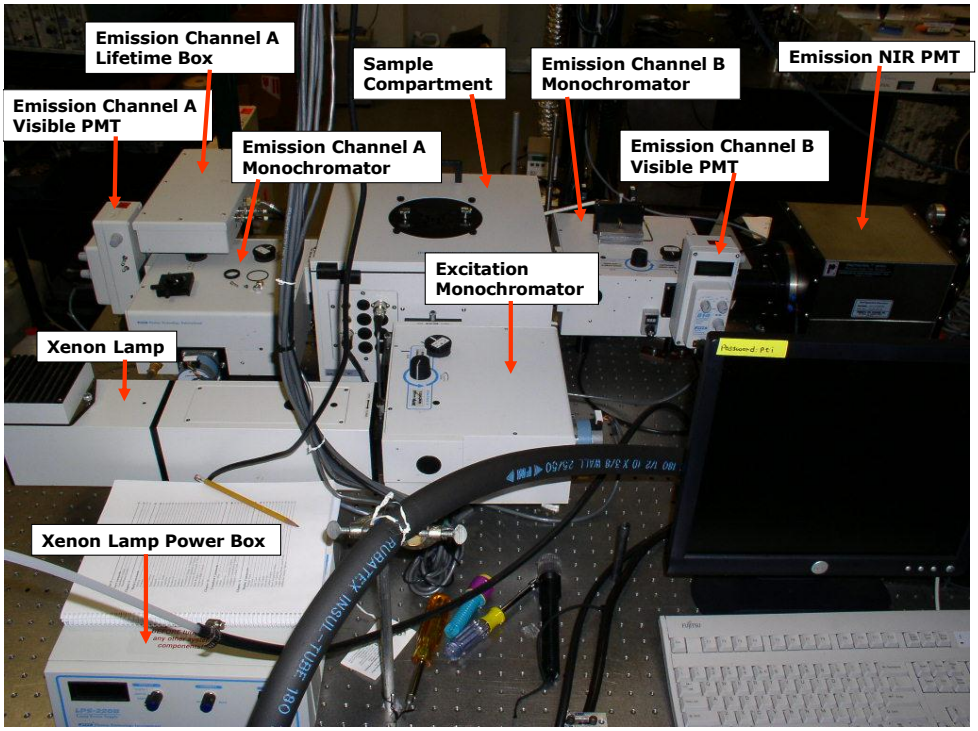

Figure C. 1: Photograph of PTI Quantamaster spectrofluorometer.

(2) Steps to turn on and off the fluorometer (without using NIR PMT)

To turn on the fluorometer, follow the steps below

1. Turn on the Xenon lamp. Make sure every other component is OFF (including computer) before pressing the "power" button on the lamp power supply. After pressing the "power" button, slowly turn up the current by rotating the knob. At some point the lamp will automatically ignited, keep turning up the power to ~45 W. If the lamp is not automatically ignited, user may need to press the "ignite" button manually. It is advised that lamp need to be warmed up by ~20-30 minutes for the excitation power to be stabilized. After lamp is warmed up, turn up the power to 59 W maximum. Note *do not* let the power exceeding 60 W, which may burn the lamp.

2. Make sure the BNC cable labeled as "B" is connected to digital "D2" port in the Byratebox. Make sure channel A and B PMTs are in digital mode with bias voltage ≤ 1000 V.

Turn on Byratebox and step motor controller box (wait until the light on the Byratebox turning to green).

3. The 1200 line/mm grating is selected for both excitation and emission monochromator, make sure the mirror switch of emission B monochromator is deflecting the fluorescence signal to visible PMT (correction file for PMT A and B is measured using 1200 line/mm grating).

4. Open the slit of monochromator to by rotating 1 turn in *both* entrance and exit port. However, it is necessary to adjust the slit width depending upon the intensity of the fluorescence signal. Note that the fluorescence signal is proportional to the square of the slit width, and both entrance and exit slit should keep approximately the same width.

5. Turn on the computer, and follow the instruction on the manual to choose the right configuration file, initialize the step motor and select the right acquisition method.

During fluorescence measurement

1. Make sure all the apertures are open. There are two apertures at the entrance and exit port of excitation monochromator, and one aperture at the entrance port of both emission monochromators.

2. Frequently check the power reading on the lamp power supply, make sure it doesn't exceed 60W.

3. Make sure the peak fluorescence intensity doesn't exceed 350,000 counts, too strong fluorescence intensity will induce nonlinearity of the detector. The fluorescence intensity can be adjusted by changing the width of the monochromator slits. Be careful if the wavelength range of the emission scan covers the excitation wavelength, the scattering from excitation might saturate the detector.

4. All the measured fluorescence spectra need to multiply by a correction file to compensate the spectral response of the detector. These correction file can be found the NLO group shared drive.

To turn off the fluorometer, follow the turning on procedure in reverse direction.

(3) Steps to turn on and off the fluorometer (using NIR PMT)

1. Fill the 10 L Dewar with liquid nitrogen. Be careful during filling process to make sure no large amount of liquid nitrogen spilled onto the body, especially to human eyes. If the Dewar is completely full, it will keep the NIR detector at a specified temperature (-80 ℃) for up to 10 hours including 2-hour cooling time. After filling the liquid nitrogen, the rubber adaptor on top of the Dewar will be *frozen*. Wait for 10-15 minutes until it warms up and gets softened before inserting the hose. A soft rubber adaptor provides a good sealing.

2. Insert hose into the Dewar, *slowly*. If too fast, the room temperature hose will boil the liquid nitrogen and spill it out. Keep the bottom of the hose at least 1 cm above the bottom of the Dewar. A common practice is first inserting the hose completely, and then pulling it up by about 1 cm.

3. Turn on the gas nitrogen cylinder, and keep the pressure between 25-35 kPa. Too high pressure will cool the detector too fast causing damage.

4. Make sure all the components are in OFF status. Turn on the cooling control box. Make sure the electromagnetic valve is working (by hearing a click sound), and the nitrogen gas is blowing out of the venting tube. Monitor the temperature indicator on the cooling control box. The temperature of the NIR PMT should be cooled down to -80 ℃ in about 10 minutes.

5. After the detector is cooled to -80 ℃, wait for at least 2 hours to make sure the core of the detector is completely cooled down.

6. Turn on the Xenon lamp as instructed in previous section.

7. Turn on the high voltage supply box for the NIR PMT by following the instructions on the manual. *Slowly* turn up the voltage to -1700 V by 100 V in each step. Sudden applying the high voltage to the NIR PMT will damage the detector.

8. Make sure the BNC cable labeled as "IR" is connected to digital "D2" port in the Byratebox. Turn on Byratebox and step motor controller box (wait until the light on the Byratebox turning to green).

9. The grating selection of the excitation monochromator depends upon the excitation wavelength. The emission monochromator is set at 600 line/mm grating and the mirror should be switched to NIR direction.

10. Follow steps 4 and 5 in turning on the fluorometer in previous section. Note that during wavelength initiation, the reading on the grating meter should multiply by 2 to reflect the reading on the computer.

During fluorescence measurement, *frequently* acquire background before fluorescence measurement. Note that the background signal may gradually increase during measurement. NIR PMT has much higher dark current counts than PMT A and B. A typical reading of dark current is between 21,000 – 30,000 counts for NIR PMT, as opposed to less than 200 counts for PMT A and B.

Another important issue during fluorescence measurement is always keep in mind to avoid the second-order diffraction leaked from the monochromator, i.e. for a monochromator selecting wavelength λ_{exc}, light with wavelength of $\lambda_{exc}/2$ may also leak out of the monochromator since the angle of second-order diffraction for $\lambda_{exc}/2$ is equal to the angle of first-

order diffraction of λ_{exc} [47]. Therefore, a long-wavelength-pass filter with appropriate cut-off wavelength is necessary to block $\lambda_{exc}/2$.

To turn off the fluorometer, follow the turning on procedure in reverse direction.

(3) 1PF spectrum and quantum yield measurement

The key to a successful fluorescence measurement is sample preparation. For a typical linear π-conjugated cyanine-like dye, the stokes-shift between absorption and fluorescence peak is usually 10-30 nm. A significant spectral overlap between absorption and fluorescence spectra will induce re-absorption of the fluorescence, thus artificially alter the fluorescence spectral shape, given the peak OD of the solution is high (OD>0.5). Therefore, to minimize the re-absorption of fluorescence, the peak OD of the solution is usually less than 0.1 (corresponding to ~80% transmittance in the absorption peak). If the quantum yield of the solution is very low, the concentration of the solution can be increased to OD~0.2, however the measured fluorescence spectrum is usually noisy (due to low quantum yield) and only reflects the approximate shape.

To measure the quantum yield (Φ_F) of the solution, a reference solution with known Φ_F is required in order to compare the fluorescence signal between sample and reference. The reference molecule should be chosen that its main absorption band overlaps the main absorption band of the sample molecule, in which case both sample and reference solutions can be excited at close excitation wavelengths. Several reference molecules are available with absorption, fluorescence peak and fluorescence quantum yield listed in Table C. 1. It is recommended that the peak ODs between sample and solvent are close with less than 10% difference. Make sure that the measuring condition remains *unchanged* when comparing fluorescence signal between sample and reference solutions, i.e. slit width of the monochromator, power of the lamp, *etc*. Using the same wavelength to excite sample and reference solution is highly recommended since

it will eliminate a major error source – excitation power. However, in some cases of which the absorption peak is significantly different between sample and solvent solution, using different wavelengths to excite sample and reference solution is inevitable. The excitation power should be carefully measured at these excitation wavelengths. A PD-300 UV or IR power meter is used to measure the excitation power.

Table C. 1: The absorption (λ_{abs}), fluorescence (λ_{FL}) peak, and fluorescence quantum yield (Φ_F) of the reference molecules [56,59,60,167].

Molecule	Solvent	λ_{abs} (nm)	λ_{FL} (nm)	Φ_F
Anthracene	ETH	357	398	0.27
Quinine Sulfate	0.1 M sulfuric acid	347	454	0.58
Rhodamine 6G	ETH	530	553	0.95
Cresyl Violet	MEOH	593	618	0.54
PD 2631	ETH	783	805	0.11

The quantum yield of sample solution can be estimated by Equation C.1 as

$$\Phi_{F,sample} = \Phi_{F,ref} \frac{\dfrac{< F >_{sample} n_{sample}^2}{OD(\lambda_{exc}^{sample})}}{\dfrac{< F >_{ref} n_{ref}^2}{OD(\lambda_{exc}^{ref})}} \frac{\Psi(\lambda_{exc}^{ref})}{\Psi(\lambda_{exc}^{sample})} \quad \text{(C. 1)}$$

where $<F>$ is the integrated fluorescence signal, n is the refractive index of the solvent, λ_{exc} is the excitation wavelength of sample and reference solution respectively; OD is the optical density, and ψ is the *photon flux* at the excitation wavelengths of sample and reference solution respectively. The photon flux is proportional to the multiplication of excitation power and excitation wavelength. For sample Φ_F larger than 2%, the absolute measurement error is ±10-

20%; however, if molecules are excited at the same wavelength, the relative error will be smaller. If the sample Φ_F is less than 2%, the noisy fluorescence spectrum could induce extra error.

(4) 1PF excitation anisotropy measurement

The fluorescence excitation anisotropy is used to determine the angle between absorption transition and fluorescence emission dipole moments. To accurately determine the excitation anisotropy, the fluorescence lifetime should be much shorter than the re-orientation time of the molecules so that molecular re-orientation does not induce any depolarization of the fluorescence signal. For molecules with large Φ_F (>20%), the fluorescence lifetime is usually longer than 500 ps; while the re-orientation time of molecule in non-viscous solvent is several hundred ps [73]. Therefore, a viscous solvent is necessary to perform excitation anisotropy. The common viscous solvents are glycerol and poly-tetrahydrofuran (pTHF). Note that pTHF might seem murky due to freezing point close to room temperature, heating up the solvent to ~50-60 ℃ will help to make solvent transparent. In some cases, the dye molecule is difficult to be dissolved into viscous solvent directly. To solve this problem, first dissolve dye molecule into ethanol (for glycerol) or THF (for pTHF) to make a concentrated solution; then put several drops of concentrated solution into viscous solvent to help it dissolve. The peak OD of the sample solution is usually less than 0.1 to avoid re-absorption of fluorescence signal.

There are two types of polarizer available with the fluorometer: Glan-Thompson polarizer (250-2200 nm) and thin-film polarizer (400-800 nm). Since excitation anisotropy measurement is essentially an excitation scan, i.e. fix the wavelength at the fluorescence peak, and change the excitation wavelength to measure relative fluorescence intensity; Glan-thompson polarizer is used to polarize the excitation light (placed after the exit slit of excitation monochromator), due to its wide coverage of wavelengths; while relatively cheap thin-film

polarizer is adopted to polarize the fluorescence light (placed in front of the entrance slit of emission monochromator) delivered to PMT A and B. To measure the excitation anisotropy with the emission wavelength longer than 800 nm, another Glan-Thompson polarizer is available to replace the thin-film polarizer. A simple way to test if the polarizer is working is to measure the anisotropy of a scattering medium (e.g. diluted milk, nano-particle suspension, *etc*) with both excitation and emission monochromator set at the same wavelength. An anisotropy value of 1 indicates the polarizer is working well.

Since the monochromator has different transmission efficiency for vertically and horizontally polarized light, the excitation anisotropy measurement is carried on by the following procedure (Figure C. 2): (a) Polarize the excitation light in horizontal direction with respect to the optics table, and measure the fluorescence light in horizontal and vertical directions, denoted as I_{HH} and I_{HV} respectively. A G factor $G = I_{HV}/I_{HH}$ is defined to calibrate the difference of transmission efficiency in two polarization directions; (b) polarize the excitation light in vertical direction, and measure the fluorescence light in horizontal and vertical directions, denoted as I_{VH} and I_{VV} respectively. The anisotropy value $r(\lambda)$ can be written as:

$$r(\lambda) = \frac{I_{VV}(\lambda) - G(\lambda) I_{VH}(\lambda)}{I_{VV}(\lambda) + 2G(\lambda) I_{VH}(\lambda)} \qquad \text{(C. 2)}$$

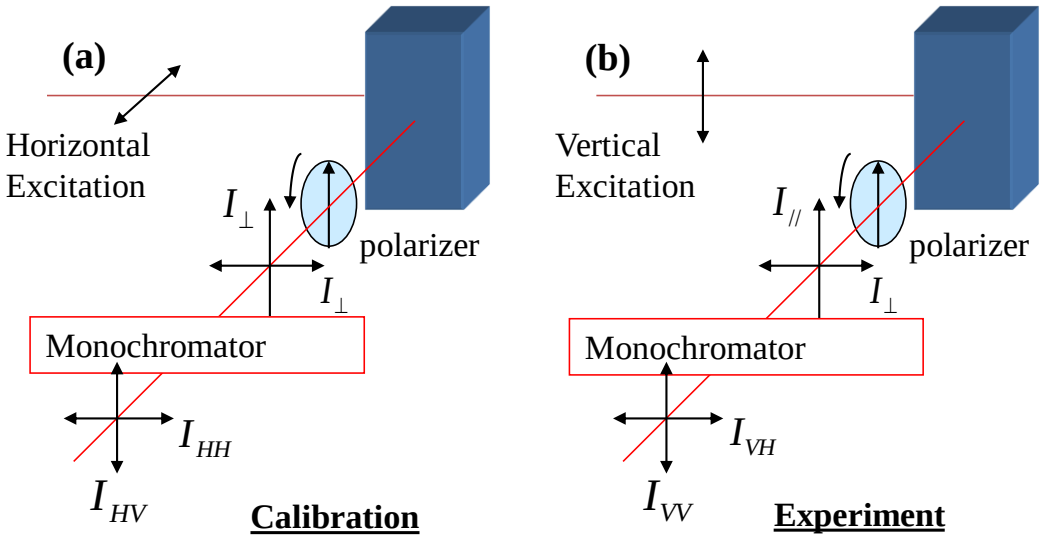

Figure C. 2: (a) geometry to calibrate the transmission efficiency of monochromator with excitation light polarized in horizontal direction; (b) excitation anisotropy experiment geometry with excitation light vertically polarized.

Since the anisotropy *r(λ)* measures the *ratio* of *I(λ)* with different polarization directions, no correction file is need for each excitation scan of *I(λ)*. It is very common that due to the modulation of excitation power spectrum of the Xenon lamp and the linear absorption spectrum of sample solution, the excitation scan curve *I(λ)* can be very peaky with intensity variation over an order of magnitude. Therefore, the slit width adjustment is necessary at different wavelengths range for best signal counts (10,000-300,000 counts). However, for each wavelengths range, the measuring condition remains *unchanged* when measuring fluorescence signal at different polarization direction, i.e. slit width of the monochromator, power of the lamp, *etc*. At wavelengths range where the fluorescence signal is weak (<30,000 counts), it is recommended to increase the integration time of the detector to 3-5 s to improve the signal to noise ratio.

APPENDIX D COPYRIGHT PERMISSION LETTERS

RSC | Advancing the Chemical Sciences

Royal Society of Chemistry
Thomas Graham House
Science Park
Milton Road
Cambridge
CB4 0WF

Tel: +44 (0)1223 420 066
Fax: +44 (0)1223 423 623
Email: contracts-copyright@rsc.org

www.rsc.org

Acknowledgements to be used by RSC authors

Authors of RSC books and journal articles can reproduce material (for example a figure) from the RSC publication in a non-RSC publication without formally requesting permission providing that the correct acknowledgement is given to the RSC publication. The acknowledgement depends on the RSC publication in which the material was published.

The form of the acknowledgements is as follows:

- For material being reproduced from an article in *New Journal of Chemistry* the acknowledgement should be in the form:
    - [Original citation] - Reproduced by permission of The Royal Society of Chemistry (RSC) on behalf of the Centre National de la Recherche Scientifique (CNRS) and the RSC
- For material being reproduced from an article *Photochemical & Photobiological Sciences* the acknowledgement should be in the form:
    - [Original citation] - Reproduced by permission of The Royal Society of Chemistry (RSC) on behalf of the European Society for Photobiology, the European Photochemistry Association, and RSC
- For material being reproduced from an article in *Physical Chemistry Chemical Physics* the acknowledgement should be in the form:
    - [Original citation] - Reproduced by permission of the PCCP Owner Societies
- For material reproduced from books and any other journal the acknowledgement should be in the form:
    - [Original citation] - Reproduced by permission of The Royal Society of Chemistry

The acknowledgement should also include a hyperlink to the article on the RSC website.

The form of the acknowledgement is also specified in the RSC agreement/licence signed by the corresponding author.

This express permission does not cover the reproduction of large portions of text from the RSC publication or reproduction of the whole article or book chapter.

A publisher of a non-RSC publication can use this document as proof that permission is granted to use the material in the non-RSC publication.

Title: Near-Unity Quantum Yields for Intersystem Crossing and Singlet Oxygen Generation in Polymethine-like Molecules: Design and Experimental Realization

Author: Scott Webster et al.

Publication: Journal of Physical Chemistry Letters

Publisher: American Chemical Society

Date: Aug 1, 2010

PERMISSION/LICENSE IS GRANTED FOR YOUR ORDER AT NO CHARGE

This type of permission/license, instead of the standard Terms & Conditions, is sent to you because no fee is being charged for your order. Please note the following:

- Permission is granted for your request in both print and electronic formats.
- If figures and/or tables were requested, they may be adapted or used in part.
- Please print this page for your records and send a copy of it to your publisher/graduate school.
- Appropriate credit for the requested material should be given as follows: "Reprinted (adapted) with permission from (COMPLETE REFERENCE CITATION). Copyright (YEAR) American Chemical Society." Insert appropriate information in place of the capitalized words.
- One-time permission is granted only for the use specified in your request. No additional uses are granted (such as derivative works or other editions). For any other uses, please submit a new request.

LIST OF REFERENCES

1. Stegeman, G. I.; Stegeman, R. A. *Nonlinear Optics: Phenomena, Materials and Devices*, to be published.

2. Boyd, R. W. *Nonlinear Optics*; Third ed.; Academic Press: Boston, 2008.

3. Göppert-Mayer, M. Über Elementarakte Mit Zwei Quantensprüngen. *Ann. Phys.* **1931**, *401*, 273-294.

4. Kaiser, W.; Garrett, C. G. B. Two-Photon Excitation in Caf_{2}: Eu^{2+}. *Phys Rev Lett* **1961**, *7*, 229-231.

5. Spangler, C. W. Recent Development in the Design of Organic Materials for Optical Power Limiting. *J. Mater. Chem.* **1999**, *9*, 2013.

6. Hagan, D. J. In *Handbook of Optics*; Third ed.; Bass, M., Ed.; McGraw Hill: New York, 2010; Vol. IV, p 13.11.

7. Zipfel, W. R.; Williams, R. M.; Webb, W. W. Nonlinear Magic: Multiphoton Microscopy in the Biosciences. *Nat Biotech* **2003**, *21*, 1369-1377.

8. Parthenopoulos, D. A.; Rentzepis, P. M. Three-Dimensional Optical Storage Memory. *Science* **1989**, *245*, 843-845.

9. Cumpston, B. H.; Ananthavel, S. P.; Barlow, S.; Dyer, D. L.; Ehrlich, J. E.; Erskine, L. L.; Heikal, A. A.; Kuebler, S. M.; Lee, I. Y. S.; McCord-Maughon, D.*et al* Two-Photon Polymerization Initiators for Three-Dimensional Optical Data Storage and Microfabrication. *Nature* **1999**, *398*, 51-54.

10. Zhao, L.; Xu, J. J.; Zhang, G.; Bu, X.; Shionoya, M. Frequency-Upconverted Organic Crystal. *Opt. Lett.* **1999**, *24*, 1793-1795.

11. Fisher, W. G.; Partridge, W. P.; Dees, C.; Wachter, E. A. Simultaneous Two-Photon Activation of Type-I Photodynamic Therapy Agents. *Photochemistry and Photobiology* **1997**, *66*, 141-155.

12. Fu, J. Dissertation, University of Central Florida, 2006.

13. Birge, R. R.; Pierce, B. M. Semiclassical Time-Dependent Theory of Two-Photon Spectroscopy. The Effect of Dephasing in the Virtual Level on the Two-Photon Excitation Spectrum of Isotachysterol. *Int. J. Quam. Chem.* **1986**, *29*, 639-656.

14. Kleinschmidt, J.; Rentsch, S.; Tottleben, W.; Wilhelmi, B. Measurement of Strong Nonlinear Absorption in Stilbene-Chloroform Solutions, Explained by the Superposition of

Two-Photon Absorption and One-Photon Absorption from the Excited State. *Chem. Phys. Lett.* **1974**, *24*, 133-135.

15. Kannan, R.; He, G. S.; Lin, T.-C.; Prasad, P. N.; Vaia, R. A.; Tan, L.-S. Toward Highly Active Two-Photon Absorbing Liquids. Synthesis and Characterization of 1,3,5-Triazine-Based Octupolar Molecules. *Chem. Mater.* **2004**, *16*, 185-194.

16. Garmire, E.; Chiao, R. Y.; Townes, C. H. Dynamics and Characteristics of the Self-Trapping of Intense Light Beams. *Phys Rev Lett* **1966**, *16*, 347-349.

17. Lallemand, P.; Bloembergen, N. Self-Focusing of Laser Beams and Stimulated Raman Gain in Liquids. *Phys Rev Lett* **1965**, *15*, 1010-1012.

18. Stegeman, G. I.; Segev, M. Optical Spatial Solitons and Their Interactions: Universality and Diversity. *Science* **1999**, *286*, 1518-1523.

19. Alfano, R. R.; Shapiro, S. L. Observation of Self-Phase Modulation and Small-Scale Filaments in Crystals and Glasses. *Phys Rev Lett* **1970**, *24*, 592-594.

20. Hales, J. M.; Matichak, J.; Barlow, S.; Ohira, S.; Yesudas, K.; Brédas, J.-L.; Perry, J. W.; Marder, S. R. Design of Polymethine Dyes with Large Third-Order Optical Nonlinearities and Loss Figures of Merit. *Science* **2010**, *327*, 1485-1488.

21. Mizrahi, V.; DeLong, K. W.; Stegeman, G. I.; Saifi, M. A.; Andrejco, M. J. Two-Photon Absorption as a Limitation to All-Optical Switching. *Opt. Lett.* **1989**, *14*, 1140-1142.

22. Marder, S. R. Organic Nonlinear Optical Materials: Where We Have Been and Where We Are Going. *Chem. Commun.* **2006**, 131-134.

23. Fessenden, R. J.; Fessenden, J. S. *Organic Chemistry*; 2nd ed.; Willard Grant Press: Boston, MA, 1982.

24. Chung, S.-J.; Zheng, S.; Odani, T.; Beverina, L.; Fu, J.; Padilha, L. A.; Biesso, A.; Hales, J. M.; Zhan, X.; Schmidt, K.*et al* Extended Squaraine Dyes with Large Two-Photon Absorption Cross-Sections. *J. Am. Chem. Soc.* **2006**, *128*, 14444-14445.

25. Padilha, L. A.; Webster, S.; Hu, H.; Przhonska, O. V.; Hagan, D. J.; Van Stryland, E. W.; Bondar, M. V.; Davydenko, I. G.; Slominsky, Y. L.; Kachkovski, A. D. Excited State Absorption and Decay Kinetics of near Ir Polymethine Dyes. *Chem. Phys.* **2008**, *352*, 97-105.

26. Albota, M.; Beljonne, D.; Brédas, J.-L.; Ehrlich, J. E.; Fu, J.-Y.; Heikal, A. A.; Hess, S. E.; Kogej, T.; Levin, M. D.; Marder, S. R.*et al* Design of Organic Molecules with Large Two-Photon Absorption Cross Sections. *Science* **1998**, *281*, 1653-1656.

27. Rumi, M.; Ehrlich, J. E.; Heikal, A. A.; Perry, J. W.; Barlow, S.; Hu, Z.; McCord-Maughon, D.; Parker, T. C.; Röckel, H.; Thayumanavan, S.*et al* Structure−Property Relationships for

Two-Photon Absorbing Chromophores: Bis-Donor Diphenylpolyene and Bis(Styryl)Benzene Derivatives. *J. Am. Chem. Soc.* **2000**, *122*, 9500-9510.

28. Pawlicki, M.; Collins, H. A.; Denning, R. G.; Anderson, H. L. Two-Photon Absorption and the Design of Two-Photon Dyes. *Angew. Chem. Int. Edit.* **2009**, *48*, 3244-3266.

29. He, G. S.; Tan, L.-S.; Zheng, Q.; Prasad, P. N. Multiphoton Absorbing Materials: Molecular Designs, Characterizations, and Applications. *Chem. Rev.* **2008**, *108*, 1245-1330.

30. Zheng, S.; Beverina, L.; Barlow, S.; Zojer, E.; Fu, J.; Padilha, L. A.; Fink, C.; Kwon, O.; Yi, Y.; Shuai, Z.*et al* High Two-Photon Cross-Sections in Bis(Diarylaminostyryl) Chromophores with Electron-Rich Heterocycle and Bis(Heterocycle)Vinylene Bridges. *Chem. Commun.* **2007**.

31. Przhonska, O. V.; Webster, S.; Padilha, L. A.; Hu, H.; Kachkovski, A. D.; Hagan, D. J.; Van Stryland, E. W. In *Advanced Fluorescence Reporters in Chemistry and Biology I: Fundamentals and Molecular Design, Springer Series in Fluorescence*; Demchenko, A. P., Ed.; Springer-Verlag: Berlin Heidelberg 2010.

32. Fu, J.; Padilha, L. A.; Hagan, D. J.; Van Stryland, E. W.; Przhonska, O. V.; Bondar, M. V.; Slominsky, Y. L.; Kachkovski, A. D. Experimental and Theoretical Approaches to Understanding Two-Photon Absorption Spectra in Polymethine and Squaraine Molecules. *J. Opt. Soc. Am. B* **2007**, *24*, 67-76.

33. Fu, J.; Padilha, L. A.; Hagan, D. J.; Van Stryland, E. W.; Przhonska, O. V.; Bondar, M. V.; Slominsky, Y. L.; Kachkovski, A. D. Molecular Structure - Two-Photon Absorption Property Relations in Polymethine Dyes. *J. Opt. Soc. Am. B* **2007**, *24*, 56.

34. Belfield, K. D.; Morales, A. R.; Hales, J. M.; Hagan, D. J.; Van Stryland, E. W.; Chapela, V. M.; Percino, J. Linear and Two-Photon Photophysical Properties of a Series of Symmetrical Diphenylaminofluorenes. *Chem. Mater.* **2004**, *16*, 2267-2273.

35. Ohta, K.; Kamada, K. Theoretical Investigation of Two-Photon Absorption Allowed Excited States in Symmetrically Substituted Diacetylenes by Ab Initio Molecular-Orbital Method. *J. of Chem. Phys.* **2006**, *124*, 124303.

36. Meyers, F.; Marder, S. R.; Pierce, B. M.; Bredas, J. L. Electric Field Modulated Nonlinear Optical Properties of Donor-Acceptor Polyenes: Sum-over-States Investigation of the Relationship between Molecular Polarizabilities (.Alpha., .Beta., And .Gamma.) and Bond Length Alternation. *J. Am. Chem. Soc.* **1994**, *116*, 10703-10714.

37. Zojer, E.; Wenseleers, W.; Pacher, P.; Barlow, S.; Halik, M.; Grasso, C.; Perry, J. W.; Marder, S. R.; Brédas, J.-L. Limitations of Essential-State Models for the Description of Two-Photon Absorption Processes: The Example of Bis(Dioxaborine)-Substituted Chromophores. *J. Phys. Chem. B* **2004**, *108*, 8641-8646.

38. Fabian, J. Tddft-Calculations of Vis/Nir Absorbing Compounds. *Dyes Pigments* **2010**, *84*, 36.

39. Hutchings, D. C.; Sheik-Bahae, M.; Hagan, D. J.; Van Stryland, E. W. Kramers-Krönig Relations in Nonlinear Optics. *Opt. Quant. Electron.* **1992**, *24*, 1-30.

40. Sheik-Bahae, M.; Hutchings, D. C.; Hagan, D. J.; Van Stryland, E. W. Dispersion of Bound Electron Nonlinear Refraction in Solids. *IEEE J. Quantum. Elect.* **1991**, *27*, 1296-1309.

41. Hales, J. M.; Zheng, S.; Barlow, S.; Marder, S. R.; Perry, J. W. Bisdioxaborine Polymethines with Large Third-Order Nonlinearities for All-Optical Signal Processing. *J. Am. Chem. Soc.* **2006**, *128*, 11362-11363.

42. Balu, M.; Padilha, L. A.; Hagan, D. J.; Van Stryland, E. W.; Yao, S.; Belfield, K.; Zheng, S.; Barlow, S.; Marder, S. Broadband Z-Scan Characterization Using a High-Spectral-Irradiance, High-Quality Supercontinuum. *J. Opt. Soc. Am. B* **2008**, *25*, 159-165.

43. Orr, B. J.; Ward, J. F. Perturbation Theory of the Non-Linear Optical Polarization of an Isolated System. *Mol. Phys.* **1971**, *20*, 513-526.

44. DeSalvo, R.; Hagan, D. J.; Sheik-Bahae, M.; Stegeman, G.; Van Stryland, E. W.; Vanherzeele, H. Self-Focusing and Self-Defocusing by Cascaded Second-Order Effects in Ktp. *Opt. Lett.* **1992**, *17*, 28-30.

45. Dick, B.; Hochstrasser, R. M.; Trommsdorff, H. P. *Nonlinear Optical Properties of Organic Molecules and Crystals*; Academic Press: Orlando, 1987.

46. Owyoung, A. Dissertation, California Institute of technology, 1971.

47. Lakowicz, J. R. *Principle of Fluorescence Spectroscopy*; 2nd ed.; Kluwer Academic/Plenum Publisher: New York, 1999.

48. Ward, J. F. Calculation of Nonlinear Optical Susceptibilities Using Diagrammatic Perturbation Theory. *Reviews of Modern Physics* **1965**, *37*, 1-18.

49. Christodoulides, D. N.; Khoo, I. C.; Salamo, G. J.; Stegeman, G. I.; Van Stryland, E. W. Nonlinear Refraction and Absorption: Mechanisms and Magnitudes. *Adv. Opt. Photon.* **2010**, *2*, 60-200.

50. Kuzyk, M. G.; Dirk, C. W. Effects of Centrosymmetry on the Nonresonant Electronic Third-Order Nonlinear Optical Susceptibility. *Phys. Rev. A* **1990**, *41*, 5098.

51. Hales, J.; Hagan, D. J.; Van Stryland, E. W.; Schafer, K.; Morales, A.; Belfield, K.; Pacher, P.; Kwon, O.; Zojer, E.; Bredas, J. Resonant Enhancement of Two-Photon Absorption in Substituted Fluorene Molecules. *J. Chem. Phys.* **2004**, *121*, 3152.

52. Zojer, E.; Beljonne, D.; Pacher, P.; Brédas, J.-L. Two-Photon Absorption in Quadrupolar Π-Conjugated Molecules: Influence of the Nature of the Conjugated Bridge and the Donor–Acceptor Separation. *Chemistry – A European Journal* **2004**, *10*, 2668-2680.

53. Cronstrand, P.; Luo, Y.; Ågren, H. Generalized Few-State Models for Two-Photon Absorption of Conjugated Molecules. *Chem. Phys. Lett.* **2002**, *352*, 262-269.

54. Monson, P. R.; McClain, W. M. Polarization Dependence of the Two-Photon Absorption of Tumbling Molecules with Application to Liquid 1-Chloronaphthalene and Benzene. *J. Chem. Phys.* **1970**, *53*, 29-37.

55. Mulliken, R. S. Intensities of Electronic Transitions in Molecular Spectra I. Introduction. *J. of Chem. Phys.* **1939**, *7*, 14-20.

56. Webster, S.; Padilha, L. A.; Hu, H.; Przhonska, O. V.; Hagan, D. J.; Van Stryland, E. W.; Bondar, M. V.; Davydenko, I. G.; Slominsky, Y. L.; Kachkovski, A. D. Structure and Linear Spectroscopic Properties of near Ir Polymethine Dyes. *J. of Luminescence* **2008**, *128*, 1927.

57. Webster, S.; Odom, S. A.; Padilha, L. A.; Przhonska, O. V.; Peceli, D.; Hu, H.; Nootz, G.; Kachkovski, A. D.; Matichak, J.; Barlow, S.*et al* Linear and Nonlinear Spectroscopy of a Porphyrin−Squaraine−Porphyrin Conjugated System. *J. Phys. Chem. B* **2009**, *113*, 14854-14867.

58. Dawson, W. R.; Windsor, M. W. Fluorescence Yields of Aromatic Compounds. *J. Phys. Chem.* **1968**, *72*, 3251-3260.

59. Kubin, R. F.; Fletcher, A. N. Fluorescence Quantum Yields of Some Rhodamine Dyes. *Journal of Luminescence* **1982**, *27*, 455-462.

60. Magde, D.; Brannon, J. H.; Cremers, T. L.; Olmsted, J. Absolute Luminescence Yield of Cresyl Violet. A Standard for the Red. *J. Phys. Chem.* **1979**, *83*, 696-699.

61. Strickler, S.; Berg, R. Relationship between Absorption Intensity and Fluorescence Lifetime of Molecules. *J. Chem. Phys.* **1962**, *37*, 814.

62. Maine, P.; Strickland, D.; Bado, P.; Pessot, M.; Mourou, G. Generation of Ultrahigh Peak Power Pulses by Chirped Pulse Amplification. *IEEE J. Quantum. Elect.* **1988**, *24*, 398-403.

63. Xu, C.; Webb, W. W. Measurement of Two-Photon Excitation Cross Sections of Molecular Fluorophores with Data from 690 to 1050 Nm. *J. Opt. Soc. Am. B* **1996**, *13*, 481-491.

64. Hales, J. Dissertation, University of Central Florida, 2004.

65. Makarov, N. S.; Drobizhev, M.; Rebane, A. Two-Photon Absorption Standards in the 550-1600 Nmexcitation Wavelength Range. *Opt. Express* **2008**, *16*, 4029-4047.

66. Makarov, N. S.; Campo, J.; Hales, J. M.; Perry, J. W. Rapid, Broadband Two-Photon-Excited Fluorescence Spectroscopy and Its Application to Red-Emitting Secondary Reference Compounds. *Opt. Mater. Express* **2011**, *1*, 551-563.

67. Sheik-Bahae, M.; Said, A. A.; Wei, T.-H.; Hagan, D. J.; Van Stryland, E. W. Sensitive Measurement of Optical Nonlinearities Using a Single Beam. *IEEE J. Quantum. Elect.* **1990**, *26*, 760-769.

68. Cirloganu, C. Dissertation, University of Central Florida, 2010.

69. Milam, D. Review and Assessment of Measured Values of the Nonlinear Refractive-Index Coefficient of Fused Silica. *Appl. Opt.* **1998**, *37*, 546-550.

70. Said, A. A.; Sheik-Bahae, M.; Hagan, D. J.; Wei, T. H.; Wang, J.; Young, J.; Van Stryland, E. W. Determination of Bound-Electronic and Free-Carrier Nonlinearities in Znse, Gaas, Cdte, and Znte. *J. Opt. Soc. Am. B* **1992**, *9*, 405-414.

71. Negres, R. A.; Przhonska, O. V.; Hagan, D. J.; Van Stryland, E. W.; Bondar, M. V.; Slominsky, Y. L.; Kachkovski, A. D. The Nature of Excited-State Absorption in Polymethine and Squarylium Molecules. *IEEE J. Sel. Top. Quant.* **2001**, *7*, 849-863.

72. Negres, R. A.; Hales, J. M.; Kobyakov, A.; Hagan, D. J.; Van Stryland, E. W. Experiment and Analysis of Two-Photon Absorption Spectroscopy Using a White-Light Continuum Probe. *IEEE J. Quantum. Elect.* **2002**, *38*, 1205-1216.

73. Webster, S.; Fu, J.; Padilha, L. A.; Przhonska, O. V.; Hagan, D. J.; Van Stryland, E. W.; Bondar, M. V.; Slominsky, Y. L.; Kachkovski, A. D. Comparison of Nonlinear Absorption in Three Similar Dyes: Polymethine, Squaraine and Tetraone. *Chem. Phys.* **2008**, *348*, 143-151.

74. Lessing, H. E.; Von Jena, A. Separation of Rotational Diffusion and Level Kinetics in Transient Absorption Spectroscopy. *Chem. Phys. Lett.* **1976**, *42*, 213-217.

75. Przhonska, O. V.; Hagan, D. J.; Novikov, E.; Lepkowicz, R.; Van Stryland, E. W.; Bondar, M. V.; Slominsky, Y. L.; Kachkovski, A. D. Picosecond Absorption Anisotropy of Polymethine and Squarylium Dyes in Liquid and Polymeric Media. *Chem. Phys.* **2001**, *273*, 235-248.

76. Gerasov, A. O.; Shandura, M. P.; Kovtun, Y. P.; Kachkovsky, A. D. The Nature of Electron Transitions in Anionic Dioxaborines, Derivatives of Aminocoumarin. *J. Phys. Org. Chem.* **2008**, *21*, 419-425.

77. Gerasov, A. O.; Shandura, M. P.; Kovtun, Y. P. Series of Polymethine Dyes Derived from 2,2-Difluoro-1,3,2-(2h)-Dioxaborine of 3-Acetyl-7-Diethylamino-4-Hydroxycoumarin. *Dyes Pigments* **2008**, *77*, 598-607.

78. Padilha, L. A.; Webster, S.; Przhonska, O. V.; Hu, H.; Peceli, D.; Ensley, T. R.; Bondar, M. V.; Gerasov, A. O.; Kovtun, Y. P.; Shandura, M. P.*et al* Efficient Two-Photon Absorbing Acceptor-Π-Acceptor Polymethine Dyes. *J. Phys. Chem. A.* **2010**, *114*, 6493-6501.

79. Padilha, L. A.; Webster, S.; Przhonska, O. V.; Hu, H.; Peceli, D.; Rosch, J. L.; Bondar, M. V.; Gerasov, A. O.; Kovtun, Y. P.; Shandura, M. P.*et al* Nonlinear Absorption in a Series of Donor-P-Acceptor Cyanines with Different Conjugation Lengths. *J. Mater. Chem.* **2009**, *19*, 7503-7513.

80. Hu, H.; Fishman, D. A.; Gerasov, A. O.; Przhonska, O. V.; Webster, S.; Padilha, L. A.; Peceli, D.; Shandura, M.; Kovtun, Y. P.; Kachkovski, A. D.*et al* Two-Photon Absorption Spectrum of a Single Crystal Cyanine-Like Dye. *J. Phys. Chem. Lett.* **2012**, *3*, 1222-1228.

81. Lepkowicz, R. S.; Przhonska, O. V.; Hales, J. M.; Fu, J.; Hagan, D. J.; Van Stryland, E. W.; Bondar, M. V.; Slominsky, Y. L.; Kachkovski, A. D. Nature of the Electronic Transitions in Thiacarbocyanines with a Long Polymethine Chain. *Chem. Phys.* **2004**, *305*, 259.

82. Bricks, J.; Ryabitskii, A.; Kachkovskii, A. Studies of 2-Azaazulenium Derivatives: The Natures of Electron Transitions in the 2-Azaazulenium Cation and in Monomethine Cyanine Dyes Bearing 2-Azaazulenium Moieties as Terminal Groups. *Eur. J. Org.Chem.* **2009**, *2009*, 3439.

83. Bricks, J.; Ryabitskii, A.; Kachkovskii, A. Studies of 2-Azaazulenium Derivatives: Unsymmetrical Trimethine Cyanine Dyes Bearing a 2-Azaazulenium Moiety as One of the Terminal Groups. *Chem. Eur. J.* **2010**, *16*, 8773.

84. Ryabitskii, A. B.; Bricks, J. L.; Kachkovskii, A. D.; Kurdyukov, V. V. Conformational Analysis of Polymethine Dyes Derived from the 2-Azaazulene. *J. Mol. Struct.* **2012**, *1007*, 52-62.

85. Webster, S.; Peceli, D.; Hu, H.; Padilha, L. A.; Przhonska, O. V.; Masunov, A. E.; Gerasov, A. O.; Kachkovski, A. D.; Slominsky, Y. L.; Tolmachev, A. I.*et al* Near-Unity Quantum Yields for Intersystem Crossing and Singlet Oxygen Generation in Polymethine-Like Molecules: Design and Experimental Realization. *J. Phys. Chem. Lett.* **2010**, *1*, 2354-2360.

86. Terenziani, F.; Przhonska, O. V.; Webster, S.; Padilha, L. A.; Slominsky, Y. L.; Davydenko, I. G.; Gerasov, A. O.; Kovtun, Y. P.; Shandura, M. P.; Kachkovski, A. D.*et al* Essential-State Model for Polymethine Dyes: Symmetry Breaking and Optical Spectra. *J. Phys. Chem. Lett.* **2010**, *1*, 1800-1804.

87. Scherer, D.; Dörfler, R.; Feldner, A.; Vogtmann, T.; Schwoerer, M.; Lawrentz, U.; Grahn, W.; Lambert, C. Two-Photon States in Squaraine Monomers and Oligomers. *Chem. Phys.* **2002**, *279*, 179-207.

88. Morley, J. O.; Morley, R. M.; Docherty, R.; Charlton, M. H. Fundamental Studies on Brooker's Merocyanine. *J. Am. Chem. Soc.* **1997**, *119*, 10192-10202.

89. Johnsen, M.; Ogilby, P. R. Effect of Solvent on Two-Photon Absorption by Vinyl Benzene Derivatives. *J. Phys. Chem. A.* **2008**, *112*, 7831-7839.

90. Zheng, Q.; Gupta, S. K.; He, G. S.; Tan, L.-S.; Prasad, P. N. Synthesis, Characterization, Two-Photon Absorption, and Optical Limiting Properties of Ladder-Type Oligo-P-Phenylene-Cored Chromophores. *Adv. Funct. Mater.* **2008**, *18*, 2770-2779.

91. Zhao, K.; Ferrighi, L.; Frediani, L.; Wang, C.-K.; Luo, Y. Solvent Effects on Two-Photon Absorption of Dialkylamino Substituted Distyrylbenzene Chromophore. *J. of Chem. Phys.* **2007**, *126*, 204509-204506.

92. Würthner, F.; Archetti, G.; Schmidt, R.; Kuball, H.-G. Solvent Effect on Color, Band Shape, and Charge-Density Distribution for Merocyanine Dyes Close to the Cyanine Limit. *Angew. Chem. Int. Edit.* **2008**, *47*, 4529-4532.

93. Terenziani, F.; Katan, C.; Badaeva, E.; Tretiak, S.; Blanchard-Desce, M. Enhanced Two-Photon Absorption of Organic Chromophores: Theoretical and Experimental Assessments. *Adv Mater* **2008**, *20*, 4641-4678.

94. Kachkovskii, A. D. The Solitonic Nature of the Electronic Structure of the Ions of Linear Conjugated Systems. *Theoretical and Experimental Chemistry* **2005**, *41*, 139-164.

95. Watkin, D. J.; Prout, C. K.; carruthers, J. R.; Betteridge, P. W. In *Chemical Crystallography Laboratory*; University of Oxford: Oxford, 1996.

96. Tyutyulkoy, N.; Fabian, J.; Mehlhorn, A.; Dietz, F.; Tadjer, A. *Polymethine Dyes. Structure and Properties*; St. Kliment Ohridski University Press: Sofia, 1991.

97. Chen, X.-W.; Liu, J.-W.; Wang, J.-H. A Highly Fluorescent Hydrophilic Ionic Liquid as a Potential Probe for the Sensing of Biomacromolecules. *J. Phys. Chem. B* **2011**, *115*, 1524-1530.

98. Polyakov, S.; Yoshino, F.; Liu, M.; Stegeman, G. Nonlinear Refraction and Multiphoton Absorption in Polydiacetylenes from 1200 to 2200 Nm. *Phys. Rev. B* **2004**, *69*, 115421.

99. Fang, H.-H.; Chen, Q.-D.; Yang, J.; Xia, H.; Ma, Y.-G.; Wang, H.-Y.; Sun, H.-B. Two-Photon Excited Highly Polarized and Directional Upconversion Emission from Slab Organic Crystals. *Opt. Lett.* **2010**, *35*, 441-443.

100. Komorowska, K.; Brasselet, S.; Dutier, G.; Ledoux, I.; Zyss, J.; Poulsen, L.; Jazdzyk, M.; Egelhaaf, H. J.; Gierschner, J.; Hanack, M. Nanometric Scale Investigation of the Nonlinear Efficiency of Perhydrotriphenylene Inclusion Compounds. *Chem. Phys.* **2005**, *318*, 12-20.

101. Zheng, M.-L.; Chen, W.-Q.; Fujita, K.; Duan, X.-M.; Kawata, S. Dendrimer Adjusted Nanocrystals of Dast: Organic Crystal with Enhanced Nonlinear Optical Properties. *Nanoscale* **2010**, *2*, 913-916.

102. Zheng, M.-L.; Fujita, K.; Chen, W.-Q.; Duan, X.-M.; Kawata, S. Two-Photon Excited Fluorescence and Second-Harmonic Generation of the Dast Organic Nanocrystals. *J. Phys. Chem. C* **2011**, *115*, 8988-8993.

103. Fang, H.-H.; Yang, J.; Ding, R.; Chen, Q.-D.; Wang, L.; Xia, H.; Feng, J.; Ma, Y.-G.; Sun, H.-B. Polarization Dependent Two-Photon Properties in an Organic Crystal. *Appl. Phys. Lett.* **2010**, *97*, 101101.

104. Klocek, P. *Handbook of Infrared Optical Materials*; Marcel Dekker Inc.: New York, 1991.

105. Toro, C.; Thibert, A.; De Boni, L.; Masunov, A. E.; Hernandez, F. E. Fluorescence Emission of Disperse Red 1 in Solution at Room Temperature. *Journal of Physical Chemistry B* **2008**, *112*, 929-937.

106. Patel, P. D.; Masunov, A. E. Theoretical Study of Photochromic Compounds. 1. Bond Length Alternation and Absorption Spectra for the Open and Closed Forms of 29 Diarylethene Derivatives. *Journal of Physical Chemistry A* **2009**, *113*, 8409-8414.

107. Masunov, A. E.; Grishchenko, S. I.; Zorkii, P. M. Effect of Specific Intermolecular Interactions on Crystalline-Structure - Uracyl Derivatives and Analogs. *Zhurnal Fiz. Khimii* **1993**, *67*, 221-239.

108. Cardenas-Jiron, G. I.; Masunov, A.; Dannenberg, J. J. Molecular Orbital Study of Crystalline P-Benzoquinone. *Journal of Physical Chemistry A* **1999**, *103*, 7042-7046.

109. Frisch, M. J.; Trucks, G. W.; Schlegel, H. B.; Scuseria, G. E.; Robb, M. A.; Cheeseman, J. R.; Montgomery, J., J. A.; Vreven, T.; Kudin, K. N.; Burant, J. C.*et al* Gaussian 2003. **2004**.

110. Passier, R.; Ritchie, J. P.; Toro, C.; Diaz, C.; Masunov, A. E.; Belfield, K. D.; Hernandez, F. E. Thermally Controlled Preferential Molecular Aggregation State in a Thiacarbocyanine Dye. *J. of Chem. Phys.* **2010**, *133*, 134508.

111. Dähne, S.; Radeglia, R. Revision Der Lewis-Calvin-Regel Zur Charakterisierung Vinyloger. Polyen- Und Polymethin ähnlicher Verbindungen. *Tetrahedron* **1971**, *27*, 3673-3693.

112. Tolbert, L. M.; Zhao, X. Beyond the Cyanine Limit: Peierls Distortion and Symmetry Collapse in a Polymethine Dye. *J. Am. Chem. Soc.* **1997**, *119*, 3253.

113. Su, W. P.; Schrieffer, J. R.; Heeger, A. J. Solitons in Polyacetylene. *Phys. Rev. Lett.* **1979**, *42*, 1698.

114. Patil, A. O.; Heeger, A. J.; Wudl, F. Optical Properties of Conducting Polymers. *Chem. Rev.* **1988**, *88*, 183-200.

115. Craw, J. S.; Reimers, J. R.; Bacskay, G. B.; Wong, A. T.; Hush, N. S. Solitons in Finite- and Infinite-Length Negative-Defect Trans-Polyacetylene and the Corresponding Brooker (Polymethinecyanine) Cations. I. Geometry. *Chem. Phys.* **1992**, *167*, 77.

116. Craw, J. S.; Reimers, J. R.; Bacskay, G. B.; Wong, A. T.; Hush, N. S. Solitons in Finite- and Infinite-Length Negative-Defect Trans-Polyacetylene and the Corresponding Brooker (Polymethinecyanine) Cations. Ii. Charge Density Wave. *Chem. Phys.* **1992**, *167*, 101.

117. Fabian, J. Symmetry-Lowering Distortion of near-Infrared Polymethine Dyes—a Study by First-Principles Methods. *Journal of Molecular Structure: THEOCHEM* **2006**, *766*, 49-60.

118. Ryabitsky, A. B.; Kachkovski, A. D.; Przhonska, O. V. Symmetry Breaking in Cationic and Anionic Polymethine Dyes. *J. Mol. Struct.-Theochem.* **2007**, *802*, 75.

119. Terenziani, F.; Painelli, A.; Katan, C.; Charlot, M.; Blanchard-Desce, M. Charge Instability in Quadrupolar Chromophores: Symmetry Breaking and Solvatochromism. *J. Am. Chem. Soc.* **2006**, *128*, 15742-15755.

120. Terenziani, F.; Sissa, C.; Painelli, A. Symmetry Breaking in Octupolar Chromophores: Solvatochromism and Electroabsorption. *J. Phys. Chem. B* **2008**, *112*, 5079-5087.

121. Mongin, O.; Porrès, L.; Moreaux, L.; Mertz, J.; Blanchard-Desce, M. Synthesis and Photophysical Properties of New Conjugated Fluorophores Designed for Two-Photon-Excited Fluorescence. *Organic Letters* **2002**, *4*, 719-722.

122. Belfield, K. D.; Bondar, M. V.; Przhonska, O. V.; Schafer, K. J.; Mourad, W. Spectral Properties of Several Fluorene Derivatives with Potential as Two-Photon Fluorescent Dyes. *Journal of Luminescence* **2002**, *97*, 141-146.

123. Bixon, M.; Jortner, J. In *Advances in Chemical Physics*; John Wiley & Sons, Inc.: 2007, p 35-202.

124. Würthner, F.; Kaiser, T. E.; Saha-Möller, C. R. J-Aggregates: From Serendipitous Discovery to Supramolecular Engineering of Functional Dye Materials. *Angew. Chem. Int. Edit.* **2011**, *50*, 3376-3410.

125. Belfield, K. D.; Bondar, M. V.; Hernandez, F. E.; Przhonska, O. V.; Yao, S. Two-Photon Absorption of a Supramolecular Pseudoisocyanine J-Aggregate Assembly. *Chem. Phys.* **2006**, *320*, 118-124.

126. Painelli, A.; Del Freo, L.; Terenziani, F. Vibronic Contributions to Resonant Nlo Responses: Two-Photon Absorption in Push–Pull Chromophores. *Chem. Phys. Lett.* **2001**, *346*, 470-478.

127. Przhonska, O. V.; Hu, H.; Webster, S.; Bricks, J. L.; Viniychuk, A. A.; Kachkovski, A. D.; Slominsky, Y. L.; Hagan, D. J.; Van Stryland, E. W. Electronic Transitions in a Series of 2-Azaazulene Polymethine Dyes with Different Pi-Conjugation Lengths. **to be submitted**.

128. Lepkowicz, R. S.; Cirloganu, C. M.; Przhonska, O. V.; Hagan, D. J.; Van Stryland, E. W.; Bondar, M. V.; Slominsky, Y. L.; Kachkovski, A. D.; Mayboroda, E. I. Absorption Anisotropy Studies of Polymethine Dyes. *Chem. Phys.* **2004**, *306*, 171.

129. Frisch, M. J.; Trucks, G. W.; Schlegel, H. B.; Scuseria, G. E.; Robb, M. A.; Cheeseman, J. R.; Montgomery, J. A., Jr.; Vreven, T.; Kudin, K. N.; Burant, J. C.*et al* Gaussian 03, Revision B.05. **2003**.

130. Fabian, J.; Hartmann, H. Chromophores of Neutral and Dicationic Thiophene-Based Oligomers – a Study by First-Principle Methods. *Dyes Pigments* **2008**, *79*, 126.

131. Kachkovskii, A. D. The Nature of Electronic Transitions in Linear Conjugated Systems. *Russ. Chem. Rev.* **1997**, *66*, 715.

132. Kachkovski, O. D.; Yushchenko, D. A.; Kachkovski, G. O.; Pilipchuk, N. V. Electronic Properties of Polymethine Systems 9: Position of Soliton Level in Charged Molecules. *Dyes Pigments* **2004**, *66*, 223.

133. Hu, H.; Fishman, D.; Webster, S.; Przhonska, O. V.; Terenziani, F.; Painelli, A.; Bricks, J. L.; Kachkovski, A. D.; Hagan, D. J.; Van Stryland, E. W. Two-Photon Absorption Spectra of a near-Infrared 2-Azaazulene Polymethine Dye with a Broken-Symmetry Ground State. **To Be Submitted**.

134. Grisanti, L.; Sissa, C.; Terenziani, F.; Painelli, A.; Roberto, D.; Tessore, F.; Ugo, R.; Quici, S.; Fortunati, I.; Garbin, E.*et al* Enhancing the Efficiency of Two-Photon Absorption by Metal Coordination. *Phys. Chem. Chem. Phys.* **2009**, *11*, 9450-9457.

135. Dewar, M. J. S. *The Molecular Orbital Theory of Organic Chemistry*; McGraw-Hill: New York, 1969.

136. El-Sayed, M. A. Spin-Orbit Coupling and the Radiationless Processes in Nitrogen Heterocyclics. *J. of Chem. Phys.* **1963**, *38*, 2834-2838.

137. Beverina, L.; Crippa, M.; Landenna, M.; Ruffo, R.; Salice, P.; Silvestri, F.; Versari, S.; Villa, A.; Ciaffoni, L.; Collini, E.*et al* Assessment of Water-Soluble Π-Extended Squaraines as One- and Two-Photon Singlet Oxygen Photosensitizers: Design, Synthesis, and Characterization. *J. Am. Chem. Soc.* **2008**, *130*, 1894-1902.

138. Ramaiah, D.; Joy, A.; Chandrasekhar, N.; Eldho, N. V.; Das, S.; George, M. V. Halogenated Squaraine Dyes as Potential Photochemotherapeutic Agents. Synthesis and Study of Photophysical Properties and Quantum Efficiencies of Singlet Oxygen Generation*. *Photochemistry and Photobiology* **1997**, *65*, 783-790.

139. Schweitzer, C.; Schmidt, R. Physical Mechanisms of Generation and Deactivation of Singlet Oxygen. *Chem. Rev.* **2003**, *103*, 1685-1758.

140. Turro, N. J. *Modern Molecular Photochemistry*; University Science Books: Sausalito, CA, 1991.

141. Drobizhev, M.; Stepanenko, Y.; Dzenis, Y.; Karotki, A.; Rebane, A.; Taylor, P. N.; Anderson, H. L. Extremely Strong near-Ir Two-Photon Absorption in Conjugated Porphyrin

Dimers: Quantitative Description with Three-Essential-States Model. *J. Phys. Chem. B* **2005**, *109*, 7223-7236.

142. Wilkinson, F.; Helman, W. P.; Ross, A. B. Quantum Yields for the Photosensitized Formation of the Lowest Electronically Excited Singlet State of Molecular Oxygen in Solution. *Journal of Physical and Chemical Reference Data* **1993**, *22*, 113-262.

143. Hellwarth, R.; Cherlow, J.; Yang, T.-T. Origin and Frequency Dependence of Nonlinear Optical Susceptibilities of Glasses. *Phy. Rev. B* **1975**, *11*, 964-967.

144. Santran, S.; Canioni, L.; Sarger, L.; Cardinal, T.; Fargin, E. Precise and Absolute Measurements of the Complex Third-Order Optical Susceptibility. *J. Opt. Soc. Am. B* **2004**, *21*, 2180-2190.

145. Hanson, E. G.; R., S. Y.; Wang, G. K. L. Experimental Study of Self-Focusing in a Liquid Crystalline Medium. *Appl. Phys.* **1977**, *14*, 65-70.

146. McMorrow, D.; Lotshaw, W. T.; Kenney-Wallace, G. A. Femtosecond Optical Kerr Studies on the Origin of the Nonlinear Responses in Simple Liquids. *IEEE J. Quantum. Elect.* **1988**, *24*, 443-454.

147. Greene, B. I.; Farrow, R. C. Direct Measurement of a Subpicosecond Birefringent Response in Cs2. *J. Chem. Phys.* **1982**, *77*, 4779.

148. Kovsh, D. I.; Yang, S.; Hagan, D. J.; Van Stryland, E. W. Nonlinear Optical Beam Propagation for Optical Limiting. *Appl. Opt.* **1999**, *38*, 5168-5180.

149. Huang, T.-H.; Hsu, C.-C.; Wei, T.-H.; Chang, S.; Yen, S.-M.; Tsai, C.-P.; Liu, R.-T.; Kuo, C.-T.; Tse, W.-S.; Chia, C. The Transient Optical Kerr Effect of Simple Liquids Studied with an Ultrashort Laser with Variable Pulsewidth. *IEEE J. Sel. Top. Quant.* **1996**, *2*, 756-768.

150. Cao, W.; Peng, Y.-H.; Leng, Y.; Lee, C. H.; Herman, W. N.; Goldhar, J. In *Organic Thin Films for Photonic Applications*; Herman, W. N., Flom, S. R., Foulger, S. H., Eds.; American Chemical society: Washington DC, 2010.

151. Burgin, J.; Guillon, C.; Langot, P. Femtosecond Investigation of the Non-Instantaneous Third-Order Nonlinear Suceptibility in Liquids and Glasses. *Appl. Phys. Lett.* **2005**, *87*, 211916.

152. Sato, Y.; Morita, R.; Yamashita, M. Study on Ultrafast Dynamic Behaviors of Different Nonlinear Refractive Index Components in Cs2 Using a Femtosecond Interferometer. *Jpn. J. Appl. Phys.* **1997**, *36*, 2109.

153. Yan, X.-Q.; Zhang, X.-L.; Shi, S.; Liu, Z.-B.; Tian, J.-G. Third-Order Nonlinear Susceptibility Tensor Elements of Cs2 at Femtosecond Time Scale. *Opt. Express* **2011**, *19*, 5559-5564.

154. Ganeev, R. A.; Ryasnyansky, A. I.; Baba, M.; Suzuki, M.; Ishizawa, N.; Turu, M.; Sakakibara, S.; Kuroda, H. Nonlinear Refraction in Cs2. *Appl. Phys. B* **2004**, *78*, 433-438.

155. Greene, B. I.; Farrow, R. C. The Subpicosecond Kerr Effect in Cs2. *Chem. Phys. Lett.* **1983**, *98*, 273.

156. Ganeev, R. A.; Ryasnyansky, A. I.; Ishizawa, N.; Baba, M.; Suzuki, M.; Turu, M.; Sakakibara, S.; Kuroda, H. Two- and Three-Photon Absorption in Cs2. *Opt. Commun.* **2004**, *231*, 431-436.

157. Yan, X.-Q.; Liu, Z.-B.; Shi, S.; Zhou, W.-Y.; Tian, J.-G. Analysis on the Origin of the Ultrafast Optical Nonlinearity of Carbon Disulfide around 800 Nm. *Opt. Express* **2010**, *18*, 26169-26174.

158. McGlynn, S. P.; Rabalais, J. W.; McDonald, J. R.; Scherr, V. M. Electronic Spectoscopy of Isoelectronic Molecules. Ii. Linear Triatomic Groupings Containing Sixteen Valence Electrons. *Chem. Rev.* **1971**, *71*, 73-108.

159. Dove, J. E.; Hipper, H.; Plach, J.; Troe, J. Ultraviolet Spectra of Vibrationally Highly Excited Cs2 Molecules. *J. Chem. Phys.* **1984**, *81*, 1209-1214.

160. Newport. Application Note 29: Prism Compressor for Ultrashort Laser Pulses. [Online Early Access]. Published Online: 2006.

161. Yan, X.-Q.; Liu, Z.-B.; Zhang, X.-L.; Zhou, W.-Y.; Tian, J.-G. Polarization Dependence of Z-Scan Measurement: Theory and Experiment. *Opt. Express* **2009**, *17*, 6397-6406.

162. Ganeev, R.; Ryasnyanskiĭ, A.; Kuroda, H. Nonlinear Optical Characteristics of Carbon Disulfide. *Opt. Spectrosc.* **2006**, *100*, 108-118.

163. Couris, S.; Renard, M.; Faucher, O.; Lavorel, B.; Chaux, R.; Koudoumas, E.; Michaut, X. An Experimental Investigation of the Nonlinear Refractive Index (N2) of Carbon Disulfide and Toluene by Spectral Shearing Interferometry and Z-Scan Techniques. *Chem. Phys. Lett.* **2003**, *369*, 318-324.

164. Lawrence, B.; Torruellas, W. E.; Cha, M.; Sundheimer, M. L.; Stegeman, G. I.; Meth, J.; Etemad, S.; Baker, G. Identification and Role of Two-Photon Excited States in a Π-Conjugated Polymer. *Phys Rev Lett* **1994**, *73*, 597-600.

165. Ferdinandus, M. R.; Reichert, M.; Dmitry, F.; Scott, W.; Hagan, D. J.; Stryland, E. W. V. In *Nonlinear Photonics* Colorado Springs, CO, 2012 (Accepted as Oral Presentation).

166. Mathis, K. S.; Kuzyk, M. G.; Dirk, C. W.; Tan, A.; Martinez, S.; Gampos, G. Mechanisms of the Nonlinear Optical Properties of Squaraine Dyes in Poly(Methyl Methacrylate) Polymer. *J. Opt. Soc. Am. B* **1998**, *15*, 871-883.

167. Melhuish, W. H. Quantum Efficiencies of Fluorescence of Organic Substances: Effect of Solvent and Concentration of the Fluorescent Solute1. *J. Phys. Chem.* **1961**, *65*, 229-235.